Reanalyzing Thermocouple Temperature Response for Evidence of Convective Flow

by

Mohammad Aghabarati

A thesis submitted in partial fulfillment of the requirements for the degree of

Master of Science

in

Geotechnical Engineering

Department of Civil and Environmental Engineering
University of Alberta

Abstract

Steam Assisted Gravity Drainage (SAGD) technology has made possible the in situ production of bitumen at commercial scale. In this study, different mechanisms involved in heat transfer through porous media above SAGD steam chambers are investigated. Semi-analytical and numerical models have been utilized in the assessment of the physics of heat transfer above steam chambers.

Real thermocouple data of SAGD operations are extracted from appended files to in-situ performance presentations submitted to the Alberta Energy Regulator (AER) by operators. Quality assurance of the extracted data is also conducted in order to minimize the fluid effects in observation wells. Semi-analytical and numerical investigation of results along with available petrophysical logs are used to estimate the location of steam chamber front and also contributing heat transfer mechanisms through the overlying strata.

“Now this is not the end. It is not even the beginning of the end. But it is, perhaps, the end of the beginning”

Winston Churchill

To my wonderful family, mother and father, sister and brothers.

Acknowledgements

I am grateful to my supervisor Dr. Chalaturnyk for giving me the opportunity to work in his research group. I'm fortunate to have him not only as a mentor for my studies but also a mentor for life. Special acknowledgement to the sponsors of the Foundation CMG Industrial Research Consortia in Reservoir Geomechanics at the University of Alberta; whose financial support give us opportunities to excel in science and engineering.

Table of Contents

Chapter 1: Introduction 1

1.1. Geology 1

1.2. Thermal Recovery of Bitumen with SAGD 5

1.3. Hypothesis 8

1.4. Objective 8

1.5. Methodology 8

Chapter 2: Literature Review 9

2.1. Heat Transfer Ahead of Steam Chamber 9

2.2. Geomechanical Effects on Permeability during SAGD 12

2.3. Thermal properties of Geomaterials 15

2.4. Observation Well Data Analysis 16

Chapter 3: Heat Transfer Mechanisms above Steam Chambers 18

3.1. Heat Conduction 19

3.1.1. One-dimensional Heat Conduction 20

3.1.1.1. One-dimensional Heat Conduction with Varying Interface Temperature 22

3.1.1.2. Temperature Distribution ahead of a Moving Front 23

3.1.1.3. Effect of Initial Formation Temperature on 1D Heat Conduction Solution 25

3.1.1.4. Uncertainty in the Value of Thermal Diffusivity 28

3.1.2. Two Dimensional Heat Conduction 31

3.1.2.1. Heat Conduction from a Fixed Hot Interface 32

3.1.2.2. Heat Conduction from a Spreading Hot Interface 38

3.1.2.3. Heat Conduction from Expanding Steam chambers 39

3.2. Heat Conduction with Convection 47

3.2.1. One-dimensional Heat Conduction with Convection 47

3.2.1.1. Effect of Magnitude of Fluid Velocity on Deviation from Pure Conduction 48

3.2.1.2. Uncertainty in the Value of Fluid Convective Velocity 52

3.2.2. Two dimensional Heat Conduction with Convection 54

3.2.2.1. Heat Conduction with Convection through an Isotropic Medium 58

3.2.2.2. Heat Conduction and Convection through an Anisotropic Medium 62

3.2.2.3. Heat Conduction with Convection from Expanding Steam Chambers 63

3.3. Summary 73

Chapter 4: Calculation of Thermal Diffusivity from Temperature Profiles 75

4.1. Thermal Diffusivity from 1D temperature profiles 75

4.1.1. Calculation of Thermal Diffusivity from 1D Analytical Conductive Solution 76

4.1.2. Effect of Fluctuating Interface Temperature 77

4.1.3. Effect of Formation Cold Temperature 79

4.1.4. Effect of Initial Temperature Conditions from Moving Interface 81

4.2. Thermal Diffusivity from 2D Conductive Temperature Profiles 83

4.3. Thermal diffusivity from 1D Conductive and Convective Temperature Profiles 85

4.4. Thermal Diffusivity from 2D Conduction and Convection Temperature Profiles 87

4.5. History Matching Temperature Profiles 88

4.5.1. History Matching of 2D Conductive Temperature Profiles 88

4.5.2. History Matching 1D Conductive and Convective Temperature Profiles 91

4.5.3. History Matching 2D Conductive and Convective Temperature Profiles 94

4.6. Summary 97

Chapter 5: Selection of Observation Wells 98

5.1. Temperature Monitoring During SAGD 98

5.1.1. Wellbore Fluid Effects on Temperature Measurements 100

5.1.2. Vertical Growth of Steam Chamber 106

5.1.3. Steam Detouring Around Impermeable Layers 106

5.1.4. Wellbore Casing Conduction 109

5.2. Selection of Data for Thermal Diffusivity Calculation 110

5.3. Summary 115

Chapter 6: Observation Well Data Analysis 116

6.1. Post-analysis of Observation Well Temperature Profiles 116

6.1.1. Conductive Case 116

6.1.1.1. Verification with Experimental results 116

6.1.1.2. History Matching with Synthetic Model 117

6.1.2. Convective Case 120

6.2. Estimation of Convective Component from temperature Profiles 122

6.2.1. Determination of vertical Fluid Velocity from Temperature Profiles 122

6.2.2. Temperature Profile Interpolation with Cubic Splines 124

6.2.3. Calculation of Vertical Fluid Velocity from Observation Well Data 125

6.3. Results Comparison of Observation Well Data Analysis 129

6.4. Summary 132

Chapter 7: Conclusions and Recommendations 133

7.1. Summary 133

7.2. Limitations 134

7.3. Recommendations 135

References 137

Appendix I: Analytical solution of heat conduction ahead of a hot interface with exponentially decreasing initial temperature 145

Appendix II: Calculation of Thermal Diffusivity from 2D Conductive Models 148

Appendix III: Observation Well Data Analyses 160

List of Tables

Table 3.1: Statistical distribution of thermal properties..28

Table 3.2: Thermal properties of solids and pore fluid used in COMSOL.......................55

Table 3.3: Properties of the geomaterials used in two-dimensional modeling. 67

Table 4.1: Back calculated thermal diffusivity based on temperature logs obtained from 2D conductive models. 85

Table 4.2: Back calculated thermal diffusivity based on temperature logs obtained from 2D conductive and convective models 87

Table 5.1: Material properties of formation and casing used in modeling by Closmann et al. (1979)..109

Table 6.1: Summary of calculated thermal diffusivities from observation well temperature profiles. 131

List of Figures

Figure 1.1: Oil sands deposits in Alberta. Figure adapted from Hein et al. (2000). 2

Figure 1.2: Depositional environment of the Lower McMurray. Figure adapted from Hein et al. (2000). 3

Figure 1.3: McMurray estuarine facies association model for channel, point bar, abandonment fill, and overbank deposits. Figure adapted from Hein et al. (2000). 4

Figure 1.4: McMurray estuarine facies association model for tidal channel, tidal flat, barrier and back barrier deposits. Figure adapted from Hein et al. (2000). 5

Figure 1.5: Steam Assisted Gravity Drainage (SAGD) 6

Figure 3.1: Hot interface contact with overburden after steam chamber rises to the top of pay zone. 21

Figure 3.2: Temperature profiles of 1D conduction heating ahead of a hot interface in an infinite medium. 21

Figure 3.3: 1D Temperature profiles within an infinite medium subject to varying interface temperature. 23

Figure 3.4: Evolution of temperature profiles ahead of a 1D moving front. 24

Figure 3.5: Transient vs. steady state 1D temperature responses ahead of an advancing front with constant front velocity. 25

Figure 3.6: 1D Temperature profiles of conduction heat transfer with T0 ∗= e − ξx as initial condition. 26

Figure 3.7: Influence of initial conditions on temperature profiles in one-dimensional heat conduction....27
Figure 3.8: Decrease in temperature response difference over time between solutions of Equation 3.5 and Equation 3.11....27
Figure 3.9: Distribution of thermal diffusivity....29
Figure 3.10: Temperature uncertainty over time at different distances from the hot interface. (a) 10m. (b) 20 m. (c) 30 m....30
Figure 3.11: CoV of temperature values of conductive heat transport after 3000 days with respect to distance from the hot interface....31
Figure 3.12: 1D Temperature distributions in a homogeneous medium after. (a) 100 days. (b) 1500 days. (c) 3000 days....33
Figure 3.13: Comparison of numerical results of 1D model in COMSOL with the analytical 1D solution in conduction heat transfer....34
Figure 3.14: Temperature monitoring along vertical lines through overburden....34
Figure 3.15 : 2 dimensional heat loss to overburden in a homogeneous medium. (a) 500 days. (b) 1500 days. (c) 3000 days....35
Figure 3.16: Temperature profiles along the monitoring lines at: (a) center. (b) midway between center and edge. (c) edge. (d) 1m from edge. (e) 2m from edge (f) 5m from edge of the hot fixed interface....36
Figure 3.17 : Deviation of temperature profiles obtained from a fixed hot interface from the 1D analytical solution. (a) center line. (b) midway between center line and edge. (c) edge of the hot interface....37

Figure 3.18: 2D temperature profiles of a spreading hot interface. (a) 500 days. (b) 1250 days. (c) 2500 days. (d) 3500 days. 40
Figure 3.19: Temperature profiles along the monitoring lines at: (a) center. (b) midway between center and edge. (c) edge. (d) 1m from edge. (e) 2m from edge (f) 5m from edge of the hot expanding interface. 41
Figure 3.20: Deviation of temperature profiles obtained from a conductive expanding hot interface from the 1D analytical solution. (a) center line. (b) midway between center line and edge. (c) edge of the hot interface. 42
Figure 3.21: Temperature monitoring locations. L1 middle of the model. L2 14m off the center of first steam chamber on the right. L3 14m off the center of second steam chamber on the right. 43
Figure 3.22: Two dimensional temperature distributions of five steam chambers with conduction through the medium over time. (a) 500 days. (b) 1500 days. (c)2500 days. (d) 3500 days. 44
Figure 3.23: Comparison of temperature profiles from two dimensional spreading steam chambers with conduction to 1D conduction case along: (a) L1 . (b) L2 . (c) L3 45
Figure 3.24: Temperature Difference between temperature profiles obtained from the two dimensional expanding chamber with conduction and 1D conduction case along: (a) L1 . (b) L2 . (c) L3..46

Figure 3.25: One-dimensional conductive and convective temperature profiles ahead of a hot interface. 48

Figure 3.26: Effect of fluid velocity (v_{fluid}) on temperature profiles. a) $vfluid = .5myear$. b) $vfluid = 2myear$. c) $vfluid = 5myear$. 49

Figure 3.27: One-dimensional temperature difference between pure conduction and conduction with convection heat transport at different fluid velocities. a) $vfluid = .5myear$. b) $vfluid = 2myear$. c) $vfluid = 5myear$. 51

Figure 3.28: Temperature uncertainty over time at different distances from the hot interface in conductive with convective heat transport with $vaverage = 2myear$ and $CoV = σvaverage = 15\%$. (a) 10m. (b) 20 m. (c) 30 m from the hot interface. 53

Figure 3.29: Uncertainty in temperature of conductive with convective heat transport after 3000 days with respect to distance from hot interface. 54

Figure 3.30: Numerical simulation of 1D conductive and convective heat transport. Temperature surfaces after: (a)500 days, (b) 1500 days. (c) 3000 days. 56

Figure 3.31: Comparison of one-dimensional analytical and numerical solutions of conduction with convective flow with constant vertical pore fluid velocity. 57

Figure 3.32: Fluid inlet and drainage paths in the two dimensional model. 58

Figure 3.33: Streamlines of fluid flow in the two dimensional isotropic model 59

Figure 3.34: Temperature distribution of two dimensional heat losses from a fixed hot interface through an isotropic medium with conduction and convection. (a) 500 days. (b) 1500 days. (c) 3000 days....................60

Figure 3.35: Comparison of temperature profiles obtained from the 2D isotropic conductive and convective heat loss from a fixed interface with 1D analytical conduction and convection solution: (a) center (b) midway between center and edge (c) edge of hot interface....................61

Figure 3.36: Streamlines of fluid flow in the two dimensional anisotropic model...........62

Figure 3.37: Temperature distribution of two dimensional heat loss from a fixed hot interface through an anisotropic medium with convection. (a) 500 days. (b) 1500 days. (c) 3000 days...64

Figure 3.38: Comparison of temperature profiles obtained from the 2D anisotropic conductive and convective heat loss from a fixed interface with 1D analytical solution. (a) center. (b) midway between center and edge. (c) edge of hot interface.................................65

Figure 3.39: Configuration of the two dimensional model with five expanding steam chambers...66

Figure 3.40: Two dimensional temperature distributions of five steam chambers with conduction and convection heat transport through the medium over time. (a) 500 days. (b) 1500 days. (c)2500 days. (d) 3500 days..69

Figure 3.41: Darcy's velocity field above steam chambers. (a) horizontal component. (b) vertical component. 70

Figure 3.42: Comparison of temperature profiles from two dimensional spreading steam chambers with conduction and convection to 1D conduction case along: (a) L1 . (b) L2 . (c) L3 71

Figure 3.43: Temperature difference between temperature profiles obtained from the two dimensional expanding chamber with conduction and convection to 1D conduction case along: (a) L1 . (b) L2 . (c) L3 72

Figure 4.1: Temperature profiles of a one-dimensional conduction case from analytical solution 76

Figure 4.2: ICEF plots of temperature profiles from 1D analytical solution.....................76

Figure 4.3: Changes in the slope of ICEF over time for the 1D analytical conduction case. 77

Figure 4.4: ICEF plots of 1D conductive temperature profiles with varying interface temperature. 78

Figure 4.5: Changes in the slope of ICEF over time for the 1D analytical conductive case with varying interface temperature...............................78

Figure 4.6: ICEF plots of temperature profiles assuming Tcold = 5℃. 79

Figure 4.7: ICEF plots of temperature profiles assuming Tcold = 15℃. 80

Figure 4.8: Deviation from the true value of thermal diffusivity associated with uncertainty in formation cold temperature...80

Figure 4.9: Temperature profiles ahead of a hot interface with initial conditions set as steady state solution of a moving front 81

Figure 4.10: ICEF plots of temperature profiles from a hot interface with initial conditions set as steady state solution of a moving front........................82

Figure 4.11: Changes in the slope of ICEF plots over time for a hot interface with initial conditions set as steady state solution of a moving front. 82

Figure 4.12: Effect of the velocity of the moving front before stopping on back calculated thermal diffusivity. 83

Figure 4.13: One-dimensional conductive and convective temperature profiles generated or calculation of thermal diffusivity. 86

Figure 4.14: ICEF of one-dimensional conductive and convective temperature profiles 86

Figure 4.15: Changes in the slope of ICEF over time from convective temperature profiles. 87

Figure 4.16: History matching of the observed behavior of 2D conductive spreading steam chambers with the back-calculated thermal diffusivity. (a) L1 . (b) L2 . (c) L3. 89

Figure 4.17: Difference between the observed behavior from the 2D conductive spreading steam chambers with the predicted values based on back calculation of thermal diffusivity. (a) L1 . (b) L2 . (c) L3. 90

Figure 4.18: Temperature profiles of conductive and convective fronts and pure conductive fronts based on the lower predicted value of thermal diffusivity. 91

Figure 4.19: Difference between temperature profiles of conductive and convective fronts and pure conductive fronts based on the lower predicted value of thermal diffusivity. 92

Figure 4.20: Temperature profiles of conductive and convective fronts and pure conductive fronts based on the higher predicted value of thermal diffusivity. 93

Figure 4.21: Difference between temperature profiles of conductive and convective fronts and pure conductive fronts based on the higher predicted value of thermal diffusivity. 93

Figure 4.22: History matching of the observed behavior of 2D conductive and convective spreading steam chambers with the back-calculated thermal diffusivity. (a) L1 . (b) L2 . (c) L3. 95

Figure 4.23: Difference between the observed behavior from the 2D conductive and convective spreading steam chambers with the predicted values based on back calculation of thermal diffusivity. (a) L1 . (b) L2 . (c) L3 96

Figure 5.1: Monitoring temperature with observation wells. Figure adapted from Suncor (2015) 99

Figure 5.2: Installation of thermocouples in an observation well. (a) Thermocouples strapped outside the casing and cemented to the formation. Photo adapted from Statoil (2014). (b) Thermocouples hanging inside the observation well. Photo adapted from Cenovus (2014) 100

Figure 5.3: Smearing effect of wellbore fluid in an observation well. Figure adapted from Griston (1989) 101

Figure 5.4: Experimental study of wellbore fluid on temperature profiles. Photo adapted from Kagawa et al. (1992). 102

Figure 5.5: Temperature response of an observation well under possible fluid wellbore effects. Data obtained from AER In-situ performance presentation submitted by Cenovus (2011). (https://www.aer.ca/documents/oilsands/insitupresentations/2011AthabascaCenovusFosterCreekSAGD8623.pdf) 103

Figure 5.6: Refluxing in the observation well. Data obtained from AER In-situ performance presentation submitted by Cenovus (2011) (https://www.aer.ca/documents/oilsands/insitupresentations/2011AthabascaCenovusFosterCreekSAGD8623.pdf) 104

Figure 5.7: Temperature history of an observation well during 5 years of monitoring. Data obtained from AER in-situ performance reports submitted by Cenovus (2015). https://www.aer.ca/documents/oilsands/insitupresentations/2015AthabascaCenovusFosterCreekSAGD8623.pdf 105

Figure 5.8: Three instances of refluxing inside OB 100/11-15-076-06W4/00. 105

Figure 5.9: Steam chamber growth through low permeability interbeds. (a) Temperature history of steam chamber growth. (b) Gamma log of OB 100/15-02-095-06W4/00. Data extracted from Suncor (2015).https://www.aer.ca/documents/oilsands/insitupresentations/2015AthabascaSuncorFirebagSAGD8870.pdf......107

Figure 5.10: Detouring of steam around an impermeable layer. (a) Temperature history recorded with observation well. (b) Petrophysical logs: Resistivity on the far left and Gamma log on the far right. Data extracted from Cenovus (2015). (https://www.aer.ca/documents/oilsands/insitu-presentations/2015AthabascaCenovusChristinaSAGD8591.pdf) 108

Figure 5.11: Difference between dimensionless temperature profiles along the wellbore casing and formation for an iron casing with 412 in diameter. Figure adapted from Closmann et al. (1979). 110

Figure 5.12: Temperature profiles of OB 100/05-11-095-06W4/00 obtained from Suncor (2015) AER in-situ performance presentation...........................112

Figure 5.13: Maximum recorded temperature in OB 100/05-11-095-06W4/00.............113

Figure 5.14: ICEF slope of temperature profiles from OB 100/05-11-095-06W4/00...113

Figure 5.15: Changes in the slope of ICEF plot over time for temperature profiles of OB 100/05-11-095-06W4/00. 114

Figure 6.1: Thermal diffusivity of oil sands measured in lab (Seto, 1985). 117

Figure 6.2: Comparison of real observation well data of OB 100/05-11-095-06W4/00 with the 1D synthetic model. 118

Figure 6.3: Gamma log of OB 100/05-11-095-06W4/00. Figure adapted from Suncor (2015)..119

Figure 6.4: Temperature profiles of OB 105/09-01-095-06W4/00 from Suncor (2013)...120

Figure 6.5: Comparison of real observation well data of OB 105/09-01-095-06W4/00 with the 1D synthetic model. 121

Figure 6.6: Gamma log of OB 105/09-01-095-06W4/00. Figure adapted from Suncor (2015)..122

Figure 6.7: Change in the dimensionless temperature profile with β. 124

Figure 6.8: Temperature profiles of OB 102/15-12-095-06W4/00. Data extracted from Suncor (2012). 126

Figure 6.9: Interpolation of a temperature profile with cubic splines.............................127

Figure 6.10: Finding the closest exponential solution from Equation 6.2 to the interpolated data. 127

Figure 6.11: Finding the closest exponential solution along the temperature profile. 128

Figure 6.12: Calculated convective fluid velocity from the closest exponential solution...128

Figure 6.13: Location of OB 12 (102/15-12-095-06W4/00) relative to pad. Figure adapted from (Suncor 2012). 129

Chapter 1: Introduction

Alberta is the largest producer of oil and gas in Canada with more than 60 percent of the total oil and equivalent production in the form of marketable bitumen in 2015 (AER, 2016). Out of 177 billion barrels of initial established crude bitumen reserves in Alberta, 11.4 billion barrels of crude bitumen have been produced with annual crude bitumen production reaching 923 million barrels of bitumen in 2015(AER, 2016).

1.1. Geology

Hein et al. (2006) provide one of the most comprehensive resources describing the geology of the McMurray Formation is “Subsurface Geology of the Athabasca Wabiskaw-McMurray Succession: Lewis-Fort McMurray Area, Northeastern Alberta (NTS 74D/74E)”. The following section provides a summary of the main points from this report.

Bitumen reserves are found mainly in four oil sands deposits in Alberta: the Athabasca, Wabasca, Cold Lake, and Peace River as shown in Figure 1.1 (Hein et al., 2000). The focus of this section will be on the regional geology of the Athabasca oil sands in northeast Alberta, where most SAGD operations are situated and the primary formation of interest is the bitumen bearing McMurray Formation.

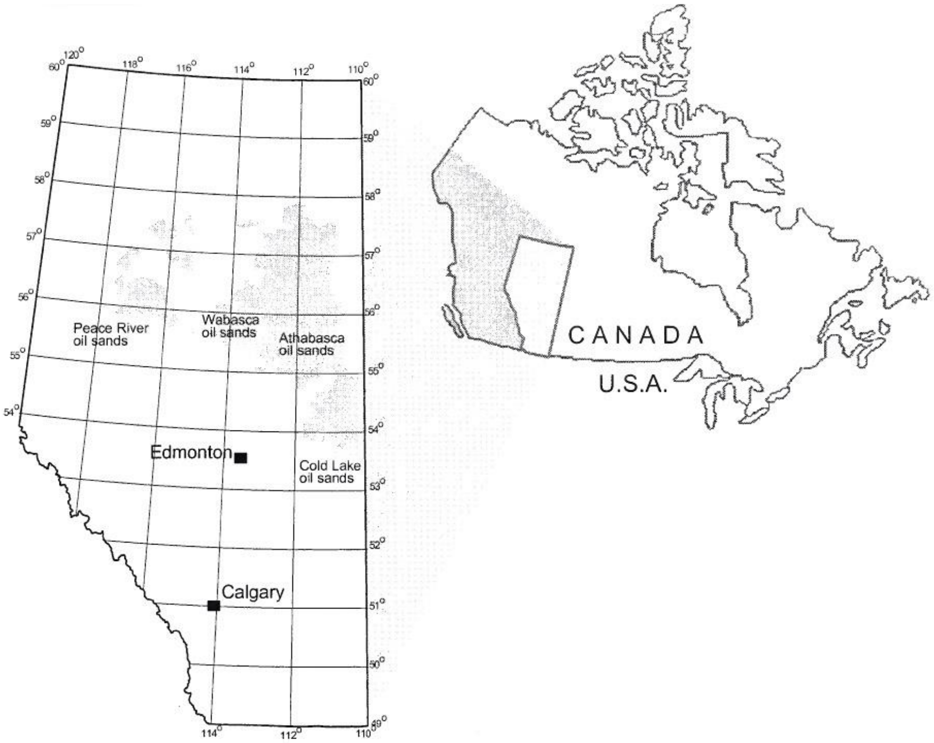

Figure 1.1: Oil sands deposits in Alberta. Figure adapted from Hein et al. (2000).

The McMurray Formation is underlain unconformably by Devonian carbonates and overlain by the Clearwater Formation. Bitumen is predominantly found in the pore spaces of the McMurray Formation. Structural pre-Cretaceous anomalies resulting from differential erosion combined with tectonic collapse by dissolution of evaporites. sinkholes, brecciation, folding and faulting close to the dissolution front are the paleokarst features associated with carbonate collapse (Hein et al., 2000). The McMurray Formation and the Wabiskaw Member of the Clearwater Formation sediment dispersal patterns are substantially impacted by these reliefs (Hein et al., 2000).

In the past, the McMurray Formation was divided into three members: Fluvial Lower McMurray, Estuarine channel and point bar middle McMurray, and coastal plain Upper McMurray. This classification, however, is used mainly in surface mining. Hein et al., (2000) observed that differentiation between Middle McMurray and Upper McMurray becomes impossible when distinctive facies or log-markers are not present. They also mentioned that biostratigraphic analyses of the previously defined Middle or Upper McMurray units did not reveal any differences in age. Therefore, they recommended the "Middle McMurray" unit be abandoned and be included in the Upper McMurray succession. In the new system three associations were introduced: McMurray fluvial, McMurray Fluvio-Estuarine, and McMurray Estuarine facies associations.

The Lower McMurray unit is a fluvial deposit and heavily channelized that unconformably overlies Devonian Carbonates (Hein et al., 2000). Clean, pebbly to medium-grained sands are the dominant facies with deposits of overbank and marsh formed on the primary channels and also isolated bedrock highs (Hein et al., 2006). Figure 1.2 shows the depositional environment of the Lower McMurray.

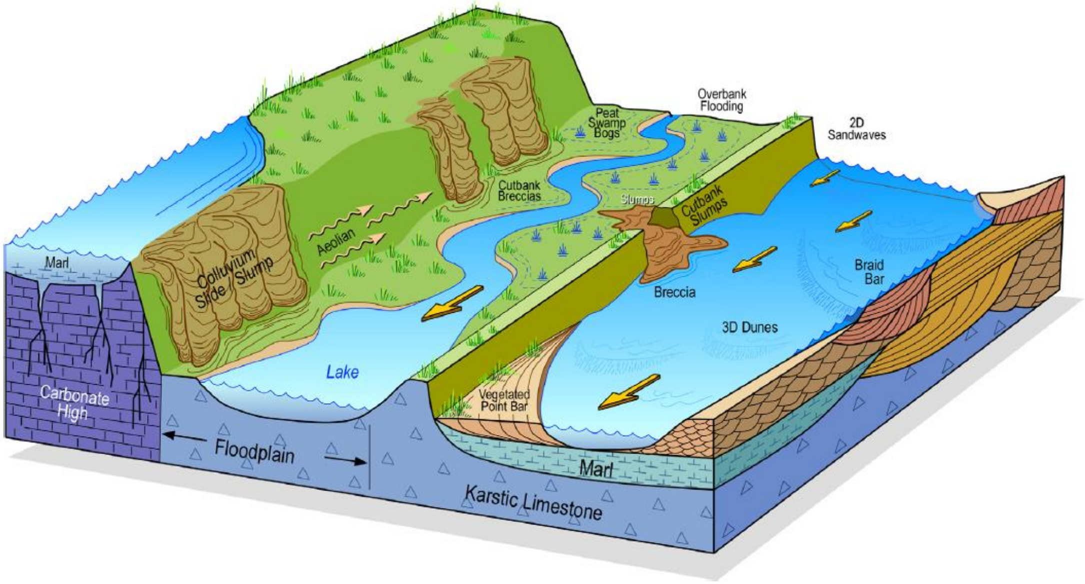

Figure 1.2: Depositional environment of the Lower McMurray. Figure adapted from Hein et al. (2000).

The McMurray fluvio-estuarine association is massive or mainly trough crossbedded and consists of clean, fine to medium grained sands. Mudstone and clast breccia interbeds are less common. Crossbedded sands grade up to bioturbated thin alternations of low angle mudstone and sand known as inclined heterolithic stratified (IHS). Abandonment channel plugs are illustrative of thicker mudstone units. Estuarine channel deposits and estuarine point bars are representative of crossbedded sands and IHS beds, respectively (Hein et al., 2006).

The McMurray Estuarine association consists of very fine to medium grained clean sand with less medium-grained to pebbly sands and common mudstone clasts. Interbedding of mudstone and sands are variable and sands grade up to bioturbated IHS units. Meandering channels and point bar depositions are the primary feature of this association respectively (Hein et al., 2006). The amount of incision determines the preservation of the uppermost deposits of the facies in this association. Figures 1.3 and 1.4 depict the depositional environments of the McMurray Estuarine facies.

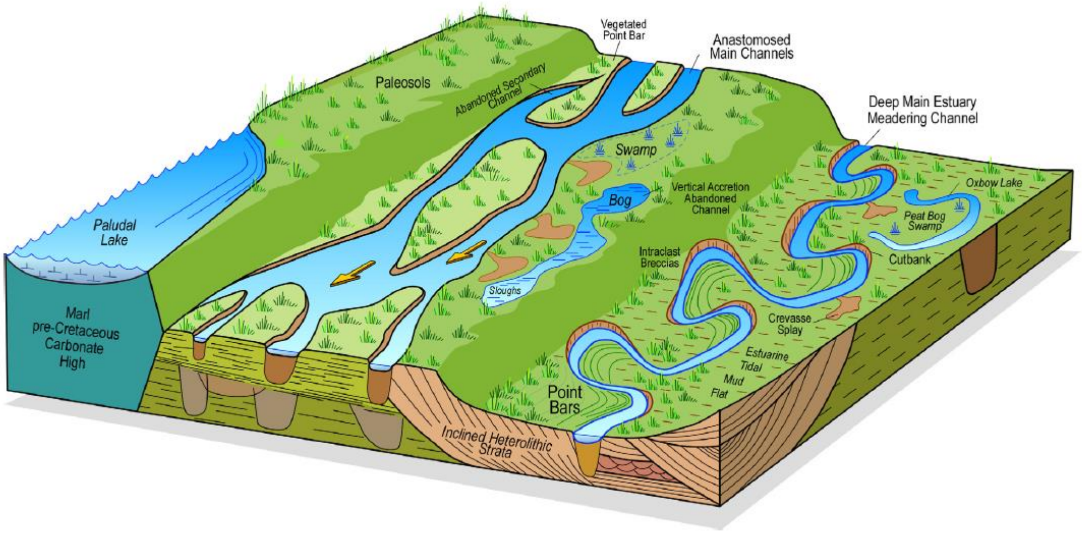

Figure 1.3: McMurray estuarine facies association model for channel, point bar, abandonment fill, and overbank deposits. Figure adapted from Hein et al. (2000).

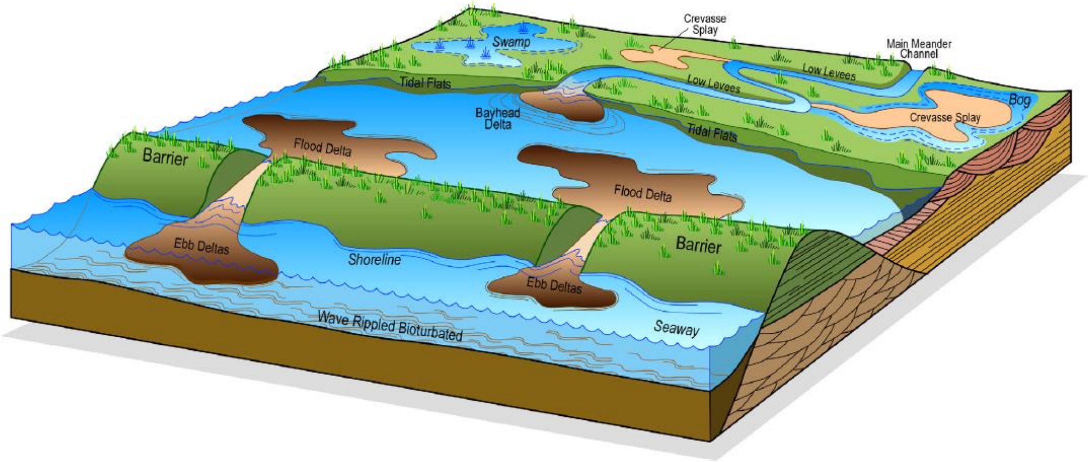

Figure 1.4: McMurray estuarine facies association model for tidal channel, tidal flat, barrier and back barrier deposits. Figure adapted from Hein et al. (2000).

1.2. Thermal Recovery of Bitumen with SAGD

There are two methods of bitumen production in Alberta: surface mining and in-situ. Currently, in-situ bitumen is produced by three practices: primary production, cyclic steam stimulation (CSS), and steam assisted gravity drainage (SAGD) (AER, 2015). Primary crude bitumen is the flow of some bitumen to a well. However, CSS and SAGD are enhanced in-situ oil recovery schemes whereby the viscosity of oil is reduced as a result of steam injection into the oil sands (AER, 2015).

In the SAGD bitumen recovery technique a pair of horizontal wells, one above the other, are drilled near the base of the reservoir. Steam is injected continuously to the well on top (injector) and tends to rise. Steam will lose its latent heat energy and heat up the bitumen resulting in a dramatic reduction of bitumen viscosity. It then falls as condensate with the heated bitumen and will be drained continuously by the producer well at the bottom on the injector (Butler, 1991). Over time, oil will be drained from the reservoir and replaced with steam, forming a steam chamber. However, vertical growth of steam chamber will be impeded by geological layers with very low permeabilities (Fustic et al., 2011). As oil is produced, steam chamber will grow laterally and deliver heat to the edges of the steam chamber. The process is shown in Figure 1.5.

All of the heat released from steam is not transferred to the reservoir and a portion of it is lost to overburden and underburden. SAGD operators monitor the creation and growth of steam chambers with observation wells and submit the recorded responses to Alberta Energy Regulator (AER) as part of their In-situ Performance Presentation.

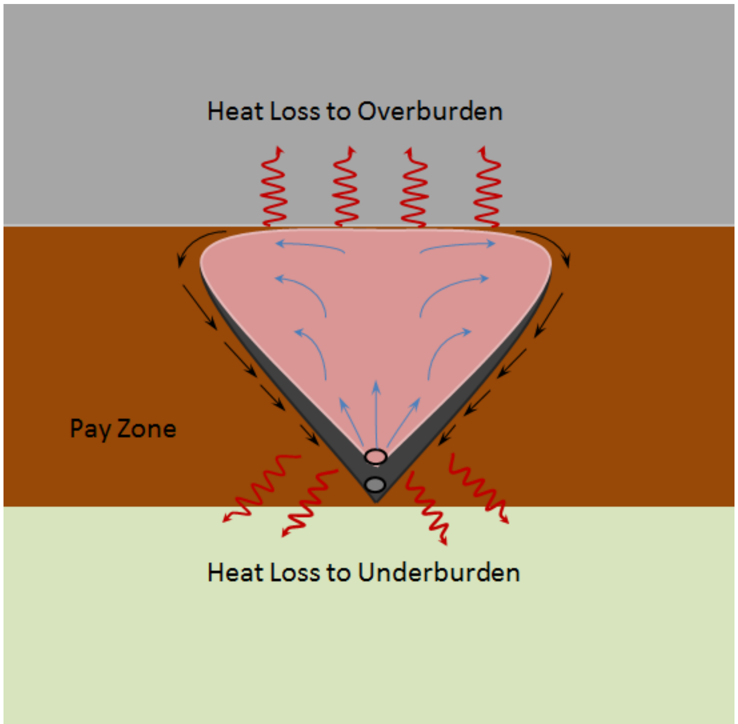

Figure 1.5: Steam Assisted Gravity Drainage (SAGD)

These observation wells record the temperature responses in the heated pay zone and also the underlying and overlying strata during the life cycle of a SAGD operation. Investigation of the recorded temperatures can help understand the physics of the mechanisms involved in heat transfer through the layers overlying the pay zone. To date, it is assumed that the dominant heat transfer mechanism by which heat is lost to overburden is conduction and convective components are believed to be negligible (Butler, 1991). The upper layers of the McMurray Formation directly above the Clearwater Formation shale caprock consist of inclined heterolithic strata (IHS) and the Wabiskaw Members. Permeability variations in IHS, in particular, are very heterogeneous and may give rise to the possibility of fluid movement through it. It is important to understand if there is fluid movement (convective flow) above the steam chamber because this may lead to pore pressure from steam injection migrating to the bottom of the Clearwater shale, a layer acting as the containment barrier of steam for SAGD operation, much sooner than what was assumed during the design phases of the operation. This possibility cannot be overlooked especially during the circulation phase of SAGD when injection pressures are higher than the operation pressures of SAGD. Therefore, the possible movement of fluid through the overlying sediments necessitates the assessment of caprock integrity from the circulation phase.

Analysis of temperature responses can also unveil the field scale thermal properties of the geomaterials above the pay zone. Thermal properties, along with hydraulic properties, dictate the rate of heat loss and, consequently, thermally induced pore pressures and stresses as a result of steam injection.

1.3. Hypothesis

The hypothesis proposed in this research is that the temperature profiles measured by thermocouples or distributed temperature fiber-optic sensors in SAGD observations wells provide insufficient evidence alone to conclude that fluid mass transfer (i.e. convection) is NOT occurring vertically above SAGD steam chambers.

1.4. Objective

The primary objective of this thesis is to understand the mechanisms by which heat is lost to the overburden. The availability of commercial SAGD monitoring data necessitates a comprehensive study of temperature responses in order to estimate thermal properties of the overlying sediments and draw objective conclusions on the contributing heat transfer mechanisms above the steam chamber.

1.5. Methodology

In order to analyze temperature logs of observation wells for detection of contributing heat transfer mechanisms above steam chambers the following steps are taken:

1. Understanding the physics of heat conduction and convection through porous media by studying synthetic models;
2. Calculation of thermal properties from temperature profiles of synthetic models and determining the influencing factors on over/under-estimation of thermal properties;
3. Verification of observation well temperature logs in order to reduce the deviation of measured values from true formation temperature distributions;
4. Analyzing real observation well temperatures and determining whether or not convection is contributing to heat loss to the caprock.

Chapter 2: Literature Review

2.1. Heat Transfer Ahead of Steam Chamber

Heat can be tranferred ahead of the steam chamber by conduction or a combination of conduction and convection. Butler and Stephens (1981) assumed in their mathematical formulation of SAGD that conduction was the dominant mechanism by which heat penetrated beyond the interface of the steam chamber. Akin (2005) also assumes that heat transfer ahead of the steam chamber is only by conduction.

Heat transfer at the edge of a steam chamber was also studied by Sharma and Gates (2011). They assumed higher water saturations at the edge of the steam chamber that will increase the relative permeability to water and thus enhance the convection of condensate into the reservoir. Sharma and Gates (2011) developed a simple analytical theory to model convective and conductive heat flow by introducing the apparent thermal diffusivity. The apparent thermal diffusivity included both conduction and convection. Energy will be carried into the cold oil sands by diffusion of the condensate by convection and the temperature profile will change to a concave-downward profile (Sharma and Gates, 2011). They concluded that the contribution of convection as a heat transfer mechanism could be relatively large at the edge of the steam chamber. Their results also showed a drop in oil effective permeability thus affecting the recovery.

Aherne and Maini (2008) defined Total Fluid-to-Steam-Ratio (TFSR) as a measure of water leaking off to the reservoir. TFSR was defined as:

$$\mathrm{TFSR} = \frac{\mathrm{H_2OProd} + \mathrm{Oil\ Prod} - \mathrm{Steam\ in\ chamber}}{\mathrm{Steam\ Inj}} \qquad \text{Equation 2.1}$$

Aherne and Maini (2008) showed that pressure drops observed in the Dover Phase B, despite maintaining a constant TFSR, suggested water leak off from the steam chamber to the reservoir in the cold region.

The mobility of water to allow convection of heat in oil sands reservoirs can be tested in the field by monitoring pressure responses in the observation wells (Aherne and Maini, 2008). A study of cold-water injection tests by Aherne and Maini (2008) showed pressure responses in the bitumen rich zones and water movement in the horizontal direction. Aherne and Maini (2008) simulated the cold water injectivity by decreasing the value of irreducible water saturation and thus making water a mobile fluid in its natural saturation in the reservoir, modifying the end points of relative permeability to water and changing the saturations by including a small amount of gas saturation and decreasing the amount of bitumen saturation.

Birrell and Putnam (2000) analyzed thermocouple data above the steam chamber to study the rate of growth of the steam chamber and also detect the barriers preventing the vertical growth of the steam chamber. They discussed the difficulties in using the classical method of finding the steam chamber top and also the rise rate due to the spacing of the thermocouples and false implications of reading thermocouple data when the steam pressure, and subsequently temperature, is reduced but bitumen is at higher temperatures. Birrell and Putnam (2000) concluded that mudbeds with millimeter thicknesses can prevent the vertical growth of the steam chamber in the SAGD process. They were also able to calculate the thermal diffusivity of the formation by analyzing observation well data.

Birrell (2003) discussed the vertical heterogeneity of the McMurray Formation on the SAGD process. He also extended his solution for calculation of thermal diffusivity to the cases where the direction of heat flow was not parallel to the observation well and formed a small angle.

Ito and Suzuki (1996) studied the SAGD process in Hangingstone reservoir numerically. The cyclic steam stimulation (CSS) process was found to be economically unfeasible for the Hangingstone reservoir. They showed while failure and compaction controls the performance of CSS processes, vertical and horizontal permeabilities have strong impact on SAGD. Permeabilities and porosities were modified by the fraction of shale contents in their model. It was mentioned that low horizontal permeability values will not allow feasible forecasts of the SAGD operation. Ito and Suzuki (1996) used arithmetic and harmonic upscaling techniques for evaluation of permeability and porosity for each grid block. In their simulations, Ito and Suzuki (1996) showed how oil and water saturations change near the steam camber edge. After analyzing the temperature data, they also concluded that convective flow was occurring and the main energy transfer was fluid convection. The convex shape of temperature, as opposed to the exponentially decreasing profile in the conductive case, was indicative of convective flow in their simulation results (Ito and Suzuki, 1996). Geomechanics manifested its effects on the shape of growth of steam chamber. Steam chamber could move both upwards and outwards and oil drain through the steam chamber when geomechanical effects were considered in the simulation (Ito and Suzuki, 1996). Ito and Suzuki (1996) concluded that by inclusion of geomechanics, higher injection pressures were required for a feasible oil production.

2.2. Geomechanical Effects on Permeability during SAGD

Geomechanical properties of oil sands change under the injection of steam. Higher temperatures and pore pressures associated to stream injection change the in-situ stress conditions of the reservoir. Bulk volume will be changed as a result of the new stress condition in the reservoir (Li et al., 2004). Changes in volume will affect petrophysical properties such as porosity, absolute permeability, relative permeability, etc. Variation in geomechanical properties can almost be entirely related to porosity changes (Li et al., 2004). Li et al. (2004) discuss the differences between conventional numerical simulations and its shortcomings in the SAGD process. Conventional geomechanical simulations assume no changes in temperatures and total stresses around the boundaries of the reservoir. In SAGD process, however, total stresses may change due to different directional deformations. Injection of steam at higher pressures than the initial reservoir pressure causes unloading due to increase in pore pressure and also an increase in total stress from volume expansion of the grain sands at higher temperatures (Li and Chalaturnyk, 2006). Shearing can occur from the increased total stresses beyond the steam chamber. While unloading does not change the configuration of sand grains with respect to each other much, relative motion of sand grains during shearing causes significant changes in pore geometry (Li and Chalaturnyk, 2006). Lab results show that volume changes associated with unloading are much smaller than that of shearing process (Li and Chalaturnyk, 2006). Li and Chalaturnyk (2006) concluded that absolute permeability and relative permeability to water increases from isotropic unloading and shear dilation during the injection of high temperature steam into oil sands. They also discuss the formulas for the estimation of absolute and relative permeability to water during unloading and shear dilation. Permeability increases more in the vertical direction than in the horizontal direction as tortuosity is affected more in the vertical direction during shearing (Li and Chalaturnyk, 2006).

Steam chamber development and drainage patterns are affected by the deformations in the reservoir (Chalaturnyk and Li, 2004; Ito and Suzuki, 1996). The effects of pore pressure and temperature changes on the pore compressibility and permeability in a decoupled reservoir-geomechanical simulation for shallow, medium, and deep reservoirs were studied by Chalaturnyk and Li (2004). They concluded that the combined effect of pore pressure increase and thermally induced stresses would result in formation deformation. Consequently, permeability values will change during the SAGD process. For a shallow reservoir there is less restraint on deformations in the vertical direction. Therefore, the increase in the magnitude of vertical stresses is less than that of in the horizontal stresses (Chalaturnyk and Li, 2004). Oil sands will undergo different stress paths during the operation. For a particular reservoir, the stress path depends on the location, time, and in-situ stress anisotropy (Chalaturnyk and Li, 2004). Generally, the combined effect of higher injection pressures and higher in-situ stress anisotropy will cause shear dilation of oil sands to occur in a shorter time during the SAGD operation (Chalaturnyk and Li, 2004).

Sequentially coupled reservoir and geomechanical simulations of the UTF phase A were completed by Li and Chalaturnyk (2009). These simulations showed the formation of the steam chamber while the uncoupled simulation did not show any steam chamber development in the reservoir. In their models mudstone with very low permeability (around 0.001 mD) became permeable as a result of shear failure. The permeability of mudstone was increased to 100 mD due to shearing. Permeability of the mudstone was increased further to 1 mD if any tensile failure had occurred (Li and Chalaturnyk, 2009). Collins et al. (2002) showed the accelerated growth of steam chamber by incorporating geomechanical effects and enhanced permeability of oil sands during the SAGD process. Geomechanical effects were found to be beneficial to the process. Operating SAGD at higher pressures will result in increased geomechanical effects, which in turn will influence the process in a positive way. Collins et al. (2002) also mentioned that permeability measurements of disturbed samples might be close to the in situ permeability at high injection pressures, which are the implicit inclusion of geomechanics. Injection of stream at high pressures will result in increase of pore pressures inside the steam chamber and also in the colder zones. Initial mobility of the water in the cold region, increased mobility due to shearing and volume increase, and existence of low bitumen saturated zones in the reservoir contribute to increase in pore pressure and thus reduction in effective stresses (Collins et al., 2002). Higher temperatures induce stresses due to the confinement of the reservoir. By assuming lateral constraints on the deformation of a shallow reservoir, horizontal stresses can increase more than vertical stresses as overburden can be lifted upwards due to expansion (Collins et al., 2002). Oil sands will expand upwards and thus will support some of the overburden load on the cold regions, thus, increasing the vertical stresses thorough the steam chamber (Collins et al., 2002). This “jacking” process is more noticeable for large steam chambers (Collins et al., 2002). The monitoring of pressures and temperatures at UTF Phase B also showed expansion and upward displacement at the onset of steaming when the steam chamber was small (Collins et al., 2002). Deformations were observed on the ground surface with almost no attenuation (Collins et al., 2002). Increased water saturation and therefore increased water mobility in the cold reservoir was inferred from this uniform increase in dilation (Collins et al., 2002). Collins et al. (2002) showed increased permeability values in their coupled geomechanical and reservoir simulation. Permeability enhancement was achieved even before failure of oil sands.

2.3. Thermal properties of Geomaterials

Thermal properties of Athabasca oil sands have been measured in the lab. Smith-Magowan et al. (1982) measured the specific heat capacity of oil sands samples over the temperature range of 50-300°C. Heat capacity of samples with different grades was measured experimentally. Smith-Magowan et al. (1982) found that specific heat capacity of Athabasca oil sands can be estimated from averaging the specific heat of the components.

Porosity, mineralogy, texture, and grain size affect thermal conductivity of sediments (Midttomme and Roaldset, 1999). Thermal conductivity of oil sands was measured by (Karim and Hanafi, 1981). They observed that thermal conductivity of oil sands was dependent on bitumen content and temperature. Somerton et al. (1974) also measured thermal conductivity of oil sands at different conditions. They observed relatively small dependency of thermal conductivity on temperature. Effects of pressure change on thermal conductivity were considered small and ignorable. Porosity, water saturation and quartz content were the parameters they used for estimation of thermal conductivity.

Thermal diffusivity of Athabasca oil sands was measured by Seto (1985). Seto (1985) observed a decrease in thermal conductivity with increasing temperature. He also reported that thermal diffusivity of the samples decreased with increasing bitumen saturation. Sample disturbance also influenced the measured thermal conductivities (Seto, 1985). Higher thermal conductivities were measured for undisturbed sample at roughly the same bitumen content (Seto, 1985).

2.4. Observation Well Data Analysis

Thermal properties of the geomaterials can also be estimated from temperature measurements of observation wells. Nzekwu et al. (1990) studied observation well temperatures for the evaluation of in-situ bitumen recovery methods in the Clearwater Formation. They could confirm the height and orientation of the vertical fracture by observation well temperature recordings and also detect convective flows away from fracture planes. Nzekwu et al. (1990) calculated a thermal diffusivity of $0.0023\ \left[\frac{m^2}{h}\right]$or $6.4 \times 10^{-7}\ \left[\frac{m^2}{s}\right]$ for the Clearwater reservoir. Vittoratos (1986) used a thermal diffusivity value of $7 \times 10^{-7}\ \left[\frac{m^2}{s}\right]$ to predict the temperature profiles. Thermal conductivity of geological formations was estimated from temperature logs and laboratory measurements of core by Seto and Bharatha (1991). In their method, they calculated the thermal conductivity of geological formations by calculating the ratio of thermal conductivities from observation well temperature logs and available correlations of Athabasca oil sand cores. Closmann and Smith (1983) used thermal conductivity values of $9.27 \times 10^{-7}\ \left[\frac{m^2}{s}\right]$ and $7.1 \times 10^{-7}\ \left[\frac{m^2}{s}\right]$ to fit the measured temperatures with the one-dimensional conduction heat transfer from a fracture plane.

Birrell and Putnam (2000) showed that for the simple one-dimensional heat transfer the inverse conjugate error function (ICEF) of dimensionless temperature profile versus depth is a straight line and they all converge to the top of the steam chamber when the steam chamber is not rising.

In the case of a rising steam chamber, Birrell and Putnam (2000) plotted the natural logarithm of dimensionless temperature versus depth and observed parallel lines in the steady state. By analyzing observation well data in the Phase A and Phase B Underground Test Facility, Birrell and Putnam (2000) could match the stop in the rise of the steam chamber to the occurrence of mud beds at the same depth. Birrell (2003) also developed the solutions to eliminate transient effects on the temperature profile by using the principle of superposition. He could find the thermal diffusivity of oil sands by three methods: form ICEF plot of dimension temperature, Natural log plot of dimensionless temperature, and direct numerical solution of the Fourier's heat transfer equation. He used the windsock method to find the angle between the direction of heat flow and thermocouple readings from observation wells. Birrell (2003) observed an unusual rise in thermal diffusivity when convective heat transfer was not included in the heat transfer analysis. Birrell (2003) detected convective heat flows at temperatures below 30°C and above 140°C.

Chapter 3: Heat Transfer Mechanisms above Steam Chambers

In this chapter several heat transfer scenarios of conduction and convection are simulated to understand the influence of thermal and hydraulic properties and also geometry effects on heat transfer. One and two-dimensional models are used for the investigation of dominant mechanisms by which heat can be transported upwards ahead of the steam chamber. Uncertainties in the value of thermal and hydraulic properties on thermal fronts are also investigated.

Generally, there are three mechanisms of heat transfer: conduction, convection, and radiation. In the current study, conduction and convection are the main heat transfer mechanisms through porous media. The governing equation of heat transfer by conduction is (Nield and Bejan, 2006):

$$(\rho c)_m \frac{\partial T}{\partial t} = \vec{\nabla}.\left(k_m \vec{\nabla} T\right) + q_m''' \qquad \text{Equation 3.1}$$

where:

T = Temperature [°C],

k_m= Thermal conductivity of the medium $\left[\frac{W}{m°C}\right]$,

ρ_m = Bulk density of the medium $\left[\frac{kg}{m^3}\right]$,

c_m = Specific heat capacity of the medium $\left[\frac{J}{kg°C}\right]$, and

q_m''' = Rate of heat generation per unit volume of the porous matrix $\left[\frac{W}{m^3}\right]$.

$\vec{\nabla}.$ = Divergence of a vector field

A convection term will be added to Equation 3.1 if there are contributions of a moving fluid in porous media and the governing equation will be (Nield and Bejan, 2006):

$$(\rho c)_m \frac{\partial T}{\partial t} + (\rho c)_f \vec{v}.\vec{\nabla}T = \vec{\nabla}.\left(k_m \vec{\nabla}T\right) + q_m''' \qquad \text{Equation 3.2}$$

where:

ρ_f = Density of the moving fluid$\left[\frac{kg}{m^3}\right]$,

c_f = Specific heat capacity of the moving fluid$\left[\frac{J}{kg°C}\right]$, and

$\vec{v}$ = Velocity of the moving fluid obtained from Darcy's law$\left[\frac{m}{s}\right]$.

In this chapter, mathematical principles of one and two dimensional heat transfer analyses are provided. Different scenarios of initial conditions and property variations are investigated. The porous medium is considered isotropic and homogeneous.

3.1. Heat Conduction

The primary focus in the research will be on the analysis of heat transfer to the upper parts of the reservoir as it will be assumed that the steam chamber will rise until it reaches a low permeability layer. Inclined heterolithic strata (HIS), interbeds of sand and silt, have low vertical permeability and can act as baffles or barriers and impede the vertical growth of steam chamber (Fustic et al., 2011). However, heat will be lost upwards to IHS layers, caprock, and ultimately overburden ahead of the steam chamber. The mechanisms by which heat can be transferred ahead of the steam chamber are conduction only or a combination of conduction and convection.

3.1.1. One-dimensional Heat Conduction

Heat loss can be dominated by conduction. Low permeability baffles or barriers will cease the vertical growth of steam chamber. Assuming that heat is conducted in the vertical direction after vertical steam chamber growth is ceased and the steam chamber has established a constant hot interface in contact with the low permeability layer, the differential equation of conductive heat transfer can be simplified to:

$$(\rho c)_m \frac{\partial T}{\partial t} = \frac{\partial}{\partial z}(k_m \frac{\partial T}{\partial z}) \qquad \text{Equation 3.3}$$

Assuming that material properties are constant, a new variable can be introduced as $\alpha = \frac{k_m}{(\rho c)_m}$ which is called thermal diffusivity. The solution to the one-dimensional differential equation in a semi-infinite domain with the following boundary conditions is given by Butler (1991) as:

$$\begin{gathered} (\rho c)_m \frac{\partial T}{\partial t} = k_m \frac{\partial^2 T}{\partial x^2} \qquad z > 0 \ , \qquad t > 0 \\ T(x, 0) = T_R \ , \qquad z > 0 \ , \\ T(0, t) = T_s, \qquad t > 0 \ , \end{gathered} \qquad \text{Equation 3.4}$$

$$T = T_R + (T_S - T_R) \operatorname{erfc}\left(\frac{z}{2\sqrt{\alpha t}}\right) \qquad \text{Equation 3.5}$$

In this equation, T_R and T_S are the temperature of the cold medium and hot surface, respectively. Temperature profiles ahead of the hot interface are shown in Figure 3.2 assuming $\alpha = 1.0 \times 10^{-6} \left[\frac{m^2}{s}\right]$, $T_S = 220[^0C]$, and $T_R = 10[^0C]$.

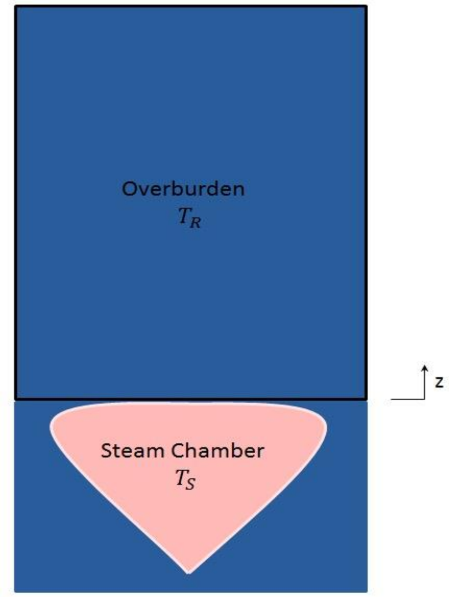

Figure 3.1: Hot interface contact with overburden after steam chamber rises to the top of pay zone.

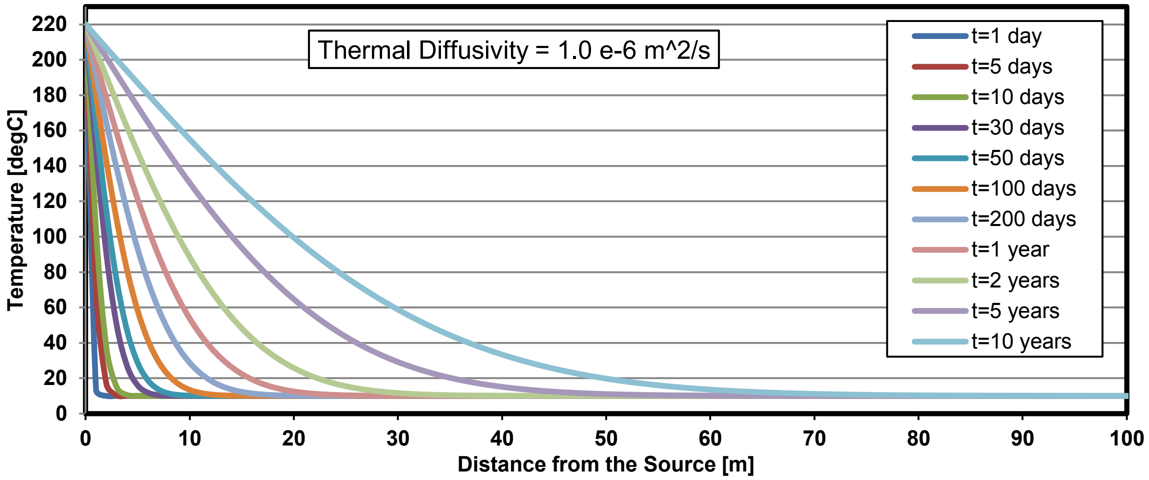

Figure 3.2: Temperature profiles of 1D conduction heating ahead of a hot interface in an infinite medium.

3.1.1.1. One-dimensional Heat Conduction with Varying Interface Temperature

In general, injected steam is in the saturated state and the temperature of the steam can be found as a function of pressure. Variation in steam injection pressure during the life of a SAGD process will result in variation of temperature inside the steam chamber and consequently the interface temperature at the top. The change in pressure can also lead to changes in the top of the chamber. At higher pressures, steam chamber can rise to higher elevations but as the pressure is lowered the chamber retreats (Ito and Ipek, 2005). Assuming that the temperature variations are not drastic and the top of the steam chamber is not advancing nor retreating, a closed form solution can be found for temperature distribution in the caprock with varying interface temperature based on the principle of superposition explained in (Birrell, 2003):

$$\begin{aligned} T(x,t) &= (T_1 - T_0)\mu_{t_1}\operatorname{erfc}\left(\frac{x}{\sqrt{4\,\alpha\,(t-t_1)}}\right) \\ &+ (T_2 - T_1)\mu_{t_2}\operatorname{erfc}\left(\frac{x}{\sqrt{4\,\alpha\,(t-t_2)}}\right) \\ &+ (T_3 - T_2)\mu_{t_3}\operatorname{erfc}\left(\frac{x}{\sqrt{4\,\alpha\,(t-t_3)}}\right) + \cdots \end{aligned} \qquad \text{Equation 3.6}$$

In this equation t_1, t_2, t_3 ... are the time values where interface temperatures are T_1, T_2, T_3 ... , respectively, and μ_{t_1} is the step function defined as (Birrell, 2003):

$$\mu_{t_1} = \begin{cases} 1 & t > t_1 \\ 0 & t < t_1 \end{cases} \qquad \text{Equation 3.7}$$

Below is an example of temperature profiles with the temperature history at the interface shown on the graph assuming $\alpha = 1.0 \times 10^{-6} \left[\frac{m^2}{s}\right]$.

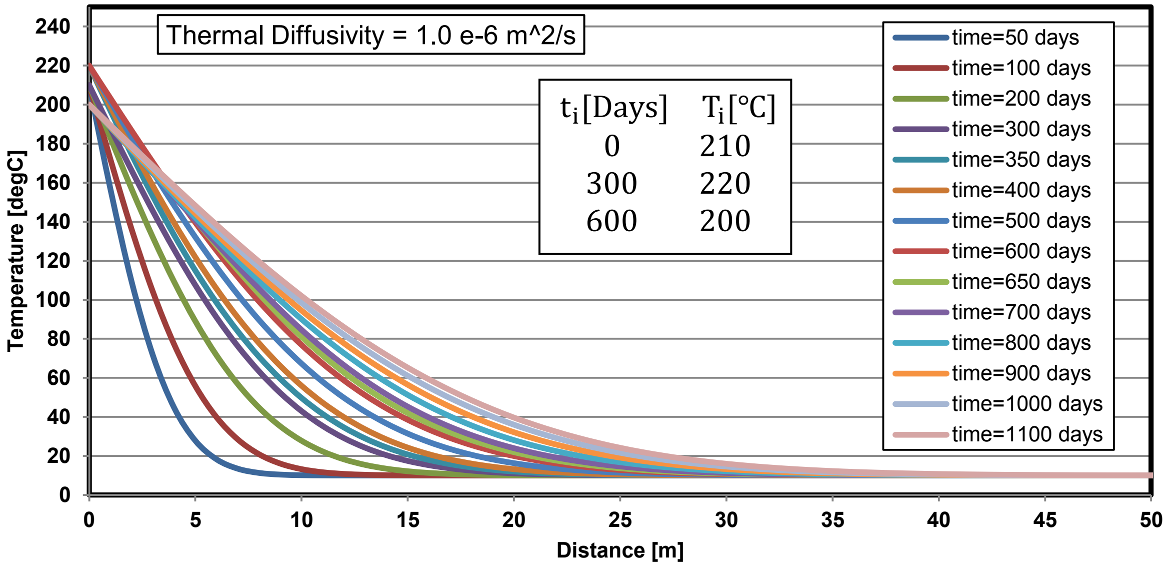

Figure 3.3: 1D Temperature profiles within an infinite medium subject to varying interface temperature.

3.1.1.2. Temperature Distribution ahead of a Moving Front

Heat will be transferred ahead of the rising steam front before an impermeable layer stops the steam chamber. The transient temperature profile ahead of an advancing front moving at a constant velocity of U can be found as (Carslaw and Jaeger, 1959):

$$T^* = \frac{1}{2}\left[\operatorname{erfc}\left(\frac{\zeta^* + t^*}{2\sqrt{t^*}}\right) + e^{-\zeta^*}\operatorname{erfc}\left(\frac{\zeta^* - t^*}{2\sqrt{t^*}}\right)\right] \qquad \text{Equation 3.8}$$

In this equation, $T^* = \frac{T - T_R}{T_S - T_R}$, $\zeta^* = \frac{U\zeta}{\alpha}$, $t^* = \frac{U^2\zeta}{\alpha}$, and $\zeta = x - Ut$.

Temperature profiles of a moving front are shown in Figure 3.4 assuming the advancing front is moving at a speed of 15 $^{m}/_{yr}$ and the same thermal properties used in the previous case.

The steady state solution of the temperature profiles ahead of a moving front is (Butler 1991):

$$T^* = e^{-\zeta^*} = e^{-\frac{U\zeta}{\alpha}} = e^{-\frac{U}{\alpha}(x-Ut)} \qquad \text{Equation 3.9}$$

A comparison of the steady state solution with the transient response is shown in Figure 3.5.

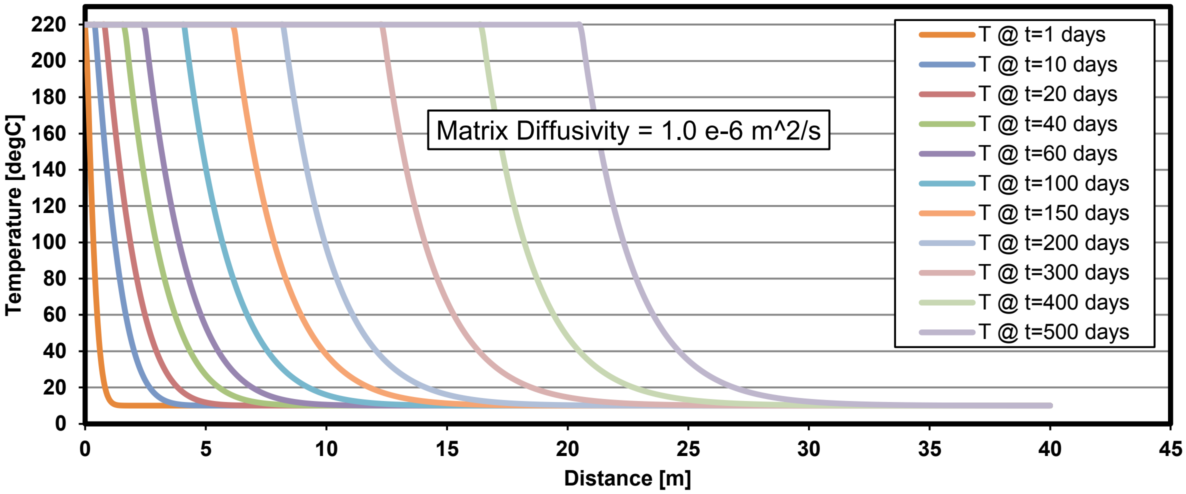

Figure 3.4: Evolution of temperature profiles ahead of a 1D moving front.

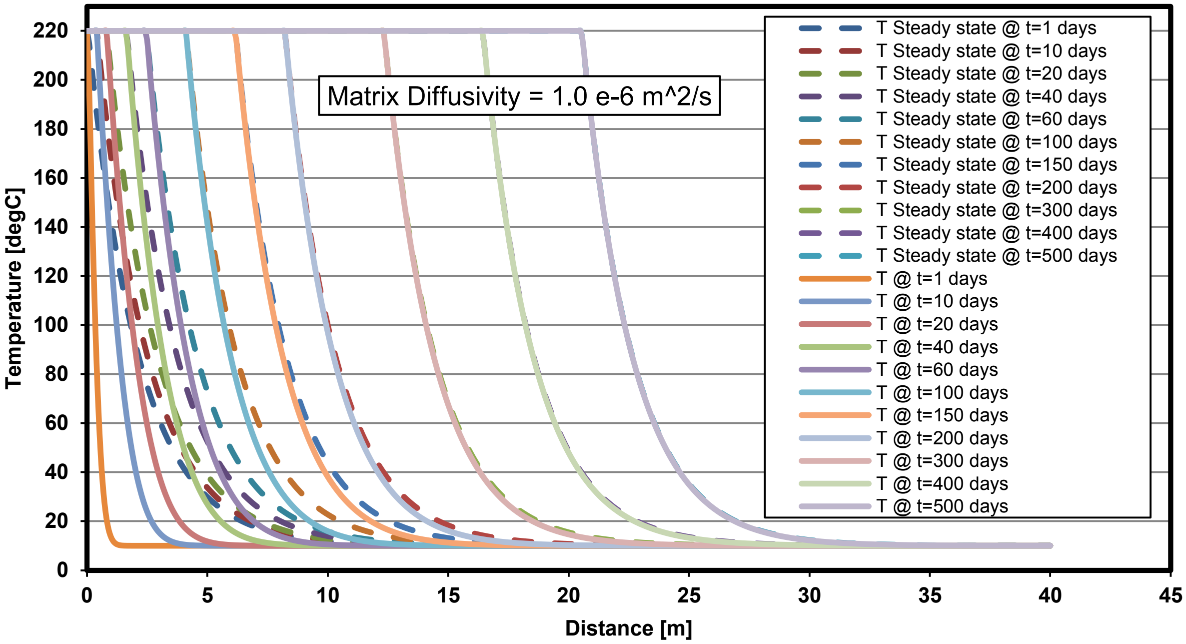

Figure 3.5: Transient vs. steady state 1D temperature responses ahead of an advancing front with constant front velocity.

As one can see, temperature response will reach the steady state after about 200 days with the assumed thermal properties and front velocity.

3.1.1.3. Effect of Initial Formation Temperature on 1D Heat Conduction Solution

If thermal properties of the pay zone and overlying layers are close to each other and a steady state temperature response is established ahead of the steam chamber before it reaches an impermeable layer, the initial state of the heat equation for the overlying layers will change from $T_0 = T_R$ to $T_0 = (T_S - T_R)e^{-\frac{U}{\alpha}x}$. A solution to this initial-boundary value problem can be found based on the Fourier integral method introduced in Brown and Chrchill (1993). The solution to the heat conduction equation with $T_0^* = e^{-\xi x}$ as the initial condition is developed in Appendix I and the final closed form solution is:

$$T^* = \frac{1}{2} e^{\alpha\ \xi^2 t} \left[e^{-\ \xi\ x} \operatorname{erfc}\left(\frac{2\ \alpha\ \ \xi\ t - x}{\sqrt{4\ \alpha\ t}} \right) - e^{\ \xi\ x} \operatorname{erfc}\left(\frac{2\ \alpha\ \ \xi\ t + x}{\sqrt{4\ \alpha\ t}} \right) \right] + \operatorname{erfc}\left(\frac{x}{\sqrt{4\ \alpha\ t}} \right) \qquad \text{Equation 3.10}$$

If $\xi = \frac{U}{\alpha}$ the solution can be simplified to:

$$T^* = \frac{1}{2} e^{\frac{U^2}{\alpha} t} \left[e^{-\frac{U}{\alpha} x} \operatorname{erfc}\left(\frac{2Ut - x}{\sqrt{4\ \alpha\ t}} \right) - e^{\frac{U}{\alpha} x} \operatorname{erfc}\left(\frac{2Ut + x}{\sqrt{4\ \alpha\ t}} \right) \right] + \operatorname{erfc}\left(\frac{x}{\sqrt{4\ \alpha\ t}} \right) \qquad \text{Equation 3.11}$$

Figure 3.6 shows temperature responses through the overlying strata over time assuming the same thermal properties and $U = 15\ ^{m}/_{yr}$.

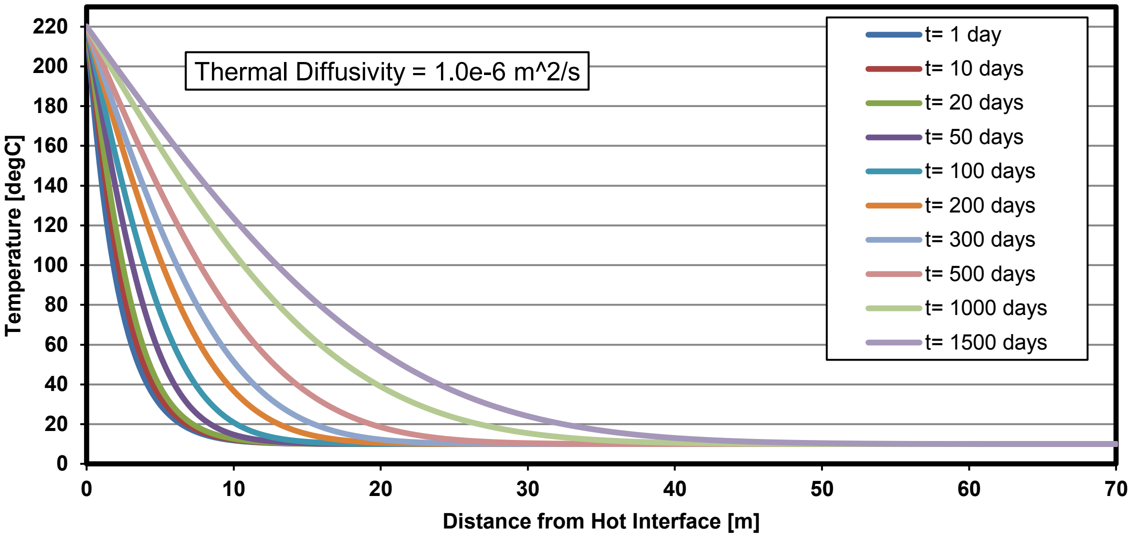

Figure 3.6: 1D Temperature profiles of conduction heat transfer with $\mathbf{T_0^* = e^{-\xi x}}$ as initial condition.

A comparison of the solutions to the heat conduction equation with $T_0 = T_R$ to $T_0 = (T_s - T_R)e^{-\xi x} + T_R$ is shown in Figure 3.7.

Over time, the difference between these solutions will decrease and they approach the same values. Figure 3.8 shows the decreasing difference between these solutions. The influence of initial conditions should not be ignored. This is an important factor in the inverse calculation of thermal diffusivity from temperature responses. As it will be shown in the following chapter, thermal diffusivity values calculated based on early temperature responses are lower than those calculated from the long term response.

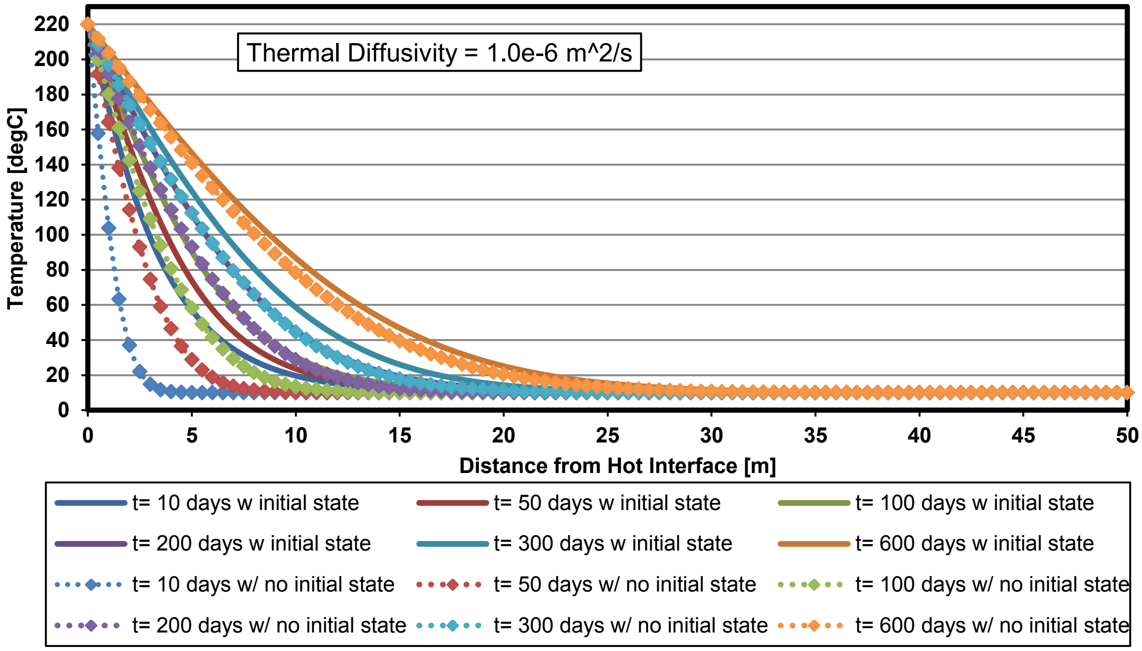

Figure 3.7: Influence of initial conditions on temperature profiles in one-dimensional heat conduction.

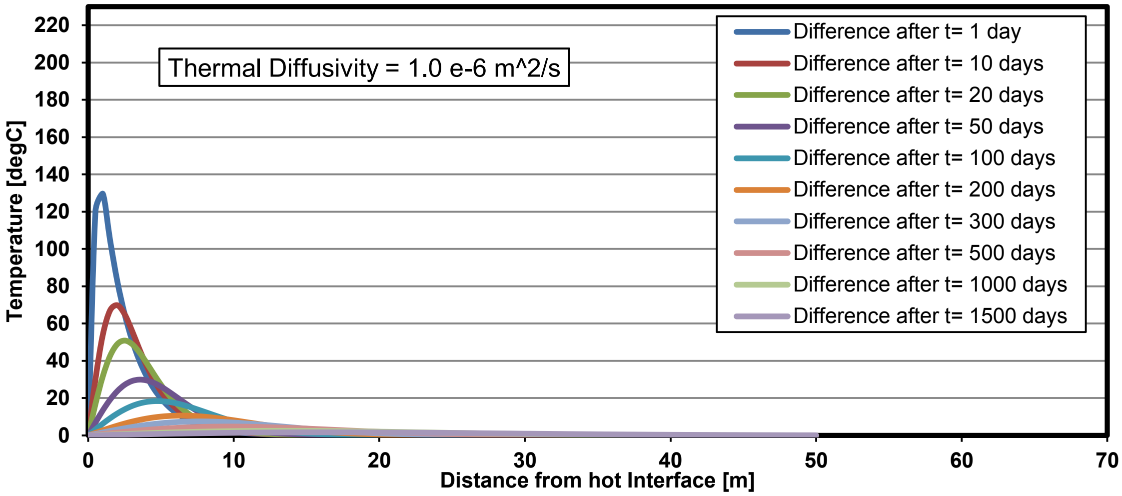

Figure 3.8: Decrease in temperature response difference over time between solutions of Equation 3.5 and Equation 3.11.

3.1.1.4. Uncertainty in the Value of Thermal Diffusivity

In order to investigate the sensitivity of temperature profiles to thermal diffusivity a simple Monte-Carlo statistical study was conducted. Based on the definition of thermal diffusivity, an uncertainty in thermal conductivity, specific heat capacity, or density can cause uncertainty in the value of thermal diffusivity. Simple Monte-Carlo statistical analyses with 1000 random samples were done on the value of thermal diffusivity and temperature profiles were calculated assuming that thermal properties of the medium were measured with the following uncertainty levels with a normal distribution summarized in Table 3.1.

Table 3.1: Statistical distribution of thermal properties.

Property	Mean μ	Standard Deviation σ	$\mathrm{CoV} = \frac{\sigma}{\mu}$ [%]
$k_m \left[\frac{W}{m°C}\right]$	2.2	0.344	10
$\rho_m \left[\frac{kg}{m^3}\right]$	2200	105	5
$c_m \left[\frac{J}{kg°C}\right]$	1000	110	10
$\alpha = \frac{k_m}{\rho c}\left[\frac{m^2}{s}\right]$	1.01 e-6	≈1.52 e-7	≈15

As one can see in Figure 3.10 the level of uncertainty increases at distances farther from the hot interface and grows over time.

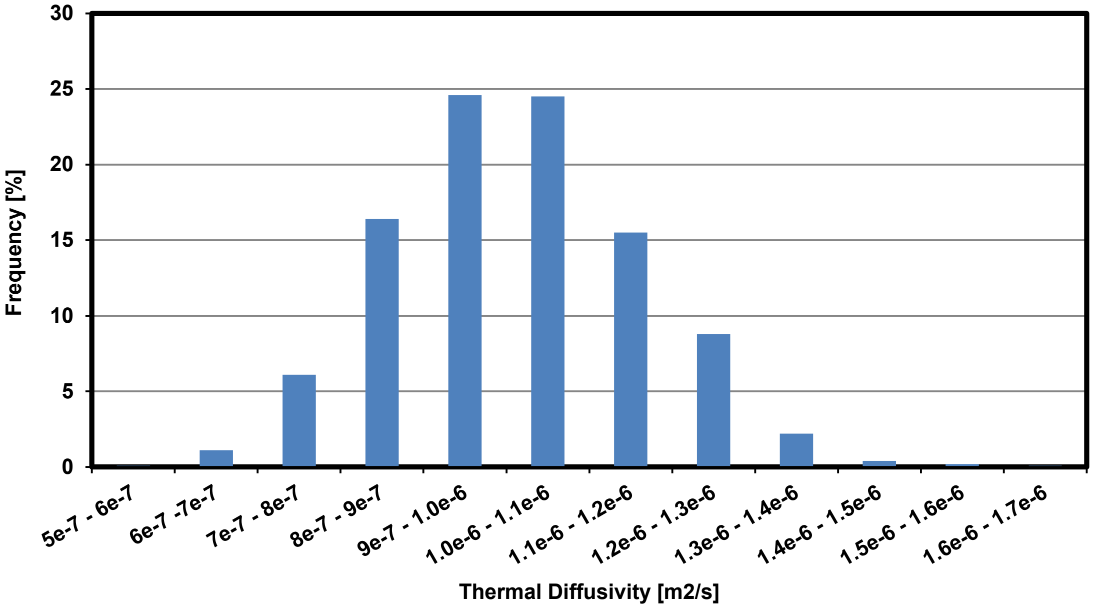

Figure 3.9: Distribution of thermal diffusivity.

Coefficient of variance $\mathrm{CoV} = \frac{\sigma}{\mu}$ can be used as a measure of uncertainty in statistical analyses. Figure 3.11 shows the level of uncertainty at different distances from the hot interface after 3000 days obtained from 1000 random cases. As it can be seen on the graph, the level of uncertainty increases as one gets farther from the hot interface. This tool can be used in the reverse estimation of thermal diffusivity from temperature profiles. Large variations in the estimated thermal diffusivity will result in large uncertainty in temperature profiles. However, real temperature profiles are generally viewed as quite consistent with little uncertainty at greater distances from the hot interface.

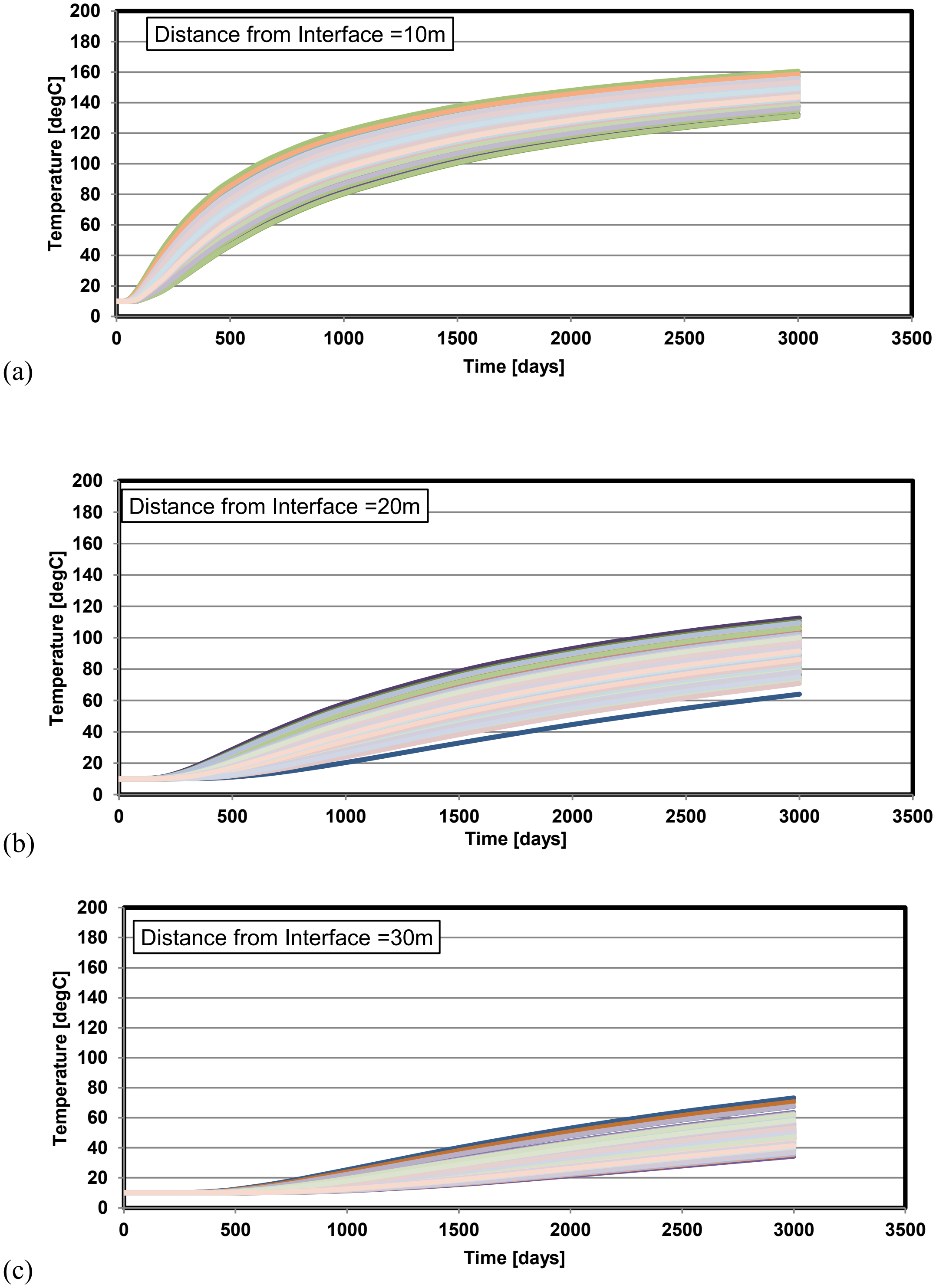

Figure 3.10: Temperature uncertainty over time at different distances from the hot interface. (a) 10m. (b) 20 m. (c) 30 m.

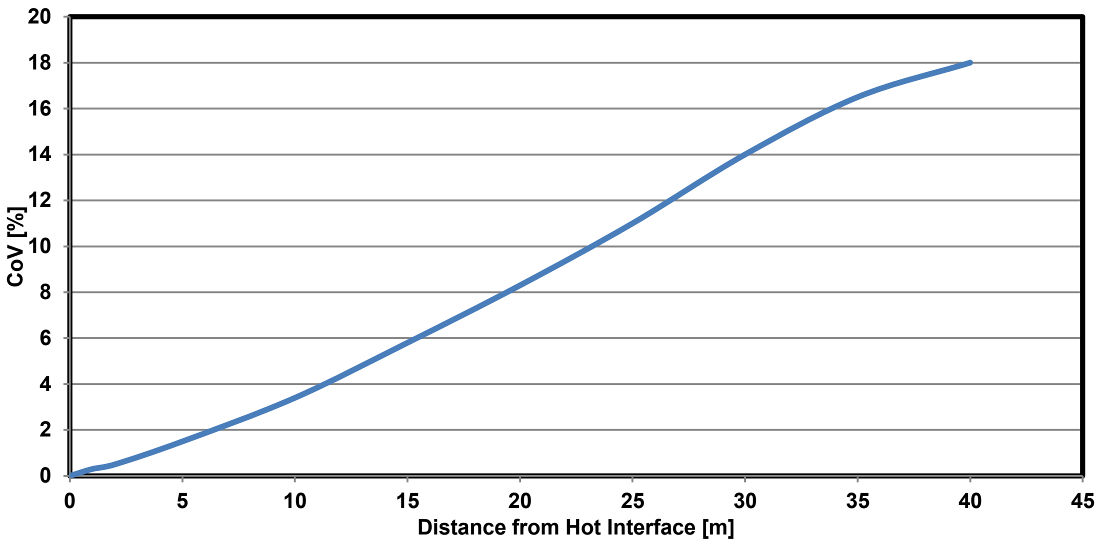

Figure 3.11: CoV of temperature values of conductive heat transport after 3000 days with respect to distance from the hot interface.

3.1.2. Two Dimensional Heat Conduction

The length of the horizontal wells in the SAGD operation is close to 1000 meters which is much larger than the lateral extent of steam chambers (approximately 70m). Therefore, two dimensional heat transfer models appear to be sufficient in the analysis of upward heat losses. In this section, two-dimensional heat transfer scenarios are investigated to assess what may occur during SAGD operations assuming the average thermal property values provided in Table 3.1. COMSOL, a finite element analysis package, was used for modeling.

Observation wells monitor field temperatures in the vertical direction and do not provide data on other directions explicitly. There is likely a need to examine the effects of anisotropy of thermal properties of the geomaterials on temperature profiles but is outside the scope of the current research. Additionally, as a result of insufficient data from field measurements in other directions, it is assumed that thermal properties are isotropic.

3.1.2.1. Heat Conduction from a Fixed Hot Interface

In order to assess the accuracy of the numerical modeling a simple one-dimensional heat conduction simulation was run using the average thermal properties defined in Table 3.1. Thermal fronts are shown in Figure 3.12. A comparison of temperature profiles obtained from the numerical simulation with the analytical solution in Figure 3.13 shows an excellent match between the numerical simulation and analytical solution.

In reality, heat loss to overburden is closer to a two-dimensional phenomenon than one-dimensional. The first case that can be investigated is a non-spreading hot interface. In this simulation, the width of the hot interface is assumed to be equal to 70 m. The boundary conditions and as well as the location of one-dimensional temperature profiles is schematically depicted in Figure 3.14. As a result of lateral conduction of heat into the medium, heat is lost not only in the vertical direction but also laterally and temperatures would not be expected to increase at the same rate as the one-dimensional case. The results of the simulation are shown in Figure 3.15. A comparison of the one-dimensional temperature profiles with the one-dimensional analytical solution is shown in Figure 3.16. As expected, the response is closer to the 1D analytical solution at the center of the hot interface but diverges from that as distance from the center increases.

In order to understand the deviation of the profiles with the 1D analytical case, the difference between the two were calculated. The results are shown in Figure 3.17 and indicate that the deviation increases as the distance from center increases. This is due to the fact that two-dimensional effects are stronger close to the edge of the hot interface.

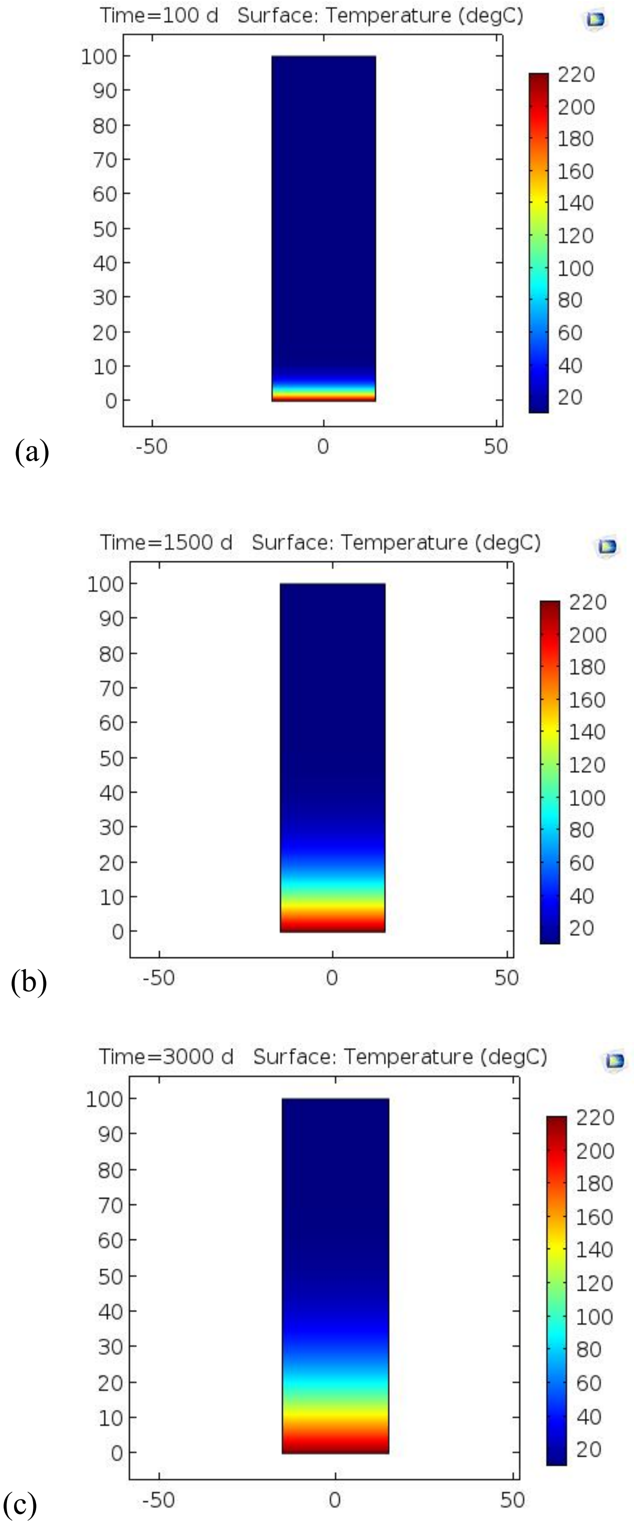

Figure 3.12: 1D Temperature distributions in a homogeneous medium after. (a) 100 days. (b) 1500 days. (c) 3000 days.

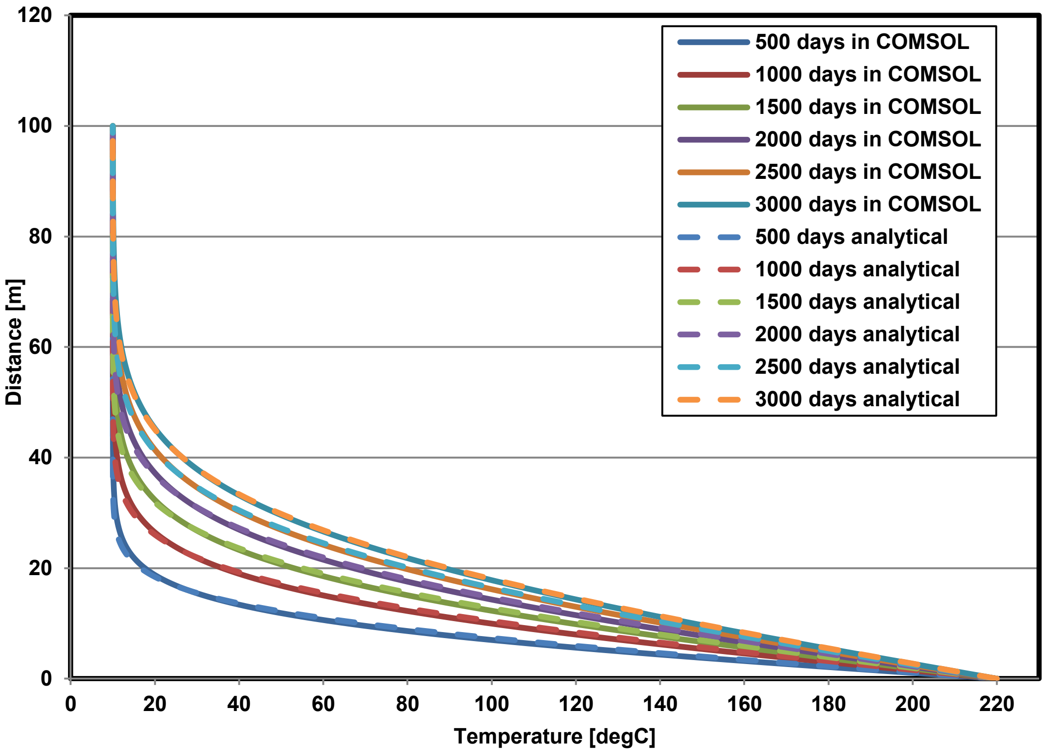

Figure 3.13: Comparison of numerical results of 1D model in COMSOL with the analytical 1D solution in conduction heat transfer.

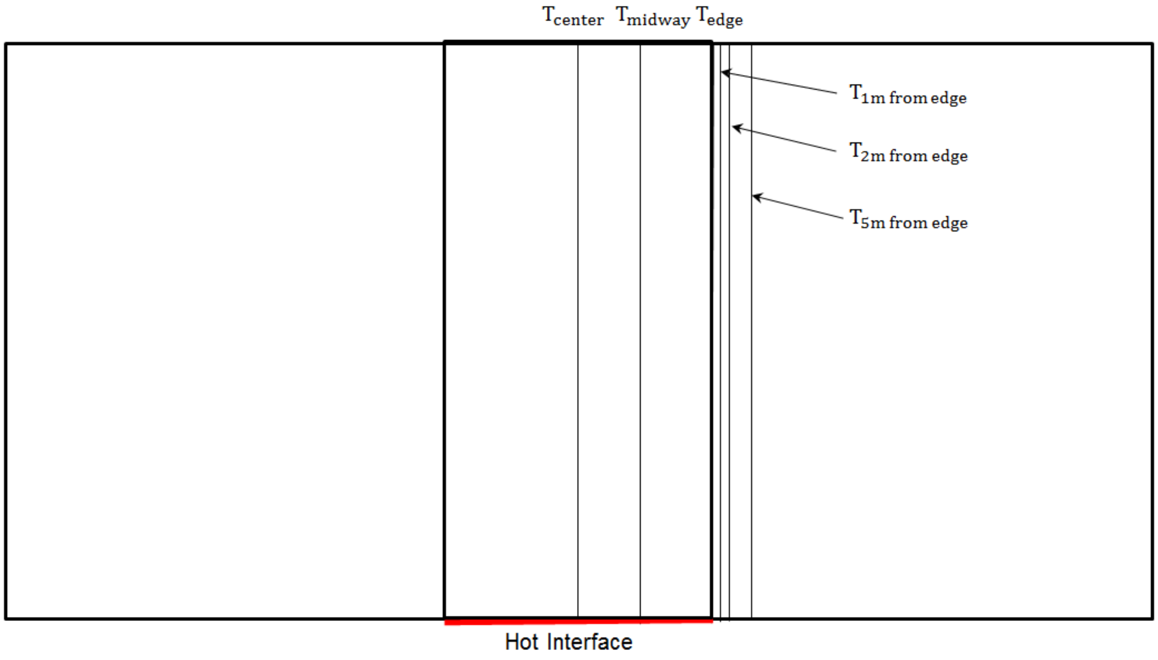

Figure 3.14: Temperature monitoring along vertical lines through overburden.

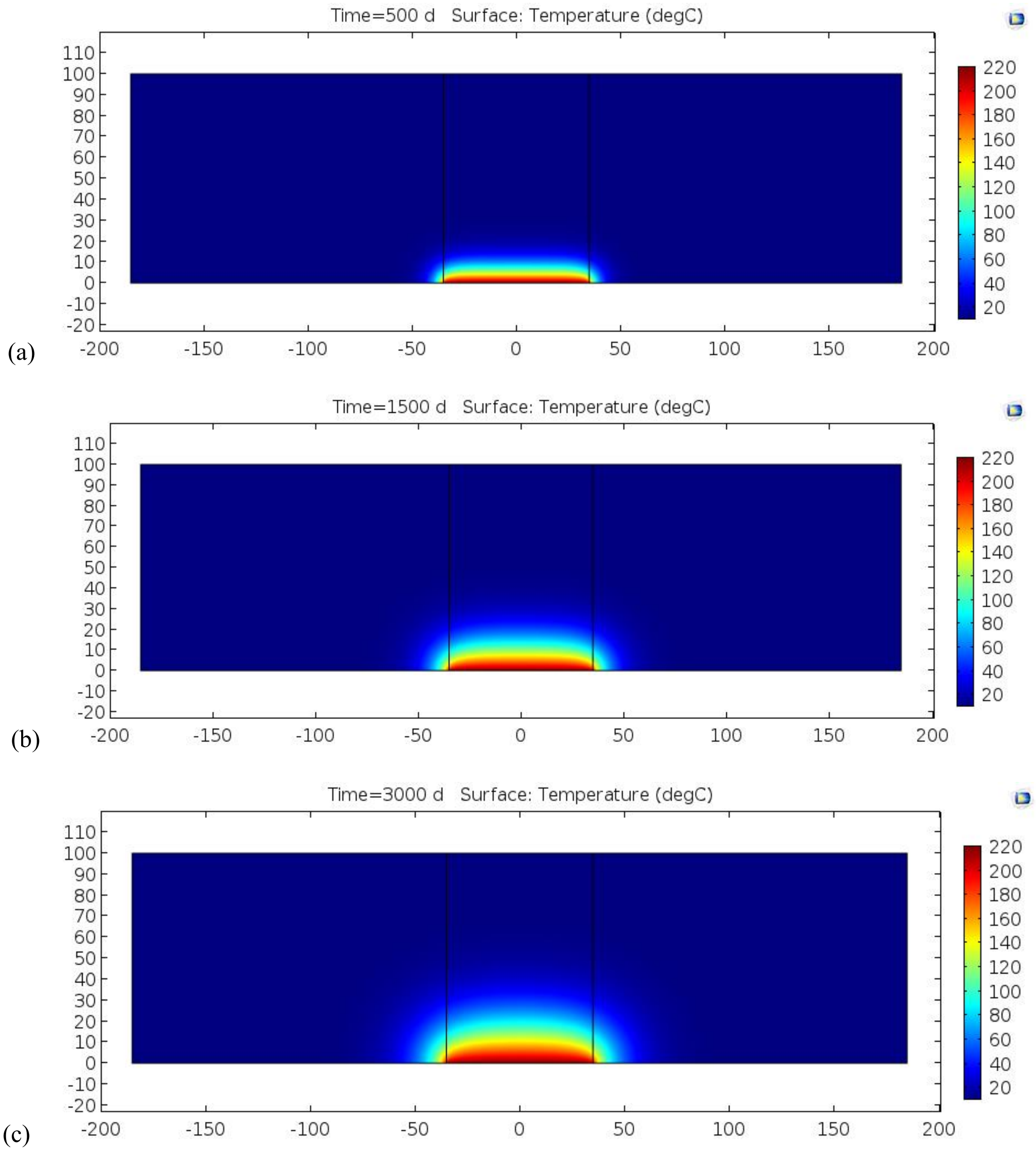

Figure 3.15 : 2 dimensional heat loss to overburden in a homogeneous medium. (a) 500 days. (b) 1500 days. (c) 3000 days.

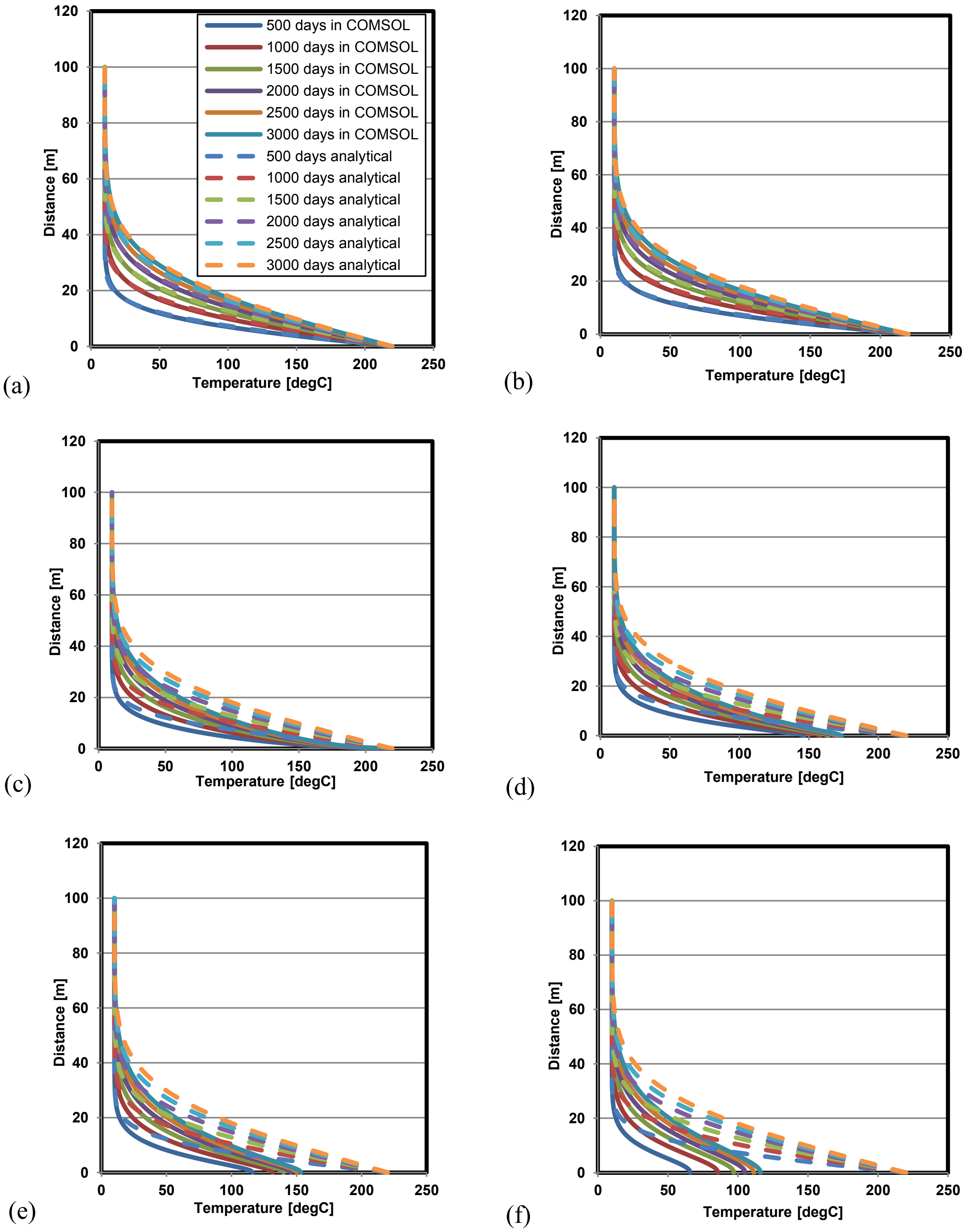

(a) (b) (c) (d) (e) (f)

Figure 3.16: Temperature profiles along the monitoring lines at: (a) center. (b) midway between center and edge. (c) edge. (d) 1m from edge. (e) 2m from edge (f) 5m from edge of the hot fixed interface.

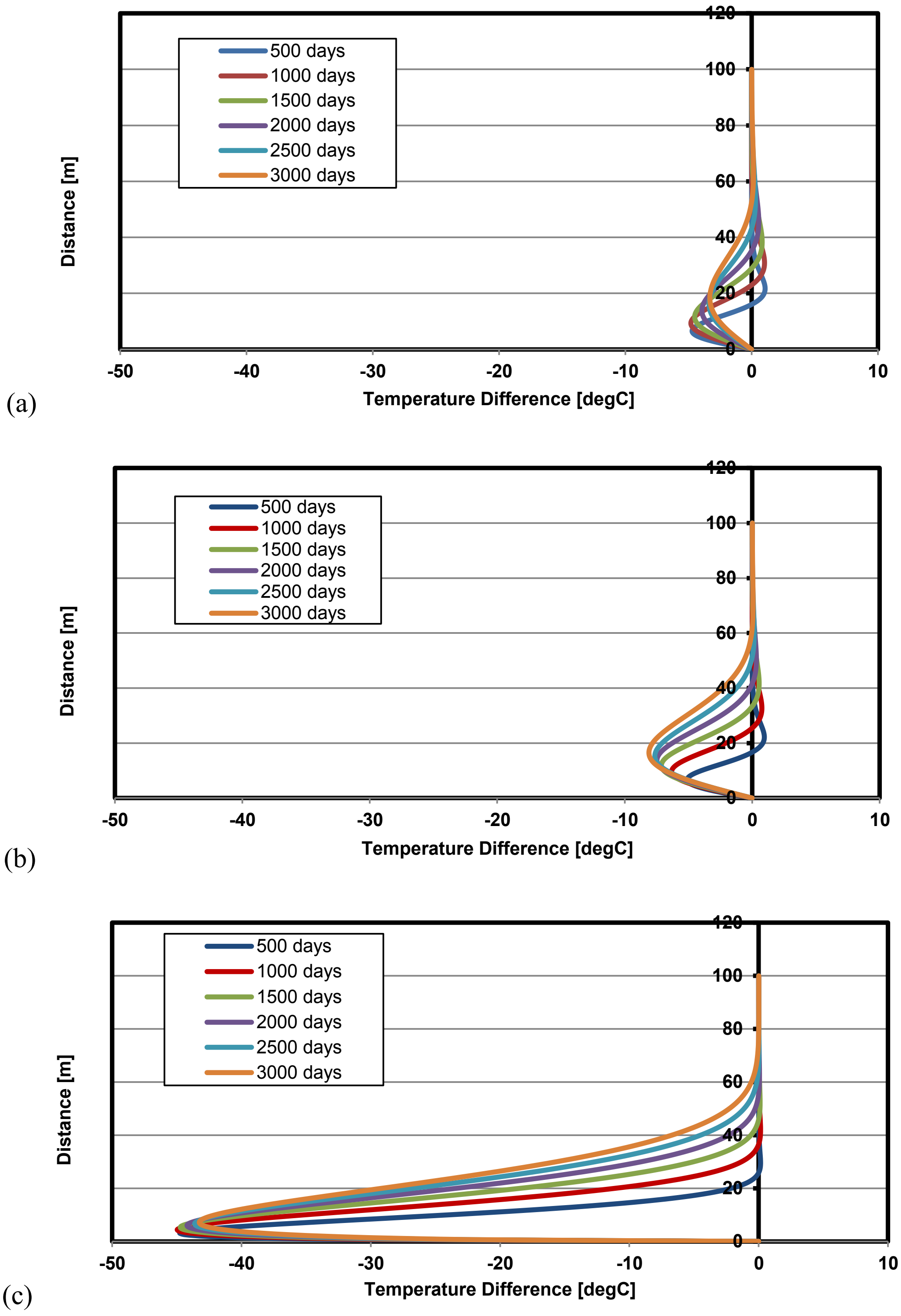

Figure 3.17 : Deviation of temperature profiles obtained from a fixed hot interface from the 1D analytical solution. (a) center line. (b) midway between center line and edge. (c) edge of the hot interface.

3.1.2.2. Heat Conduction from a Spreading Hot Interface

Another scenario that is closer to reality is the case of a spreading hot interface. In this case, it is assumed that the hot interface is expanding to 35m from each side, a total of 70 m, for the first 2500 days (approximately 7 years) and then stops growing and continues to lose heat to the overburden till 3500 days (approximately 10 years).

The 2D temperature profiles for simulations under these conditions are shown in Figure 3.18. One-dimensional temperature profiles along the lines depicted in Figure 3.14 are also compared with the one-dimensional analytical solution. In order to be consistent, initial time of temperature profiles along the lines that pass through the hot interface were shifted to the moment the hot interface was in full contact with the medium and then it was compared to the 1D analytical solution.

In the case of a spreading hot zone, the hot interface is exposed to the cold medium constantly and loses heat at higher rates compared to a stationary interface (Butler, 1991). As a result, temperatures at the center won't build up as fast as expected compared to the non-spreading case and deviations from the 1D analytical solution are greater than the case of a stationary hot interface, as illustrated in Figure 3.19.

As shown in Figure 3.20, temperatures are even higher than the 1D conduction case at areas close to the edge and the magnitude of deviation increases at areas closer to the edge of the spreading hot interface. Over time, deviations from the one-dimensional conduction case have decreased while the affected vertical interval increased.

This phenomenon will influence interpretation of the inverse calculation of thermal diffusivity by the method described Chapter 4. Thermal diffusivities are predicted lower when it's calculated at the edges of a stationary hot interface. The higher temperature values at the edges of the spreading front may lead one to expect a higher value of thermal diffusivity from temperature profiles. However, it will be shown in Chapter 4 that the back calculated thermal diffusivity from temperature profiles are even lower than the case of the fixed hot interface. Higher temperatures are a result of conduction of heat in two dimensions before the interface reaches that zone not from higher rates of conduction.

3.1.2.3. Heat Conduction from Expanding Steam chambers

This next series of exploratory modeling studies examines the impact of growing steam chambers on temperature responses of observation wells. The assumptions of the model are as follow: i) five neighboring steam chambers, representative of a pad, are assumed to reach the top of the pay zone during the very early stages of the operation and then grow laterally; ii) the shape of the growth of steam chambers is assumed to be an expanding triangle; iii) it was assumed that the steam chambers will keep growing laterally until they coalesce after 2500 days; iv) the simulation was run for a period of 3500 days and v) steam chambers were spaced 70 m from each other.

The model consists of overburden, caprock, IHS, pay zone, and underburden. In the heat transfer module of COMSOL the surrounding temperature is held constant and equal to the initial temperature. Thermal properties of the layers are assumed to be equal. Thermal conductivity of the pay zone inside the steam chamber is increased 5 orders of magnitude relative to the surrounding so that temperature is equal and uniform inside the steam chamber. Thermal properties of all the layers are assumed to be equal. More details on the configuration of the model are provided in3.2.2.3.

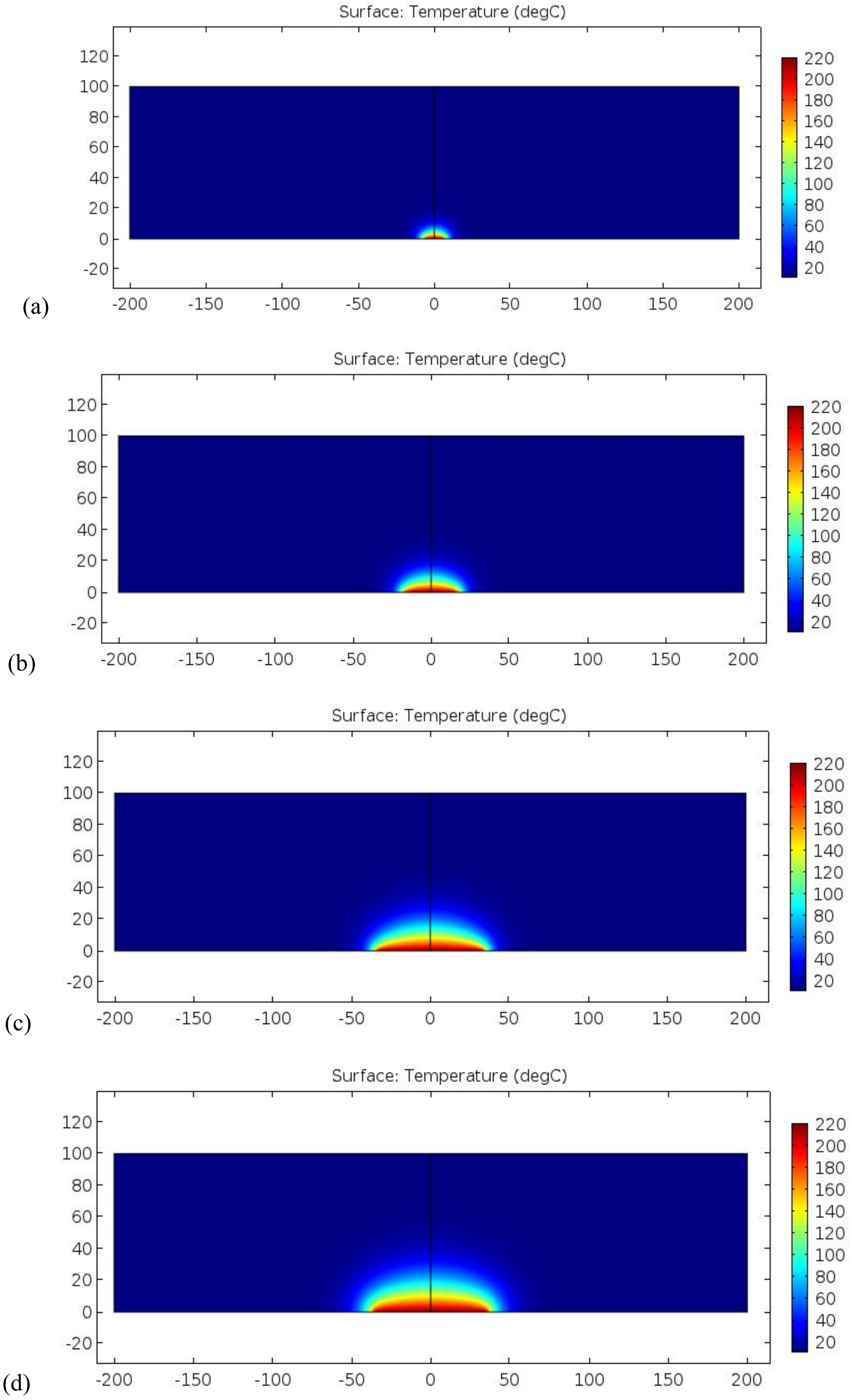

Figure 3.18: 2D temperature profiles of a spreading hot interface. (a) 500 days. (b) 1250 days. (c) 2500 days. (d) 3500 days.

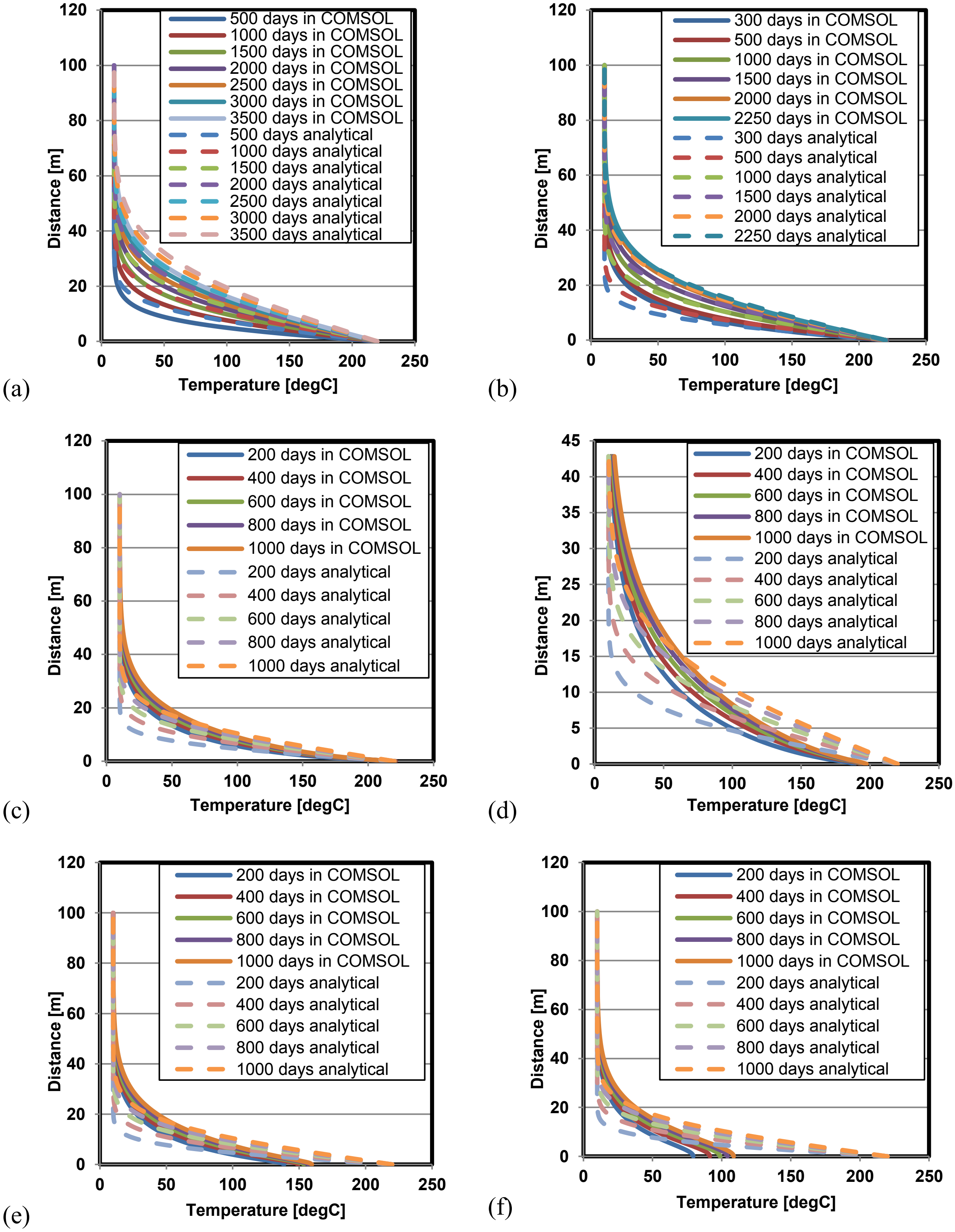

Figure 3.19: Temperature profiles along the monitoring lines at: (a) center. (b) midway between center and edge. (c) edge. (d) 1m from edge. (e) 2m from edge (f) 5m from edge of the hot expanding interface.

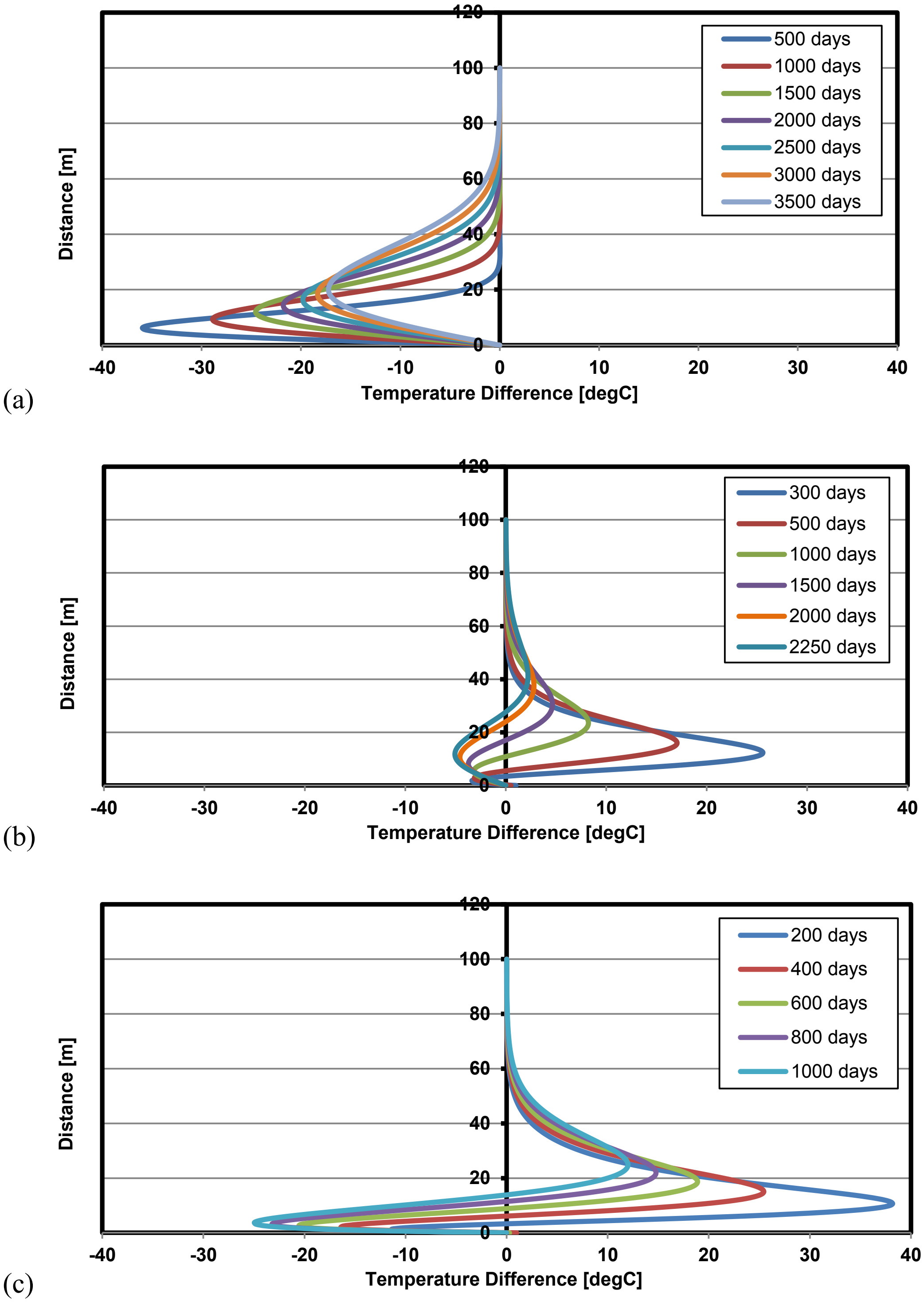

Figure 3.20: Deviation of temperature profiles obtained from a conductive expanding hot interface from the 1D analytical solution. (a) center line. (b) midway between center line and edge. (c) edge of the hot interface.

Temperature surfaces are shown in Figure 3.22. In order to study the effect of monitoring location on temperature profiles three monitoring locations shown on Figure 3.21 were used. L_1 is exactly at the center of the model, L_2 is 14m off the center of the first steam chamber on the right side, and L_3 is 14m off the center of the second steam chamber on the right. The initial time was shifted to the moment the hot interface reached the monitoring lines for comparison of the results with the 1D conduction model.

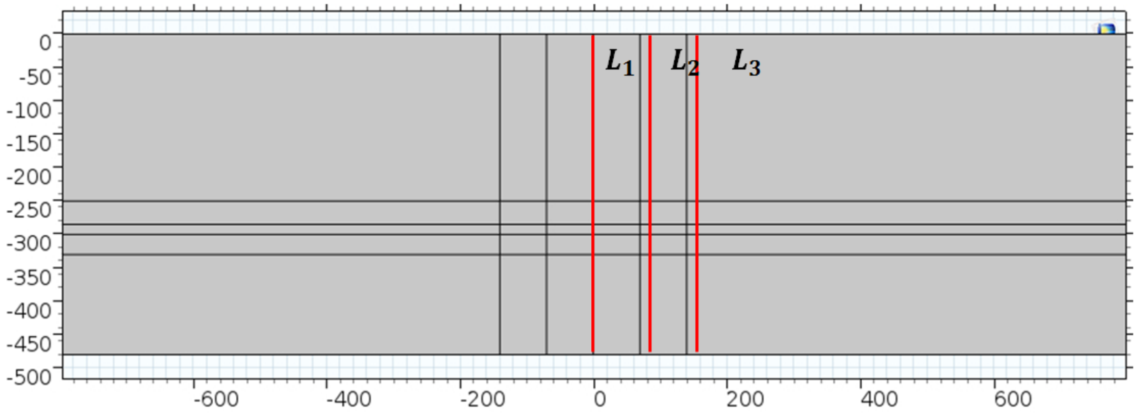

Figure 3.21: Temperature monitoring locations. $\mathbf{L_1}$ middle of the model. $\mathbf{L_2}$ 14m off the center of first steam chamber on the right. $\mathbf{L_3}$ 14m off the center of second steam chamber on the right.

Temperature profiles along these lines shown in Figure 3.23 indicate that the solution of 1D conduction is greater from the two dimensional solution along L_1 but is less than temperature values along L_2 and L_3 . The difference between temperature profiles and one-dimensional conduction case is shown in Figure 3.43. The difference between the two scenarios is decreasing over time.

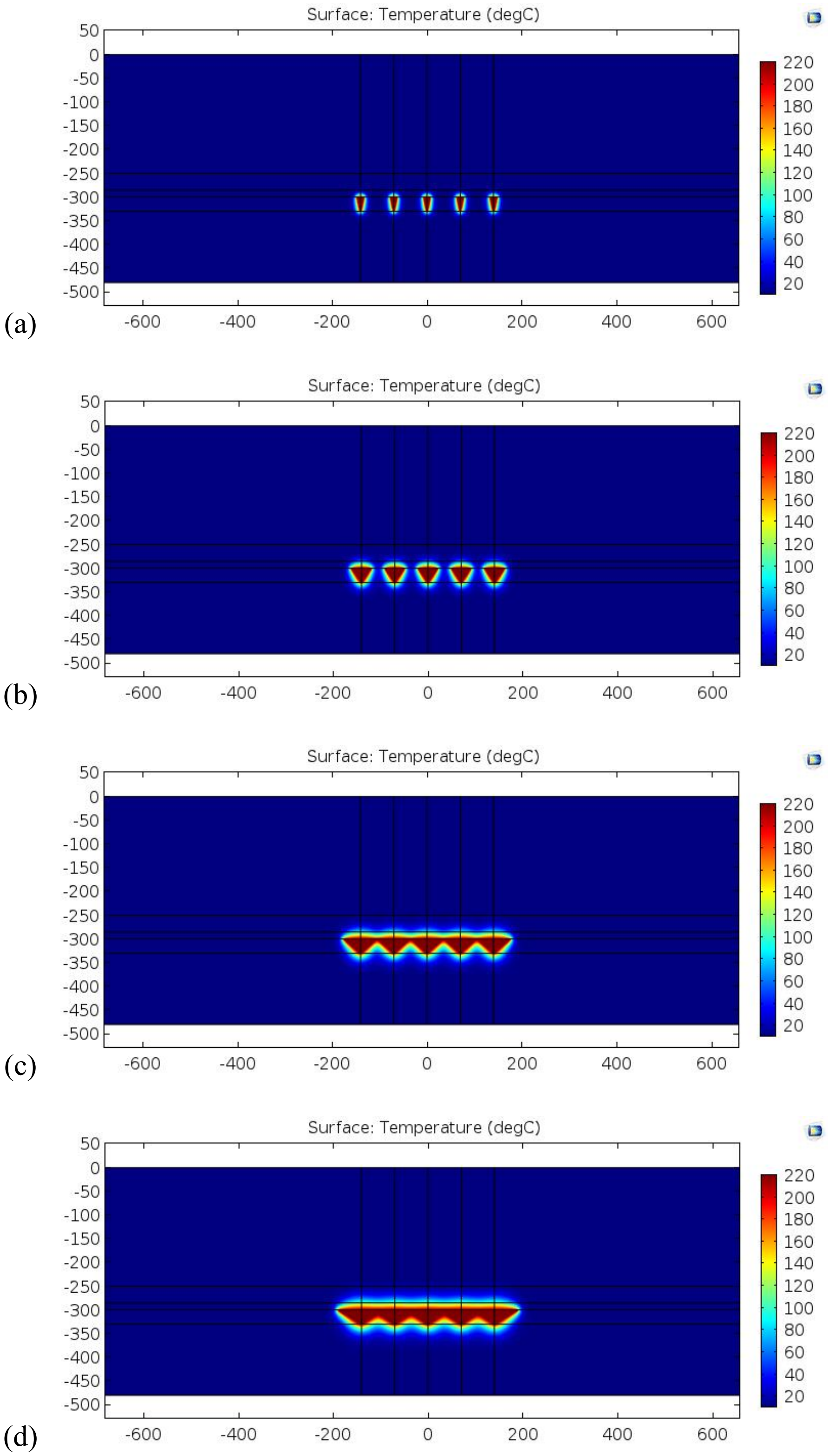

Figure 3.22: Two dimensional temperature distributions of five steam chambers with conduction through the medium over time. (a) 500 days. (b) 1500 days. (c)2500 days. (d) 3500 days.

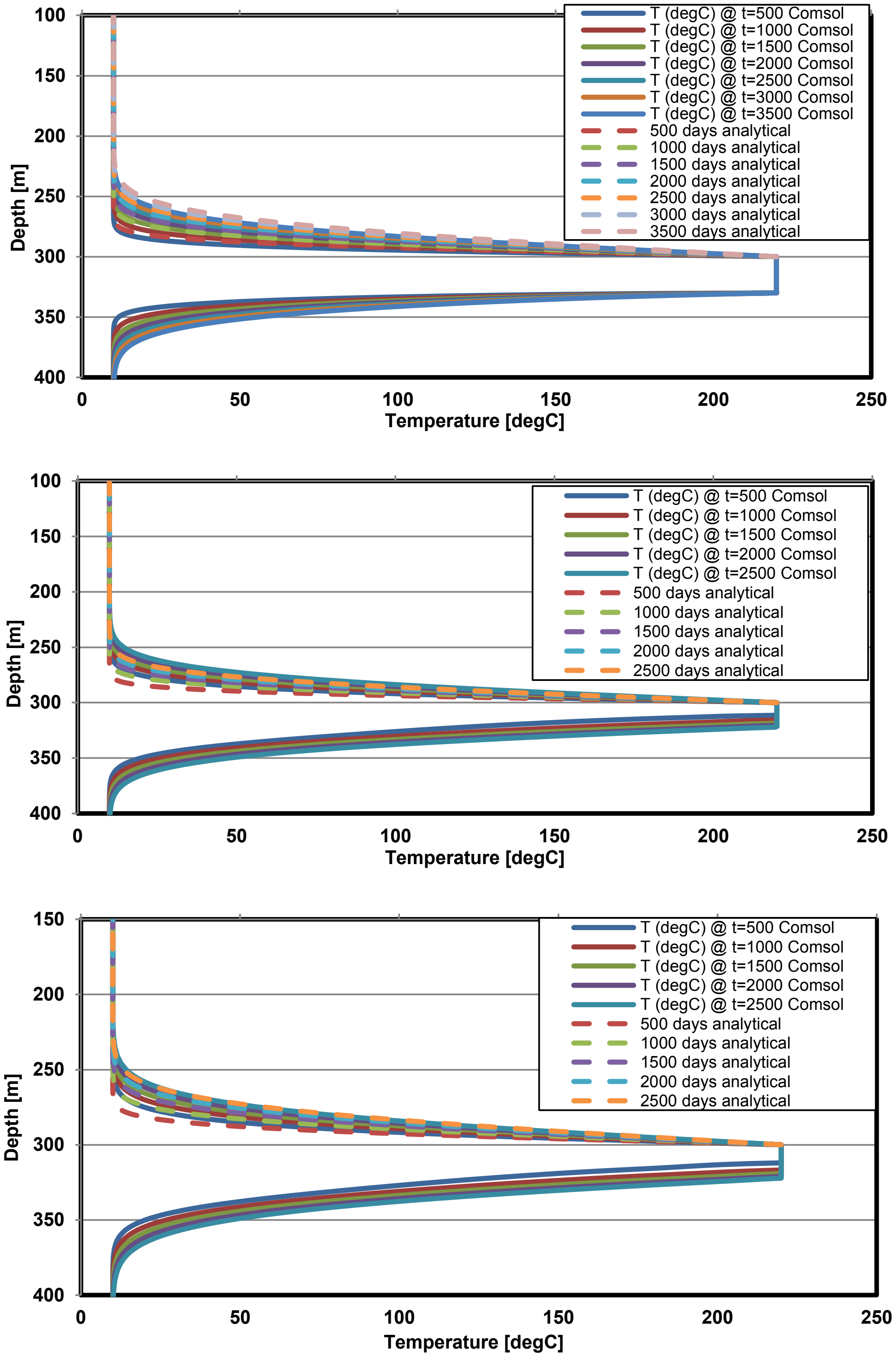

(a)

(b)

(c)

Figure 3.23: Comparison of temperature profiles from two dimensional spreading steam chambers with conduction to 1D conduction case along: (a) $\mathbf{L_1}$. (b) $\mathbf{L_2}$. (c) $\mathbf{L_3}$.

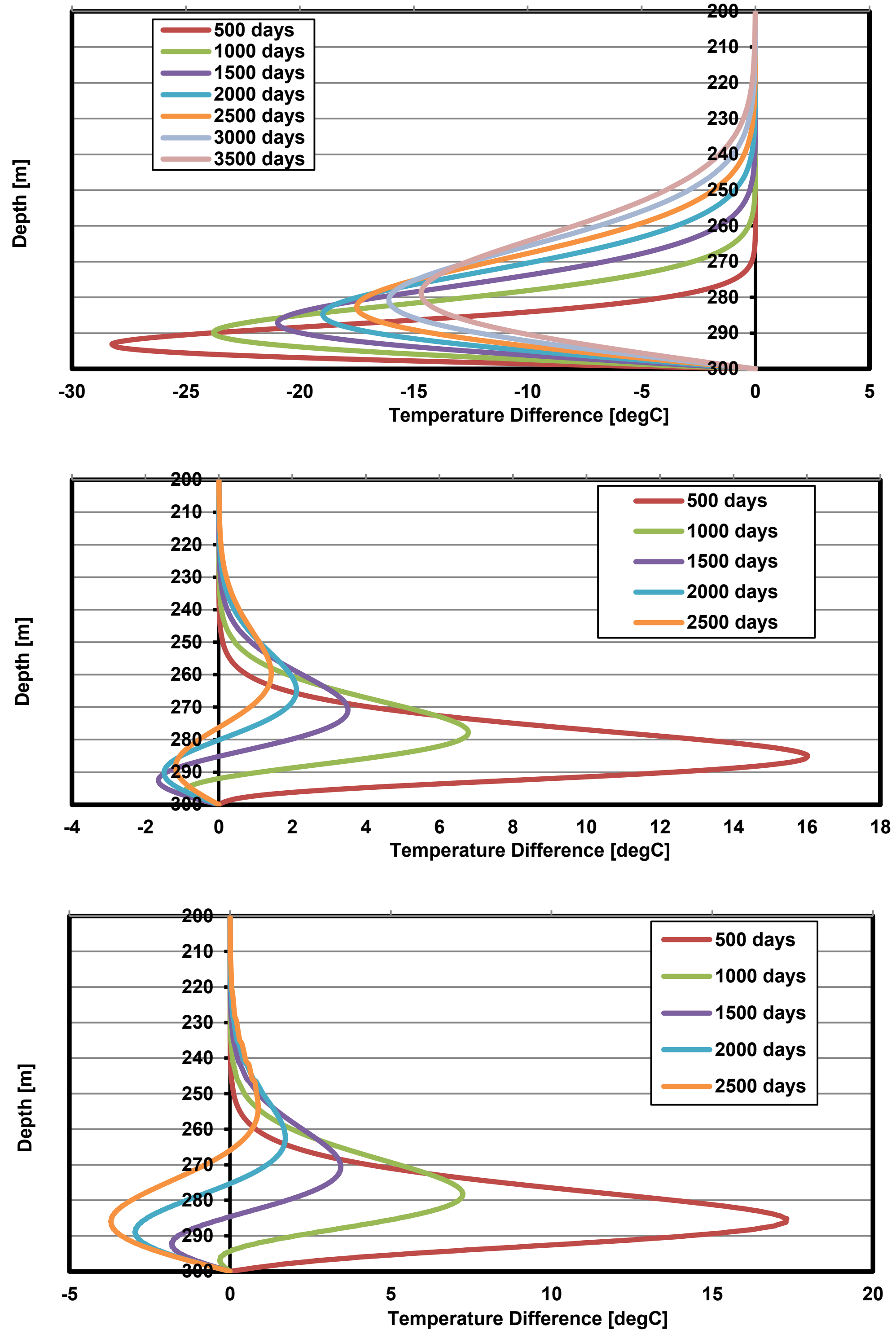

Figure 3.24: Temperature Difference between temperature profiles obtained from the two dimensional expanding chamber with conduction and 1D conduction case along: (a) $\mathbf{L_1}$. (b) $\mathbf{L_2}$. (c) $\mathbf{L_3}$.

3.2. Heat Conduction with Convection

Diffusion of hot pore fluid can convect heat through the porous medium. The diffusion of pore fluid results in pore pressure migration ahead of the steam chamber as well. During the SAGD operation steam condenses at the edge of the steam chamber and hot water is able to diffuse if the medium is permeable enough.

The governing equation of convective heat transfer is:

$$(\rho c)_m \frac{\partial T}{\partial t} + (\rho c)_f \vec{v}.\vec{\nabla} T = \vec{\nabla}.\left(k_m \vec{\nabla} T\right) + q_m''' \qquad \text{Equation 3.12}$$

In the following sections, one and two dimensional heat conduction with convection cases are investigated in different scenarios and temperature profiles are obtained based on the location of the monitoring location.

3.2.1. One-dimensional Heat Conduction with Convection

In the case of one-dimensional heat conduction with convection, the governing equation will be:

$$(\rho c)_m \frac{\partial T}{\partial t} + (\rho c)_f v \frac{\partial T}{\partial x} = k_m \frac{\partial^2 T}{\partial x^2} + q_m''' \qquad \text{Equation 3.13}$$

Assuming that the thermal properties of the medium are constant and the velocity of hot diffusing fluid is also constant, an analytical closed form solution in the semi-infinite medium with the following boundary conditions can be obtained as (Van Genuchten and Alves, 1982):

$$\begin{aligned} &(\rho c)_m \frac{\partial T}{\partial t} + (\rho c)_f v \frac{\partial T}{\partial x} = k_m \frac{\partial^2 T}{\partial x^2} \qquad z > 0 \ , \qquad t > 0 \\ &\qquad T(x, 0) = T_R \ , \qquad z > 0 \ , \qquad\qquad \text{Equation 3.14} \\ &\qquad T(0, t) = T_s, \qquad t > 0 \ , \end{aligned}$$

$$T(x,t) = T_R + \frac{1}{2}(T_S - T_R)\left[\operatorname{erfc}\left(\frac{x - \frac{(\rho c)_f v}{(\rho c)_m}t}{\sqrt{4\alpha t}}\right) + e^{\left(\frac{(\rho c)_f x}{k_m}\right)}\left(\frac{x + \frac{(\rho c)_f v}{(\rho c)_m}t}{\sqrt{4\alpha t}}\right)\right] \qquad \text{Equation 3.15}$$

Figure 3.25 shows the temperature profiles with average thermal properties of the medium in Table 3.1 and assuming $\rho_f = 1000\frac{kg}{m^3}$, $c_f = 4200\frac{J}{kg°C}$, and $v = 2\frac{m}{year}$.

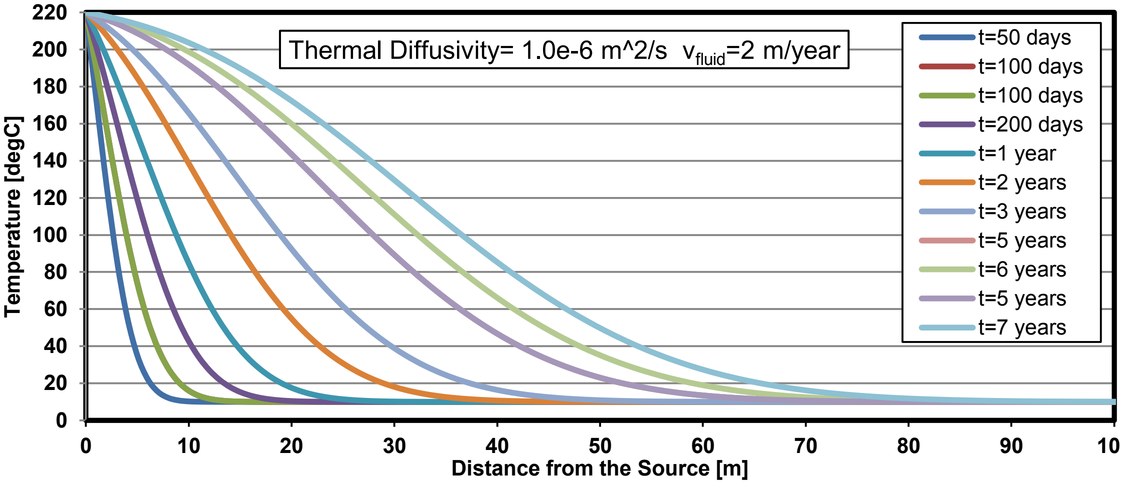

Figure 3.25: One-dimensional conductive and convective temperature profiles ahead of a hot interface.

3.2.1.1. Effect of Magnitude of Fluid Velocity on Deviation from Pure Conduction

The impact of the convective heat component is significantly dependent on the magnitude of the velocity of the hot fluid. Figure 3.26 compares temperature profiles of conductive heat transfer to three conductive and convective heat transfer cases with the same thermal properties but different fluid velocity magnitudes. Hot fluid is able to transfer energy ahead of the interface. It can be seen that the difference between pure conduction and conduction with convection profiles increases over time at further distances from the interface.

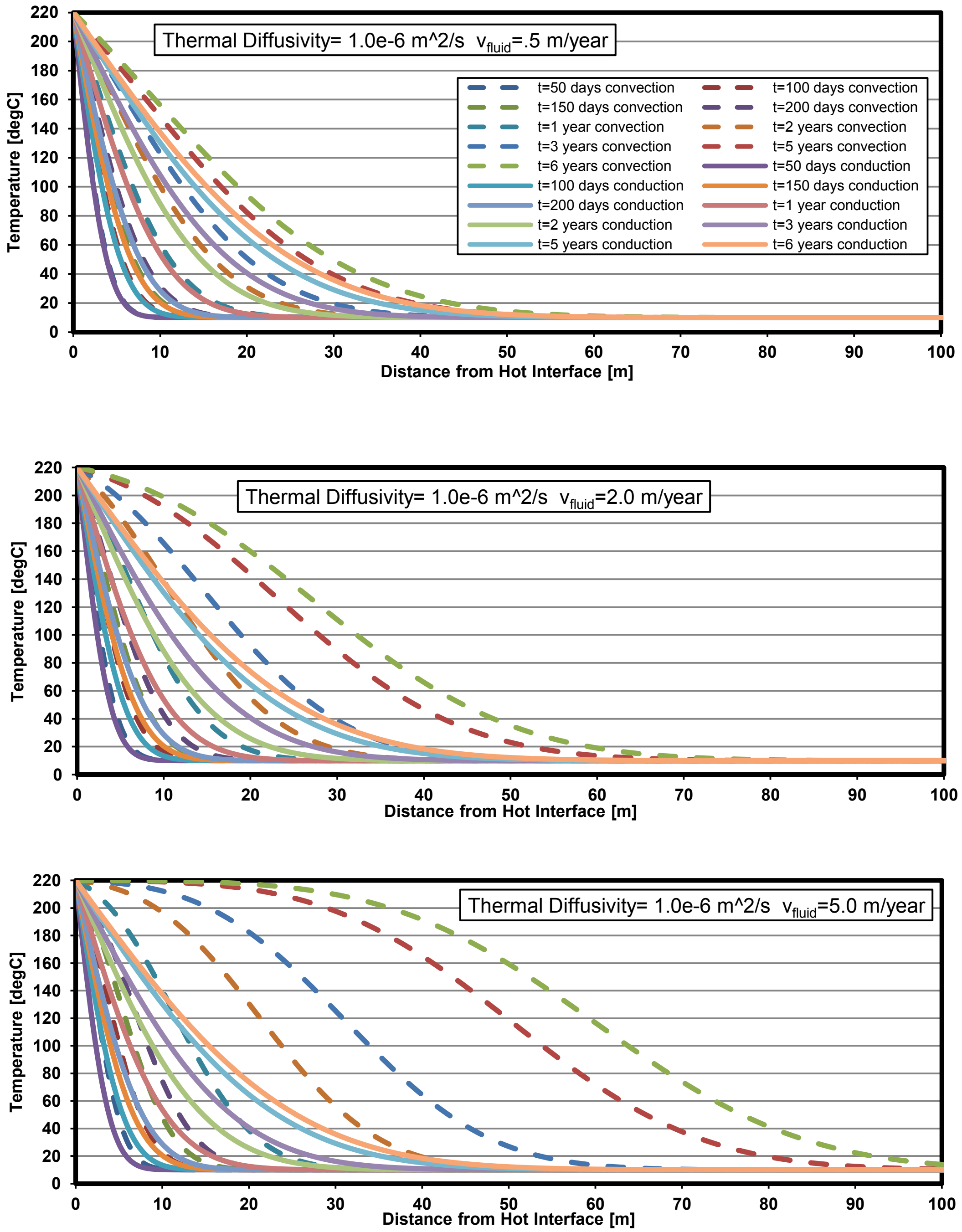

(a)

(b)

(c)

Figure 3.26: Effect of fluid velocity (v_{fluid}) on temperature profiles. a) $\mathbf{v_{fluid}} = .5\,\frac{\mathbf{m}}{\mathbf{year}}$. b) $\mathbf{v_{fluid}} = 2\,\frac{\mathbf{m}}{\mathbf{year}}$. c) $\mathbf{v_{fluid}} = 5\,\frac{\mathbf{m}}{\mathbf{year}}$.

It can be seen in Figure 3.27 that the difference in temperature distributions is highly dependent on the convective velocity and variation of fluid velocity in only one order of magnitude is resulting in dramatic differences in transport of heat. With the thermal properties assumed, there is very little difference between pure conduction and conduction with convection at low diffusive velocities, i.e. $0.5\frac{m}{year}$, but the difference increases dramatically at higher velocities, i.e. $5\frac{m}{year}$, specifically in the far field.

The detection of convective flows in the observation wells requires a measurable difference between the pure conductive and conductive with convective temperature profiles. It will be explained in Chapter 5 that the presence of water in the observation wells smears temperature measurements up to about 20m above the top of the hot interface. It can be seen in Figure 3.27 that depending on the velocity of the moving fluid, peak differences between pure conduction and conduction with convection cases occur about 20-40m ahead of the hot interface. Therefore, the contribution of convection can be detected in the observation wells beyond the smeared interval if the magnitude of the convective flow is high enough.

The presence of a zone with high relative permeability to water near the steam chamber (thief zone) results in rapid condensation and diffusion of hot water through the medium. The source of energy is not infinite in the real world. There is a maximum pressure and rate at which steam can be injected into the formation. Therefore, rapid condensation and diffusion of hot water prevents the formation of a steam chamber in the pay zone.

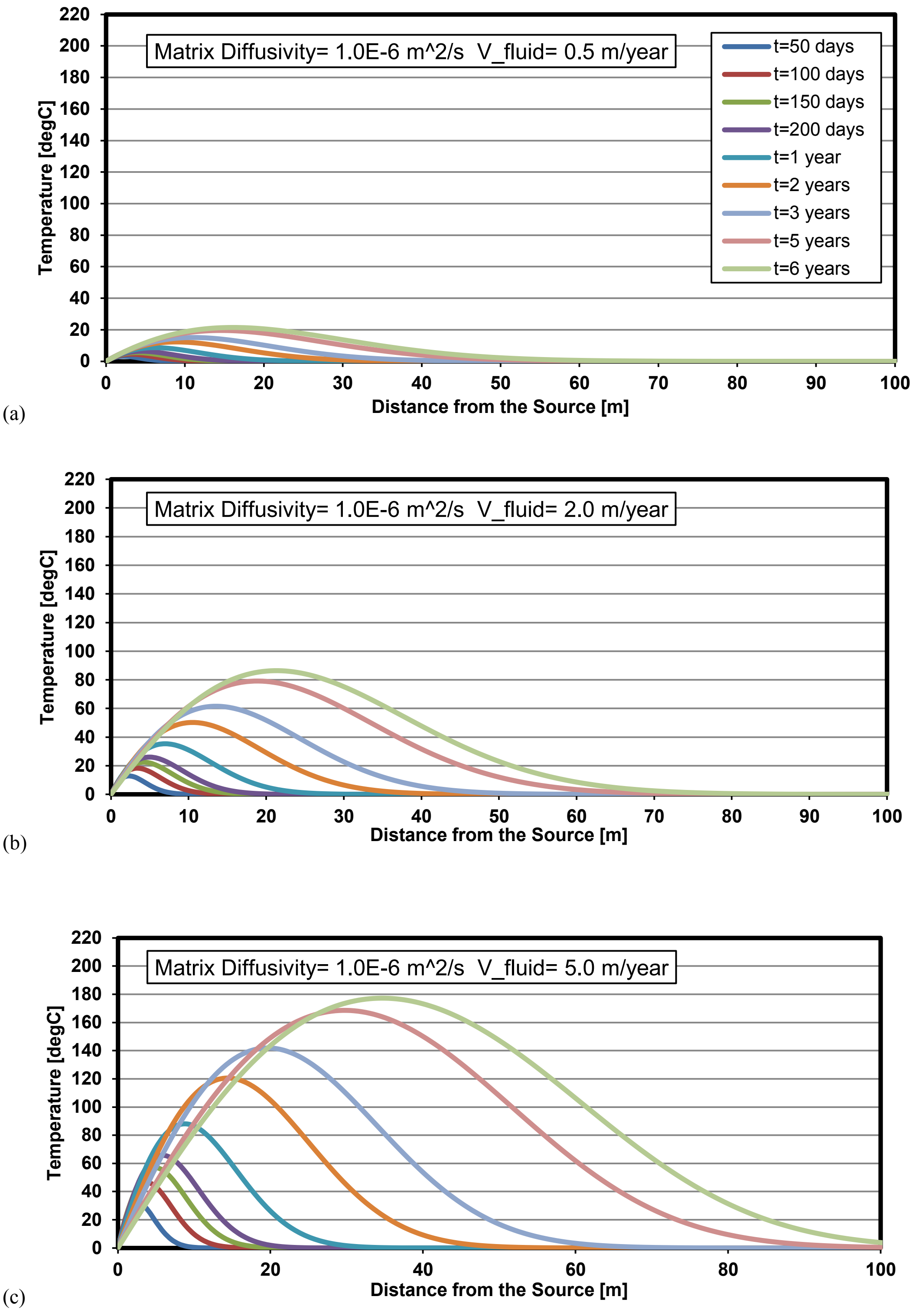

Figure 3.27: One-dimensional temperature difference between pure conduction and conduction with convection heat transport at different fluid velocities. a) $\mathbf{v_{fluid}} = .5\,\frac{\mathbf{m}}{\mathbf{year}}$. b) $\mathbf{v_{fluid}} = 2\,\frac{\mathbf{m}}{\mathbf{year}}$. c) $\mathbf{v_{fluid}} = 5\,\frac{\mathbf{m}}{\mathbf{year}}$.

3.2.1.2. Uncertainty in the Value of Fluid Convective Velocity

The influence of uncertainty in fluid velocity on temperature profiles can also be investigated in a similar fashion to the conduction heat analysis in the previous section. In this study thermal properties of the medium are assumed to be constant and the velocity of the fluid is considered to follow a normal distribution. It is assumed that the normal distribution of the velocity has a mean value of $\mathrm{v}_{\mathrm{average}} = 2\,\frac{\mathrm{m}}{\mathrm{year}}$ and $\mathrm{CoV} = \frac{\sigma}{\mathrm{v}_{\mathrm{average}}} = 15\%$. A Monte Carlo study with 2000 samples was run for the statistical analysis. Uncertainties in temperature at different distances from the hot interface are shown in Figure 3.28. Uncertainty in temperature is higher at locations further from the source.

Coefficient of variance of temperature after 3000 days is calculated as a function of distance. Figure 3.29 indicates that uncertainty (CoV) increases as the distance from the hot interface increases.

However, as it can be observed in Figure 3.28-(a), maximum uncertainty does not necessarily occur at later times. This is due to the fact that temperatures will eventually reach closer to the maximum hot interface temperature at shorter distances from the hot interface compared to longer distances.

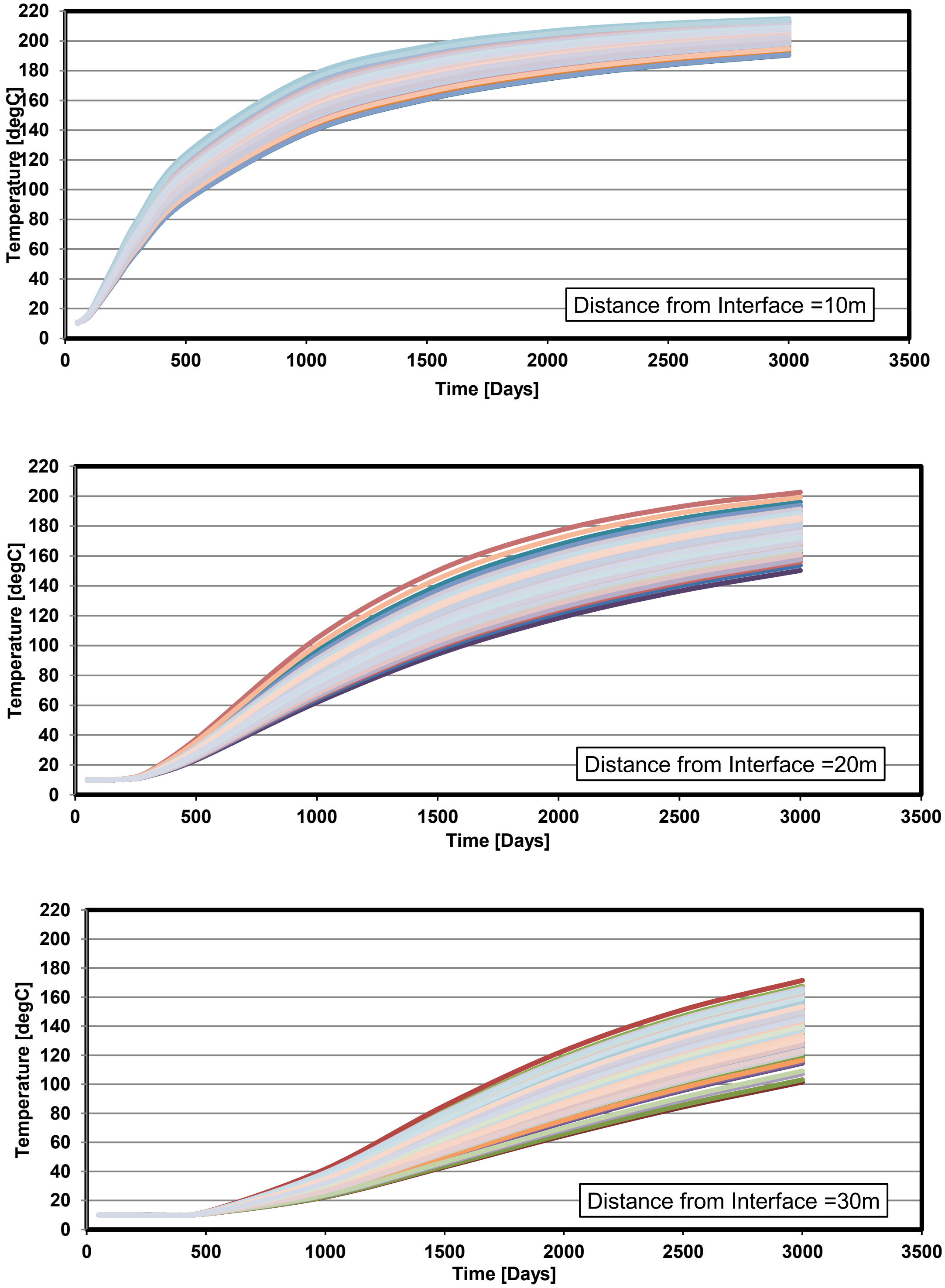

(a)

(b)

(c)

Figure 3.28: Temperature uncertainty over time at different distances from the hot interface in conductive with convective heat transport with $\mathbf{v_{average}} = \mathbf{2}\,\frac{\mathbf{m}}{\mathbf{year}}$ and $\mathbf{CoV} = \frac{\boldsymbol{\sigma}}{\mathbf{v_{average}}} = \mathbf{15\%}$. (a) 10m. (b) 20 m. (c) 30 m from the hot interface.

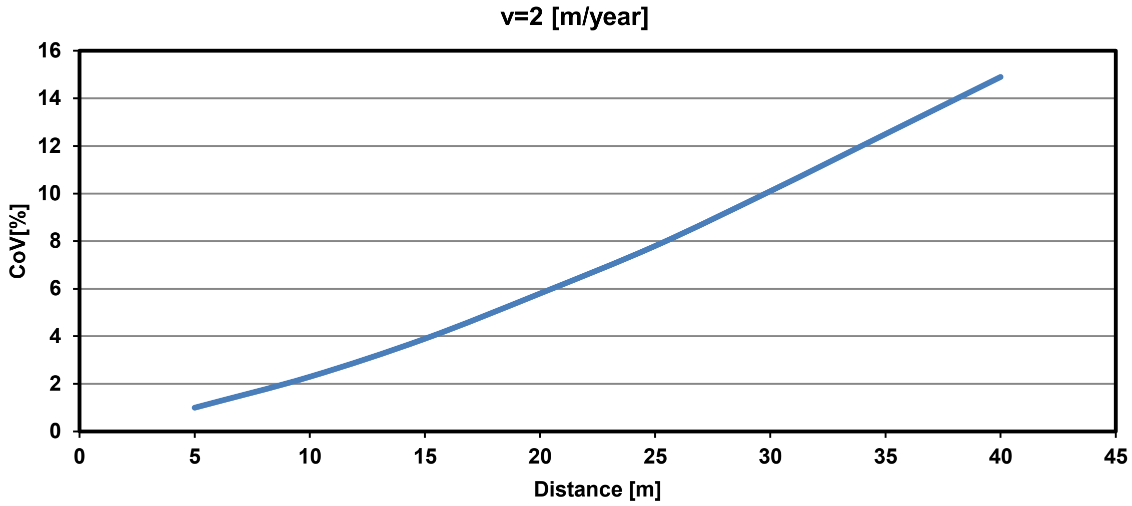

Figure 3.29: Uncertainty in temperature of conductive with convective heat transport after 3000 days with respect to distance from hot interface.

3.2.2. Two dimensional Heat Conduction with Convection

Two dimensional heat transfer scenarios have been modeled in COMSOL. Thermal properties of the medium are dependent on the properties of the skeleton and the pore fluid (Magowan et al., 1982). One way of evaluating equivalent thermal properties of the medium is by averaging the properties based on the occupied volume by the associated phase (Nield and Bejan, 2006). Thermal properties are then averaged as:

$$k_m = (1-\varphi)k_s + \varphi k_f$$

$$(\rho c)_m = (1-\varphi)(\rho c)_s + \varphi(\rho c)_f \qquad \text{Equation 3.16}$$

where:

k_m = equivalent thermal conductivity of medium;

k_s = thermal conductivity of solids;

k_f = thermal conductivity of pore fluid;

$(\rho c)_m$ = equivalent density and specific heat of the medium;

$(\rho c)_s$ = density and specific heat of the solids;

$(\rho c)_f$ = density and specific heat of pore fluid; and

φ = porosity of the medium.

In order to check the accuracy of the numerical solution, simulation outputs of COMSOL are compared with the analytical solution of the problem stated in 3.2.1. Assumed thermal properties of the solids and pore fluid are summarized in Table 3.2. Simulation outputs are shown in Figure 3.30.

Temperature profiles are compared in Figure 3.31. As one can see, analytical and numerical solutions perfectly match and there is no sensible difference between them.

Table 3.2: Thermal properties of solids and pore fluid used in COMSOL.

Property	Solids	Water
Density $\left[\frac{\text{kg}}{\text{m}^3}\right]$	2500	1000
thermal conductivity $\left[\frac{\text{W}}{\text{m°C}}\right]$	2.56	0.7
specific heat capacity $\left[\frac{\text{J}}{\text{kg°C}}\right]$	700	4200
Porosity [%]	18.37	

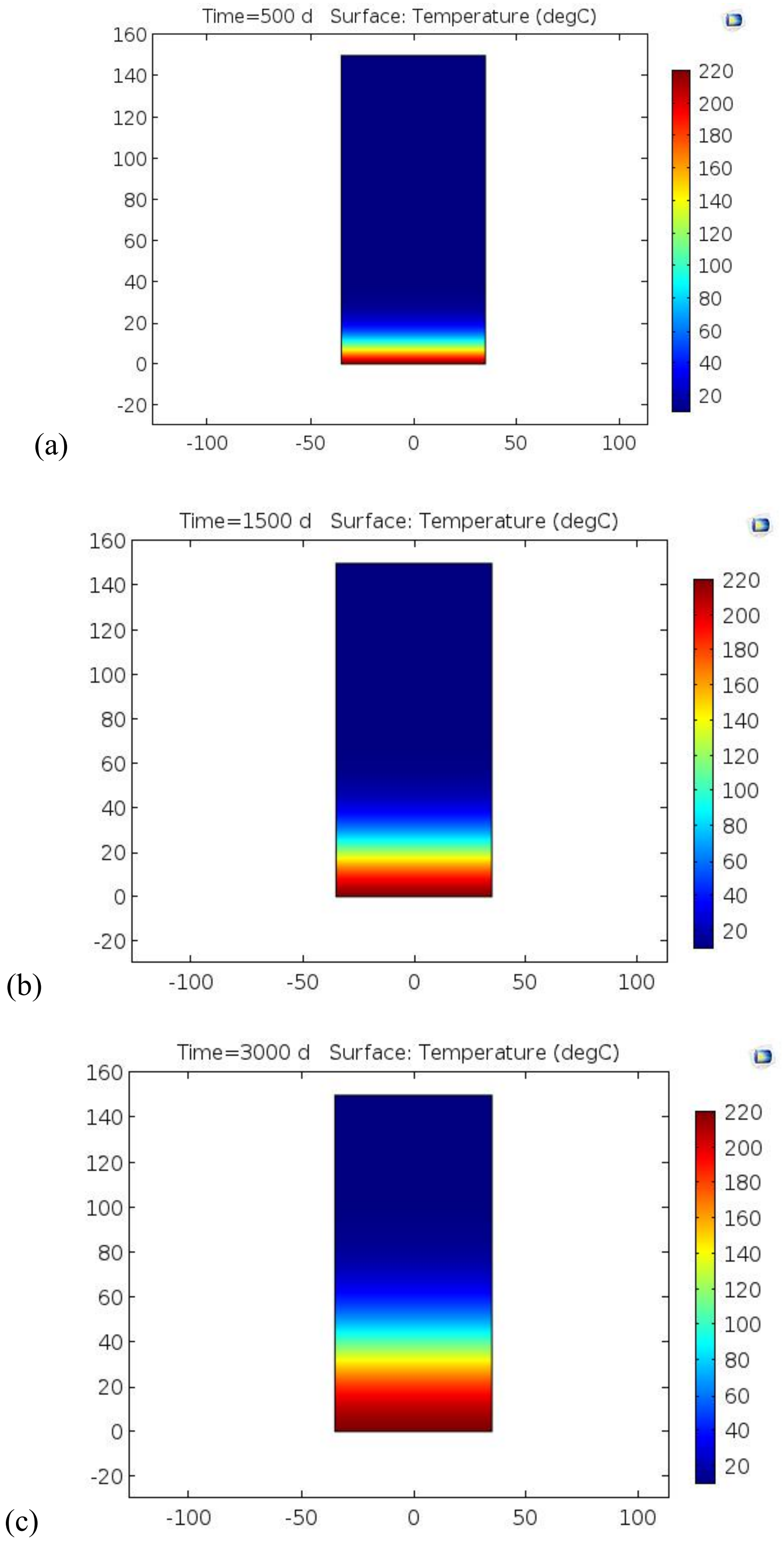

Figure 3.30: Numerical simulation of 1D conductive and convective heat transport. Temperature surfaces after: (a)500 days, (b) 1500 days. (c) 3000 days.

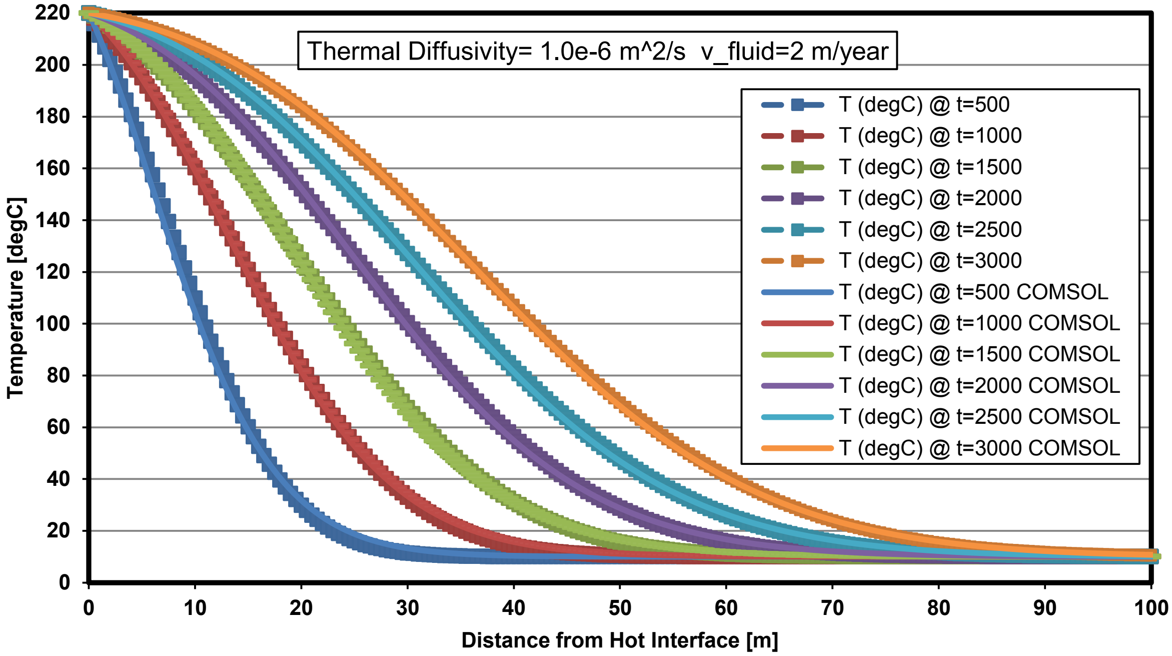

Figure 3.31: Comparison of one-dimensional analytical and numerical solutions of conduction with convective flow with constant vertical pore fluid velocity.

Two cases of heat conduction with convection from a hot interface are investigated. One of them is heat transport from a fixed hot interface. Two dimensional effects and anisotropy of the permeability field are investigated in this case. In the other case, a more detailed model with 5 laterally growing steam chambers is simulated. In the second model the effect of the location of monitoring on data collection and detection of convective flows is investigated.

For these cases, heat is lost to the overburden by both convection and conduction. The contribution of the convective component is dependent on the magnitude of the velocity of the diffusing fluid. Based on Darcy's law the difference between injection pressure and in-situ pressure and the effective permeability to the moving phase are two key parameters in determining the magnitude of the convective component. Higher-pressure differences and effective permeabilities will result in increased convective flows.

In the following simulations, it is assumed that bitumen is almost immobile and water is the mobile phase by which heat can be diffused. The complex multiphase behavior of bitumen and steam inside the steam chamber is not covered in this study and heat transfer beyond the condensation front with water as the mobile phase is only modeled. The pressure and temperature of the interface is also assumed to be equal to the saturation state of steam inside the steam chamber.

3.2.2.1. Heat Conduction with Convection through an Isotropic Medium

Two cases of heat conduction with convection from a fixed interface are studied. In one case the vertical velocity of the diffusing fluid is defined at the interface and it is allowed to spread through the *homogenous and isotropic* medium and drain to the lateral sides and top of the medium. No drainage was allowed from the bottom flanks. In the other case the permeability of the medium is increased in the horizontal direction by a magnitude of 100. This scenario is close to the heterogeneity that could be expected in the permeability of IHS layers. The configuration of the model is shown in Figure 3.32.

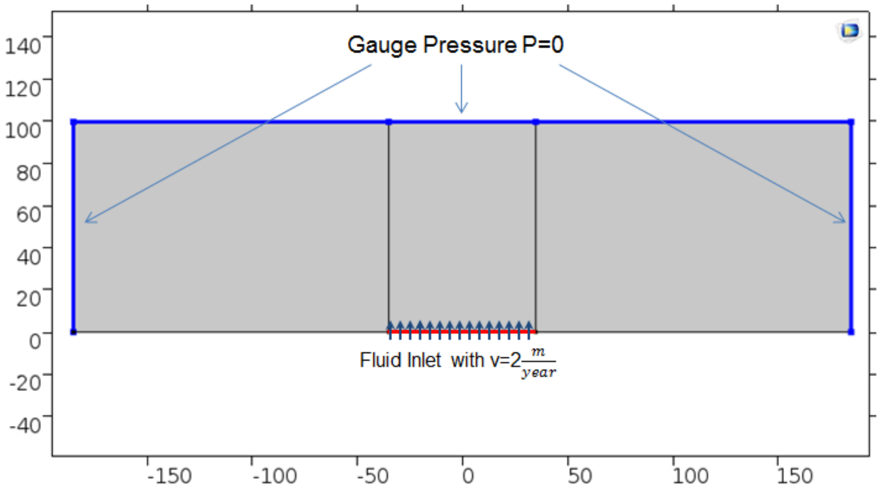

Figure 3.32: Fluid inlet and drainage paths in the two dimensional model.

Permeability and viscosity will determine the pressure field. The dependency of dynamic viscosity and specific heat capacity of the fluid on temperature is not covered in this study. In the isotropic case, the value of permeability and viscosity is considered to be 10mD and $2 \times 10^{-4}\mathrm{Pa.s}$, respectively. Figure 3.33 illustrates the flow paths of the fluid. Temperature distributions are shown in Figure 3.34.

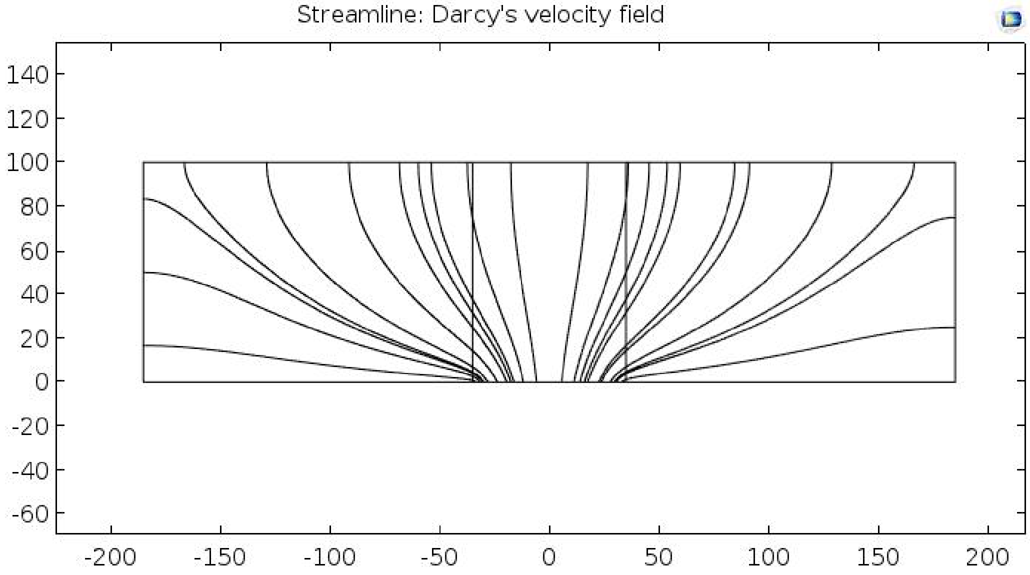

Figure 3.33: Streamlines of fluid flow in the two dimensional isotropic model

The flow paths are mainly vertical above the hot interface with little lateral flows. The magnitude of the lateral flows increases close to the edges of the interface. The solution of the two dimensional heat conduction with convection along three monitoring locations within the hot interface, shown in Figure 3.14, were compared with the one-dimensional analytical solution in Figure 3.35. Two-dimensional conductive and convective effects both contribute to deviation from the one-dimensional solution. As one can see, temperature profiles deviate more from the one-dimensional solution around the edges of the hot interface.

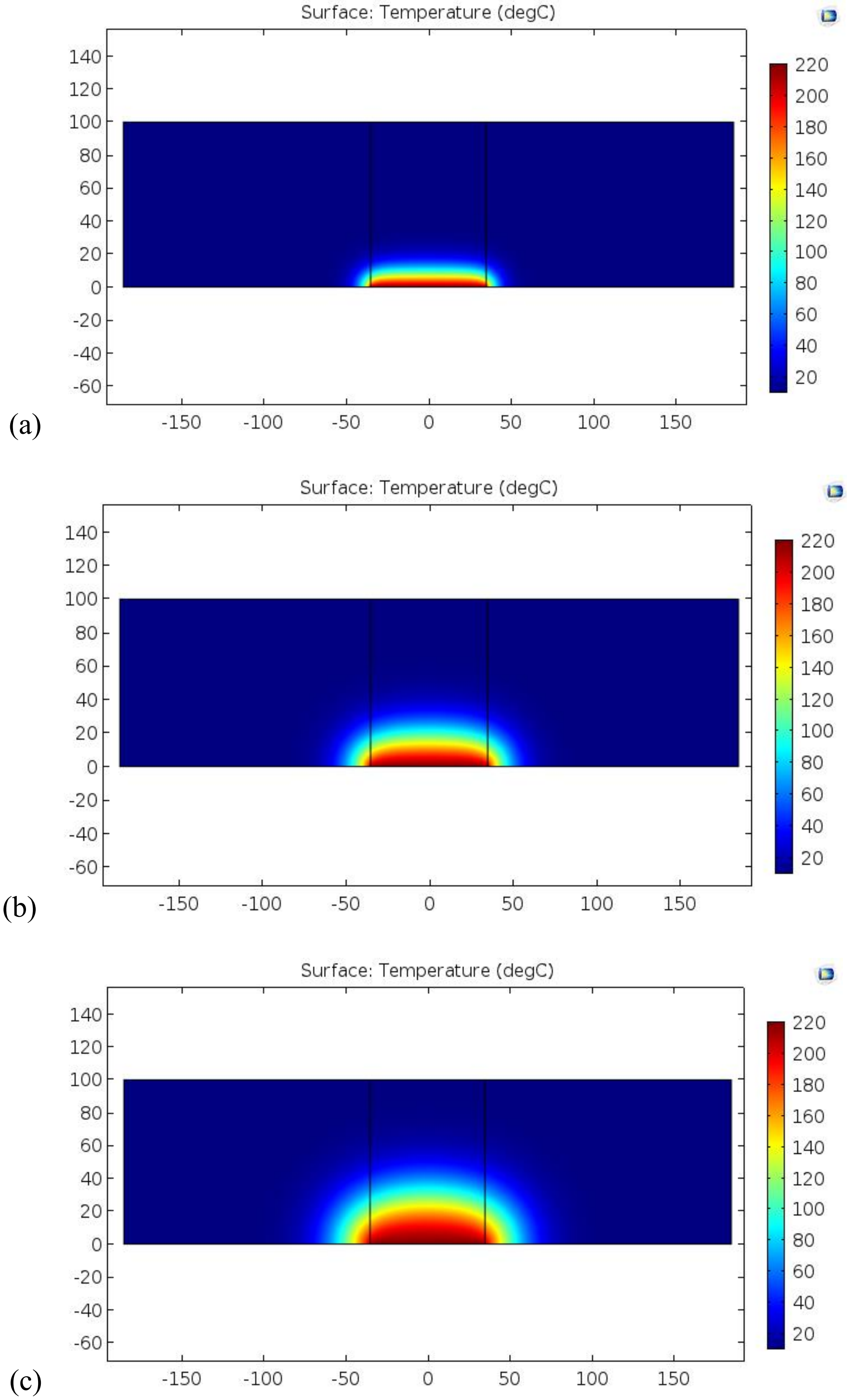

Figure 3.34: Temperature distribution of two dimensional heat losses from a fixed hot interface through an isotropic medium with conduction and convection. (a) 500 days. (b) 1500 days. (c) 3000 days.

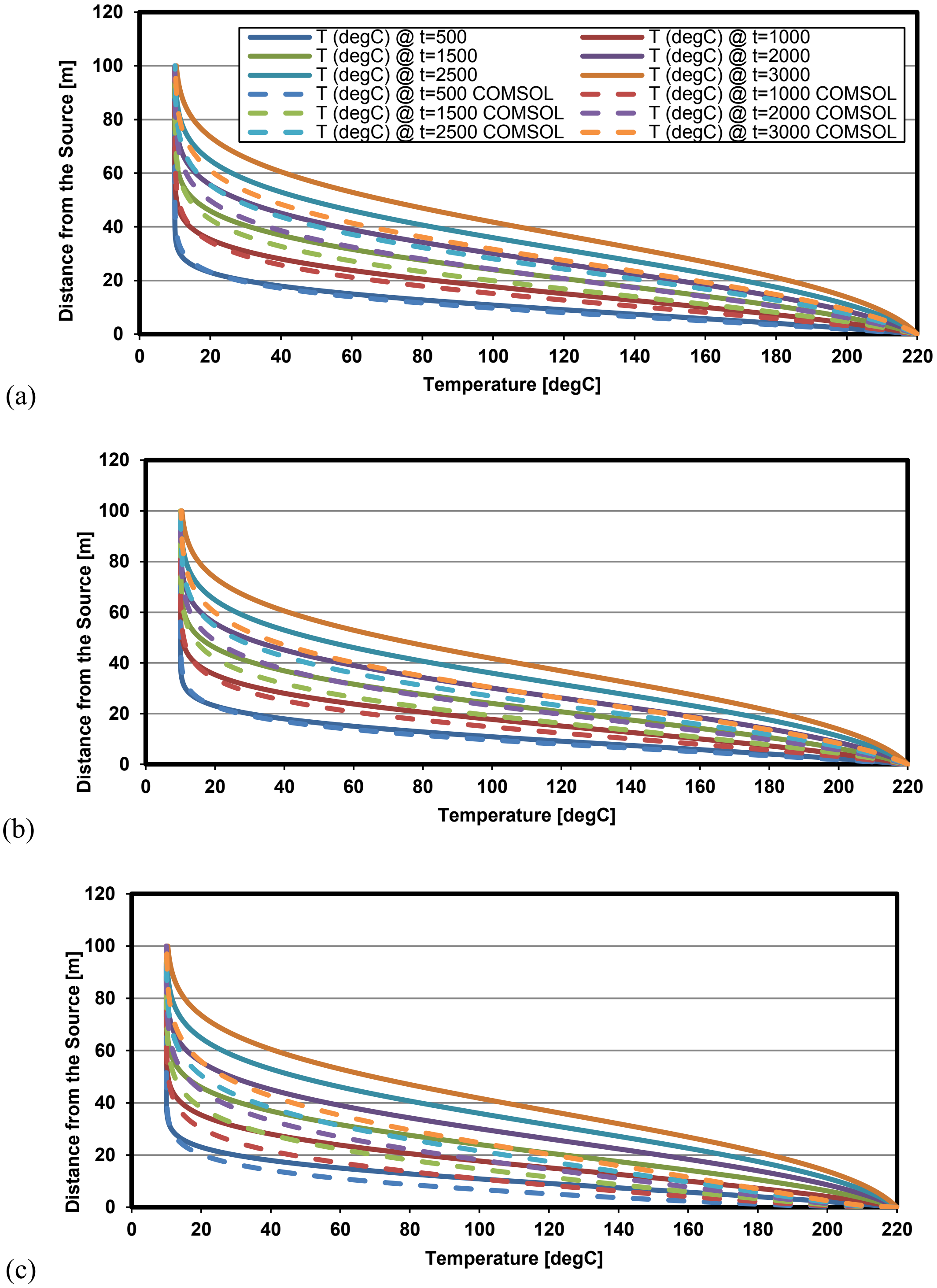

Figure 3.35: Comparison of temperature profiles obtained from the 2D isotropic conductive and convective heat loss from a fixed interface with 1D analytical conduction and convection solution: (a) center (b) midway between center and edge (c) edge of hot interface.

3.2.2.2. Heat Conduction and Convection through an Anisotropic Medium

The presence of low permeability interbeds in IHS layers reduces the vertical permeability dramatically. In the second model, the horizontal permeability of the medium was increased by 100 times compared to the vertical permeability. The drainage boundary conditions were the same as in the isotropic model. Streamlines show more fluid movement in the horizontal direction in Figure 3.36. Figure 3.37 shows the two dimensional temperature distributions in an anisotropic medium with vertical permeability of 10 mD and horizontal permeability of 1D.

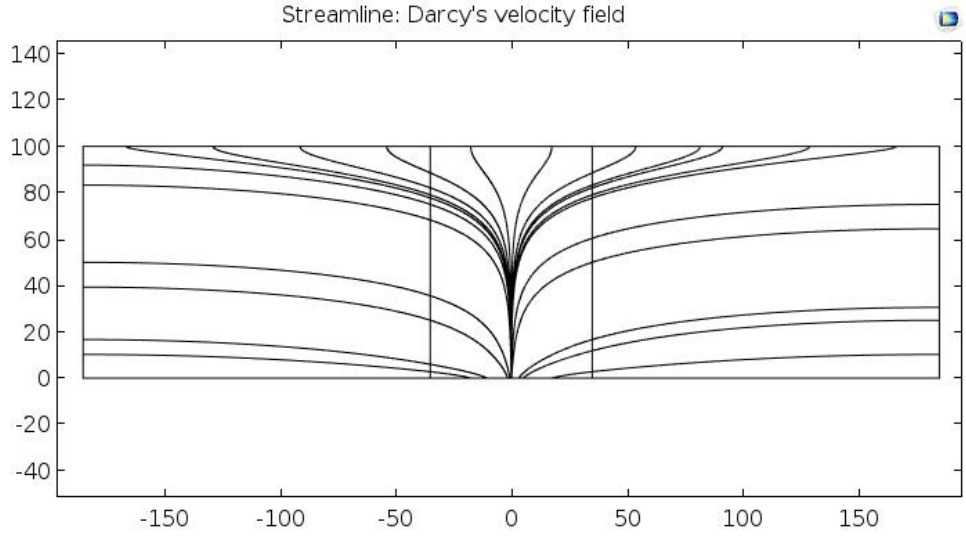

Figure 3.36: Streamlines of fluid flow in the two dimensional anisotropic model.

Anisotropy in the permeability field causes huge deviations from the one-dimensional solution. Hot fluid is able to move more easily in the horizontal direction than the vertical. Therefore, energy is transported more in the lateral direction compared to the vertical and temperatures will not build up quickly in the vertical direction ahead of the hot interface. The deviation is intuitively expected to be higher close to the edges of the hot interface than in the middle. More deviation is also expected as the offset from the center is increased.

One-dimensional temperature monitoring, along the same lines, from the two dimensional temperature profiles are compared to the one-dimensional heat transfer. As one can see, deviation is much greater from the isotropic case. Lu and Ge (1996) also mentioned that lateral fluid movements cause noticeable deviation from the one-dimensional solution.

3.2.2.3. Heat Conduction with Convection from Expanding Steam Chambers

In the second case, growing steam chambers are modeled assuming the configuration and thermal properties of the model were identical to the conductive case.

Heat transfer in porous media and poroelasticity modules within COMSOL were coupled in the modeling. In order to minimize the effects of boundary conditions on the geomechanical (poroelastic) solution the model is extended 2000m from each side. Geomechanical boundary conditions are set as no movement at the bottom, $u = v = 0$, and rollers on the sides. The geomechanical module is set as linear isotropic (except for permeability of IHS) poroelastic material with the inclusion of thermal stresses. The initial effective stress state is set as gravitational overburden stress in the vertical direction and the effective horizontal stresses are assumed to follow the equation:

$$\sigma'_{\mathrm{H}} = \sigma'_{\mathrm{h}} = \frac{\vartheta}{1 - \vartheta}\sigma'_{\mathrm{v}} \qquad \text{Equation 3.17}$$

where ϑ is the Poisson's ratio of the medium. Since this study is not focused on rock strength parameters, porosity, Young's Modulus, and Poisson's ratio are assumed to be constant and equal for all layers.

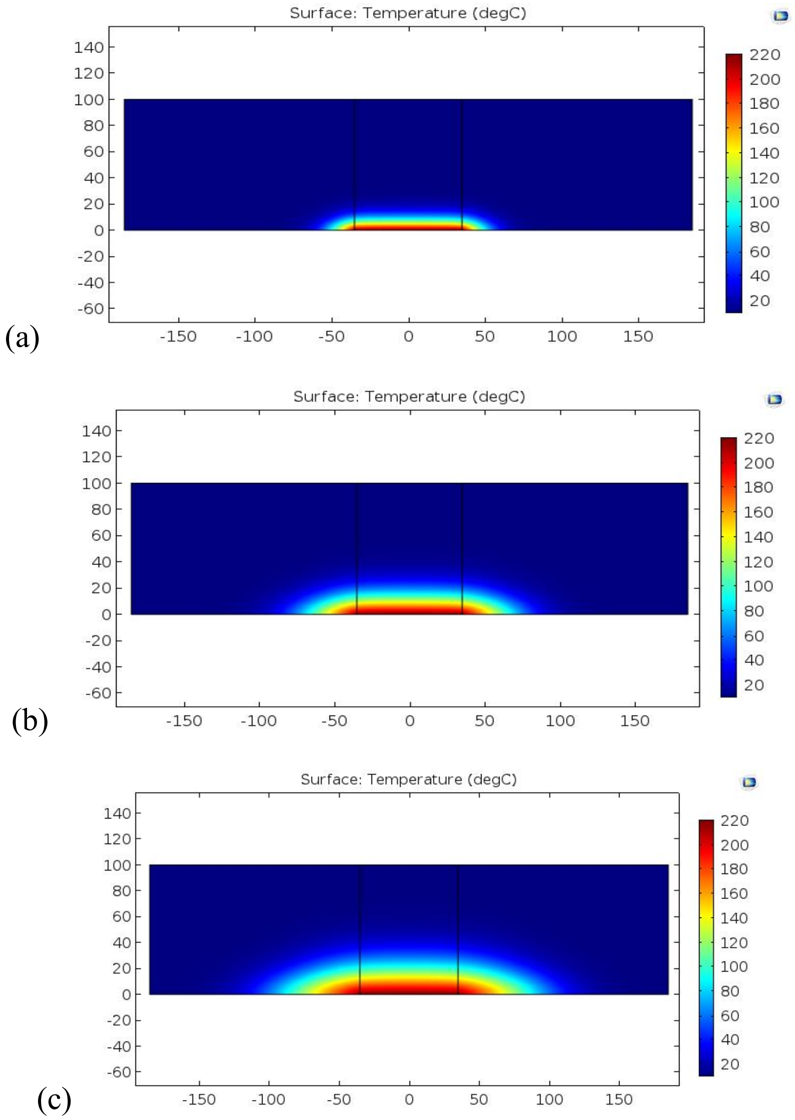

Figure 3.37: Temperature distribution of two dimensional heat loss from a fixed hot interface through an anisotropic medium with convection. (a) 500 days. (b) 1500 days. (c) 3000 days.

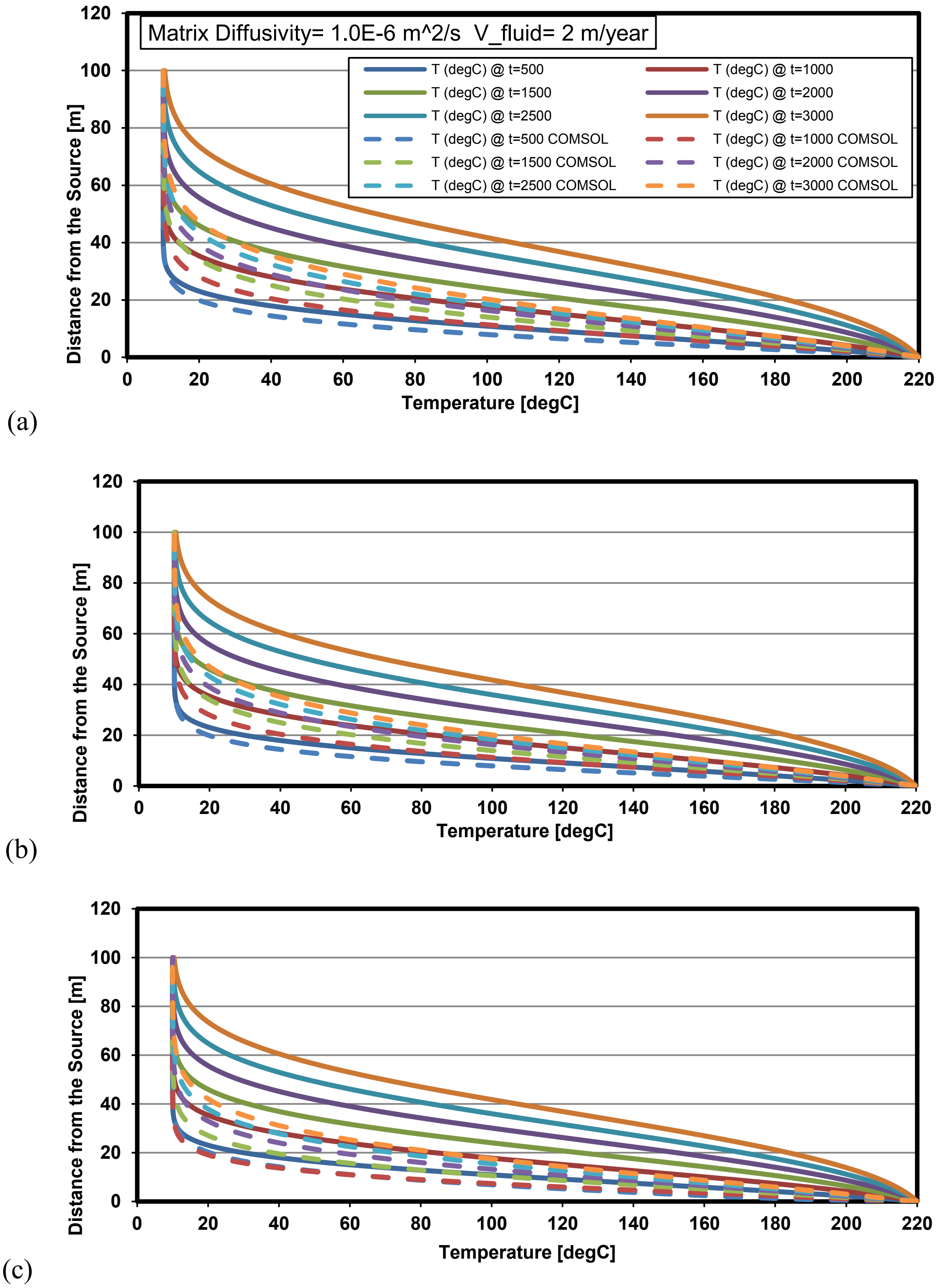

Figure 3.38: Comparison of temperature profiles obtained from the 2D anisotropic conductive and convective heat loss from a fixed interface with 1D analytical solution. (a) center. (b) midway between center and edge. (c) edge of hot interface.

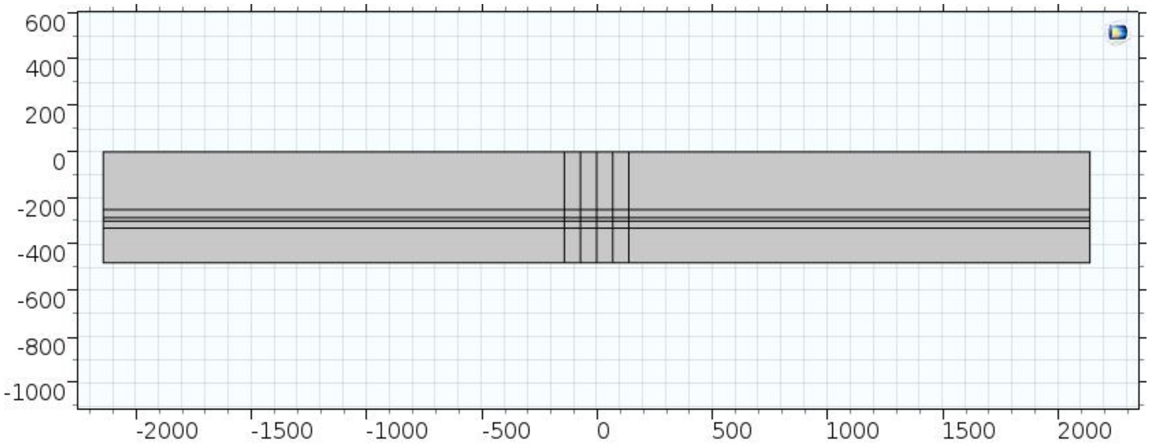

Figure 3.39: Configuration of the two dimensional model with five expanding steam chambers.

The initial pore pressure is set as hydrostatic from the surface to the bottom of caprock. The initial pressure of the IHS, pay zone, and underburden are set uniform and equal to each other. Biot's coefficient is also assumed to be one. The flow boundary conditions are set as hydraulic from the top to the bottom of the caprock and constant at the boundaries of the IHS, pay zone, and underburden so that no flow is occurring from the sides into or outside the model at the initial state. In order to increase the stability of the model the permeability of pay zone inside the steam chambers was not changed. It was observed in the results that pore pressures increased almost uniformly to the injection pressure in the area close to the steam chambers. Therefore, the need for changing permeability was not required. Geomaterial properties of each layer are summarized in Table 3.3.

Table 3.3: Properties of the geomaterials used in two-dimensional modeling.

Layer	Height [m]	Bulk Density $\left[\frac{\mathrm{kg}}{\mathrm{m}^3}\right]$	Bulk Heat Capacity $\left[\frac{\mathrm{J}}{\mathrm{kg}°\mathrm{C}}\right]$	Bulk Thermal Conductivity	Coefficient of thermal Expansion $\left[\frac{1}{°\mathrm{C}}\right]$	Youngs's Modulus [MPa]	Poisson's ratio	Porosity [%]	In-situ pore pressure	In-situ stress state	Permeability [mD]
Overburden	250	2200	1000	2.2	5×10^{-6}	2000	0.4	18.37	Hydrostatic	$\sigma_v = \rho_b g h$ $\sigma'_H = \sigma'_h = \frac{\vartheta}{1-\vartheta}\sigma'_v$	0.001
Caprock	35	2200	1000	2.2	5×10^{-6}	2000	0.4	18.37	Hydrostatic	$\sigma_v = \rho_b g h$ $\sigma'_H = \sigma'_h = \frac{\vartheta}{1-\vartheta}\sigma'_v$	0.00001
IHS	15	2200	1000	2.2	5×10^{-6}	2000	0.4	18.37	1500 [kPa]	$\sigma_v = \rho_b g h$ $\sigma'_H = \sigma'_h = \frac{\vartheta}{1-\vartheta}\sigma'_v$	$k_v = 10$ $k_h = 1000$
Pay zone	30	2200	1000	2.2	5×10^{-6}	2000	0.4	18.37	1500 [kPa]	$\sigma_v = \rho_b g h$ $\sigma'_H = \sigma'_h = \frac{\vartheta}{1-\vartheta}\sigma'_v$	0.05
Underburden	150	2200	1000	2.2	5×10^{-6}	2000	0.4	18.37	1500 [kPa]	$\sigma_v = \rho_b g h$ $\sigma'_H = \sigma'_h = \frac{\vartheta}{1-\vartheta}\sigma'_v$	0.001

Temperature surfaces are plotted in Figure 3.40. The higher permeability of the IHS convects heat in the vertical and horizontal direction. The magnitude of the fluid flow is greater in the horizontal direction than the vertical. Heat is transported sideways by the moving fluid and increases the temperature in the far field beyond the reach of conduction.

Interpretation of the observation well data for detection of convective flows is also dependent on the location at which the data is located. In order to study the effect of monitoring location on temperature profiles three monitoring locations shown on Figure 3.21 were used. The contribution of convective heat transport is higher at the areas close to the edge of the pad compared to the top of steam chambers. In order to compare the results with the conduction model, the initial time was shifted to the moment the hot interface reached the monitoring lines.

Temperature profiles along these lines, as shown in Figure 3.42, indicate that the deviation from conduction is greater as the location of a monitoring line gets closer to the edge of the steam chamber. The difference between temperature profiles and one-dimensional conduction case is shown in Figure 3.43. The difference between the two scenarios is maintained about 30m above the hot interface. The magnitude of the difference is high enough to be detected by the observation well if it is located close to the edge of the steam chamber.

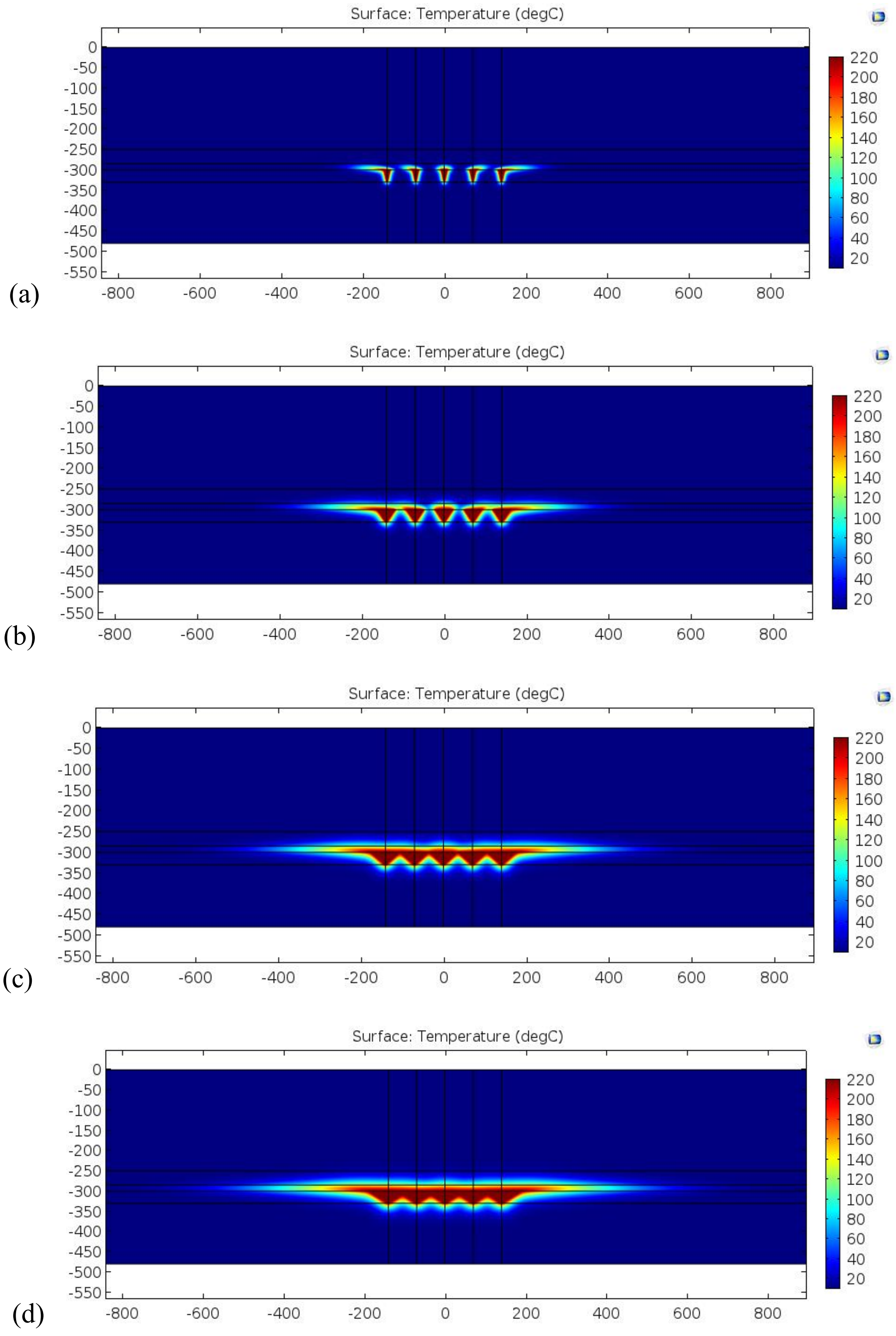

Figure 3.40: Two dimensional temperature distributions of five steam chambers with conduction and convection heat transport through the medium over time. (a) 500 days. (b) 1500 days. (c)2500 days. (d) 3500 days.

The Darcy velocity field illustrated in Figure 3.41 shows much higher magnitude in the horizontal direction than the vertical. Therefore, the determination of the contribution of convective flow by temperature profiles is not only dependent on the permeability and injection pressure, but also on the location of observation well. As the observation well gets closer to the edge of the pad, more lateral convective flow and therefore more contribution of convection should be expected. However, the one-dimensional vertical model of convective flow cannot be used for the process of temperature profiles as they are heavily influenced by the lateral flow (Lu and Ge ,1996).

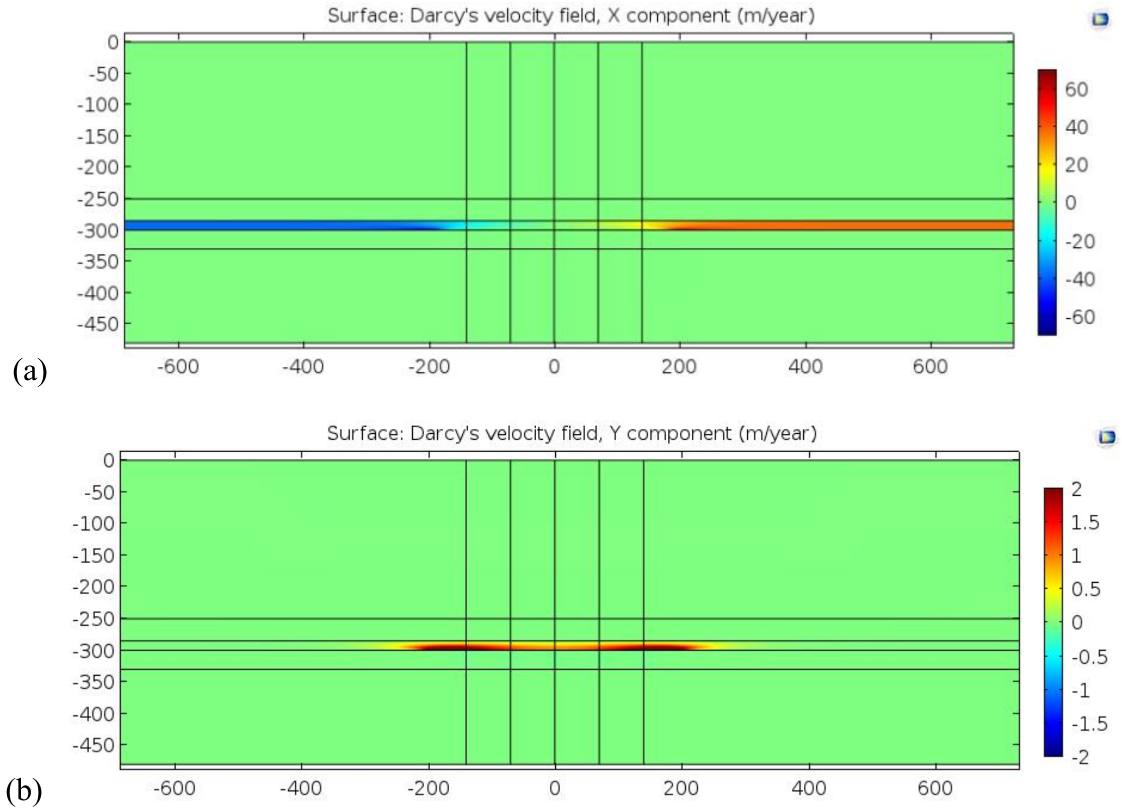

Figure 3.41: Darcy's velocity field above steam chambers. (a) horizontal component. (b) vertical component.

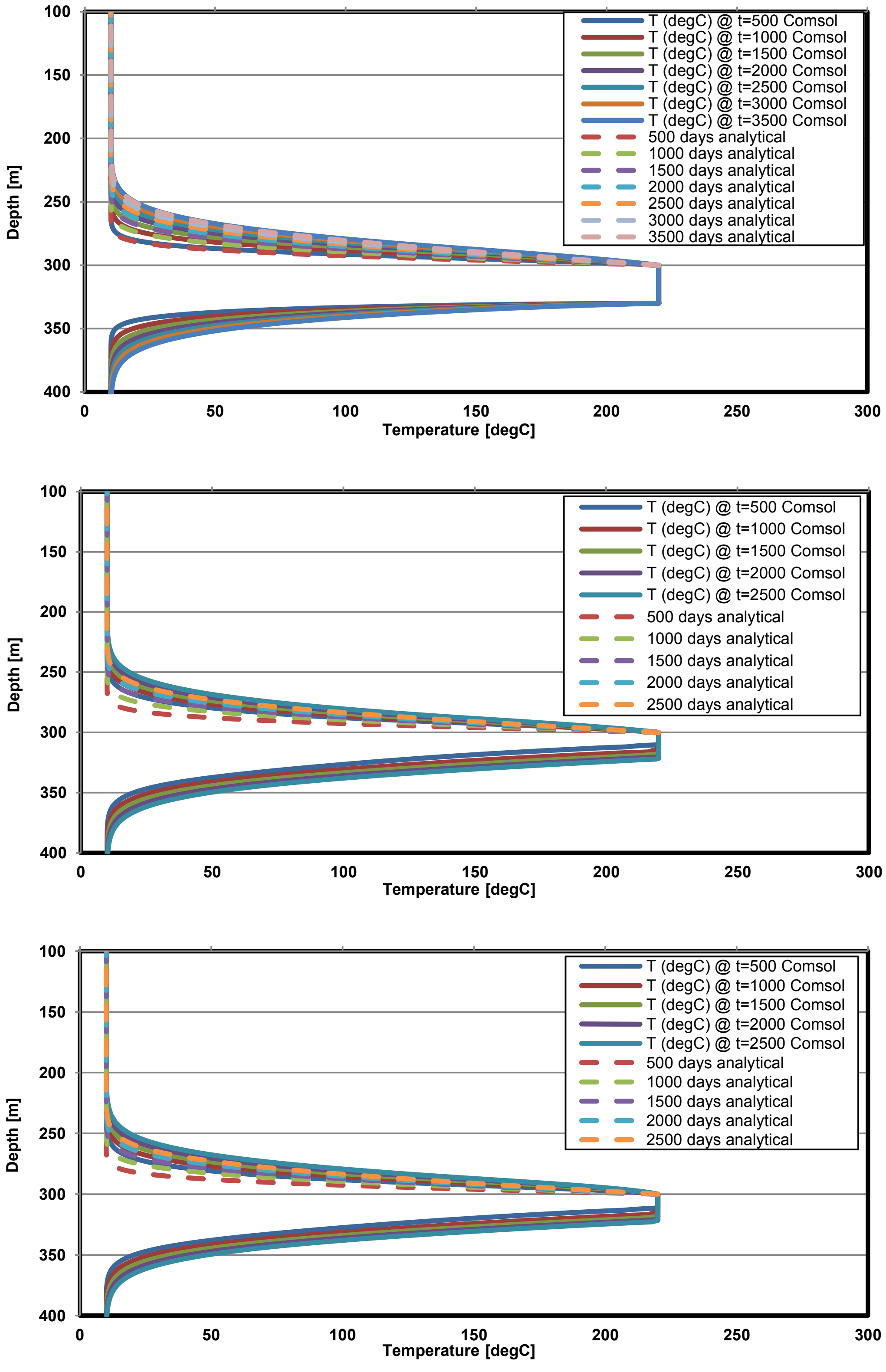

Figure 3.42: Comparison of temperature profiles from two dimensional spreading steam chambers with conduction and convection to 1D conduction case along: (a) $\mathbf{L_1}$. (b) $\mathbf{L_2}$. (c) $\mathbf{L_3}$.

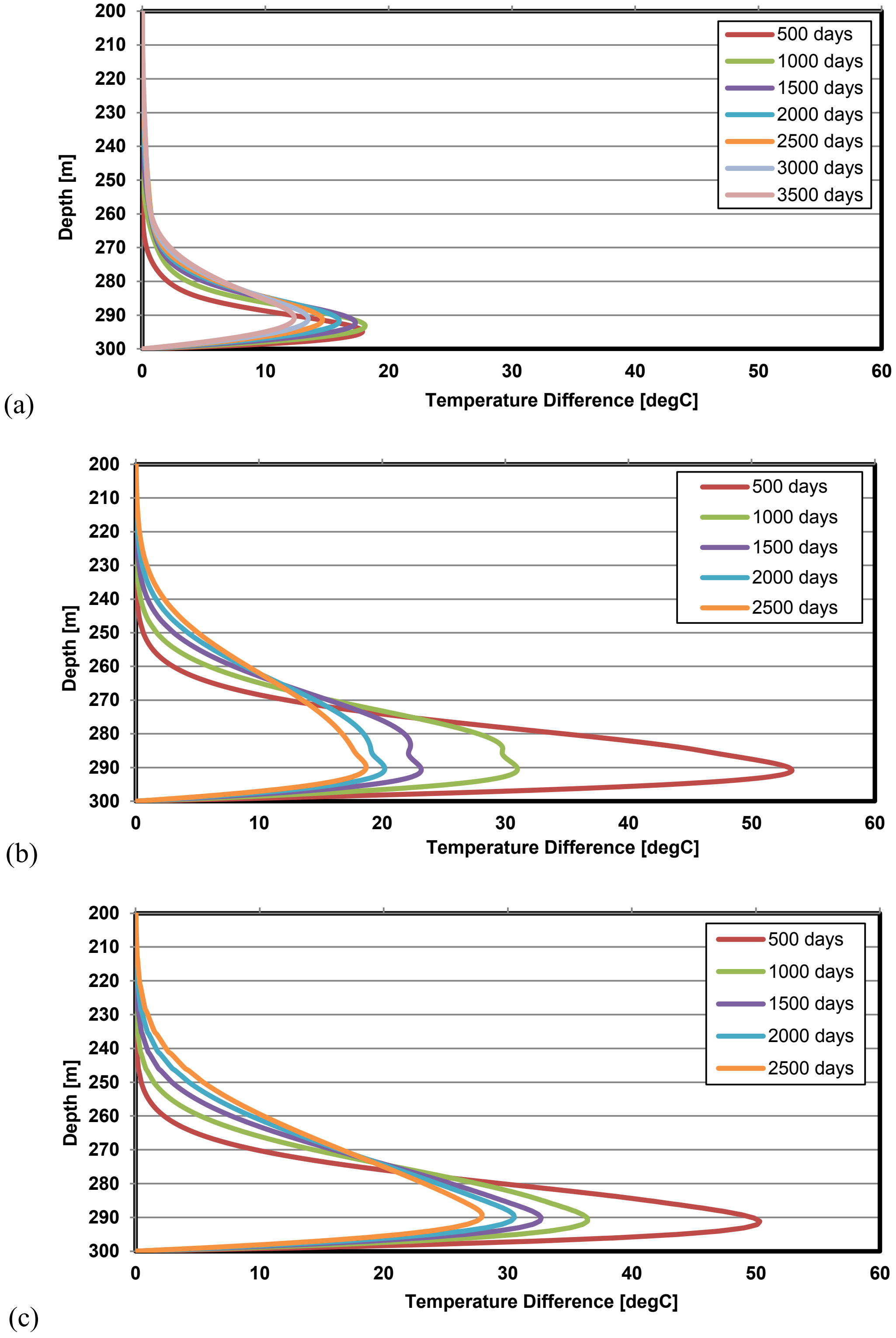

Figure 3.43: Temperature difference between temperature profiles obtained from the two dimensional expanding chamber with conduction and convection to 1D conduction case along: (a) $\mathbf{L_1}$. (b) $\mathbf{L_2}$. (c) $\mathbf{L_3}$.

3.3. Summary

In this chapter, several heat transfer scenarios were investigated. The effects of initial conditions, uncertainty in controlling parameters of heat transport, two-dimensional spread of energy, and location of monitoring wells were studied. The effect of initial temperature distribution of the medium based on steady state condition of a moving front on the solution of one-dimensional heat conduction was investigated. It was observed that the difference between the two solutions decreased over time.

It was shown that uncertainty in temperature profiles increases at distances farther from the hot interface as a result uncertainty in thermal diffusivity of the medium. The effect of uncertainty in the magnitude of the velocity of convective component was also investigated. Uncertainty in temperature also increased at farther distances from the hot interface in the conduction with convection case.

Two dimensional heat transfer scenarios were also compared to the one-dimensional heat transfer. Temperature profiles along monitoring lines were compared to the one-dimensional solution. Deviation from the one-dimensional solution was observed in both conduction and conduction with convection scenarios. In the case of pure conductive heat transfer more deviation was observed as the monitoring location was positioned close to the edge of the hot interface. The deviation was also greater for the case of an expanding hot interface compared to the fixed hot interface.

Temperature profiles of two-dimensional heat conduction with convection scenarios were also compared to the one-dimensional solution. Similar to the conductive case, the deviation increased as the monitoring location was positioned closer to the edge of the hot interface. The effect of anisotropy of permeability was also studied in the conduction with convection heat transport scenarios. More deviation from the one-dimensional solution was observed in the anisotropic case.

The position of the monitoring location on detection of convective heat transport was studied. It was shown that the difference between the temperature profiles of two-dimensional conductive and convective models and one-dimensional heat transport is dependent on the location of the monitoring line. As it was noticed in the simulations, anisotropy can lead to lower upward convective flows. More convective heat flows were present close to the edges of the pad compared to the middle. Consequently, more deviation was observed from the one-dimensional conductive case, as the monitoring line was located close to the edge of the pad. Detection of convective flows with observation wells requires enough vertical fluid movement. While there might exist large lateral convective flows, low vertical diffusive velocities might lead to no convective flow detection with the observation well.

Thermal properties of the medium were assumed constant and independent of pressure and temperature in the synthetic models. However, the variation of geomaterials' properties, specifically the McMurray and Clearwater Formations, should not be oversimplified if an exact model with low levels of uncertainty is required. The anisotropy and heterogeneity of permeability in IHS is also a challenging issue that needs to be considered in modeling.

The results of this chapter can help understand the controlling parameters and their relative impact on analyzing real observation well data.

Chapter 4: Calculation of Thermal Diffusivity from Temperature Profiles

In this chapter a method for inverse calculation of thermal diffusivity from temperature profiles is discussed and conclusions based on these calculations are used in subsequent chapters to estimate thermal properties based on field measurements.

Thermal diffusivity is the key controlling parameter in heat conduction to the overburden. Based on the method proposed by Birrell (2003), thermal diffusivity can be calculated from temperature logs of a non-moving steam chamber. The method is described as calculating the inverse conjugate error function (ICEF) of the non-dimensional temperature. In the case of a non-moving front, ICEF of the non-dimensional temperature will show a straight line on the plot. The slope of the ICEF plot is calculated in the next step. The change in the slope of the ICEF plot is calculated over time. Thermal diffusivity is then estimated as one quarter of the slope of ICEF powered to minus two over time. In the mathematical form, it is written as (Birrell, 2003):

$$\alpha = \frac{1}{4}\frac{\partial}{\partial t}\left(\frac{\partial}{\partial x}\mathrm{erfc}^{-1}(T^{*})\right)^{-2} \qquad \text{Equation 4.1}$$

Birrell and Putnam (2000) also propose how the top of the steam chamber can be estimated from ICEF plots. Additional details on the calculation of thermal diffusivity and top of steam chamber from temperature profiles can be found in Birrell and Putnam (2000).

4.1. Thermal Diffusivity from 1D temperature profiles

In the case of one-dimensional heat loss to the caprock, thermal diffusivity can be calculated from temperature measurements with the observation wells. In this section, thermal diffusivity is calculated from temperature profiles generated from the synthetic models and then compared to the real value by which the temperature profiles were generated.

4.1.1. Calculation of Thermal Diffusivity from 1D Analytical Conductive Solution

In this case, thermal diffusivity is calculated from the 1D conduction temperature profiles. Thermal diffusivity is assumed to be $1 \times 10^{-6} \left[\frac{m^2}{s}\right]$ and 14 temperature profiles during 1100 days are generated for back calculation of thermal diffusivity. Temperature profiles are shown in Figure 4.1. ICEF plots of the non-dimensional temperature profiles are calculated and shown in Figure 4.2. Changes in the slope of ICEF plot to power minus 2 over time are shown in Figure 4.3.

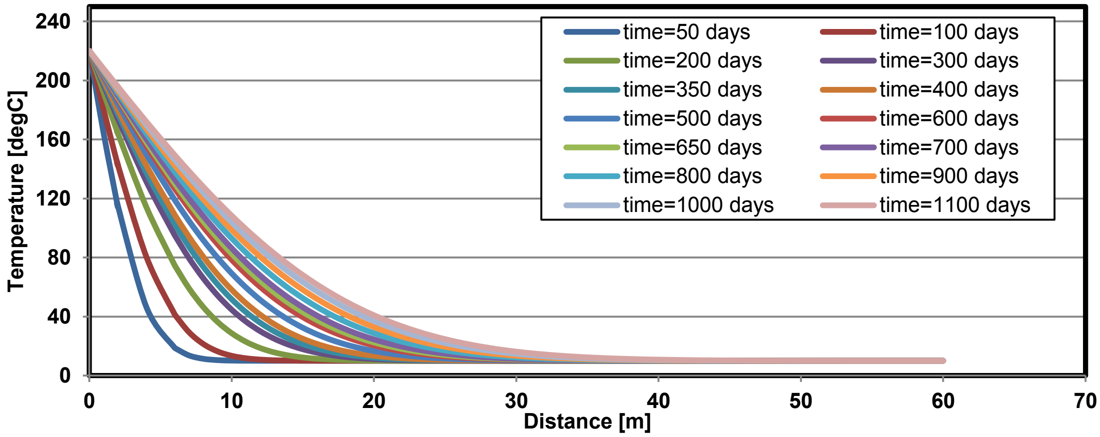

Figure 4.1: Temperature profiles of a one-dimensional conduction case from analytical solution

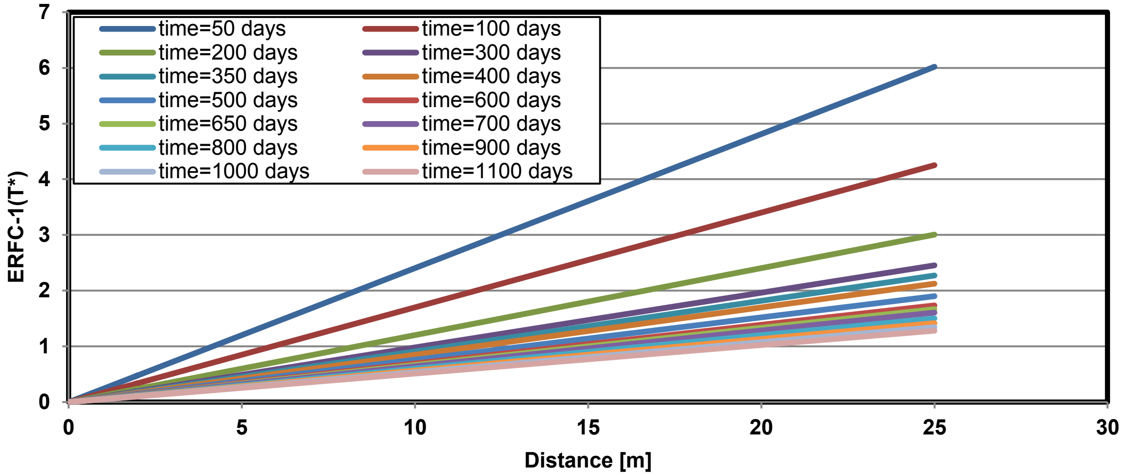

Figure 4.2: ICEF plots of temperature profiles from 1D analytical solution

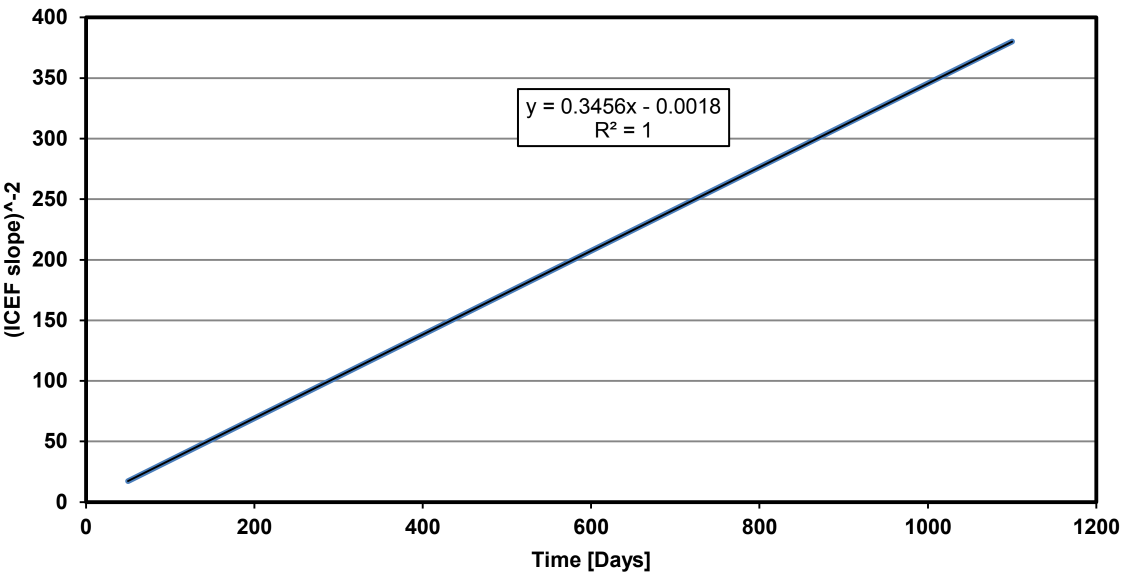

Figure 4.3: Changes in the slope of ICEF over time for the 1D analytical conduction case.

Thermal diffusivity is then calculated as:

$$\alpha = \frac{1}{4}\frac{\partial}{\partial t}\left(\frac{\partial}{\partial x}\operatorname{erfc}^{-1}(T^{*})\right)^{-2} = \frac{1}{4} \times 0.3456 = .0864\left[\frac{m^2}{day}\right] = 1 \times 10^{-6}\left[\frac{m^2}{s}\right]$$

The calculated thermal diffusivity matches the exact value that was used for the generation of temperature profiles.

4.1.2. Effect of Fluctuating Interface Temperature

As it was mentioned before, steam injection pressure changes during SAGD. Steam chamber temperature fluctuations in observation wells can be approximately in the range of $20℃$. A synthetic model was generated with the same temperature history shown in Figure 3.3 and $\alpha = 1.0 \times 10^{-6}\left[\frac{m^2}{s}\right]$. Temperature profiles were nondimensionalized by the temperature of the interface. ICEF plots of temperature profiles are shown in Figure 4.4. The estimated thermal diffusivity is equal to $1.03 \times 10^{-6}\left[\frac{m^2}{s}\right]$. As it can be seen, the calculated thermal diffusivity is very close to the value by which the profiles were generated. Therefore, it can be concluded that in the range of assumed thermal properties as long as the fluctuations in interface temperature are not drastic, i.e. 10% variation, and temperature profiles are non-dimensionalized with the concurrent interface temperature, the proposed method of back calculating thermal diffusivity will provide reasonable estimates of its magnitude.

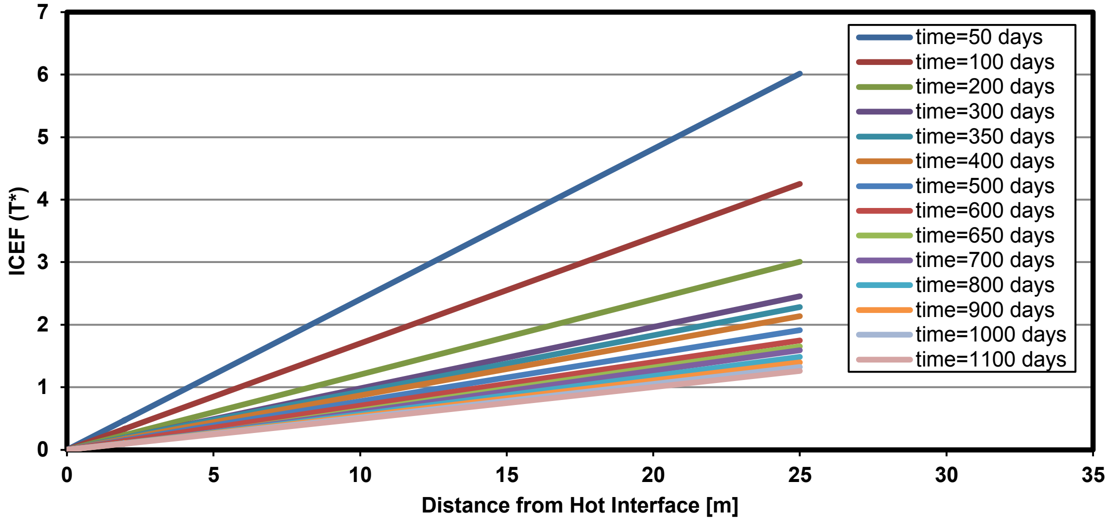

Figure 4.4: ICEF plots of 1D conductive temperature profiles with varying interface temperature.

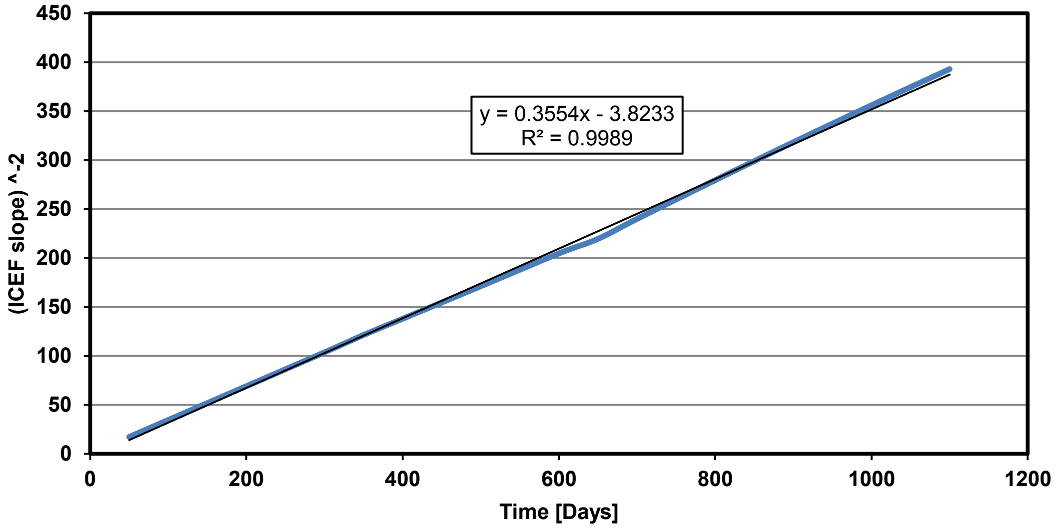

Figure 4.5: Changes in the slope of ICEF over time for the 1D analytical conductive case with varying interface temperature.

4.1.3. Effect of Formation Cold Temperature

The effect of uncertainty in in-situ temperature of the formation before the operation on the evaluation of thermal diffusivity is also investigated. The temperature of the cold region was forced to deviate from the true value of 10°C by 5°C in the normalization of temperature profiles and back calculation of thermal diffusivity. The ICEF plot of temperature profiles with cold temperatures less than the true value of 10°C by 5°C is shown in Figure 4.6.

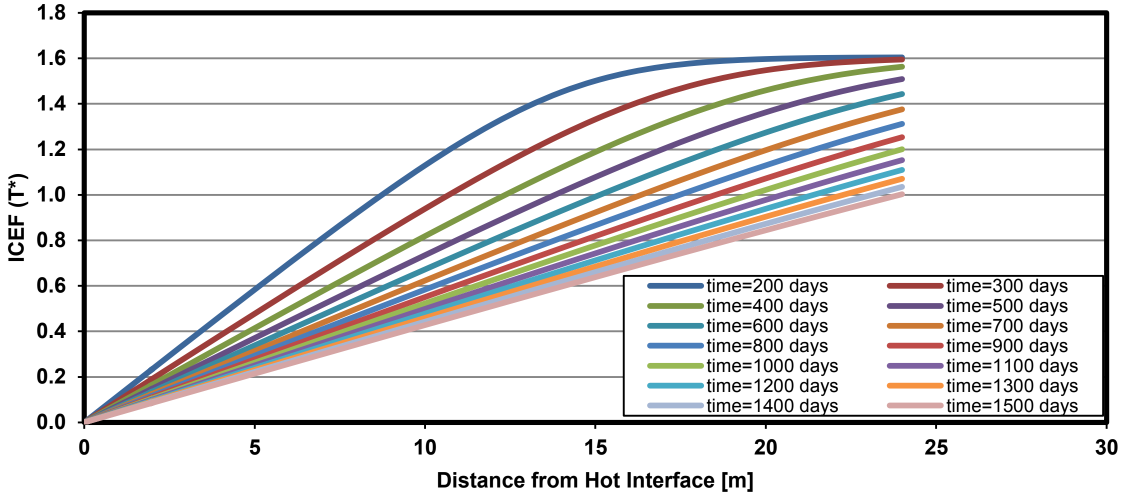

Figure 4.6: ICEF plots of temperature profiles assuming $\mathbf{T_{cold}} = \mathbf{5}$°C.

The ICEF plot of the temperature profiles generated by assuming the temperature of the cold medium at 15°C is shown in Figure 4.7.

However, the back calculation of thermal diffusivity is not greatly impacted by missing the true value of cold formation temperature. The calculated thermal diffusivity and relative error from its true value are plotted in Figure 4.8. The associated error in the estimation is less than 2% for the assumed thermal properties.

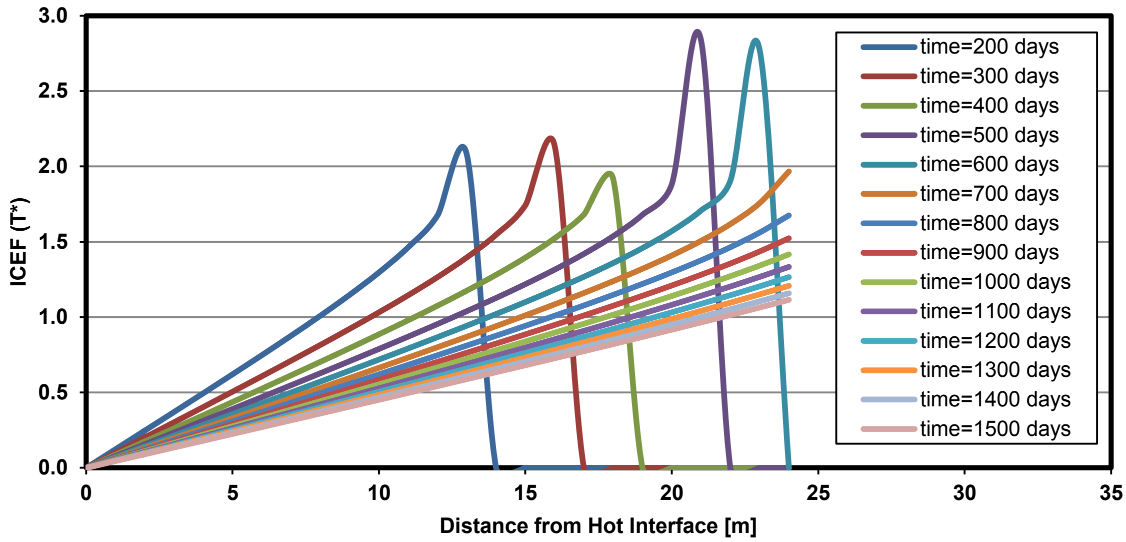

Figure 4.7: ICEF plots of temperature profiles assuming $\mathbf{T_{cold}} = \mathbf{15}$℃.

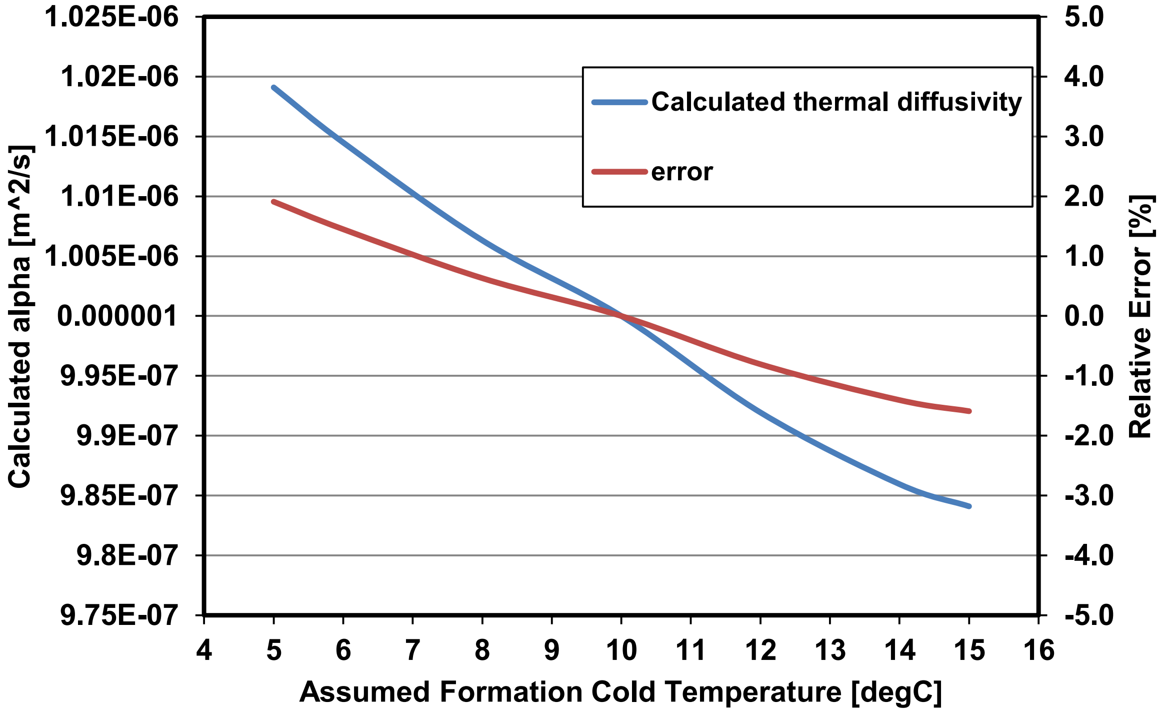

Figure 4.8: Deviation from the true value of thermal diffusivity associated with uncertainty in formation cold temperature.

4.1.4. Effect of Initial Temperature Conditions from Moving Interface

Heat can be transported ahead of an upward moving steam chamber before an impermeable layer stops its growth. The solution to the one-dimensional heat conduction with initial conditions set as the steady state solution of the moving front was developed in 3.1.1.3. A synthetic model with the same properties and velocity of moving front as explained in 3.1.1.3 was created and temperature profiles, shown in Figure 4.9, were used for calculation of thermal diffusivity.

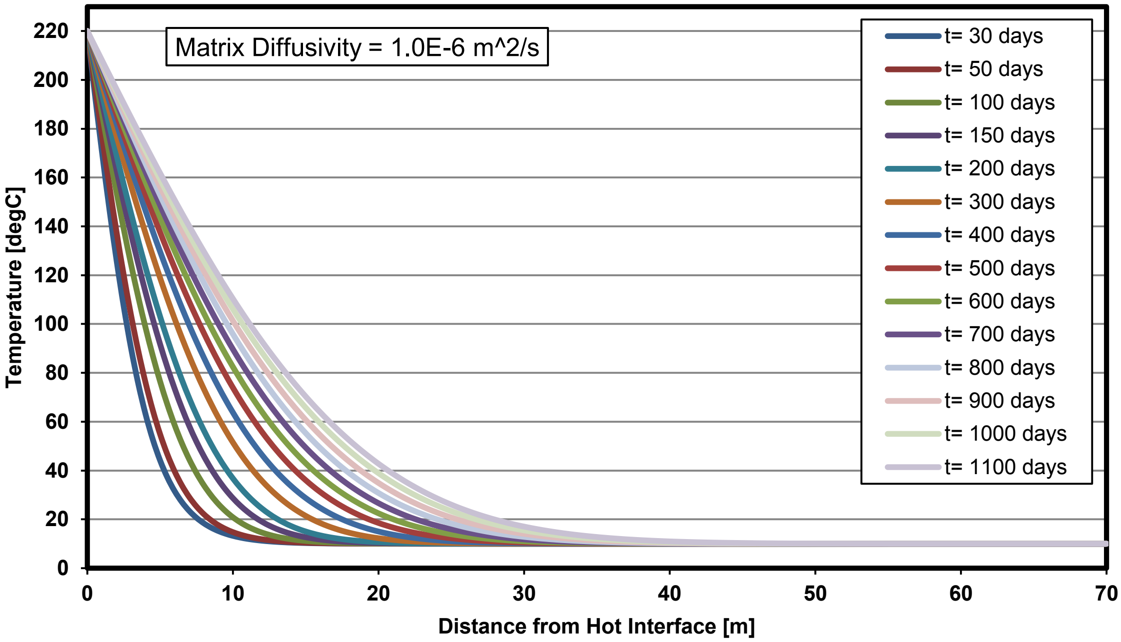

Figure 4.9: Temperature profiles ahead of a hot interface with initial conditions set as steady state solution of a moving front

ICEF plots of temperature profiles are shown in Figure 4.10. The linear behavior is not observed until after 300 days. The change in the slope of ICEF plot is calculated and shown in Figure 4.11. As one can see, the inclusion of the response in the early stages will result in lower values of thermal diffusivity ($8.04 \times 10^{-7} \left[\frac{m^2}{s}\right]$). However, the calculated value is closer to reality once the early response is dropped and the long-term response is used. The calculated value of thermal diffusivity based on temperature profiles after 300 days is equal to $9.53 \times 10^{-7} \left[\frac{m^2}{s}\right]$ which is lower but closer to the true value.

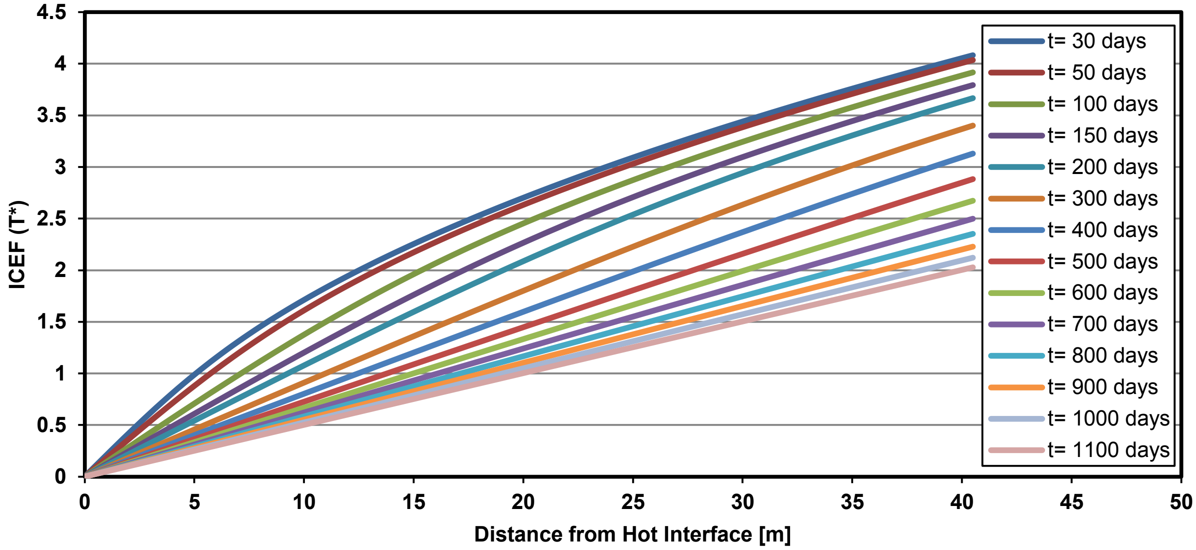

Figure 4.10: ICEF plots of temperature profiles from a hot interface with initial conditions set as steady state solution of a moving front.

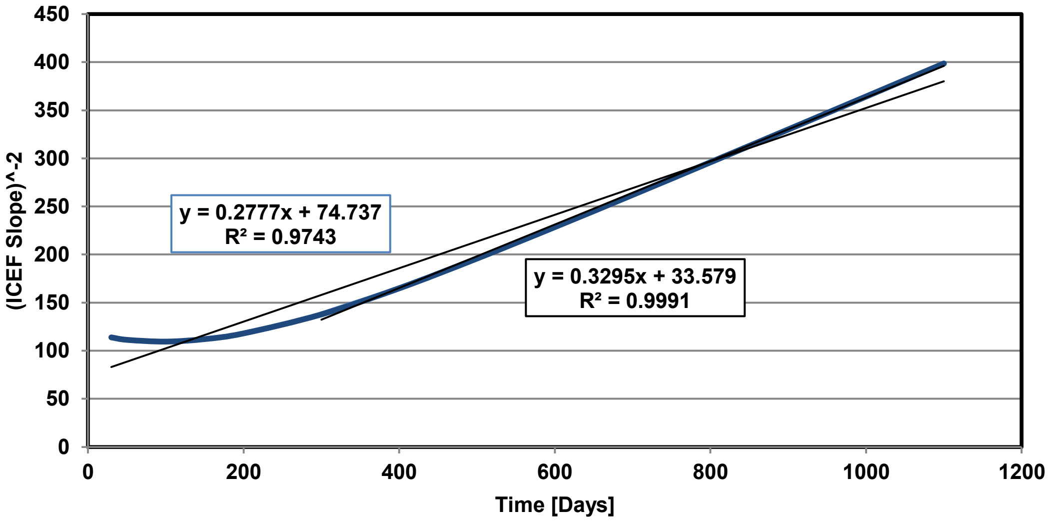

Figure 4.11: Changes in the slope of ICEF plots over time for a hot interface with initial conditions set as steady state solution of a moving front.

The velocity of the moving front by which the steam chamber has advanced before stopping at a barrier impacts the prediction of thermal diffusivity as well. Figure 4.12 shows the dependency of predicted thermal diffusivity from temperature profiles, generated after 300 days of steam chamber arrival, on the velocity of the moving front. A greater amount of heat is transported ahead of the moving front at lower speeds, which will create more diversion from the virgin state of the formation. Therefore, the calculated thermal diffusivity is significantly impacted at lower front velocities.

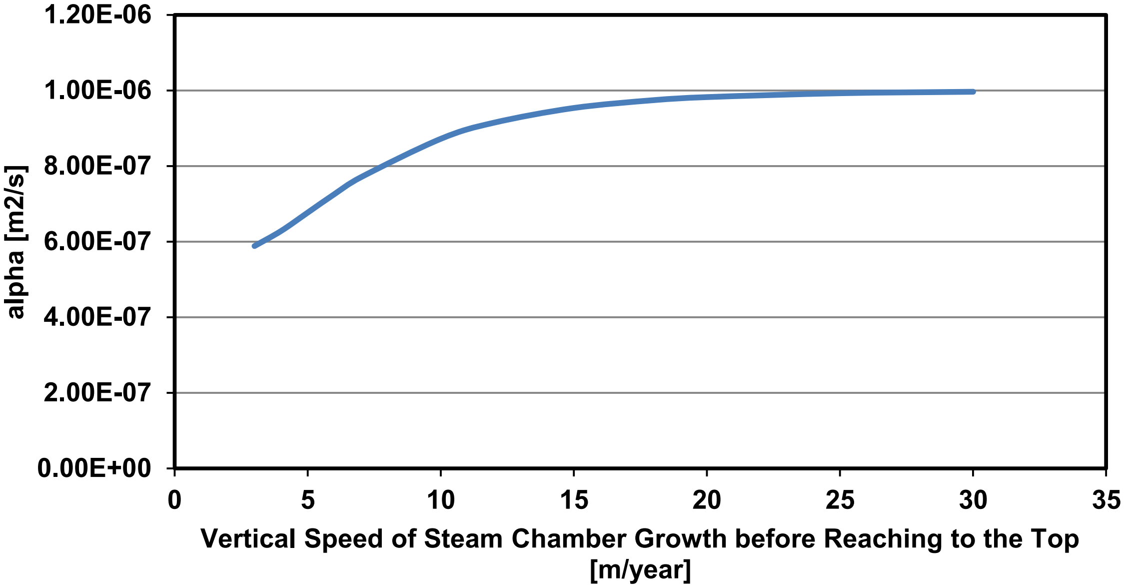

Figure 4.12: Effect of the velocity of the moving front before stopping on back calculated thermal diffusivity.

4.2. Thermal Diffusivity from 2D Conductive Temperature Profiles

The effects of 2D heat conduction and convection on calculation of thermal diffusivity obtained from 1D temperature monitoring are studied in this section. In the case of a fixed hot interface described in Section 3.1.2.1 thermal diffusivity was calculated based on the temperature profiles of monitoring locations at the center, midway between the center and the edge, and the edge. Thermal diffusivity was calculated from temperature profiles of a spreading front at the same locations. Thermal diffusivity was also back calculated from the neighboring steam chambers. The results are summarized in Table 4.1. As mentioned previously, temperatures will not build up in front of the hot interface as fast as the one-dimensional case. Consequently, the back calculation of thermal diffusivity with the prescribed method will be an underestimation of the real value. Deviation from the real value is higher for a spreading front. This is due to the fact that a spreading front is constantly exposed to the cold medium (Butler, 1991). Higher temperature gradients lead to more lateral heat conduction and slower temperature build-up ahead of the front. However, the comparison of the temperature profiles with the one-dimensional case in Figure 3.20 may lead one to expect a higher back calculated value. In response to that, a closer look at the temperature profiles indicates that although temperatures are higher in the far field, they lag behind the one-dimensional case in the near field, i.e. the first 15 to 20m. Higher temperatures are a result of laterally conducted heat and temperatures are in fact higher because of a higher initial value and the rate of temperature build up is not as fast as the one-dimensional case. ICEF plots of the calculations are summarized in Appendix II. It is clear on the IECF plots that the rate of change in temperature profiles are lagging behind the one-dimensional case than being ahead of them. Therefore, the back calculated value is lower than the true value on which the 2D model was based. The calculated thermal diffusivity deviates more from the true value in the case of the spreading interface as the offset of the monitoring location from center increases.

Table 4.1: Back calculated thermal diffusivity based on temperature logs obtained from 2D conductive models.

Location of Temperature Observation	Calculated Thermal Diffusivity $\left[\frac{m^2}{s}\right]$		
	Fixed Hot Interface	Spreading Hot Interface	Neighboring Steam Chambers
Center of Steam Chamber	9.29×10^{-7}	6.81×10^{-7}	7.32×10^{-7}*
Midway between edge and Center	8.20×10^{-7}	6.80×10^{-7}	7.72×10^{-7}**
Edge of Stem chamber	9.28×10^{-7}	6.70×10^{-7}	7.70×10^{-7}***

*Along L_1
**Along L_2
***Along L_3

4.3. Thermal diffusivity from 1D Conductive and Convective Temperature Profiles

The question might arise as to how the conductive and convective temperature fronts manifest themselves on the ICEF plot. In order to study the behavior of conductive and convective temperature fronts, the one-dimensional case with a convective velocity of $v = 2\frac{\mathrm{m}}{\mathrm{year}}$ was generated and then the procedure of back calculation of thermal diffusivity was followed. Temperature profiles are shown on Figure 4.13. ICEF graphs of the profiles are plotted on Figure 4.14. The behavior of ICEF graphs are almost linear similar to the conduction case. In order to increase the accuracy of calculations, the slope of the ICEF graphs were calculated from 10m ahead of the hot interface onward.

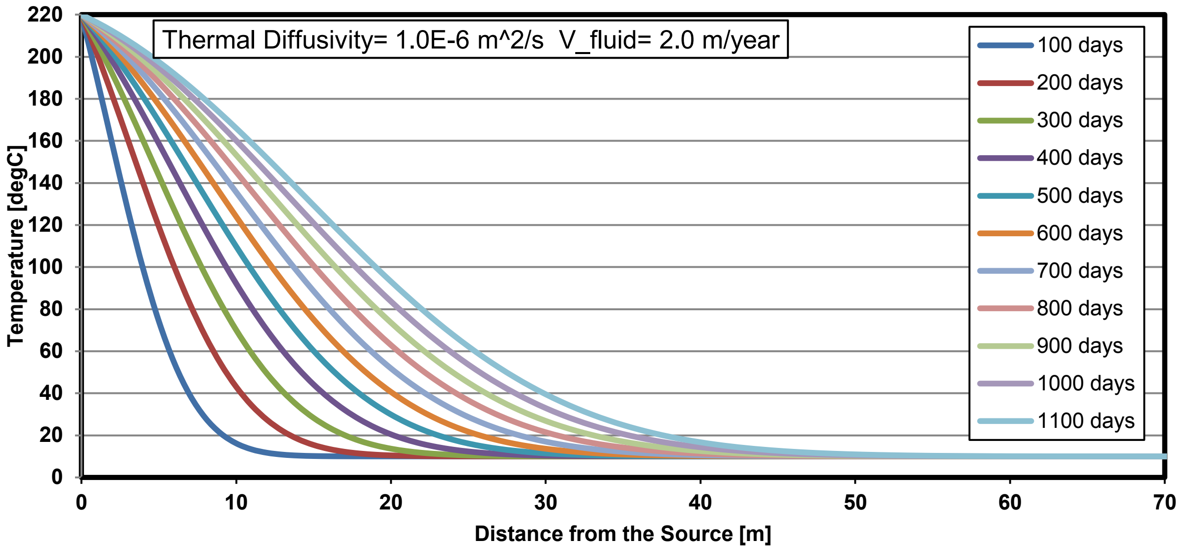

Figure 4.13: One-dimensional conductive and convective temperature profiles generated or calculation of thermal diffusivity.

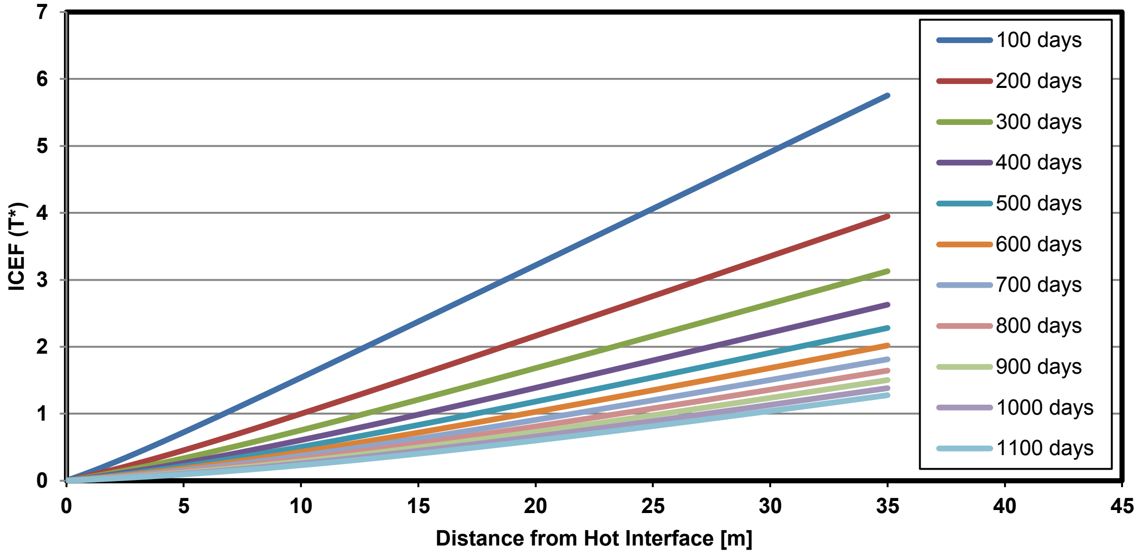

Figure 4.14: ICEF of one-dimensional conductive and convective temperature profiles

However, once the slope of ICEF graphs are calculated and plotted against time, as shown in Figure 4.15, the behavior of temperature profiles over time becomes different from the conduction case. A linear behavior of change over time is not observed anymore. Calculation of thermal diffusivity from the short term response and long term response both yield values that are higher than the value that the model was based on. The calculated value from the long-term behavior is a huge overestimation of thermal diffusivity which cannot be true.

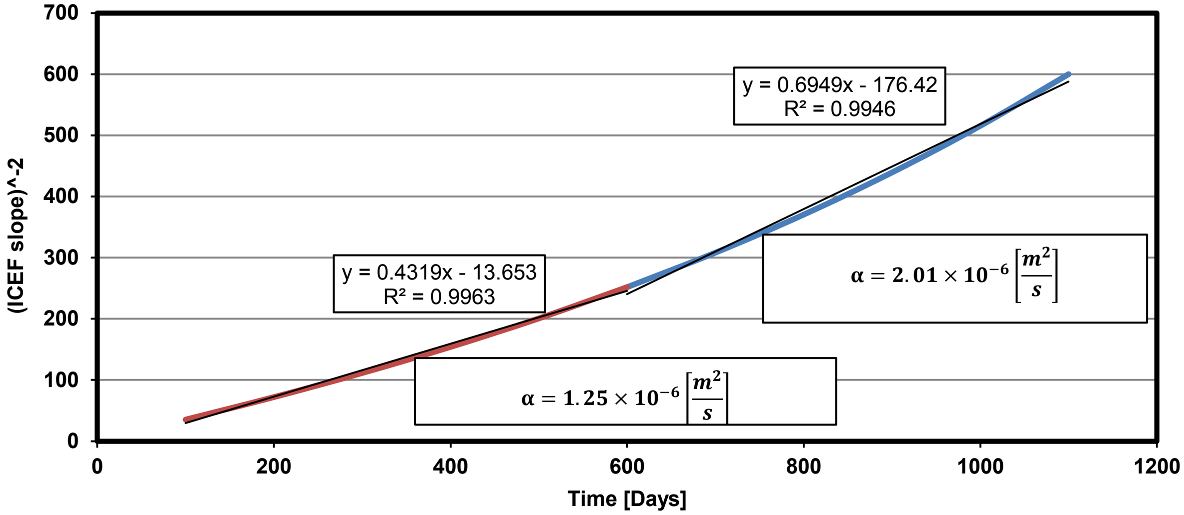

Figure 4.15: Changes in the slope of ICEF over time from convective temperature profiles.

4.4. Thermal Diffusivity from 2D Conduction and Convection Temperature Profiles

Similar to the two dimensional pure conduction case, thermal diffusivity was calculated from the temperature profiles along the monitoring lines of the expanding steam chambers with conduction and convection heat transport. ICEF plots of the calculations are included in Appendix II. The results are summarized in Table 4.2.

Table 4.2: Back calculated thermal diffusivity based on temperature logs obtained from 2D conductive and convective models

Location of Temperature Observation	Calculated Thermal Diffusivity $\left[\frac{m^2}{s}\right]$
Along L_1	8.40×10^{-7}
Along L_2	8.37×10^{-7}
Along L_3	1.25×10^{-6}

The effect of convection heat transport can be seen on the back-calculated thermal diffusivity. The back calculated thermal diffusivity from the model with conduction and convection is higher than the pure conduction model. As mentioned previously, the convective effects are stronger close to the edge of the pad. Thermal diffusivity is also higher close to the edges of the pad. Similar to the 1D conductive and convective case, the back calculated thermal diffusivity is even higher than the value on which the case was based.

4.5. History Matching Temperature Profiles

The comparison between the observed profiles and the predicted profiles from back calculation can help understand the differences in thermal diffusivity values. In this section, temperature profiles of the models are compared with the one-dimensional synthetic models based on the back-calculated thermal diffusivity.

4.5.1. History Matching of 2D Conductive Temperature Profiles

The expanding steam chambers model is the closest modeling scenario to the reality of the SAGD process. Temperature profiles of the two dimensional model of the expanding steam chambers model above the steam chambers were compared to the temperature prediction based on the back-calculated thermal diffusivity. These comparisons are illustrated in Figure 4.16. The difference between the observed and predicted behavior is shown in Figure 4.17. It can be seen that the difference between the observed and predicted temperature profiles is decreasing over time for the first 20m ahead of the hot interface but there is a slight increase after that. The deviation also increases as the offset from the center increases.

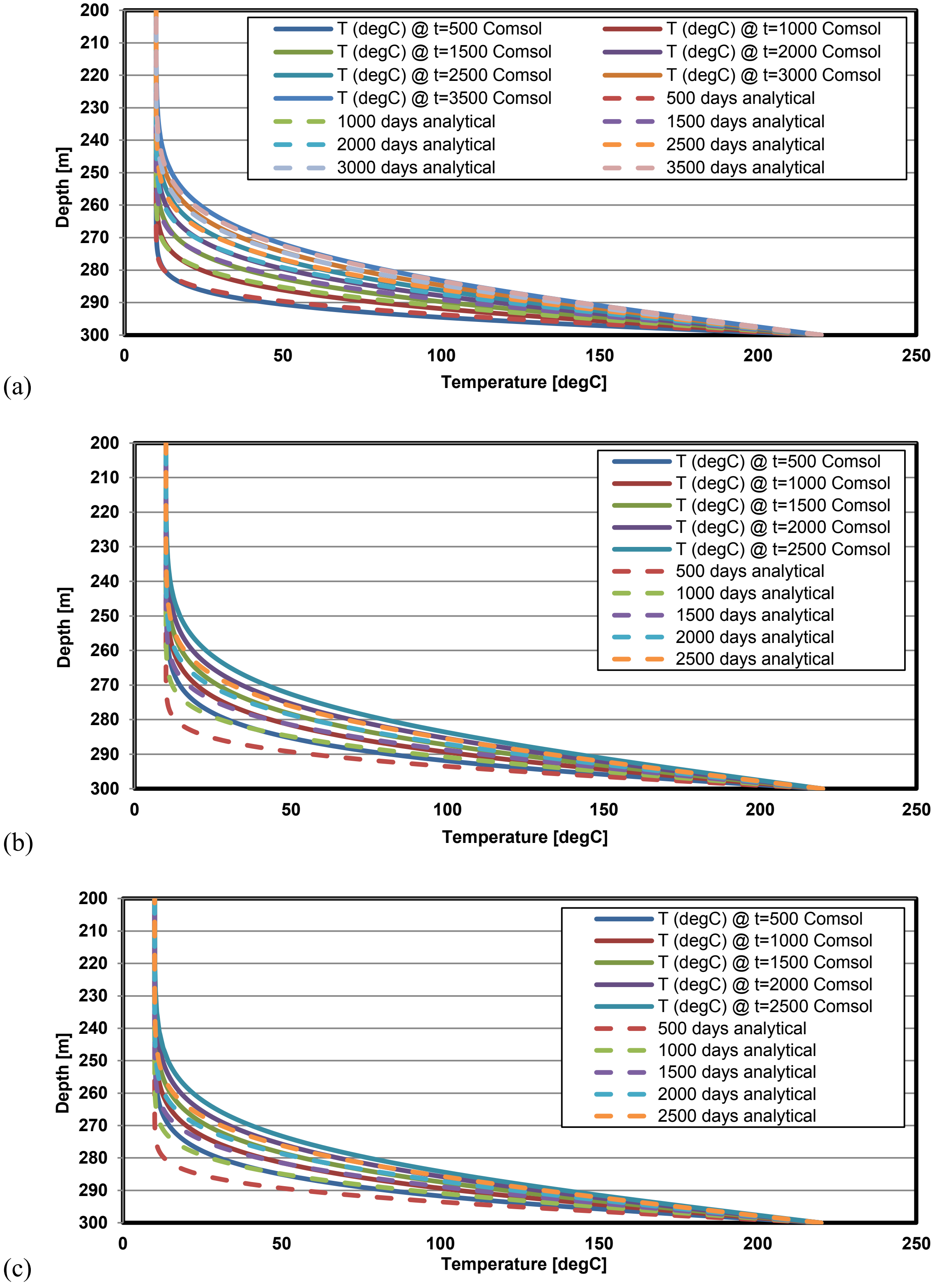

Figure 4.16: History matching of the observed behavior of 2D conductive spreading steam chambers with the back-calculated thermal diffusivity. (a) $\mathbf{L_1}$. (b) $\mathbf{L_2}$. (c) $\mathbf{L_3}$.

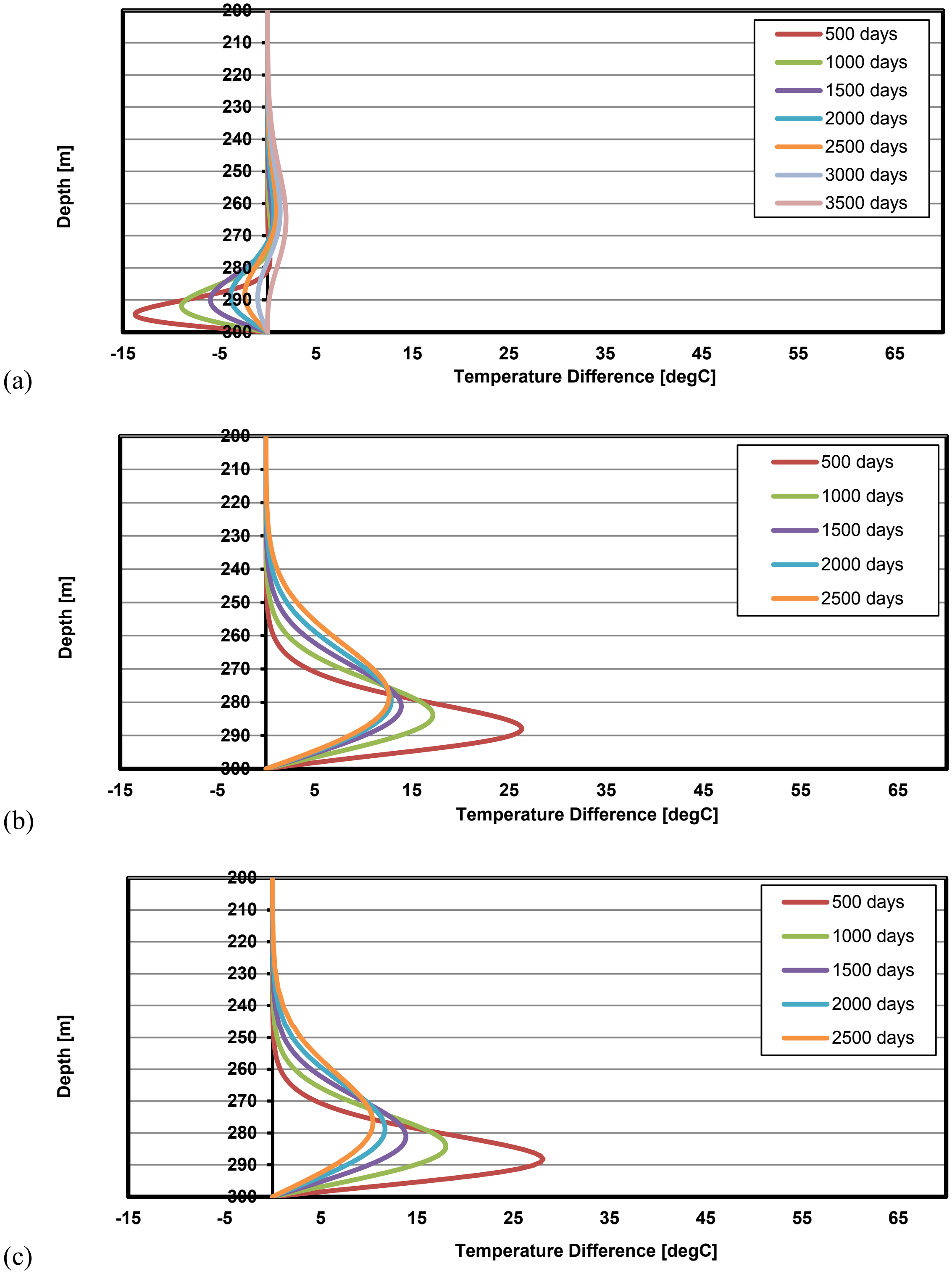

Figure 4.17: Difference between the observed behavior from the 2D conductive spreading steam chambers with the predicted values based on back calculation of thermal diffusivity. (a) $\mathbf{L_1}$. (b) $\mathbf{L_2}$. (c) $\mathbf{L_3}$.

4.5.2. History Matching 1D Conductive and Convective Temperature Profiles

Thermal diffusivity of the 1D conduction and convection model was calculated in the previous section. If a conduction model with the thermal diffusivity of $\alpha = 1.25 \times 10^{-6} \left[\frac{m^2}{s}\right]$ is generated and compared with the original model, as shown in Figure 4.18, upon which the back calculation of thermal conductivity was based, significant differences are observed in temperature response. Figure 4.19 illustrates the magnitude of difference between the original model with conduction and convection heat transport and the predicted response based on back calculation of thermal diffusivity. The temperature difference grows over time and reaches a maximum of 50℃ at 15m ahead of the steam chamber after 1100 days which is easily above the error of detection in the observation wells.

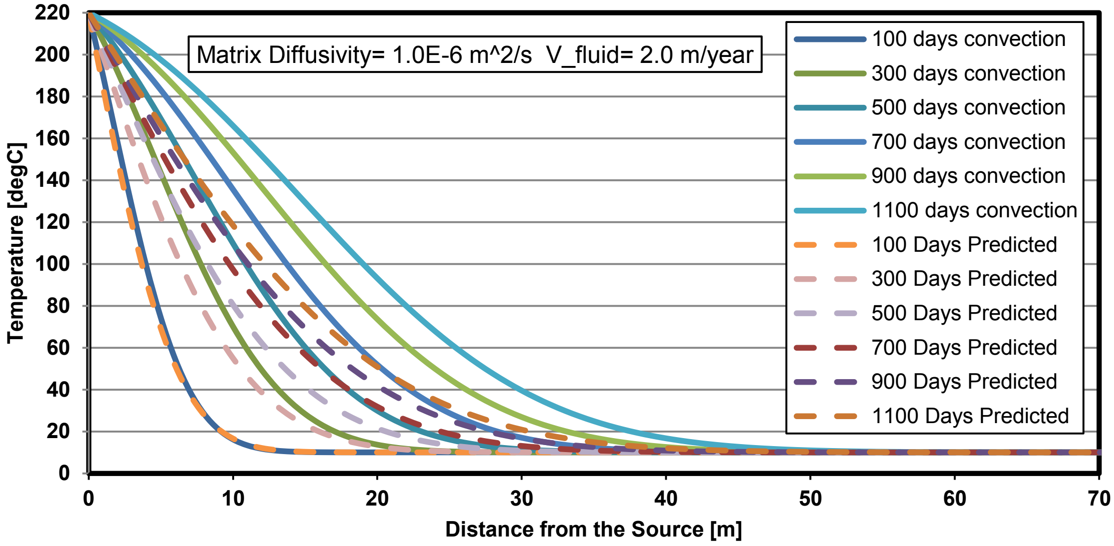

Figure 4.18: Temperature profiles of conductive and convective fronts and pure conductive fronts based on the lower predicted value of thermal diffusivity.

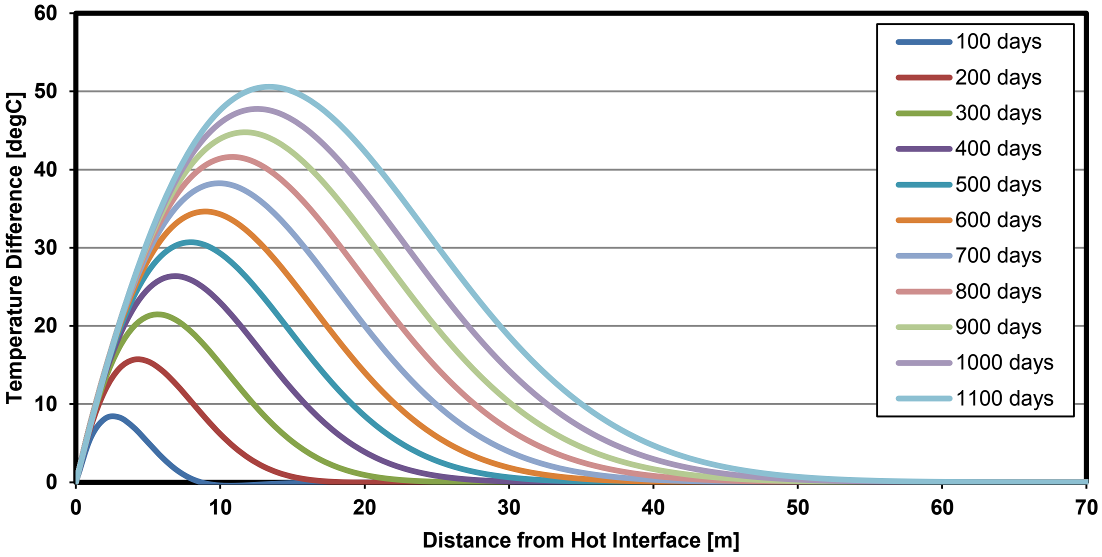

Figure 4.19: Difference between temperature profiles of conductive and convective fronts and pure conductive fronts based on the lower predicted value of thermal diffusivity.

The comparison of temperature profiles generated with the higher thermal diffusivity, $\alpha = 2.01 \times 10^{-6} \left[\frac{m^2}{s}\right]$ (Figure 4.20) also shows a detectable difference between the observed and predicted profiles. Temperatures are overestimated in the near field and underestimated in the far field. Similar to the previous case, Figure 4.21 shows that the difference between the conductive and convective and pure conductive cases grows over time and reaches a maximum of almost 30°C about 15m ahead of the hot interface after 1100 days. This difference can also be detected by the observation wells during the thermal operation. The high value of thermal diffusivity is by itself indicative of abnormal conductive behavior as well.

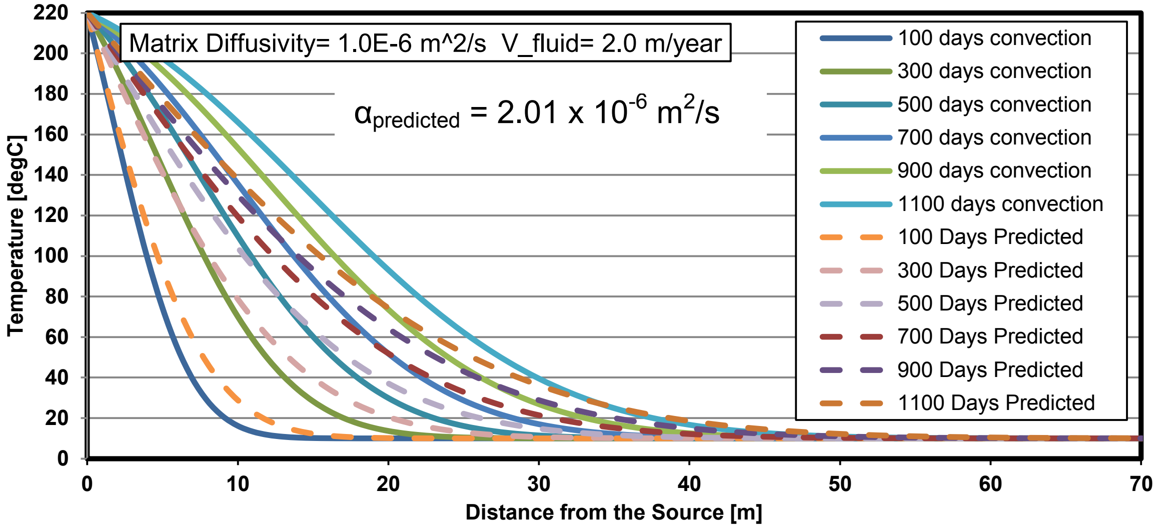

Figure 4.20: Temperature profiles of conductive and convective fronts and pure conductive fronts based on the higher predicted value of thermal diffusivity.

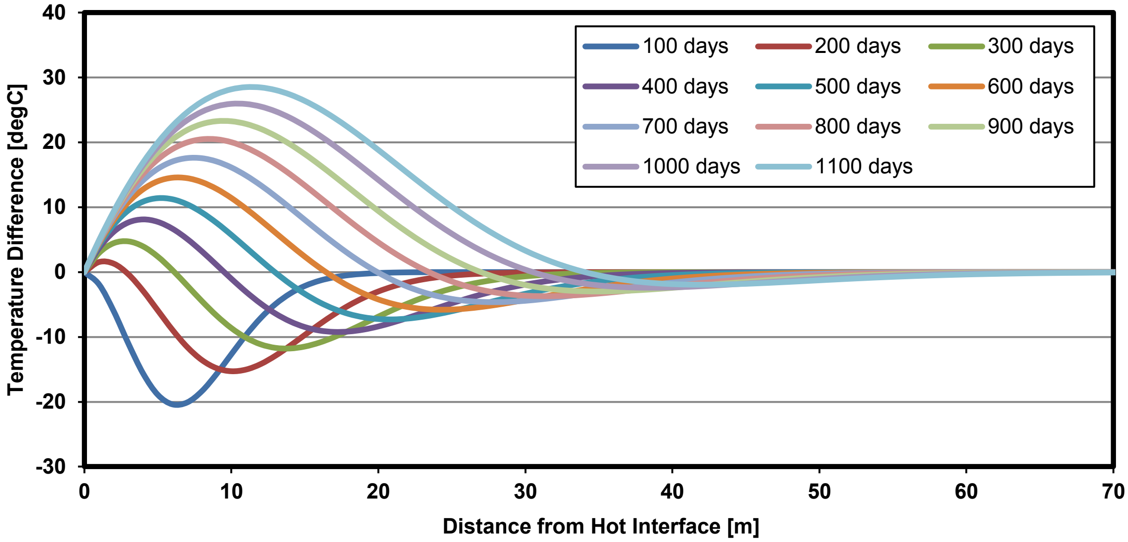

Figure 4.21: Difference between temperature profiles of conductive and convective fronts and pure conductive fronts based on the higher predicted value of thermal diffusivity.

4.5.3. History Matching 2D Conductive and Convective Temperature Profiles

Similar to the conductive case, temperature profiles of the expanding steam chambers model were compared to a 1D conductive model based on the back-calculated thermal diffusivity. The results are shown in Figure 4.22. The difference between the observed and predicted temperatures above the steam chambers is shown in Figure 4.23.

It can be seen that the difference between the observed and predicted temperature profiles is more in the conduction and convection model compared to the pure conduction model. Convective flows are stronger close to the edge of the pad. It can be seen that the deviation from the 1D analytical solution has also increased as the monitoring line is moved closer to the edge of the pad.

The difference between the observed and predicted temperatures 20m above the steam chambers is close to 15℃ after 1000 days in the pure conductive model. In the conduction and convection model, however, the difference between the observed and predicted temperatures at the same location is close to 35℃.

Higher back calculated thermal diffusivities in the conduction and convection model, especially at the edge of the pad, are also indicative of the contribution of convection in upward heat transport.

Detection of convective flows is dependent on both the back-calculated thermal diffusivity and temperature difference in history matching. By comparing the graphs of Figure 4.17 to Figure 3.23 one can see that the detection of convective flows cannot be concluded solely from the magnitude of difference in history matching the thermal response. Higher temperature differences and higher back calculated thermal diffusivities are observed when the contribution of convective heat flow is substantial enough. This criterion will be used in the analysis of the real observation well data in Chapter 6.

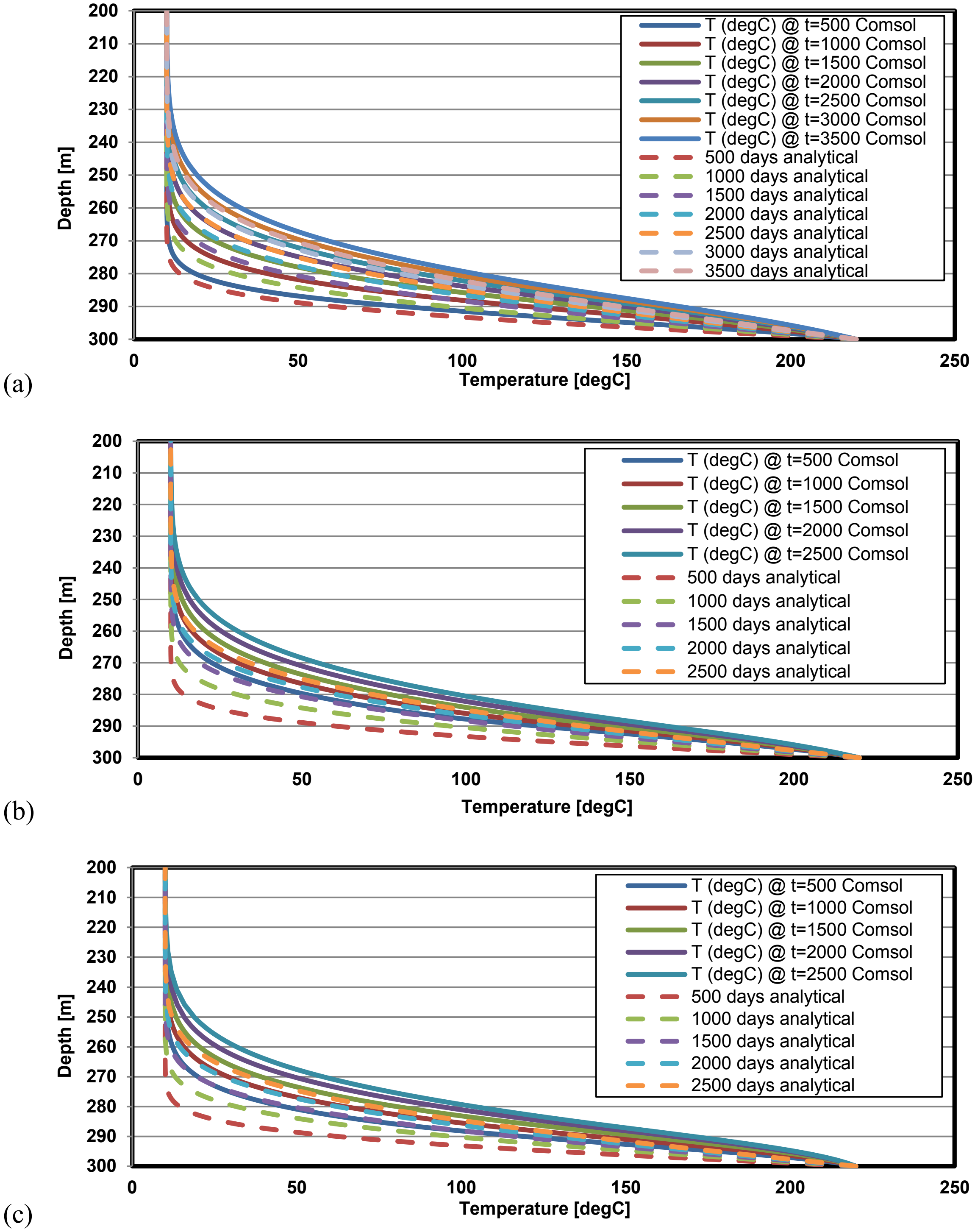

Figure 4.22: History matching of the observed behavior of 2D conductive and convective spreading steam chambers with the back-calculated thermal diffusivity. (a) $\mathbf{L_1}$. (b) $\mathbf{L_2}$. (c) $\mathbf{L_3}$.

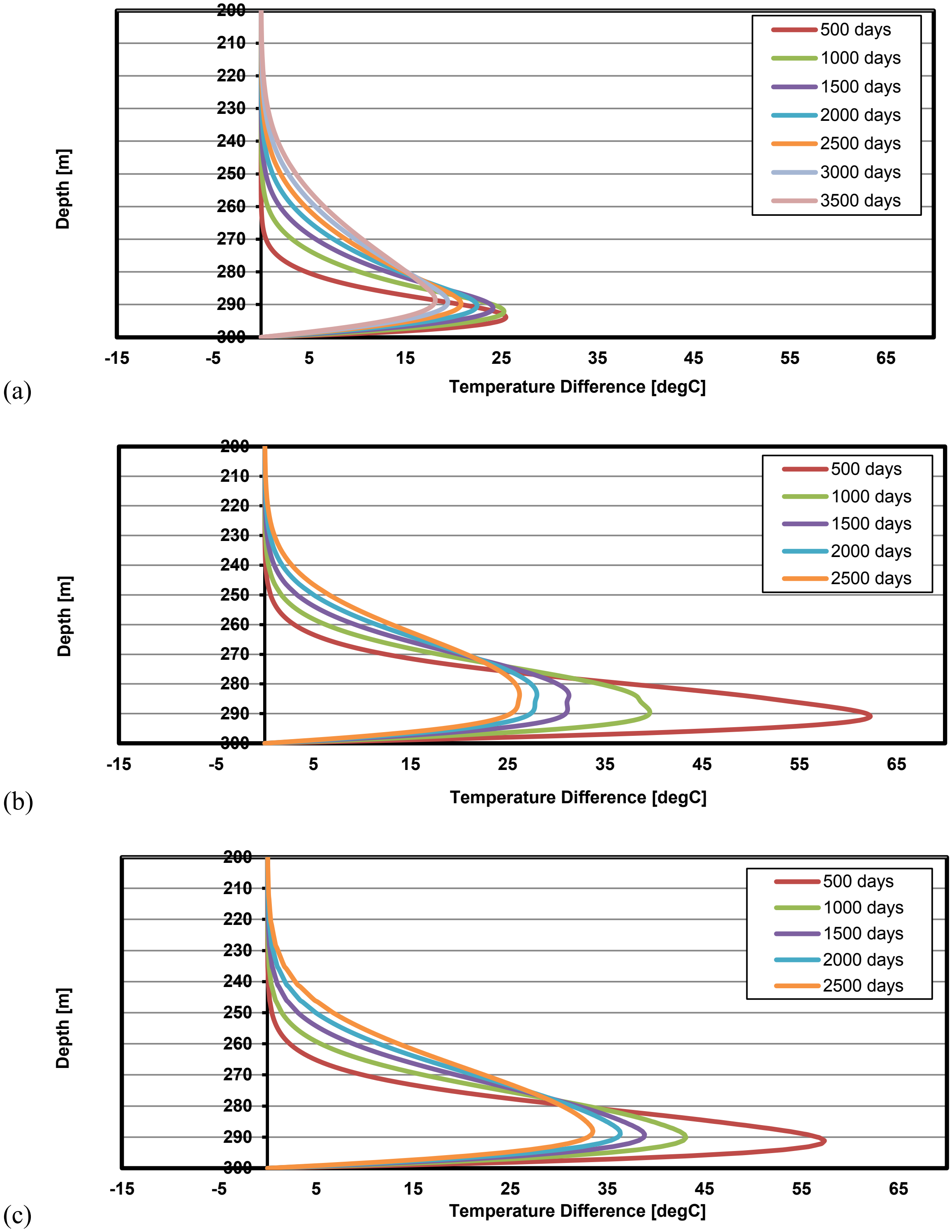

Figure 4.23: Difference between the observed behavior from the 2D conductive and convective spreading steam chambers with the predicted values based on back calculation of thermal diffusivity. (a) $\mathbf{L_1}$. (b) $\mathbf{L_2}$. (c) $\mathbf{L_3}$.

4.6. Summary

Thermal diffusivity was calculated from temperature profiles generated by synthetic models. The parameters by which the calculated thermal diffusivity could be influenced were investigated. The influence of initial temperature state ahead of a moving front should not be neglected. Calculated thermal diffusivities can be lower than the true value if the vertical speed of steam chamber is low before it stops at an impermeable layer. Associated errors with missing the true formation cold temperature were small. The behavior of a one-dimensional conductive and convective synthetic model was also investigated. It was observed that the shape of graphs was not similar to conductive case and the back-calculated thermal diffusivity couldn’t match the temperature profiles.

Two-dimensional effects also lead to a lower back-calculated thermal diffusivity. The deviation is higher in the case of a spreading hot interface compared to a fixed one. The back-calculated thermal diffusivity from temperature profiles of a two-dimensional conduction and convection model are heavily dependent on the location of monitoring line. Higher values of thermal diffusivity, especially close to the edge of the pad where the convective flows are stronger, were calculated.

History matching of the observed and predicted temperatures of the two dimensional conductive and convective model showed that the mismatch is larger and over a wider range above the steam chambers compared to the pure conduction case.

Higher thermal diffusivities associated with higher mismatch in history matching can be used as a criterion for the detection of convective flows.

Chapter 5: Selection of Observation Wells

Monitoring programs are conducted in order to understand the performance of an oil recovery process, mitigate the risks, and increase oil recovery from the reservoir. There are four major ways of monitoring chamber development during the SAGD operation (Cenovus 2010): seismic, observation wells, volumetrics, and specialized logging and coring. In this research, data from observation wells are used for the investigation of heat transfer mechanisms ahead of steam chambers.

5.1. Temperature Monitoring During SAGD

Observation wells provide real time and direct measurement of temperature and pressure during the operation. Temperature sensors and piezometers are installed in observation wells to monitor the state of steam chambers. The monitored zone can include the underburden, pay zone, and overburden. Currently, there are two methods used for temperature measurement: thermocouples and fiber optics sensors. In this study temperature surveys conducted by thermocouples are used for the investigation of heat transfer mechanisms.

Thermocouples are spaced evenly from each other and measure the temperatures along the well. The configuration of a typical observation well with thermocouples is shown in Figure 5.1. Thermocouples can be hung inside the observation well or strapped to the outside of the casing and cemented to the formation as shown in Figure 5.2.

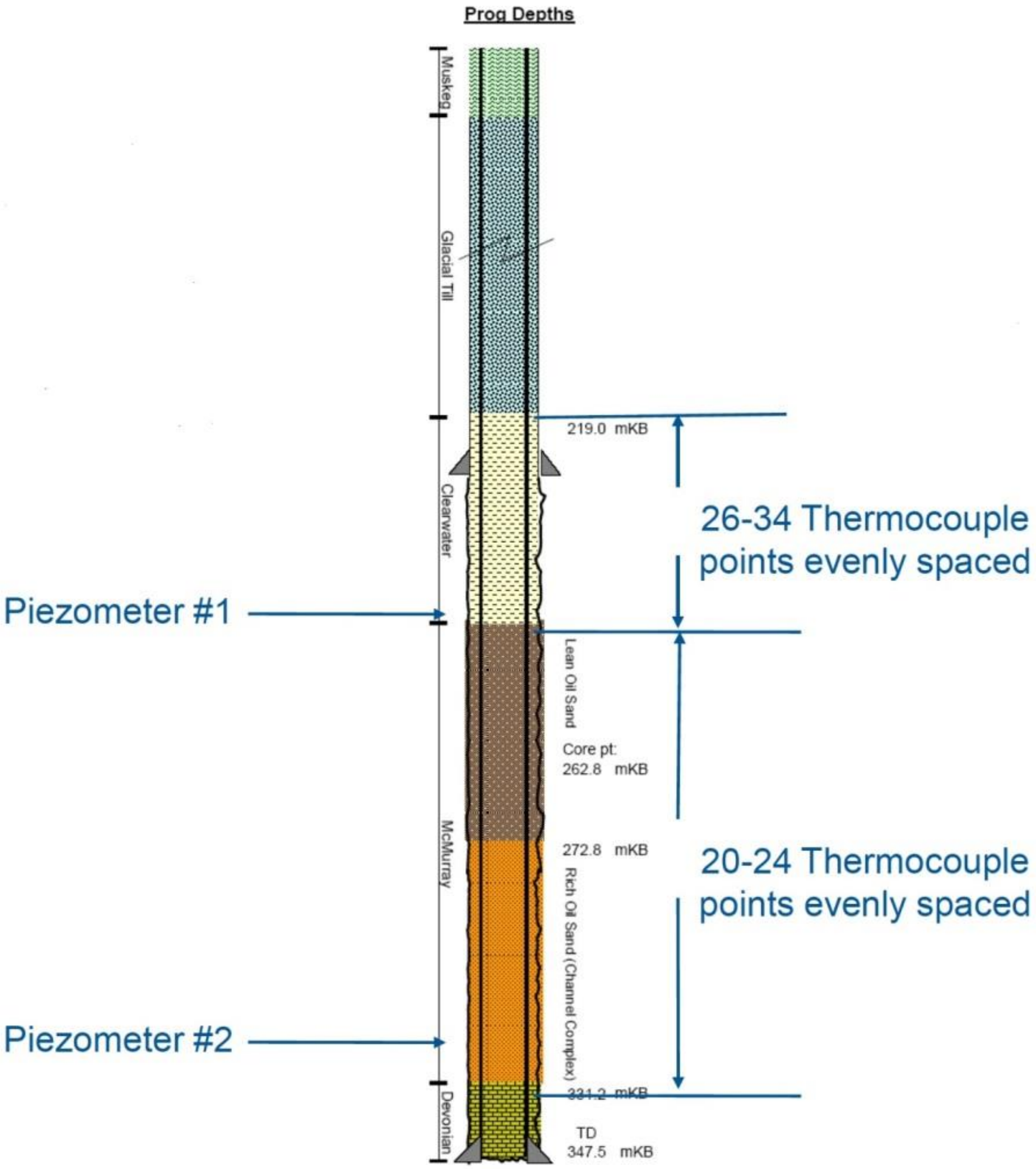

Figure 5.1: Monitoring temperature with observation wells. Figure adapted from Suncor (2015).

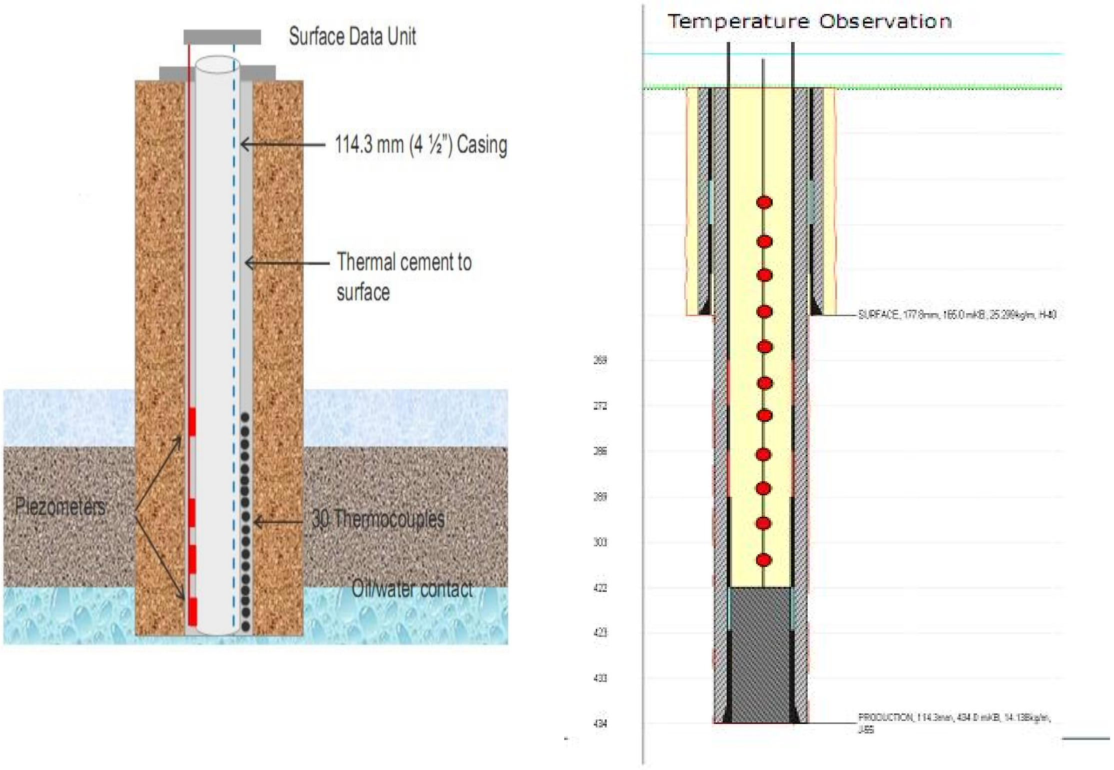

(a) (b)

Figure 5.2: Installation of thermocouples in an observation well. (a) Thermocouples strapped outside the casing and cemented to the formation. Photo adapted from Statoil (2014). (b) Thermocouples hanging inside the observation well. Photo adapted from Cenovus (2014).

5.1.1. Wellbore Fluid Effects on Temperature Measurements

Water can be present in the observation well during temperature surveys. As the water in the well is heated, buoyancy flows can develop inside the well and transfer heat from the deeper zones with higher temperatures upwards to the zones with lower temperatures (Griston, 1989). This phenomenon can lead to smearing in measured values (Griston, 1989). Temperature profiles of two surveys with water and air in the observation well are shown in Figure 5.3 (Griston, 1989). Temperature survey from the dried up wellbore is a closer representative of true temperature profile inside the formation (Griston, 1989). Measured temperatures in the water filled wellbore are below the true value above the heated zone and higher than the true value ahead of that. The peak temperature is also lower for the water filled observation well compared to the dried wellbore (Griston, 1989). It can be seen that the accurate depth of the top of the heated zone is also missed in the water-filled wellbore.

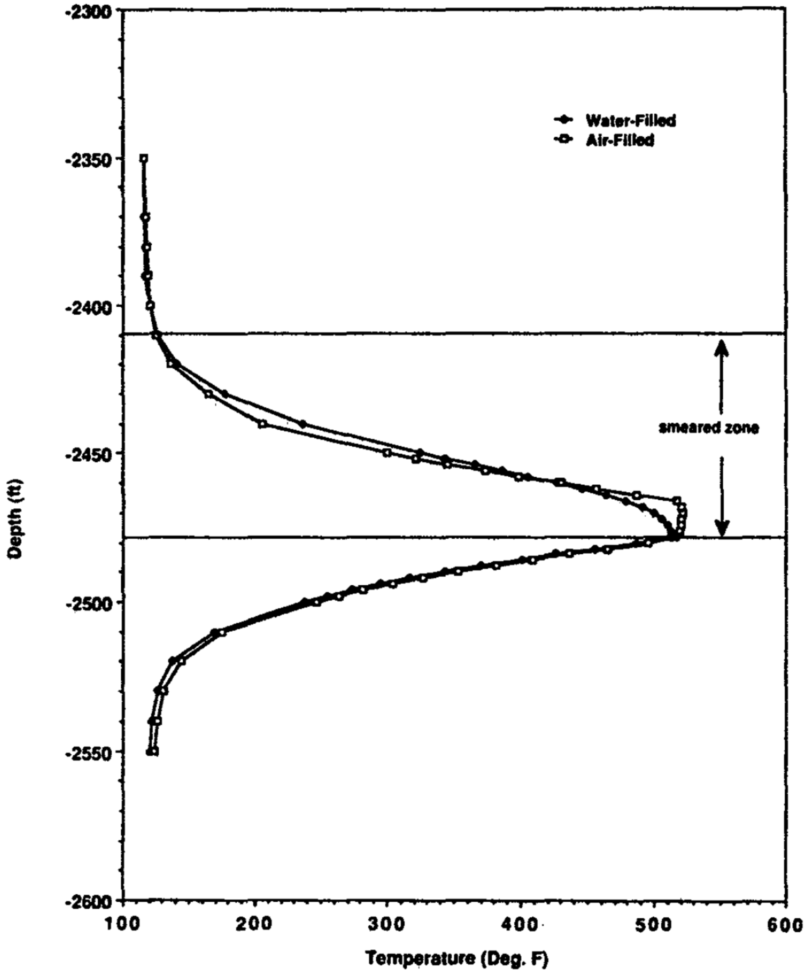

Figure 5.3: Smearing effect of wellbore fluid in an observation well. Figure adapted from Griston (1989).

Kagawa et al. (1992) also studied the effect of wellbore fluid convection on temperature profiles. Maximum temperature of the heated zone was reported below 100°C in their experiments. They observed a turbulent mixing zone above the heated zone, as shown in Figure 5.4. They also calculated the top of the heated zone by a graphical method.

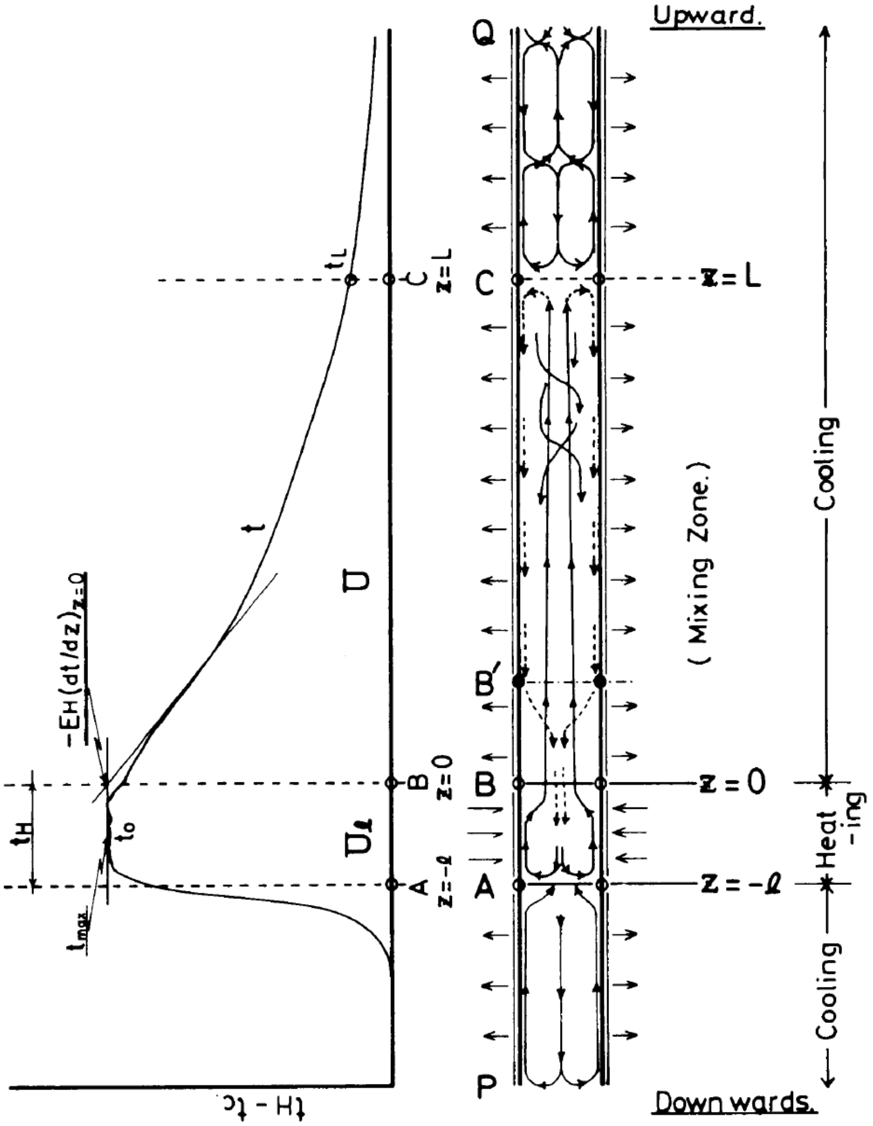

Figure 5.4: Experimental study of wellbore fluid on temperature profiles. Photo adapted from Kagawa et al. (1992).

This phenomenon was observed during the study of temperature observation wells in SAGD as well. Figure 5.5 shows the temperature response of an observation well with possible smearing in the recorded temperatures.

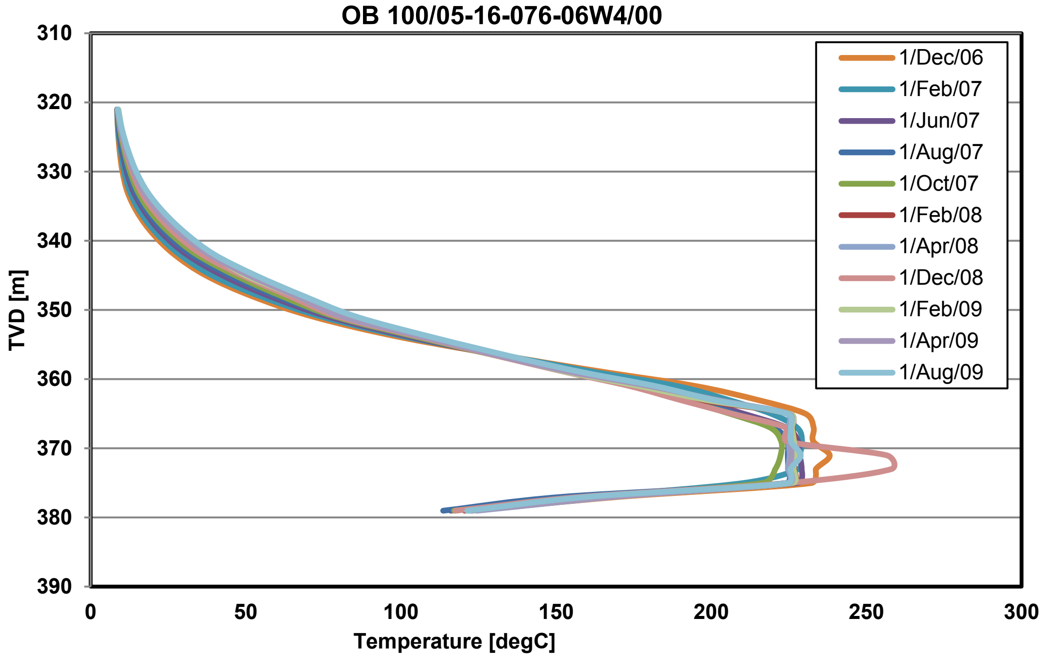

Figure 5.5: Temperature response of an observation well under possible fluid wellbore effects. Data obtained from AER In-situ performance presentation submitted by Cenovus (2011). (https://www.aer.ca/documents/oilsands/insitupresentations/2011AthabascaCenovusFosterCreekSAGD8623.pdf)

The completion records of this observation well were not available at the time of writing the thesis. A solid conclusion cannot be drawn on whether or not the temperature profiles were under the influence of natural convection of wellbore fluid at the time the survey was done. However, the same observation well is showing boiling at later times, which strongly suggests that temperature profiles were affected by wellbore fluid during the previous surveys. Figure 5.6 shows the temperature profiles of the same observation well when the water was boiling inside the wellbore. The column of boiling water is about 20m high. Temperatures are highly smeared from the true values below and above the refluxing interval.

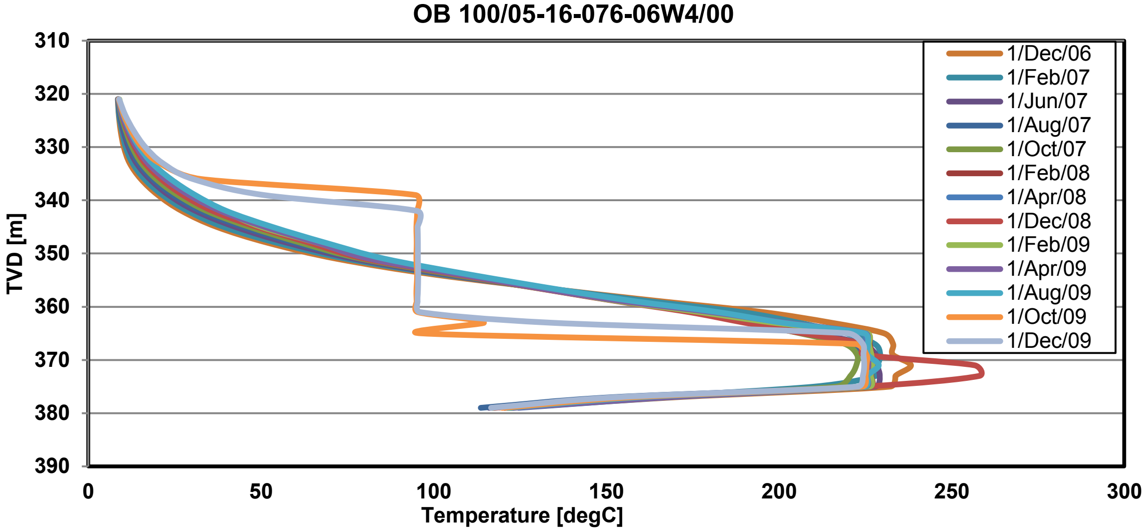

Figure 5.6: Refluxing in the observation well. Data obtained from AER In-situ performance presentation submitted by Cenovus (2011) (https://www.aer.ca/documents/oilsands/insitupresentations/2011AthabascaCenovusFosterCreekSAGD8623.pdf)

Boiling can also happen multiple times inside the wellbore. Figure 5.7 shows the temperature history of an observation well during 5 years of monitoring. Figure 5.8 shows the recorded response at each depth over time. It can be seen on the plot that the observation well has gone through 3 instances of boiling.

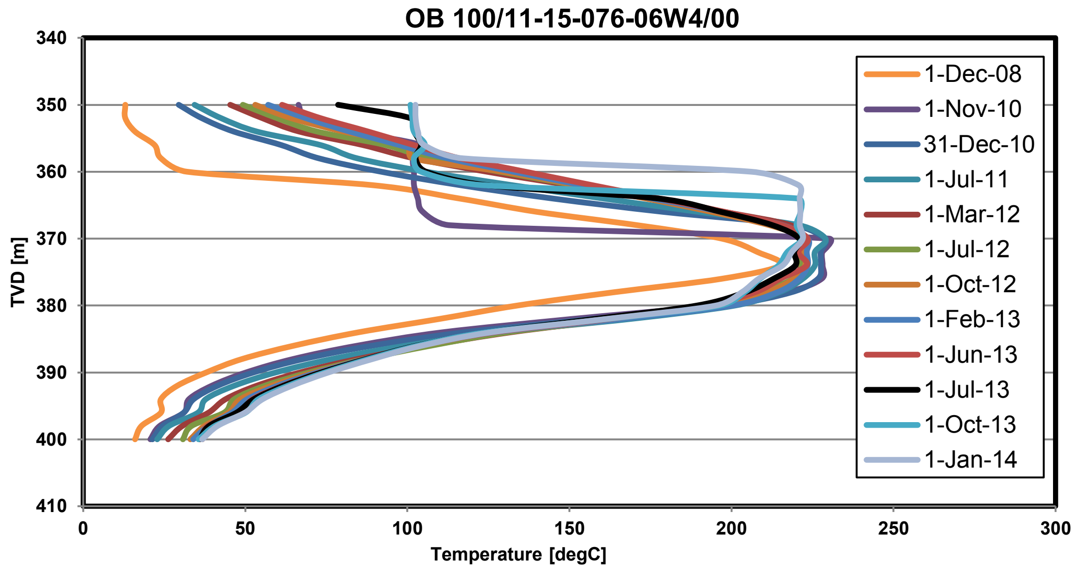

Figure 5.7: Temperature history of an observation well during 5 years of monitoring. Data obtained from AER in-situ performance reports submitted by Cenovus (2015). https://www.aer.ca/documents/oilsands/insitupresentations/2015AthabascaCenovusFosterCreekSAGD8623.pdf

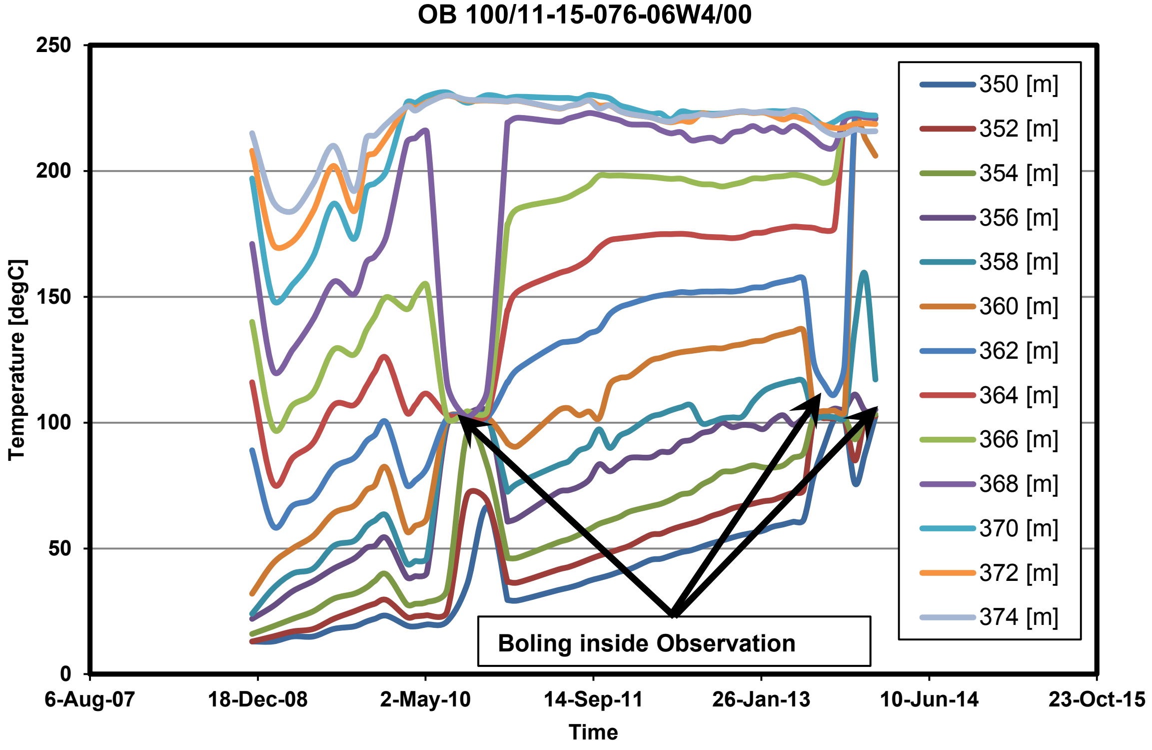

Figure 5.8: Three instances of refluxing inside OB 100/11-15-076-06W4/00.

5.1.2. Vertical Growth of Steam Chamber

The growth of steam chamber can continue until it finally reaches the top of the pay zone or its growth can be arrested when it hits a very thick impermeable layer. Figure 5.9 shows the temperature history of a steam chamber that has initially stopped at around 320m TVD. Interbeds of low permeability can be seen on the gamma log where the steam chamber has initially stopped. Steam chamber has started growing vertically again until it has reached to the bottom of another low permeability zone at 300m TVD.

5.1.3. Steam Detouring Around Impermeable Layers

The presence of a sufficiently thick impermeable layer can stop the vertical growth of the steam chamber. However, steam can detour around the impermeable layer and rise to the upper parts through more permeable layers (Ito and Ipek, 2005).

Figure 5.10 shows an example of a steam chamber that stopped at a relatively impermeable layer. It can be seen on the gamma and resistivity log that thick enough interbeds with low bitumen concentration and high fines content exist between 363m to 352m TVD.

The muddy interbeds have acted as a baffle in front of the steam chamber. The steam chamber has initially stopped at 363m TVD. Over time, steam has detoured the low permeability zone and reached to the upper parts of the pay zone. Heat is being transported from steam to the impermeable zone both at top and bottom. The temperature of the baffle has eventually reached to the steam chamber temperature.

Estimation of the top of the steam chamber from observation well temperature recordings of a steam chamber that is migrating around low permeability intervals, a “detouring” steam chamber, is difficult and associated with very high uncertainties. Temperature recordings of such cases are heavily influenced by lateral heating from the irregular steam chamber as well. Steam has reached to the other parts of the formation beyond the monitoring zone. It is also possible that steam chamber has grown vertically in other parts of the formation without being detected by the observation well.

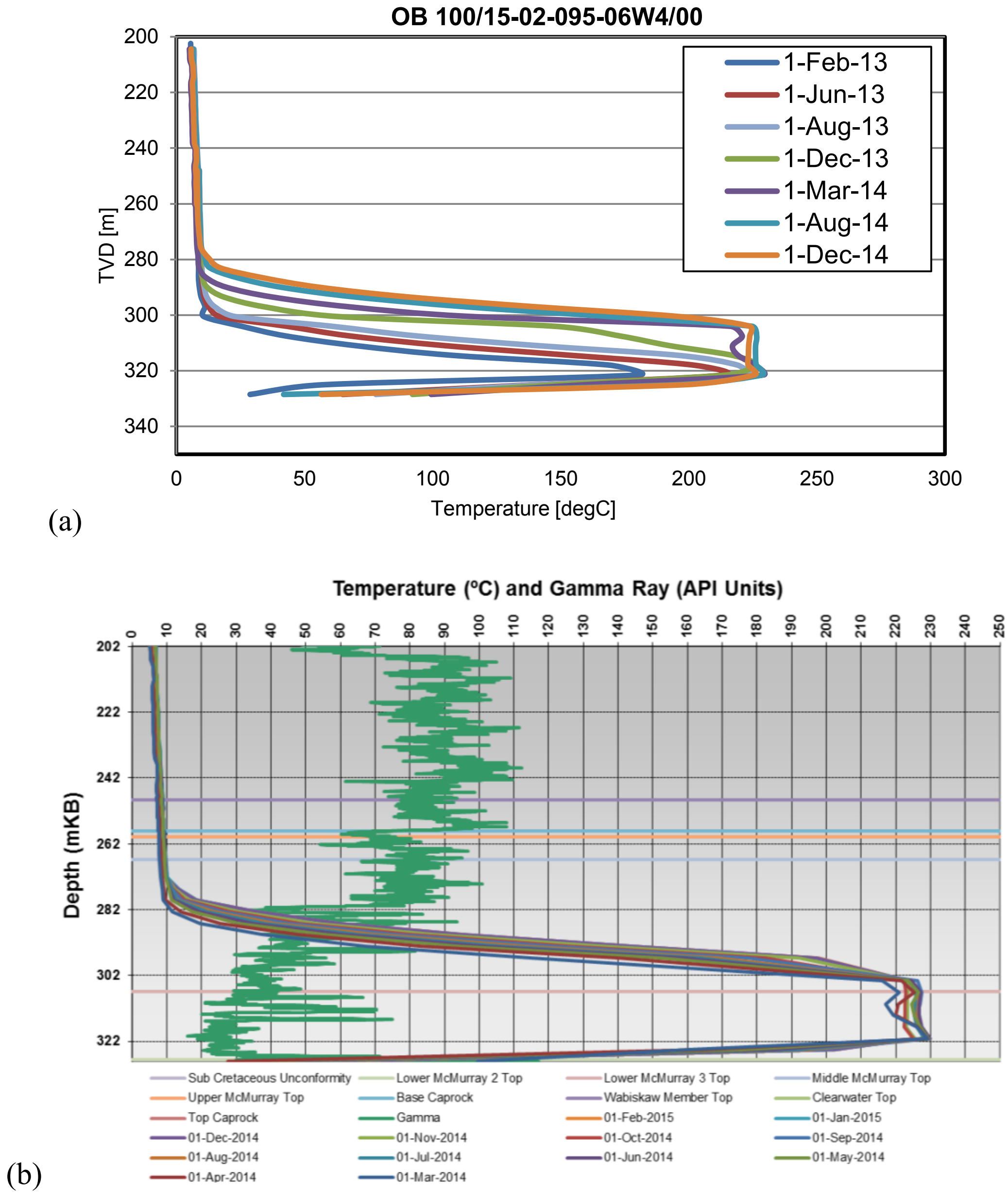

Figure 5.9: Steam chamber growth through low permeability interbeds. (a) Temperature history of steam chamber growth. (b) Gamma log of OB 100/15-02-095-06W4/00. Data extracted from Suncor (2015).https://www.aer.ca/documents/oilsands/insitupresentations/2015AthabascaSuncorFirebagSAGD8870.pdf

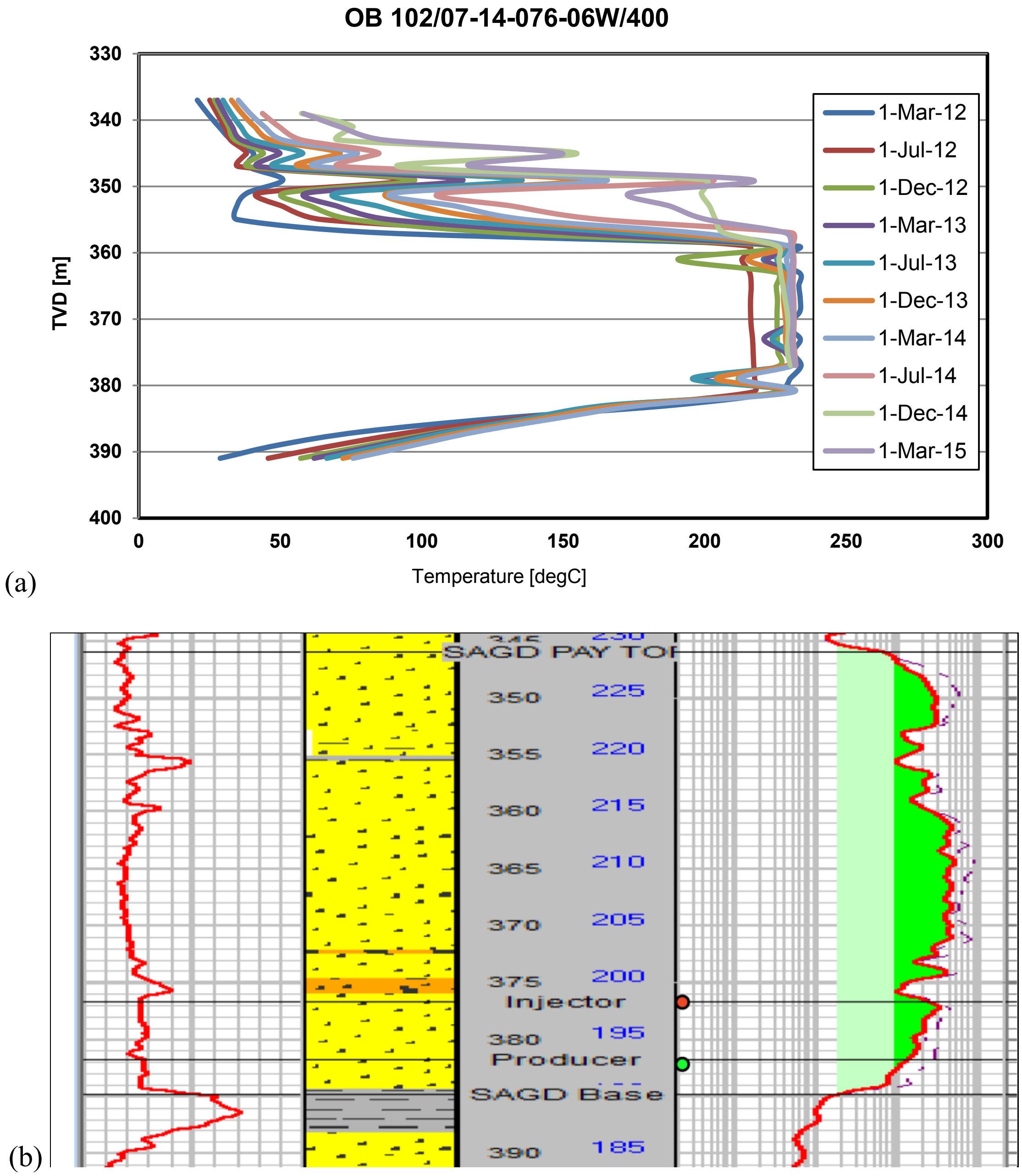

Figure 5.10: Detouring of steam around an impermeable layer. (a) Temperature history recorded with observation well. (b) Petrophysical logs: Resistivity on the far left and Gamma log on the far right. Data extracted from Cenovus (2015). (https://www.aer.ca/documents/oilsands/insitu-presentations/2015AthabascaCenovusChristinaSAGD8591.pdf)

* Depth correction was applied to data from Cenovus (2015) AER in-situ performance presentation.

5.1.4. Wellbore Casing Conduction

Thermal conductivity of casing is higher than the geomaterials. Therefore, heat can be conducted upwards by the casing faster compared to the formation. However, heat is lost sideways from the casing if the temperature of the casing goes above the formation temperature (Closmann et al., 1979). Closmann et al. (1979) studied the effect of a heat conducting well casing. The difference between dimensionless temperature distribution of the casing and formation is plotted on Figure 5.11. Thermal properties of the formation and casing material are summarized in Table 5.1. It was assumed that the observation well casing is made of iron with $4\frac{1}{2}$ in diameter.

Table 5.1: Material properties of formation and casing used in modeling by Closmann et al. (1979)

Material	Thermal Conductivity $\left[\frac{\mathrm{W}}{\mathrm{m°C}}\right]$	Thermal diffusivity $\left[\frac{\mathrm{m}^2}{\mathrm{day}}\right]$
Formation	2.200	0.0905
Casing	45.0	1.018

The difference between formation temperature and casing temperature is small. As shown in Figure 5.11 the difference decreases rapidly over time and there is negligible difference after 3 months (Closmann et al., 1979).

Therefore, it appears that temperature measurements are not influenced by conduction along the observation well casing and thermocouples are measuring the true value of the formation temperature provided the observation well is dry and not influenced by wellbore fluid.

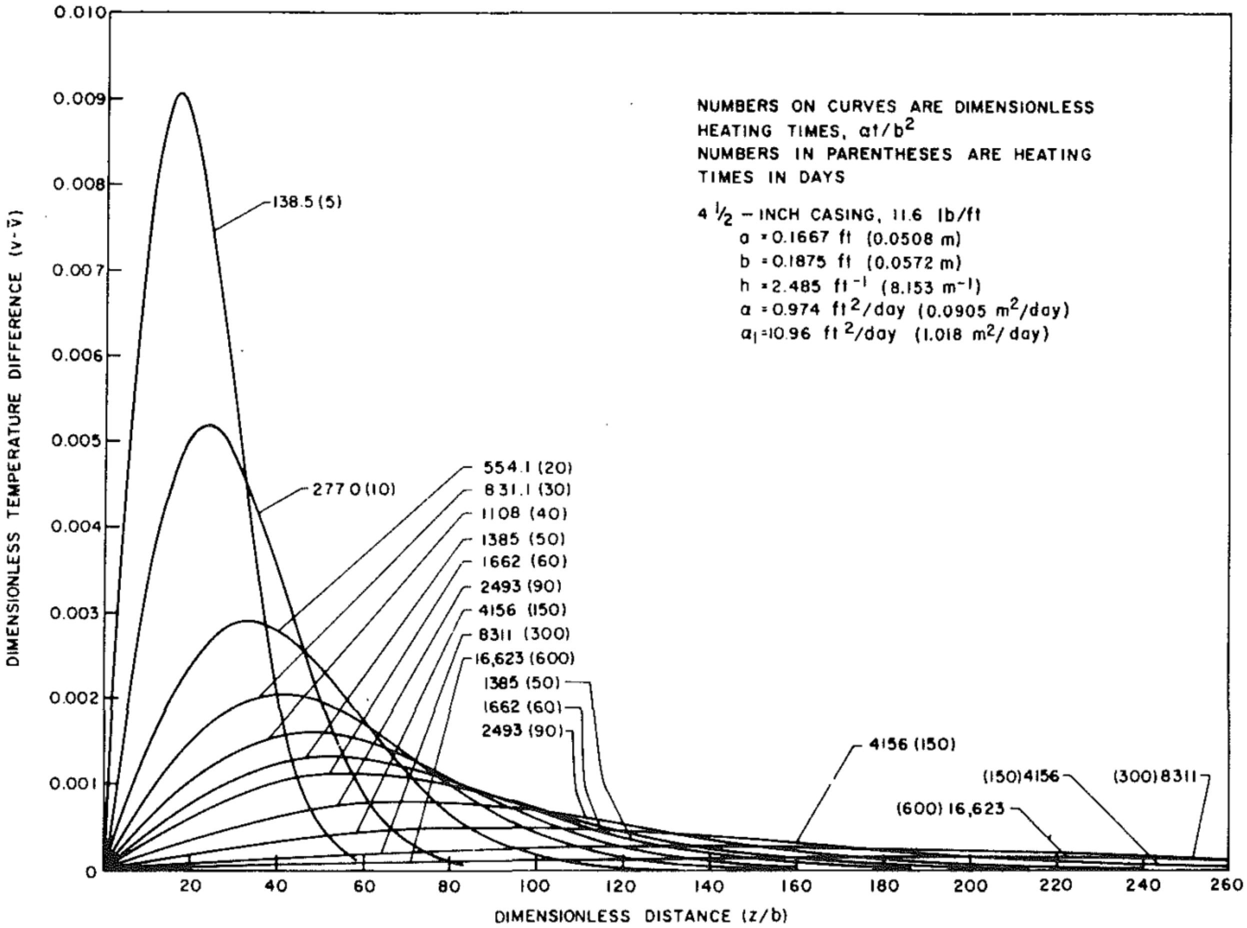

Figure 5.11: Difference between dimensionless temperature profiles along the wellbore casing and formation for an iron casing with **$4\frac{1}{2}$ in** diameter. Figure adapted from Closmann et al. (1979).

5.2. Selection of Data for Thermal Diffusivity Calculation

Major factors affecting the quality of data collection from observation wells were discussed in the previous section. They included the effects of temperature smearing inside the wellbore, refluxing, baffles, and barriers. Data from observation wells with no boiling incidents was analyzed in order to reduce the uncertainties in measured values. Completion records of observation wells were not available from public domain and determination of this issue that temperatures were the true values inside the formation or smeared was not possible. This issue was resolved by excluding temperature values of the first 10m above the maximum recorded temperature from the calculations. This assumption appears to be reasonable by looking at the graphs on Figure 5.3. It can be seen that the difference between temperature surveys of water filled and dried wellbore is not significant at distances greater than 10m above the heated zone.

And as shown in Figure 5.10, data collected from steam chambers similar to the “detouring” case lack the quality of representing one-dimensional heat loss to the caprock. Heat is being transported from the sides to the vicinity of the observation well. Determination of the true location of the top of steam chamber also becomes a challenge that requires more data from the geology of the area. It is hard to justify the use of data from these cases for one-dimensional models. Therefore, they have not been included in the investigation of heat transfer mechanisms ahead of the steam chamber.

As discussed in Chapter 4, the initial conditions ahead of the moving front have a considerable impact on the back-calculated thermal diffusivity. This factor was not overlooked in the selection of observation wells and every attempt was made to choose observation wells that showed a rapid rise of the steam chamber to the top of the reservoir.

The procedure of selecting real observation well temperature data which best represent one-dimensional heat transfer, involved several steps. Initially, data was extracted from the Appendices of in-situ performance presentations/reports submitted to AER by SAGD operators (https://www.aer.ca/data-and-publications/activity-and-data/in-situ-performance-presentations).

Temperature profiles of a selected observation well are plotted, as shown in Figure 5.12. This example shows rapid vertical growth of the steam chamber and it has reached the top of the reservoir over a relatively short period of time. Therefore, it was assumed the effects of temperature initial conditions would be small for this dataset.

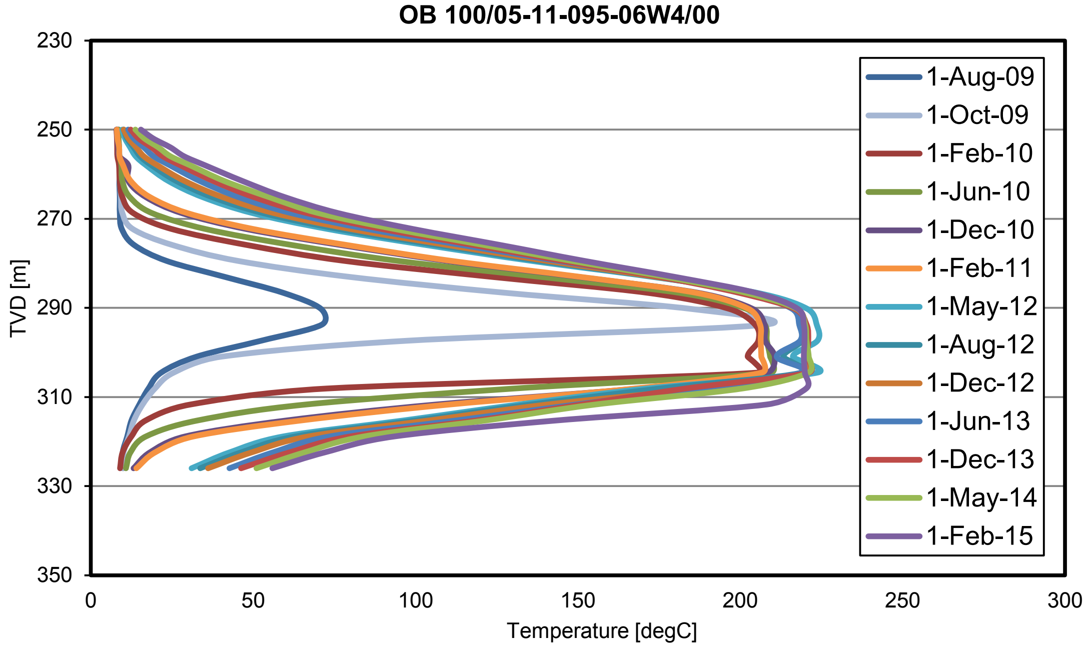

Figure 5.12: Temperature profiles of OB 100/05-11-095-06W4/00 obtained from Suncor (2015) AER in-situ performance presentation.

The maximum-recorded temperature in an observation well is selected from a plot of maximum temperature versus time, as shown in Figure 5.13. For this example, the temperature of steam chamber is almost constant at 220℃ after May 2012. Fluctuations in the maximum temperature are not drastic. As discussed in Chapter 4, back calculation of thermal diffusivity is not significantly impacted if the change in maximum interface temperature is not substantial.

In the next step, the ICEF plots of the temperature profiles were calculated. It was assumed that the maximum temperature in the formation was the measured peak value in the observation well. Formation cold temperature was also assumed to be equal to the coldest temperature that was measured over an interval. It was estimated that the initial cold temperature was at 7.8℃.

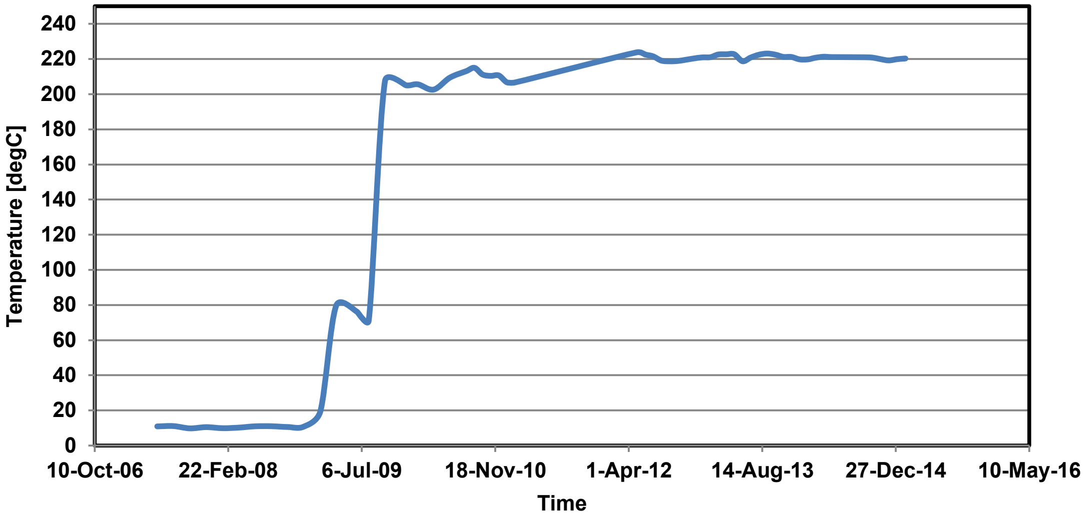

Figure 5.13: Maximum recorded temperature in OB 100/05-11-095-06W4/00.

ICEF plots of temperature profiles above the steam chamber are shown in Figure 5.14. In order to avoid possible temperature smearing from wellbore fluid the slope of ICEF plots were calculated from 280m to 270m for the short-term response and from 280m to 260m for the long-term response.

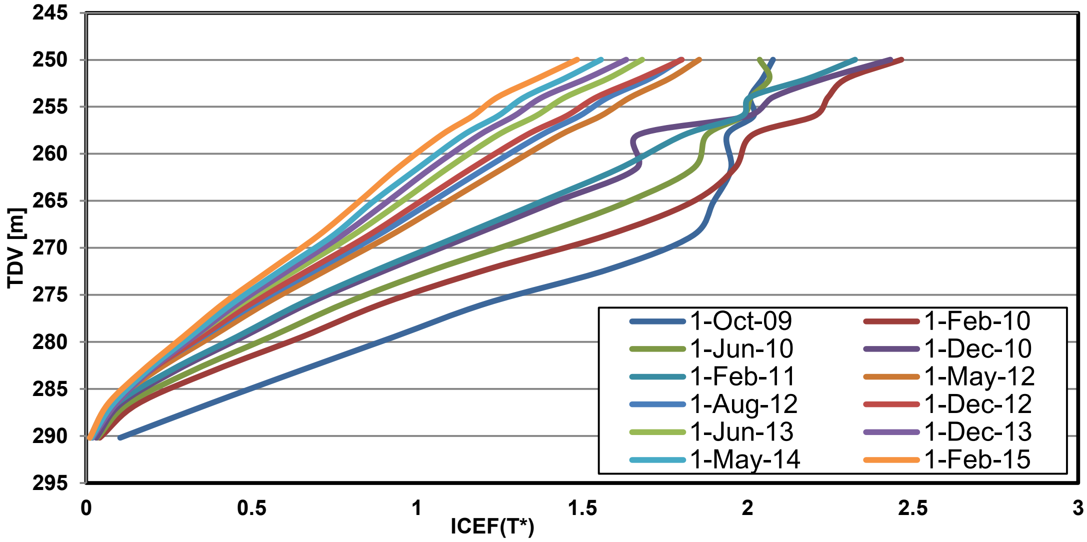

Figure 5.14: ICEF slope of temperature profiles from OB 100/05-11-095-06W4/00.

The change of the slope of ICEF plots over time is shown in Figure 5.15. Thermal diffusivity is then calculated from the linear part of the graph. In this case thermal diffusivity is equal to $\alpha = 9.41 \times 10^{-7} \left[\frac{m^2}{s}\right]$.

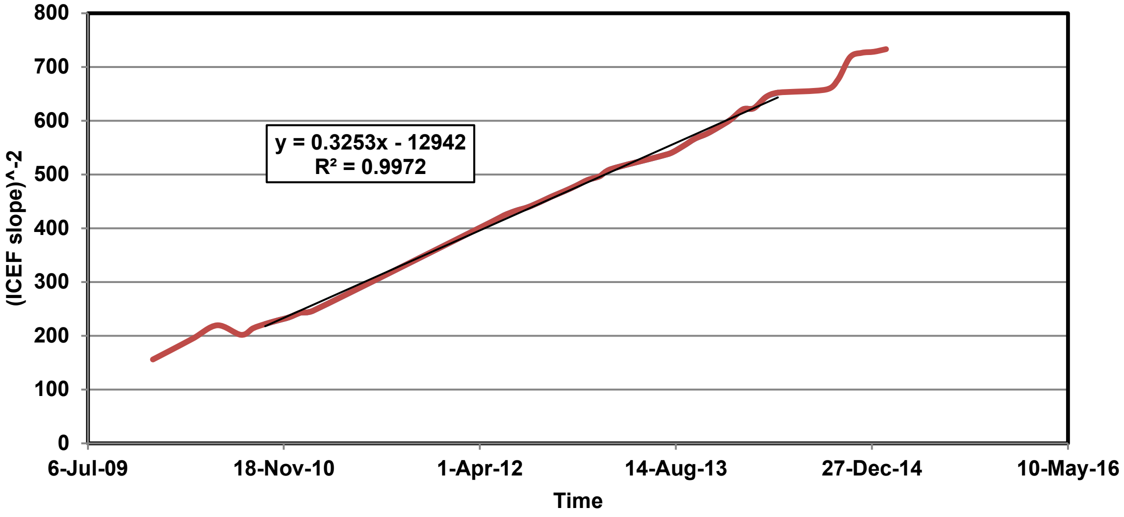

Figure 5.15: Changes in the slope of ICEF plot over time for temperature profiles of OB 100/05-11-095-06W4/00.

Birrell (2003) provides an explanation of the estimation of the angle between temperature isotherms and observation well. In this study, it is considered that the assumptions made during selection of observation well makes the direction of heat flow almost parallel to the observation well and the difference between the calculated thermal diffusivity and the true value is negligible.

Moreover, the post processing of the calculated thermal diffusivity includes history matching with a one-dimensional model. Thermal diffusivity should again be multiplied by the same correction factor in order to compare the prediction of the 1D model with the measurements. Therefore, the inclusion of calculating the angle between the observation well and heat flow is not necessary as long as the history match is done in one dimension and along the observation well.

5.3. Summary

In this chapter the major factors that affect the measurement of true temperature distributions in the formation were studied. The effect of wellbore fluid should not be ignored. Smearing of temperature profiles can lead to misinterpretation of the top of the heated zone. Water can also boil inside the observation well. Boiling can totally smear the temperatures below and above the refluxing column of water. The effect of casing conduction on temperature profiles was concluded to be negligible.

Temperature recordings of real observation wells also illustrated vertical growth of steam chamber and steam “detouring” around an impermeable zone. Slow vertical growth of the steam chamber will change the temperature ahead of the steam chamber and negatively impact the calculation of thermal diffusivity. Lateral heating is associated with steam detouring and deviates the temperature response more from one-dimensional upward heat transfer.

The procedure of selecting an observation well and analysis of data was provided. In the next chapter the implications of the calculated thermal diffusivity and determination of dominant mechanisms of heat transport are discussed.

Chapter 6: Observation Well Data Analysis

In this chapter, temperature profiles of observations wells are investigated to understand the contributing heat transport mechanisms ahead of the steam chambers. Temperature surveys are extracted from Appendices of AER in-situ performance presentations of commercial SAGD operations. Temperature recordings of more than 25 wells were collected over the monitoring period of commercial SAGD operations. The procedure outlined in the Chapter 5 was followed in the selection of the observation wells. Based on the proposed criteria, 10 observation wells were selected for the analysis of upward heat transport mechanisms ahead of the steam chamber. The graphs of the temperature recordings are provided in Appendix III.

6.1. Post-analysis of Observation Well Temperature Profiles

6.1.1. Conductive Case

The procedure of calculating thermal diffusivity was explained in Chapter 4. In this section, the results of back calculation of thermal diffusivity from temperature profiles are used for the determination of contributing heat transport mechanisms.

6.1.1.1. Verification with Experimental results

Calculated thermal diffusivity from temperature profiles is compared to the published experimental results of tests run on McMurray samples. The back calculated thermal diffusivity is close to the values that were obtained from lab measurements. Laboratory measurements of thermal diffusivity of oil sands are shown in Figure 6.1. The upper parts of McMurray Formation are not fully water saturated and bitumen exists, with lower percentage, in the pore space of IHS. It can be seen on the graphs that thermal diffusivity calculated from temperature profiles is very close to the values of lab results.

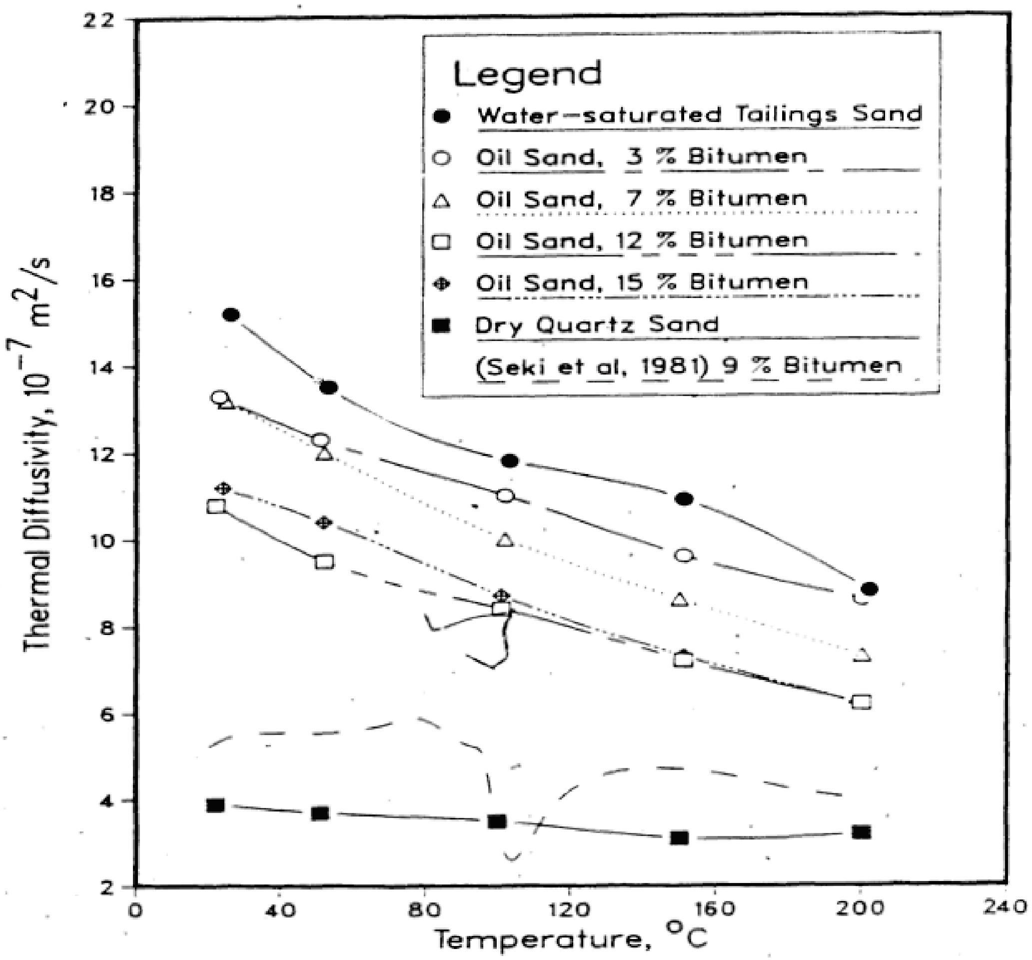

Figure 6.1: Thermal diffusivity of oil sands measured in lab (Seto, 1985).

6.1.1.2. History Matching with Synthetic Model

It was shown in Chapter 4 that two-dimensional effects would result in lower thermal conductivity values. The history matching of the conductive cases with the back calculated thermal diffusivity showed a decreasing trend up to 20m ahead of the steam chamber and a slight increase ahead of that.

A synthetic conductive model was generated assuming $\alpha = 9.41 \times 10^{-7} \left[\frac{m^2}{s}\right]$. The top of the steam chamber was calculated from ICEF plots and estimated to be at 286m TVD. It was also assumed that steam chamber has reached to the top around 1-Oct-2009 (Figure 5.12) and has established a hot interface after that. Temperature profiles of the synthetic model are compared to the real values in Figure 6.2.

In this case, the difference between real observation well data and the synthetic model is decreasing for the first 20m and a slight increase is observed ahead of that. The synthetic model is in fact predicting the real behavior within an acceptable margin. Therefore, it can be concluded that for this observation well the dominating scenario by which heat is transported to the overburden is conduction and the contribution of a convective flow is negligible.

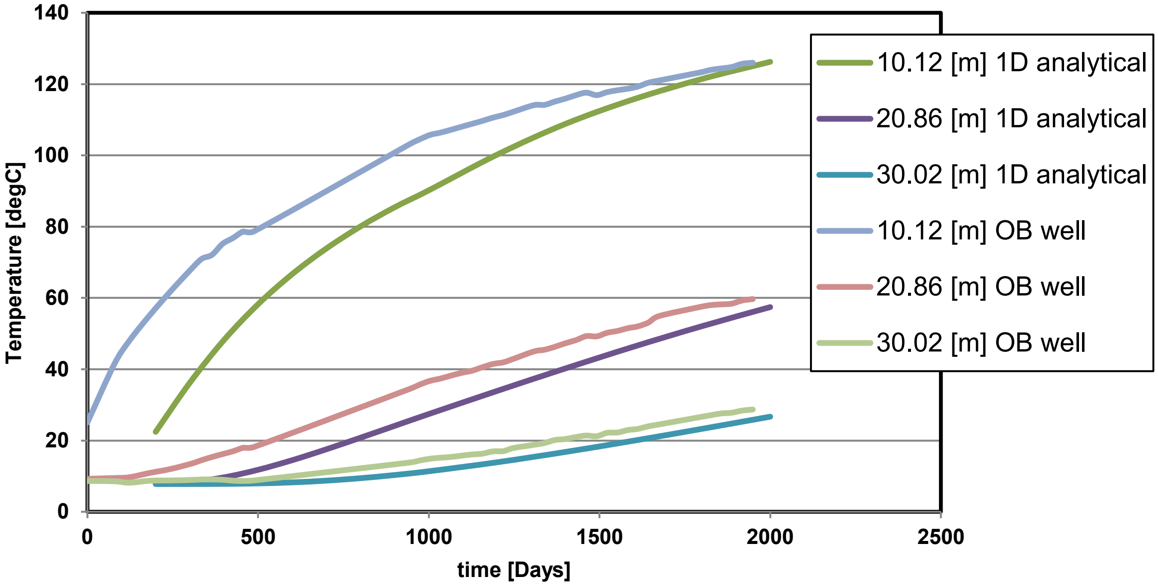

Figure 6.2: Comparison of real observation well data of OB 100/05-11-095-06W4/00 with the 1D synthetic model.

The possibility of a convective flow ahead of the steam chamber can also be studied by looking at the petrophysical logs. The gamma log of the observation well is shown in Figure 6.3. It indicates the existence of very thick layers with high fines content above the steam chamber. Layers with high fines content have very low permeability and do not allow the hot pore fluid to diffuse through them. The domination of conduction as the major contributor to heat transport ahead of the steam chamber for this observation well can therefore be concluded by the support of comparing the calculated thermal diffusivity with lab results, history matching, and gamma log of the overlying strata.

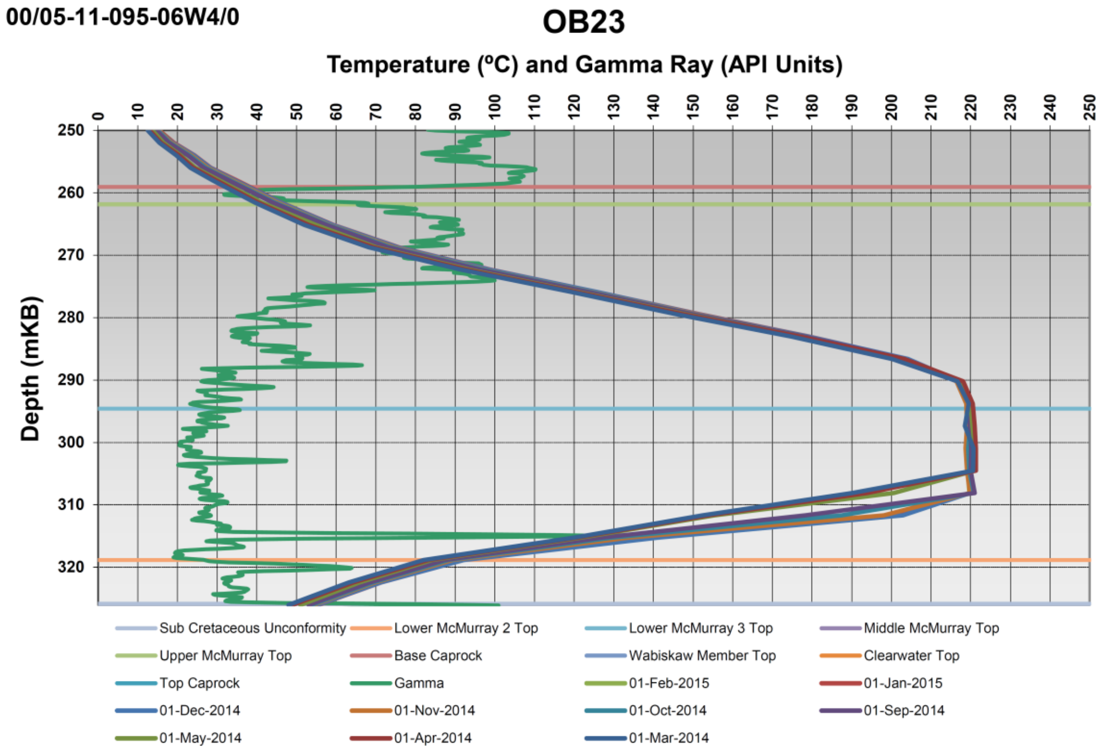

Figure 6.3: Gamma log of OB 100/05-11-095-06W4/00. Figure adapted from Suncor (2015).

6.1.2. Convective Case

Data from another observation well is analyzed for the detection of convective flows. Temperature profiles are shown in Figure 6.4. The process of calculating thermal diffusivity is included in Appendix III. The back calculated thermal diffusivity is equal to $\alpha = 1.24 \times 10^{-6} \left[\frac{m^2}{s}\right]$. This value is higher compared to the conduction case. The calculated value is also high when it is compared to the experimental results shown in Figure 6.1.

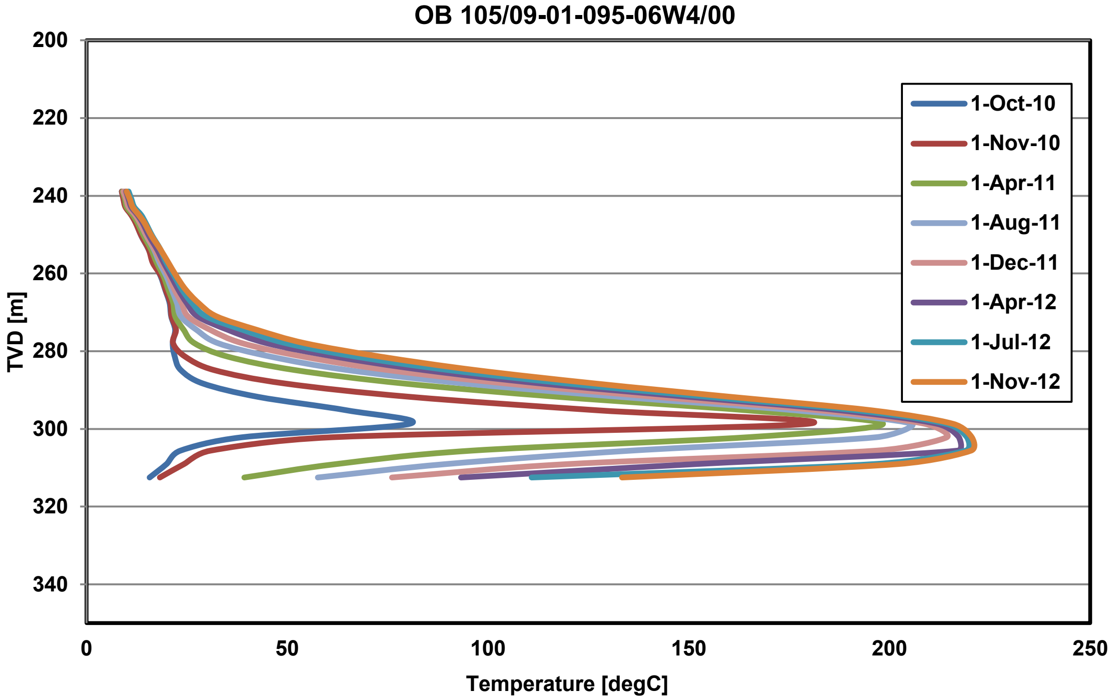

Figure 6.4: Temperature profiles of OB 105/09-01-095-06W4/00 from Suncor (2013).

Temperature history of the observation well was compared with a synthetic model. It was assumed from ICEF plots that the top of steam chamber it at 297.9m TVD and the steam chamber has established a hot interface after 1-Nov-2010. Temperature recordings were compared at three locations ahead of the steam chamber. Figure 6.5 shows the comparison of measured temperature values with the synthetic model. Contrary to the conduction-only model, the measured values and the synthetic model estimates do not match. The difference between the two temperature profiles at 23.4m above the steam chamber is about 20°C. Therefore, one can conclude that a conductive scenario cannot dominate heat transfer for this case and there is upward fluid movement contributing to heat transport towards the caprock.

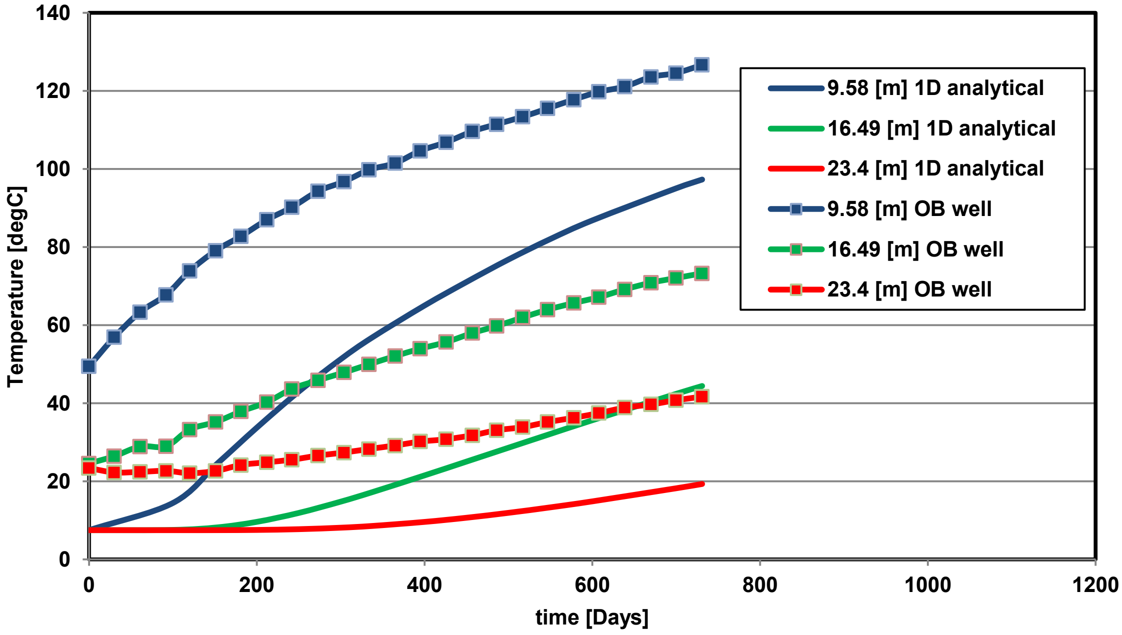

Figure 6.5: Comparison of real observation well data of OB 105/09-01-095-06W4/00 with the 1D synthetic model.

Figure 6.6 shows the gamma log of OB 105/09-01-095-06W4/00 . It can be seen that a low fines content interval exists above 299m TVD. Layers with low fines content above the top of steam chamber may be permeable enough to allow diffusion of hot fluid ahead of the steam chamber. Permeability to water is highly dependent on the saturation of the water phase as well. Water saturation can be estimated from resistivity logs. Resistivity log of this well was not available at the time of writing the thesis. However, the existence of a water permeable zone above the steam chamber is highly probable through which hot water can convect heat above.

The existence of a non-negligible convective component is therefore supported by higher thermal diffusivity values compared to lab results, inability to history match the temperature profiles, and detection of possible thick permeable enough layers above the steam chamber from petrophysical logs.

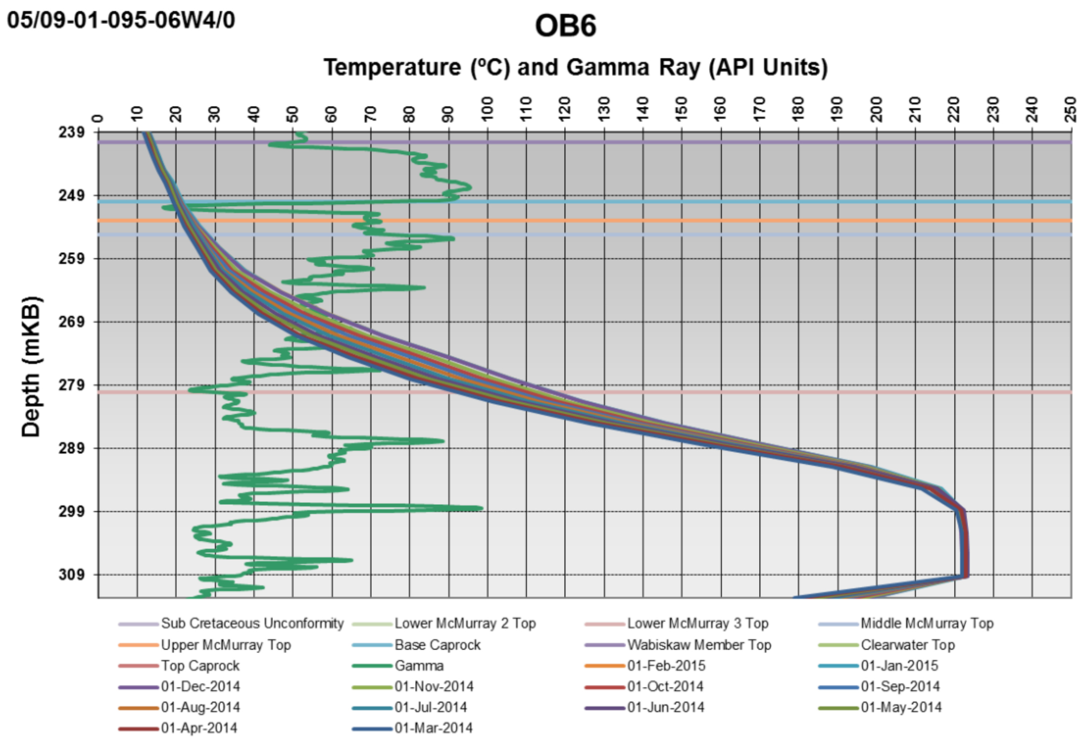

Figure 6.6: Gamma log of OB 105/09-01-095-06W4/00. Figure adapted from Suncor (2015).

6.2. Estimation of Convective Component from temperature Profiles

6.2.1. Determination of vertical Fluid Velocity from Temperature Profiles

The estimation of vertical movement of water from a type-curve method is explained by Bredehoeft and Papaopulos (1965). Assuming the fluid and heat are moving in one direction and temperature profiles are at the steady state, the one-dimensional governing equation of heat transfer will become (Bredehoeft and Papaopulos, 1965):

$$\frac{\partial^2 T}{\partial z^2} - \frac{(\rho c)_f}{k_m}\frac{\partial T}{\partial z} = 0 \qquad \text{Equation 6.1}$$

The parameters are the same as defined in Equation 3.2.

The solution to the differential equation with the following boundary conditions will be (Bredehoeft and Papaopulos, 1965):

$$\frac{\partial^2 T}{\partial z^2} - \frac{(\rho c)_f}{k_m} v_f \frac{\partial T}{\partial z} = 0$$

$$z = 0 \quad , \quad T = T_O$$

$$z = L \quad , \quad T = T_L \qquad \text{Equation 6.2}$$

$$\frac{T_z - T_O}{T_L - T_O} = \frac{e^{\left(\frac{\beta z}{L}\right)} - 1}{e^{(\beta)} - 1}$$

In this equation $\beta = \frac{(\rho c)_f v_f L}{k_m}$. The change in dimensionless temperature profile with β is shown in Figure 6.7.

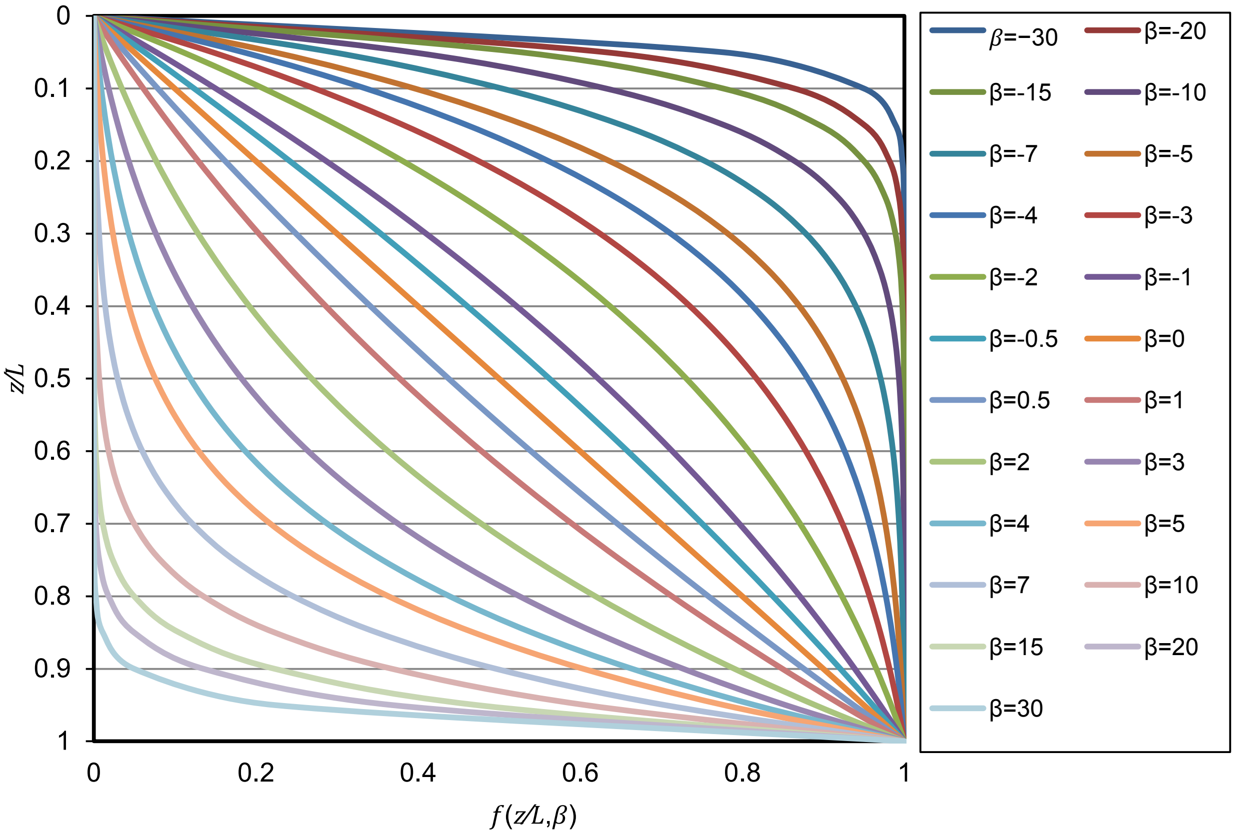

Figure 6.7: Change in the dimensionless temperature profile with **β**.

In the case of conduction $\beta = 0$ and the shape of the temperature profile between the measuring points will be a straight line. Any deviation from linear changes in the temperature profile is indicative of a convective flow between the measuring points.

Assuming that the change in temperature over time is slow and temperature profiles are close to a quasi-steady state, the same technique can be used for the estimation of convective component of heat transport.

6.2.2. Temperature Profile Interpolation with Cubic Splines

The first step in analyzing the data is interpolation of temperature profiles between the measuring points. The simplest method of temperature interpolation is linear change between the measuring points. However, linear interpolation of data between measuring points results in no detection of convection. In order to overcome these challenges, natural cubic splines were used for the interpolation of temperature profiles. Cubic spline data interpolation has the advantage of continuous first and second derivative (Hoffman and Frankel, 2001). Therefore, they have the ability to represent the curvature of change between two measuring points.

The interpolation of data with spline curves follows the equation (Hoffman and Frankel, 2001):

$$\begin{aligned} f_i(x) &= \frac{f_i''}{6(x_{i+1}-x_i)}(x_{i+1}-x)^3 + \frac{f_{i+1}''}{6(x_{i+1}-x_i)}(x-x_i)^3 \\ &+ \left[\frac{f_i}{x_{i+1}-x_i} - \frac{f_i''(x_{i+1}-x_i)}{6}\right](x_{i+1}-x) \\ &+ \left[\frac{f_{i+1}}{x_{i+1}-x_i} - \frac{f_{i+1}''(x_{i+1}-x_i)}{6}\right](x-x_i) \end{aligned}$$

Equation 6.3

where:

$$\begin{aligned} &(x_i-x_{i-1})f_{i-1}'' + 2(x_{i+1}-x_{i-1})f_i'' + (x_{i+1}-x_i)f_{i+1}'' \\ &= 6\frac{f_{i+1}-f_i}{x_{i+1}-x_i} - 6\frac{f_i-f_{i-1}}{x_i-x_{i-1}} \end{aligned}$$

Equation 6.4

More details on the interpolation of data by standard cubic splines can be found in Hoffman and Frankel (2001).

6.2.3. Calculation of Vertical Fluid Velocity from Observation Well Data

In this section, the process of finding the magnitude of the velocity of convective fluid by the curve-type fitting method is explained. Temperature profiles of OB 102/15-12-095-06W4/00 are shown in Figure 6.8.

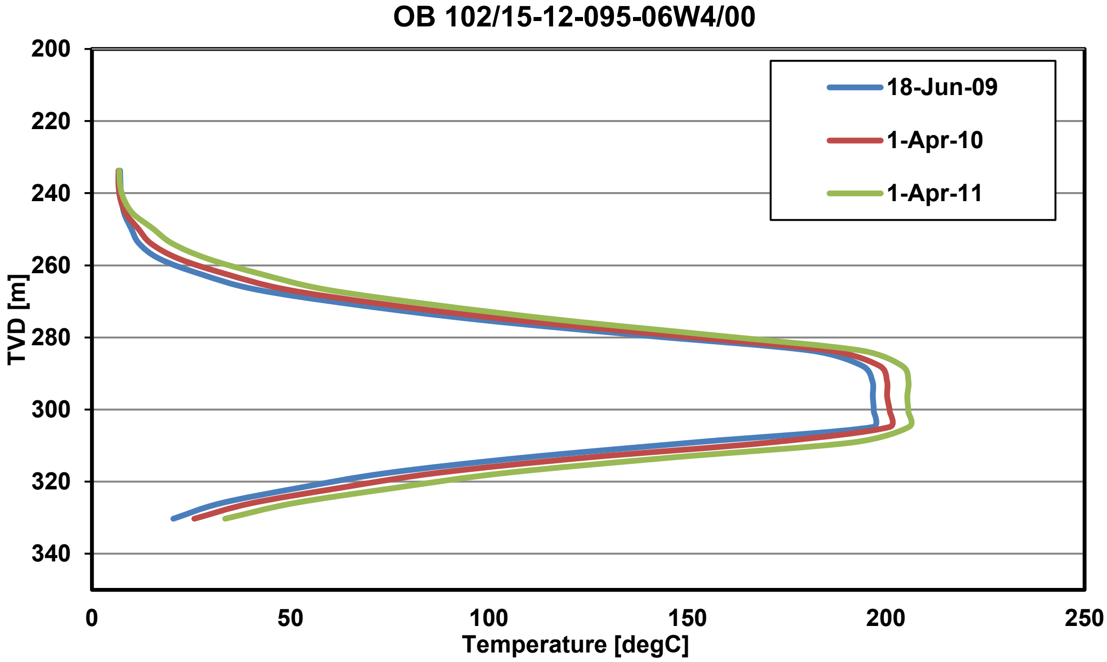

Figure 6.8: Temperature profiles of OB 102/15-12-095-06W4/00. Data extracted from Suncor (2012).

Figure 6.9 shows the data points and cubic spline interpolation of the data for one temperature survey. nIn the next step, the temperature profile between two points was matched to the closest solution of Equation 6.2 by changing β. Figure 6.10 shows the process of finding the closest exponential solution from Equation 6.2 to the interpolated data. The closest solution of the exponential solution to the interpolated temperature profile is shown in Figure 6.11. The exponential solutions are matching the interpolated data quite well. The calculated β was then used for calculation of vertical fluid velocity. Thermal properties were assumed to be equal to the values in Table 3.3. Figure 6.12 shows the magnitude of the calculated velocity by this method. The maximum velocity of the moving fluid is detected near the edges of the steam chamber. Very low convective flows are calculated inside the steam chamber, which is indicative of the consistency of the results.

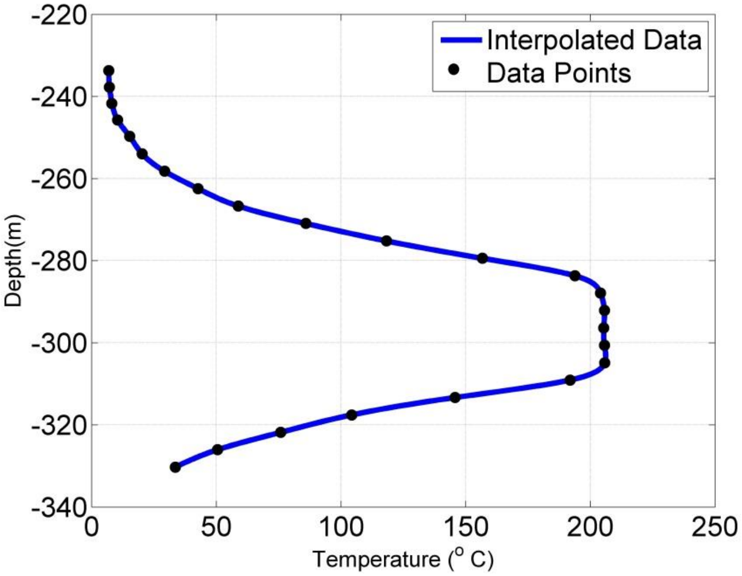

Figure 6.9: Interpolation of a temperature profile with cubic splines.

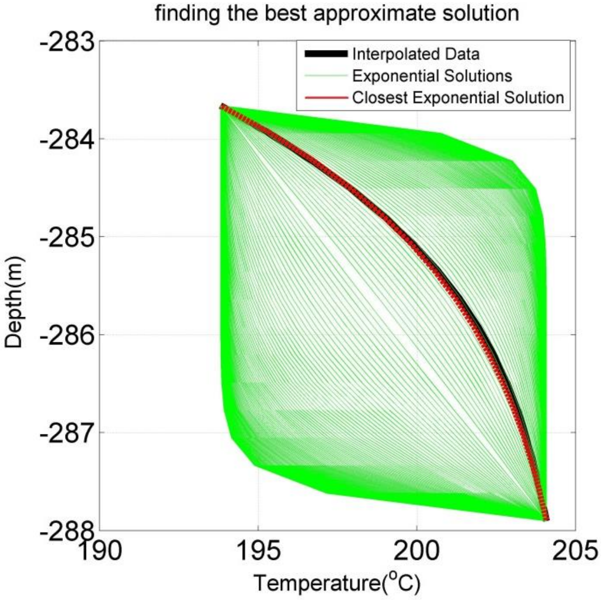

Figure 6.10: Finding the closest exponential solution from Equation 6.2 to the interpolated data.

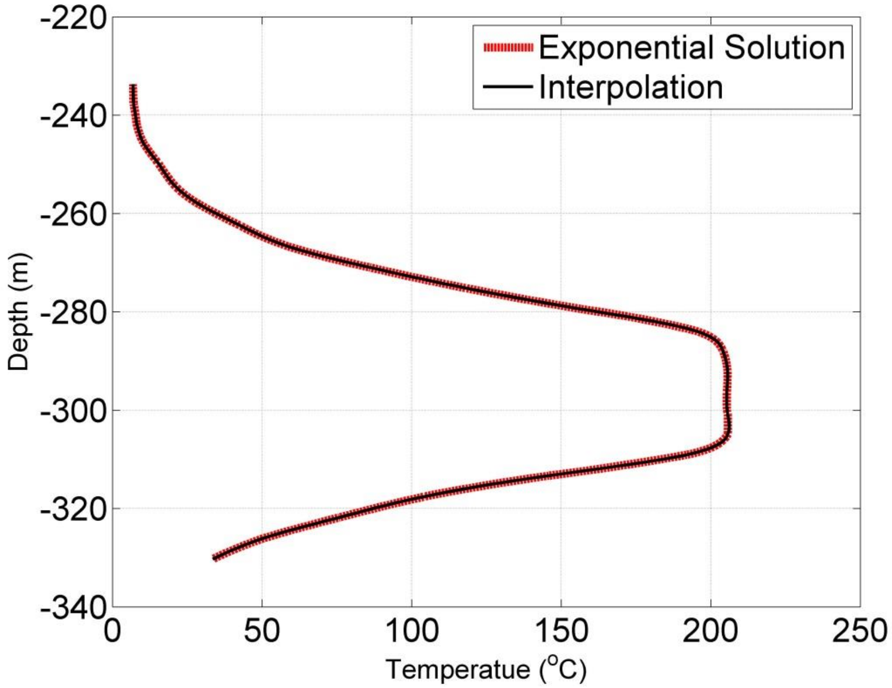

Figure 6.11: Finding the closest exponential solution along the temperature profile.

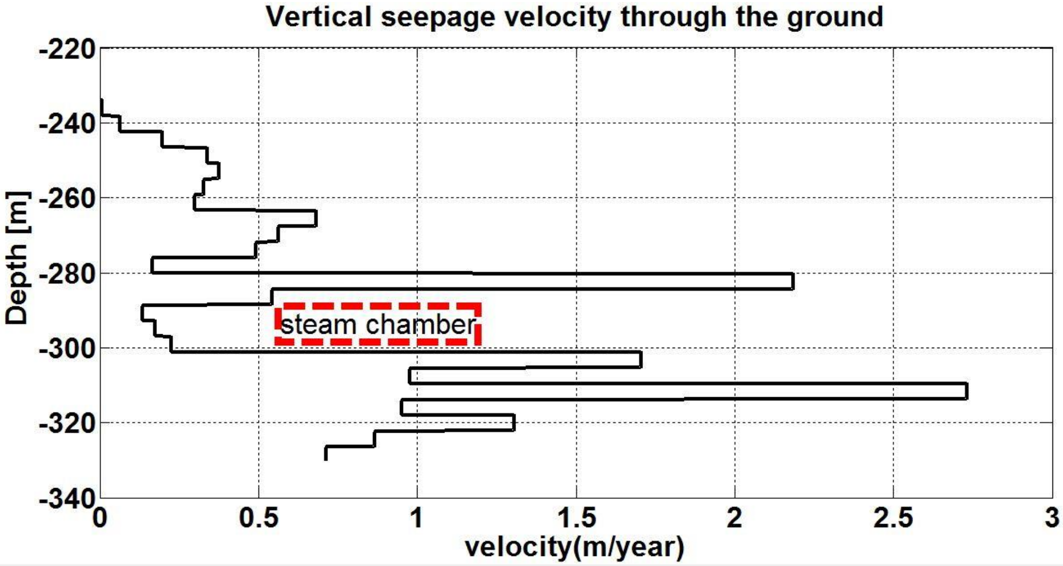

Figure 6.12: Calculated convective fluid velocity from the closest exponential solution.

The location of the observation well is shown in Figure 6.13. The observation well is close to the monitoring location along L_2 shown in Figure 3.21 in the synthetic model.

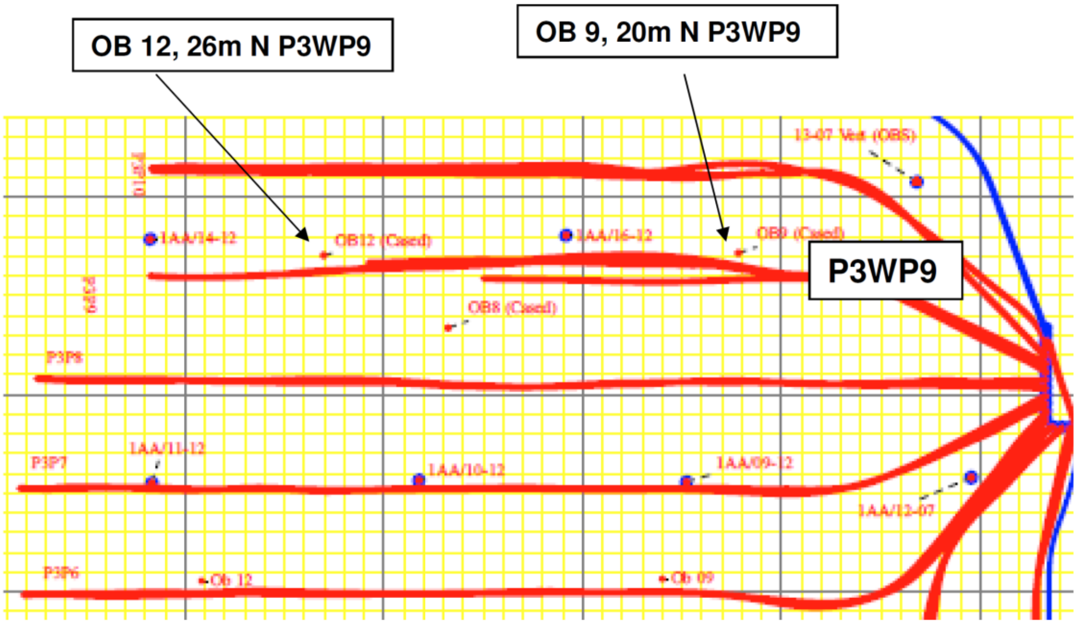

Figure 6.13: Location of OB 12 (102/15-12-095-06W4/00) relative to pad. Figure adapted from (Suncor 2012).

Caution should be used in the analysis of temperature profiles by this method. The completion records of the observation wells were not available at the time of writing the thesis. Therefore, it is not possible to determine whether or not wellbore fluid effects influenced the observation well temperature measurements. The effect of lateral fluid flow on the temperature profile should not be ignored as well (Lu and Ge, 1996). As mentioned previously, the temperature distributions along monitoring lines close to the edge of the pad are not only under the influence of vertical fluid movement but also affected by lateral flow of the convecting fluid.

6.3. Results Comparison of Observation Well Data Analysis

Thermal Diffusivity was calculated from 10 observation wells. The results are summarized in Table 6.1. The graphs of temperature logs and thermal diffusivity calculations are provided in

Appendix III. It can be seen that average thermal diffusivity from observation well data above the steam chamber is less than $1 \times 10^{-6} \left[\frac{m^2}{s}\right]$. This value is close to the lab results reported by Seto (1985) in the temperature range above a steam chamber. The agreement between calculated thermal diffusivities from observation well data and lab results is indicative of reliability in the method. In the cases where the calculated thermal diffusivity is higher than expected the possibility of a convective heat component can be investigated by history matching the temperature measurements with a synthetic model and analyzing petrophysical logs.

Table 6.1: Summary of calculated thermal diffusivities from observation well temperature profiles.

Observation Well UWI	$\boldsymbol{\alpha \left[\frac{m^2}{s}\right] \times 10^{-6}}$
105/09-01-095-06W4/00	1.24
102/15-12-095-06W4/00	0.84
100-05-02-095-06W4/00	0.86
100/05-11-095-06W4/00	0.94
104/14-02-095-06W4/00	1.18
100/02-02-095-06W4/00	0.74
103/08-01-095-06W4/00	1.10
109/14-36-094-06W4/00	1.03
100/02-14-076-06W4/00	1.10
100/09-11-076-06W4/00	0.76

6.4. Summary

In this chapter the outputs of calculating thermal diffusivity were used for investigation of contributing heat transfer mechanisms above the steam chamber. Heat conduction and convection scenarios of real observation well data were investigated. Calculated thermal diffusivities from temperature logs were compared to lab measurements. Temperature profiles were then history matched with the calculated thermal diffusivity. Acceptable match was observed in the case of conduction. The difference between the measured data and the synthetic model decreased over time. In the convective case, however, the synthetic model was not able to match the history of observation well and the difference between the observed and predicted temperature values did not decrease sensibly over time.

Interpolation of petrophysical logs can also provide information on the possibility of existence of permeable layers above the steam chamber. Low permeability layers with very high fines content should be expected above the conductive cases while low fines content layers should be expected to be present above a convective case.

Estimation of the magnitude of fluid velocity from temperature profiles was also explained. The use of this method is strictly dependent on the accurate measurement of temperature inside the observation well. Wellbore fluid can totally smear the temperature measurements and lead to erroneous conclusions on the calculation of convective heat transport ahead of the steam chamber. Anisotropy in the permeability of overlying strata can also influence the analysis of temperature profiles for the detection of vertical convective fluid. Horizontal flows of fluid and heat can have significant effects on the vertical temperature profiles if the magnitude of lateral fluid flow is comparable to the vertical.

Chapter 7: Conclusions and Recommendations

7.1. Summary

One and two dimensional heat transfer mechanisms ahead of a hot interface were studied with synthetic models. The effects of varying interface temperature, initial temperature of the medium and uncertainty in the value of thermal properties on temperature distribution were studied in conduction 1D cases. Investigation of different scenarios highlighted the deviation of temperature response for 2D conduction from the 1D solution. The contribution of convection in heat transport was studied in 1D and 2D models as well. It was shown that the location of temperature monitoring is crucial in the detection of convective flows in 2D models.

Thermal properties of the material were calculated by analyzing temperature response of the medium. The influencing parameters by which the properties can deviate from the true value were detected. 2D effects resulted in underestimation of thermal properties from temperature profiles of conductive models. Prediction of temperatures with 1D models based on back calculated thermal properties showed a mismatch with the observed temperatures of the 2D models. The difference between the observed and predicted temperatures was higher when convection was involved. Higher thermal diffusivities were calculated in the conductive and convective models as well.

Major factors affecting the measurement of true temperature distributions in the formation were studied. The effect of wellbore fluid should not be ignored. The effect of casing conduction on temperature profiles was concluded to be negligible. The procedure of selecting an observation well and analysis of data was provided to minimize the effects of deviation from the virgin temperature and lateral heat transport toward the observation well.

Temperature measurements from observation wells of SAGD operations were investigated for the determination of contributing mechanisms of upward heat transfer ahead of a steam chamber. The outputs of calculating thermal diffusivity were used for investigation of contributing heat transfer mechanisms. Heat conduction and convection scenarios of real observation well data were studied. The determination of the contributing heat transfer mechanisms was investigated by comparing the calculated thermal properties to the measured lab results, history matching the measured temperatures with a synthetic model, and analyzing petrophysical logs. Estimation of the magnitude of fluid velocity from temperature profiles by the type-curve method and the limitations and requirements of using such method were also explained.

7.2. Limitations

Pore fluid type, fluid saturation, mineralogy, texture, and temperature are among the factors that can change the thermal properties of geomaterials. In the analysis of observation well temperature measurements it was assumed that thermal properties of the geomaterials were homogeneous and isotropic. The dependency of the properties on temperature and pressure were not included.

The accuracy of the measured temperatures with observation wells needs to be studied more comprehensively. Although excluding some temperature recordings lowered the level of uncertainty, true formation temperatures can still be different from the reported values.

The use of a one-dimensional model for detection of convective flows ahead of steam chamber is associated with high uncertainties. Heterogeneity and anisotropy of hydraulic and thermal properties of the McMurray and Clearwater Formations necessitate comprehensive modeling studies with low uncertainties for the determination of convective flows ahead of a steam chamber. Geomechanical effects can change the hydraulic properties of geomaterials significantly. Coupling reservoir properties with geomechanical deformations is necessary for the prediction of fluid flow inside the reservoir and overlying strata. Another important factor that determines the flow regime inside the reservoir is the regional in-situ pore pressure of the formations.

It was also assumed that water is the only phase by which heat can be convected ahead of the steam chamber. A multiphase heat transfer analysis is required to validate this assumption, which is beyond the scope of this work.

Temperature history matching of the 2D models was associated with differences between the observed and predicted values even when the monitoring location was at the middle of the model. 2D models are therefore necessary for a better study and history match of heat loss to the overburden.

7.3. Recommendations

In order to lower the uncertainties on thermal and hydraulic properties of the geomaterials more laboratory tests should be conducted. Heat loss to the overburden is a key factor during the recovery of heavy oil with thermal operations such as SAGD and CSS. Knowledge on the thermal properties of the overburden can help model the heat loss and generation of thermal stresses more accurately.

The inclusion of heterogeneity and anisotropy of thermal and hydraulic properties in a multiphase study of heat transport and coupled with geomechanical deformations can lead to more robust conclusions on the contributing mechanisms by which heat is being transported upwards above steam chambers. Pressure measurements inside the observation wells can also help calibrate the reservoir and geomechanical models and determine whether pressure changes are representative of fluid connectivity or geomechanical loading.

References

Aherne, A. L. and Maini, B. Fluid Movement in the SAGD Process: A Review of the Dover Project. Journal of Canadian Petroleum Technology, 47(1): 31-37.

Akin, S. 2005. Mathematical Modeling of Steam Assisted Gravity Drainage. Journal of Canadian Petroleum Technology, SPE Reservoir Evaluation and Engineering, 8(5): 372-376.

Alberta Energy Regulator (AER). 2015. ST98-2015 Alberta's Energy Reserves 2014 and Supply/Demand Outlook 2015-2024. Alberta Energy Regulator, Calgary, AB, Canada. Retrieved from: https://www.aer.ca/data-and-publications/statistical-reports/st98

Alberta Energy Regulator (AER). 2016. ST98-2016 Alberta's Energy Reserves 2015 and supply/Demand Outlook 2016-2025 Executive Summary. Alberta Energy Regulator, Calgary, AB, Canada. Retrieved from: https://www.aer.ca/data-and-publications/statistical-reports/st98

Birrell, G. E. and Putnam, P. E. 2000. A Study of the Influence of Reservoir Architecture on SAGD Steam Chamber Development at the Underground Test Facility, Northeastern Alberta, Canada, Using a Graphical Analysis of Temperature Profiles. Canadian International Petroleum Conference, 4-8 June, Calgary, Alberta. Petroleum Society of Canada, Paper 2000-104.

Birrell, G. 2003. Heat Transfer Ahead of a SAGD Steam Chamber: A Study of Thermocouple Data From Phase B of the Underground Test Facility (Dover Project). Journal of Canadian Petroleum Technology, 42(3): 40-47.

Bredehoeft, J. D. and Papadopoulos, I. S. 1965. Rates of vertical groundwater movement estimated from the Earth's thermal profile. Water Resources Research, 1(2): 325-328.

Brown, J. W. and Churchill, R. V. 1993. Fourier Series and Boundary Value Problems-5th Edition. McGraw-Hill, Inc. ISBN 0-07-008202-2

Butler, R. M. 1991. Thermal Recovery of Oil and Bitumen. Prentice Hall Inc., Englewood Cliffs, New Jersey 07632. ISBN: 0-13-914953-8

Butler, R. M. and Stephens, D. J. 1981. The Gravity Drainage of Steam-heated Heavy Oil to Parallel Horizontal Wells. Journal of Canadian Petroleum Technology, 20(2): 90-96.

Carslaw, H. S. and Jaeger, J. C. 1959. Conduction of Heat in Solids. Oxford: Clarendon Press, 1959, 2nd Edition.

Cenovus. 2010. Cenovus Christina Lake In-Site Oil Scheme 2010 Update ERCB Office June 8, 2010. Data Retrieved from: https://www.aer.ca/data-and-publications/activity-and-data/in-situ-performance-presentations

Cenovus. 2011. Cenovus Christina Lake In-Site Oil Scheme 2010-2011 Update ERCB Office June 15, 2011. Data Retrieved from: https://www.aer.ca/data-and-publications/activity-and-data/in-situ-performance-presentations

Cenovus. 2012. Cenovus Christina Lake In-Site Oil Scheme 2011-2012 Update ERCB Office June 20, 2012. Data Retrieved from: https://www.aer.ca/data-and-publications/activity-and-data/in-situ-performance-presentations

Cenovus. 2013. Cenovus Christina Lake In-Site Oil Scheme (8591) 2012-2013 Update ERCB Office June 19, 2013. Data Retrieved from: https://www.aer.ca/data-and-publications/activity-and-data/in-situ-performance-presentations

Cenovus. 2014. Cenovus Christina Lake In-Site Oil Scheme 8591 2013 Update Subsurface Calgary June 4, 2014. Data Retrieved from: https://www.aer.ca/data-and-publications/activity-and-data/in-situ-performance-presentations

Cenovus. 2015. Cenovus Christina Lake In-Site Oil Scheme 8591 2015 Update Subsurface June 24, 2015. Data Retrieved from: https://www.aer.ca/data-and-publications/activity-and-data/in-situ-performance-presentations

Chalaturnyk, R. J. and Li, P. 2004. When Is It Important to Consider Geomechanics in SAGD Operations? Journal of Canadian Petroleum Technology, 43(4): 53-61.

Closmann, P. J. and Smith, R. A. 1983. Temperature Observations and Steam-Zone Rise in the Vicinity of a Steam-Heated Fracture. Society of Petroleum Engineers Journal, 23(4): 575-586.

Closmann, P. J., Jones, E. R., and Vogel, E. A. 1979. Effect of a Heat-Conducting Well Casing on Temperature Distribution in an Observation Well. ASME. Journal of Energy Resources Technology, 101(1): 20-27.

Collins, R. M., Carlson, M. R., Walters, D. A., and Settari, A. 2002. Geomechanical and Thermal Reservoir Simulations Demonstrates SAGD Enhancement Due to Shear Dilation. SPE/ISRM Rock Mechanics Conference, 20-23 October, Irving, Texas. Society of Petroleum Engineers, SPE-78237-MS.

EnCana. 2007. EnCana Christina Lake In-Situ Oil Sands Scheme 2007 Update June 8, 2007. Data Retrieved from: https://www.aer.ca/data-and-publications/activity-and-data/in-situ-performance-presentations

EnCana. 2008. EnCana Christina Lake In-Situ Oil Sands Scheme 2008 Update ERCB Office June 27, 2008. Data Retrieved from: https://www.aer.ca/data-and-publications/activity-and-data/in-situ-performance-presentations

EnCana. 2009. EnCana Christina Lake In-Situ Oil Scheme 2009 Update ERCB Office June 12, 2009. Data Retrieved from:

https://www.aer.ca/data-and-publications/activity-and-data/in-situ-performance-presentations

Fustic, M., Bennett, B., Adams, J., Huang, H., MacFarlane, B., Leckie,. A. A., and Larter, S. 2012. Bitumen and Heavy Oil Geochemistry: A Tool for Distinguishing Barriers from Baffles in Oil Sands Reservoirs. Bulletin of Canadian Petroleum Geology, 59(4): 295-316.

Griston, S. 1989. Fluid Effects in Temperature Observation Wells. SPE Annual Technical Conference and Exhibition, 8-11 October, San Antonio, Texas. Society of Petroleum Engineers, SPE-19740-MS.

Hein, F. J., Cotterill, D. K., and Berhane H. 2000. An Atlas of Lithofacies of the McMurray Formation Athabasca Oil Sands Deposit, Northeastern Alberta: Surface and Subsurface. Alberta Energy and Utilities Board, EUB/AGS Earth Sciences Report 2000-07, 217 p.

Hein, F. J., Cotterill, D. K., and Rice, R. J. 2006. Subsurface Geology of the Athabasca Wabiskaw-McMurray Succession: Lewis-Fort McMurray Area, Northern Alberta (NTS 74D/74E). Alberta Energy and Utilities Board, EUB/AGS Earth Sciences Report 2006-06, 67 p.

Hoffman, J. D. and Frankel S. 2001. Numerical Methods for Engineers and Scientists, CRC Press; 2 edition (May 31 2001). ISBN: 0-82-470443-6

Ito, Y. and Ipek, G. 2005. Steam Fingering Phenomenon during SAGD Process. SPE International Thermal Operations and Heavy Oil Symposium, 1-3 November, Calgary, Alberta, Canada. Society of Petroleum Engineers, SPE-97729-MS.

Ito, Y. and Suzuki, S. 1996. Numerical Simulation of the SAGD Process in the Hangingstone Oil Sands Reservoir. Annual Technical Meeting, June 10 - 12, Calgary, Alberta. Petroleum Society of Canada, PETSOC-96-57.

Kagawa, S. Kiyoshi, N., Sakata, M., Imazato, H., and Miyauchi, T. 1992. Experimental Study on the Analysis of Temperature Observation. Journal of the Japan Petroleum Institute, 35(1): 56-64.

Karim, G. A. and Hanafi, A. 1981. The Thermal Conductivity of Oil Sands. The Canadian Journal of Chemical Engineering, 59(4): 461-464.

Li, P. and Chalaturnyk, R. J. 2006. Permeability Variations Associated With Shearing and Isotropic Unloading During the SAGD Process. Journal of Canadian Petroleum Technology, 45(1): 54-61.

Li, P. and Chalaturnyk, R. J. 2009. History Match of the UTF Phase A Project with Coupled Reservoir Geomechanical Simulation. Journal of Canadian Petroleum Technology, 48(1): 29-35.

Li, P., Chalaturnyk, R. J., and Polikar, M. 2004. Issues with reservoir geomechanical simulation of the SAGD process. Journal of Canadian Petroleum Technology, 43(5): 30-40.

Lu, N. and Ge, S. 1996. Effect of Horizontal Heat and Fluid Flow on the Vertical Temperature Distribution in a Semiconfining Layer. Water Resources Research, 32(5): 1449-1453.

Midttome, K. and Roaldset, E. 1999. Thermal Conductivity of Sedimentary Rocks: Uncertainties in Measurement and Modelling. Geological Society 158, Special Publications, London: 45-60.

Nield, D.A. and Bejan, A. 2006. Convection in Porous Media. Springer-Verlag (January 1992) ISBN: 978-0-387-29096-6

Nzekwu, B. I., Hallam, R. J., and Williams, G. J. J. 1990. Interpretation of Temperature Observations From a Cyclic-Steam/In-Situ-Combustion Project. SPE Reservoir Engineering, 5(2): 163-169.

Seto, A. C. 1985. Thermal Testing of Oil Sands. M.Sc. Thesis, Department of Civil Engineering, University of Alberta, Edmonton, Alberta, Canada.

Seto, A. C. and Bharatha, S. 1991. Thermal Conductivity Estimation from Temperature Logs. SPE International Thermal Operations Symposium, 7-8 February, Bakersfield, California. Society of Petroleum Engineers, SPE-21542-MS.

Sharma, J. and Gates, I. D. 2011. Convection at the Edge of a Steam-Assisted-Gravity-Drainage Steam Chamber. SPE Journal, 16(3): 503-512.

Smith-Magowan, D., Skauge, A., and Helper, L. G. 1982. Specific Heats of Athabasca oil Sands and Components. Journal of Canadian Petroleum Technology, 21(3): 28-32.

Somerton, W. H., Keese, J. A., and Chu, S. L. 1974. Thermal Behavior of Unconsolidated Oil Sands. Society of Petroleum Engineers Journal, 14(5): 513-521.

Statoil. 2014. Statoil Canada Ltd. Leismer SAGD Project Approval No. 10935L Leismer SAGD (January 1-December 31, 2013) Annual D054 Performance Presentation Alberta Energy Regulator March 5, 2014. Data Retrieved from: https://www.aer.ca/data-and-publications/activity-and-data/in-situ-performance-presentations

Suncor Energy. 2007. Firebag Project Commercial In-situ Oil Sands Project Approval No. 8870, Annual AEUB Review Presentation-May 30, 2007. Data Retrieved from: https://www.aer.ca/data-and-publications/activity-and-data/in-situ-performance-presentations

Suncor Energy. 2008. 2008 ERCB Annual Review Suncor Firebag April 30th, 2008. Data Retrieved from: https://www.aer.ca/data-and-publications/activity-and-data/in-situ-performance-presentations

Suncor Energy. 2009. Suncor Firebag 2009 ERCB Performance Presentation Commercial Scheme Approval No. 8870 Experimental Scheme Approval no. 8683 May 5th and 6th, 2009. Data Retrieved from: https://www.aer.ca/data-and-publications/activity-and-data/in-situ-performance-presentations

Suncor Energy. 2010. Suncor Firebag 2010 ERCB Performance Presentation Commercial Scheme Approval No. 8870 May 11th and 12th, 2010. Data Retrieved from:

https://www.aer.ca/data-and-publications/activity-and-data/in-situ-performance-presentations

Suncor Energy. 2011. Suncor Firebag 2011 ERCB Performance Presentation Commercial Scheme Approval No. 8870 May 4th and 5th, 2011. Data Retrieved from: https://www.aer.ca/data-and-publications/activity-and-data/in-situ-performance-presentations

Suncor Energy. 2012. Suncor Firebag 2012 ERCB Performance Presentation Commercial Scheme Approval No. 8870 May 15th to 16th, 2012. Data Retrieved from: https://www.aer.ca/data-and-publications/activity-and-data/in-situ-performance-presentations

Suncor Energy. 2013. Suncor Firebag 2013 ERCB Performance Presentation Commercial Scheme Approval No. 8870 May 1st and 2nd, 2013. Data Retrieved from: https://www.aer.ca/data-and-publications/activity-and-data/in-situ-performance-presentations

Suncor Energy. 2014. Suncor Firebag 2014 AER Performance Presentation Commercial Scheme Approval No. 8870 May 6 and 7, 2014. Data Retrieved from: https://www.aer.ca/data-and-publications/activity-and-data/in-situ-performance-presentations

Suncor Energy. 2015. Suncor Firebag 2015 AER Performance Presentation Commercial Scheme Approval No. 8870 May 7, 2015. Data Retrieved from: https://www.aer.ca/data-and-publications/activity-and-data/in-situ-performance-presentations

Van Genuchten, M. T. and Alves, W. J. 1982. Analytical solutions of the One-Dimensional Convective-Dispersive Solute Transport Equation (No. 157268). Technical Bulletins from United States Department of Agriculture, Economic Research Service. 151 p.

Vinsome P K.W and Westerveld J. 1980. A Simple Method For Predicting Cap And Base Rock Heat Losses In Thermal Reservoir Simulators. Journal of Canadian Petroleum Technology, 19(3): 87-90.

Vittoratos, E. 1986. Interpretation of Temperature Profiles From the Steam-Stimulated Cold Lake Reservoir. SPE California Regional Meeting, 2-4 April, Oakland, California. Society of Petroleum Engineers, SPE-15050-MS.

Appendix I: Analytical solution of heat conduction ahead of a hot interface with exponentially decreasing initial temperature

In this section, a closed form analytical solution to the one-dimensional heat conduction equation in a semi-infinite medium subject to initial condition $T^* = e^{-\frac{U}{\alpha}x}$ is presented. The procedure of finding the solution is followed by the Fourier integral method explained in (Brown, et al., 1993). The initial boundary value problem is defined as:

$$\frac{\partial T^*}{\partial t} = \alpha \frac{\partial^2 T^*}{\partial z^2} \qquad , \quad z > 0 \ , \quad t > 0$$

$$T^*(z,0) = e^{-\frac{U}{\alpha}z} = e^{-\xi z} \qquad , \quad z > 0$$

$$T^*(0,t) = 1 \qquad , \quad t > 0$$

First, a new function,$w(z,t)$, is defined as $w(z,t) = T^*(z,t) - 1$ in order to homogenize the boundary condition at $z = 0$. The new initial boundary value problem will be:

$$\frac{\partial w}{\partial t} = \alpha \frac{\partial^2 w}{\partial z^2} \qquad , \quad z > 0 \ , \quad t > 0$$

$$w(z,0) = e^{-\frac{U}{\alpha}z} - 1 = e^{-\xi z} - 1 = f(z) \qquad , \quad z > 0$$

$$w(0,t) = 0 \qquad , \quad t > 0$$

Using the Fourier integral method, the solution to this problem is (Brown, et al., 1993):

$$w(0,t) = \frac{1}{\sqrt{4\pi\alpha t}} \int_0^\infty f(s) \left[e^{\left(-\frac{(s-x)^2}{4\alpha t}\right)} - e^{\left(-\frac{(s+x)^2}{4\alpha t}\right)} \right] ds$$

$$f(z) = e^{-\xi z} - 1 \quad \Rightarrow \quad w(x,t) = \frac{1}{\sqrt{4\pi\alpha t}} \int_0^\infty \left(e^{-\xi s} - 1\right) \left[e^{\left(-\frac{(s-x)^2}{4\alpha t}\right)} - e^{\left(-\frac{(s+x)^2}{4\alpha t}\right)} \right] ds$$

$$w(x,t) = \frac{1}{\sqrt{4\pi\alpha t}} \left\{ \int_0^\infty e^{-\xi s} \left[e^{\left(-\frac{(s-x)^2}{4\alpha t}\right)} - e^{\left(-\frac{(s+x)^2}{4\alpha t}\right)} \right] ds - \int_0^\infty \left[e^{\left(-\frac{(s-x)^2}{4\alpha t}\right)} - e^{\left(-\frac{(s+x)^2}{4\alpha t}\right)} \right] ds \right\}$$

A closed form solution can be found for both the integral terms. For the first term, one has:

$$\int_0^\infty e^{-\xi s}\left[e^{\left(-\frac{(s-x)^2}{4\alpha t}\right)}-e^{\left(-\frac{(s+x)^2}{4\alpha t}\right)}\right]ds=\int_0^\infty e^{-\xi s}e^{\left(-\frac{(s-x)^2}{4\alpha t}\right)}ds-\int_0^\infty e^{-\xi s}e^{\left(-\frac{(s+x)^2}{4\alpha t}\right)}ds$$

$$\int_0^\infty e^{-\xi s}e^{\left(-\frac{(s-x)^2}{4\alpha t}\right)}ds=\int_0^\infty e^{\left(-\xi s-\frac{(s-x)^2}{4\alpha t}\right)}ds=\int_0^\infty e^{\left(-\frac{4\alpha t\xi s+(s-x)^2}{4\alpha t}\right)}ds$$

$$=\int_0^\infty e^{\left(-\frac{(s-x+2\alpha t\xi)^2-4\alpha^2t^2\xi^2+4\alpha\xi tx}{4\alpha t}\right)}ds=\int_0^\infty e^{\alpha t\xi^2-\xi x}e^{-\left(\frac{s-x+2\alpha t\xi}{\sqrt{4\alpha t}}\right)^2}ds$$

$$=e^{\alpha t\xi^2-\xi x}\int_0^\infty e^{-\left(\frac{s-x+2\alpha t\xi}{\sqrt{4\alpha t}}\right)^2}ds$$

Introducing a new variable, p, as $p=\frac{s-x+2\alpha t\xi}{\sqrt{4\alpha t}}$ the integral will take the form of:

$$p=\frac{s-x+2\alpha t\xi}{\sqrt{4\alpha t}}\qquad\Rightarrow\qquad dp=\frac{ds}{\sqrt{4\alpha t}}$$

$$\Rightarrow\quad e^{\alpha t\xi^2-\xi x}\int_0^\infty e^{-\left(\frac{s-x+2\alpha t\xi}{\sqrt{4\alpha t}}\right)^2}ds=\sqrt{4\alpha t}e^{\alpha t\xi^2-\xi x}\int_{\frac{2\alpha t\xi-x}{\sqrt{4\alpha t}}}^\infty e^{-p^2}dp$$

The answer to $\int_{\frac{2\alpha t\xi-x}{\sqrt{4\alpha t}}}^\infty e^{-p^2}dp$ can be found as:

$$\int_{\frac{2\alpha t\xi-x}{\sqrt{4\alpha t}}}^\infty e^{-p^2}dp=\int_0^\infty e^{-p^2}dp-\int_0^{\frac{2\alpha t\xi-x}{\sqrt{4\alpha t}}}e^{-p^2}dp=\frac{\sqrt{\pi}}{2}\left[1-\operatorname{erf}\left(\frac{2\alpha t\xi-x}{\sqrt{4\alpha t}}\right)\right]$$

$$=\frac{\sqrt{\pi}}{2}\operatorname{erfc}\left(\frac{2\alpha t\xi-x}{\sqrt{4\alpha t}}\right)$$

$$\Rightarrow\int_0^\infty e^{-\xi s}e^{\left(-\frac{(s-x)^2}{4\alpha t}\right)}ds=\sqrt{\pi\alpha t}e^{\alpha t\xi^2-\xi x}\operatorname{erfc}\left(\frac{2\alpha t\xi-x}{\sqrt{4\alpha t}}\right)$$

In finding the solution to $\int_0^\infty e^{-\xi s}e^{\left(-\frac{(s-x)^2}{4\alpha t}\right)}ds$, x was treated as a constant and no integration was taken on it. So the answer to $\int_0^\infty e^{-\xi s}e^{\left(-\frac{(s+x)^2}{4\alpha t}\right)}ds$ can be easily found by replacing x with $-x$ in the equation above:

$$\Rightarrow \int_0^{\infty} e^{-\xi s} e^{\left(-\frac{(s-x)^2}{4\alpha t}\right)} ds = \sqrt{\pi\alpha t}\, e^{\alpha t \xi^2 + \xi x} \operatorname{erfc}\left(\frac{2\alpha t\xi + x}{\sqrt{4\alpha t}}\right)$$

The solution to the second term can also be found using a similar approach. In this case, one can assume that $\xi = 0$ and use the solutions developed for the first part

$$\int_0^{\infty} \left[e^{\left(-\frac{(s-x)^2}{4\alpha t}\right)} - e^{\left(-\frac{(s+x)^2}{4\alpha t}\right)}\right] ds = \sqrt{\pi\alpha t}\left[\operatorname{erfc}\left(\frac{-x}{\sqrt{4\alpha t}}\right) - \operatorname{erfc}\left(\frac{x}{\sqrt{4\alpha t}}\right)\right]$$

$$= \sqrt{\pi\alpha t}\left[1 - \operatorname{erf}\left(\frac{-x}{\sqrt{4\alpha t}}\right) - 1 + \operatorname{erf}\left(\frac{x}{\sqrt{4\alpha t}}\right)\right]$$

The error function is an odd function. Therefore, $\operatorname{erf}\left(\frac{-x}{\sqrt{4\alpha t}}\right) = -\operatorname{erf}\left(\frac{x}{\sqrt{4\alpha t}}\right)$ and:

$$\int_0^{\infty} \left[e^{\left(-\frac{(s-x)^2}{4\alpha t}\right)} - e^{\left(-\frac{(s+x)^2}{4\alpha t}\right)}\right] ds = \sqrt{\pi\alpha t}\left[\operatorname{erf}\left(\frac{x}{\sqrt{4\alpha t}}\right) + \operatorname{erf}\left(\frac{x}{\sqrt{4\alpha t}}\right)\right] = 2\sqrt{\pi\alpha t}\operatorname{erf}\left(\frac{x}{\sqrt{4\alpha t}}\right)$$

So the solution can be obtained as:

$$w(x,t) = \frac{1}{\sqrt{4\pi\alpha t}}\left[\sqrt{\pi\alpha t}\, e^{\alpha t\xi^2 - \xi x}\operatorname{erfc}\left(\frac{2\alpha t\xi - x}{\sqrt{4\alpha t}}\right) - \sqrt{\pi\alpha t}\, e^{\alpha t\xi^2 + \xi x}\operatorname{erfc}\left(\frac{2\alpha t\xi + x}{\sqrt{4\alpha t}}\right)\right.$$
$$\left. - 2\sqrt{\pi\alpha t}\operatorname{erf}\left(\frac{x}{\sqrt{4\alpha t}}\right)\right]$$

$$\Rightarrow w(x,t) = \frac{1}{2} e^{\alpha t\xi^2}\left[e^{-\xi x}\operatorname{erfc}\left(\frac{2\alpha t\xi - x}{\sqrt{4\alpha t}}\right) - e^{\xi x}\operatorname{erfc}\left(\frac{2\alpha t\xi + x}{\sqrt{4\alpha t}}\right)\right] - \operatorname{erf}\left(\frac{x}{\sqrt{4\alpha t}}\right)$$

And the solution to the original initial boundary value problem will be:

$$T^*(z,t) = w(z,t) + 1 \qquad \Rightarrow$$

$$T^*(z,t) = \frac{1}{2} e^{\alpha t\xi^2}\left[e^{-\xi x}\operatorname{erfc}\left(\frac{2\alpha t\xi - x}{\sqrt{4\alpha t}}\right) - e^{\xi x}\operatorname{erfc}\left(\frac{2\alpha t\xi + x}{\sqrt{4\alpha t}}\right)\right] - \operatorname{erf}\left(\frac{x}{\sqrt{4\alpha t}}\right) + 1$$

$$= \frac{1}{2} e^{\alpha t\xi^2}\left[e^{-\xi x}\operatorname{erfc}\left(\frac{2\alpha t\xi - x}{\sqrt{4\alpha t}}\right) - e^{\xi x}\operatorname{erfc}\left(\frac{2\alpha t\xi + x}{\sqrt{4\alpha t}}\right)\right] + \operatorname{erf c}\left(\frac{x}{\sqrt{4\alpha t}}\right)$$

In this equation $\xi = \frac{U}{\alpha}$. So the final closed solution is:

$$T^*(z,t) = \frac{1}{2} e^{\frac{U^2}{\alpha}t}\left[e^{-\frac{U}{\alpha}x}\operatorname{erfc}\left(\frac{2Ut - x}{\sqrt{4\alpha t}}\right) - e^{\frac{U}{\alpha}x}\operatorname{erfc}\left(\frac{2Ut + x}{\sqrt{4\alpha t}}\right)\right] + \operatorname{erf c}\left(\frac{x}{\sqrt{4\alpha t}}\right)$$

Appendix II: Calculation of Thermal Diffusivity from 2D Conductive Models

Temperature Profiles along the monitoring lines are shown below.

Case 1: Fixed hot interface

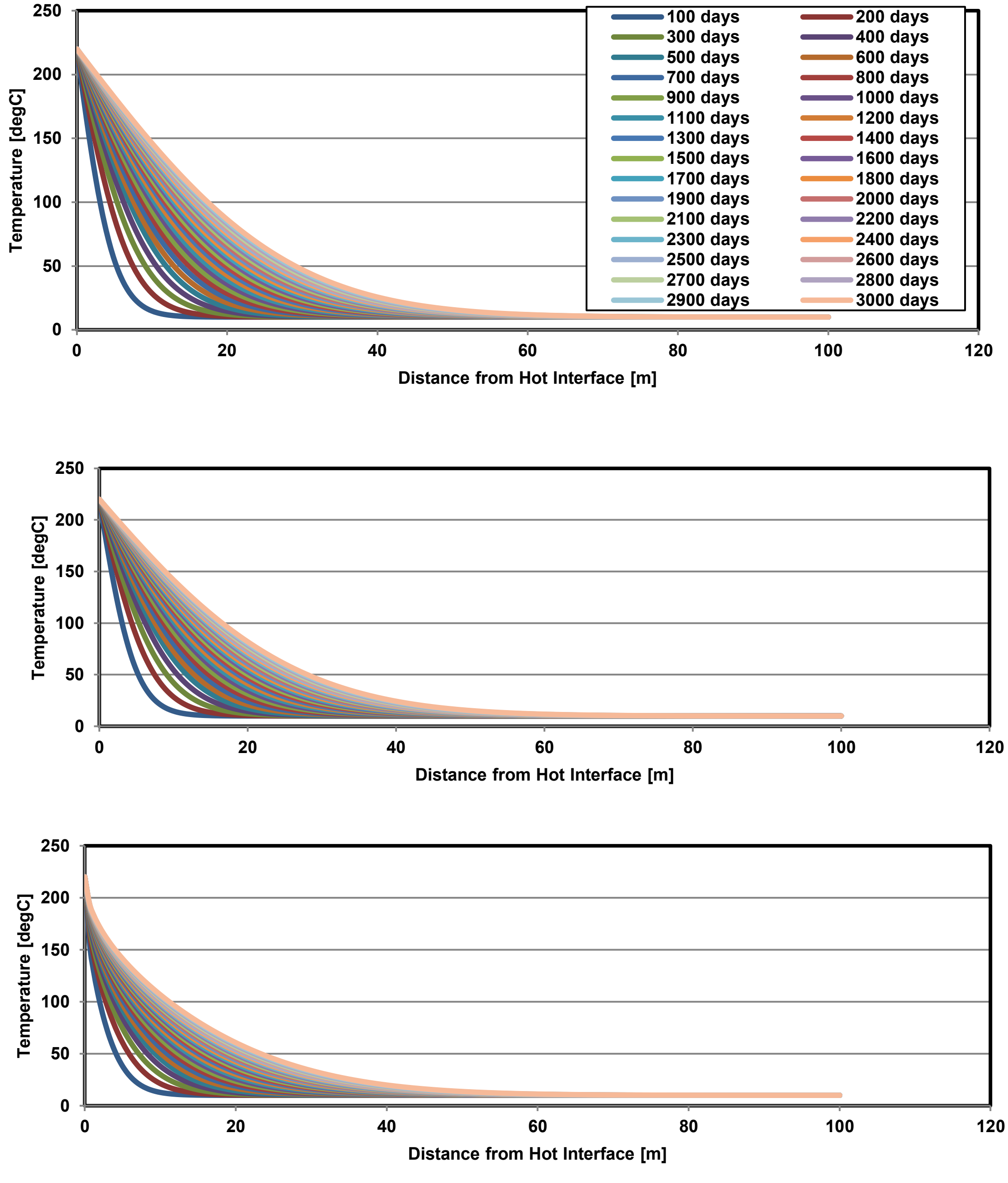

Temperature profiles. (a) center line. (b) midway between center line and edge. (c) edge of the hot interface.

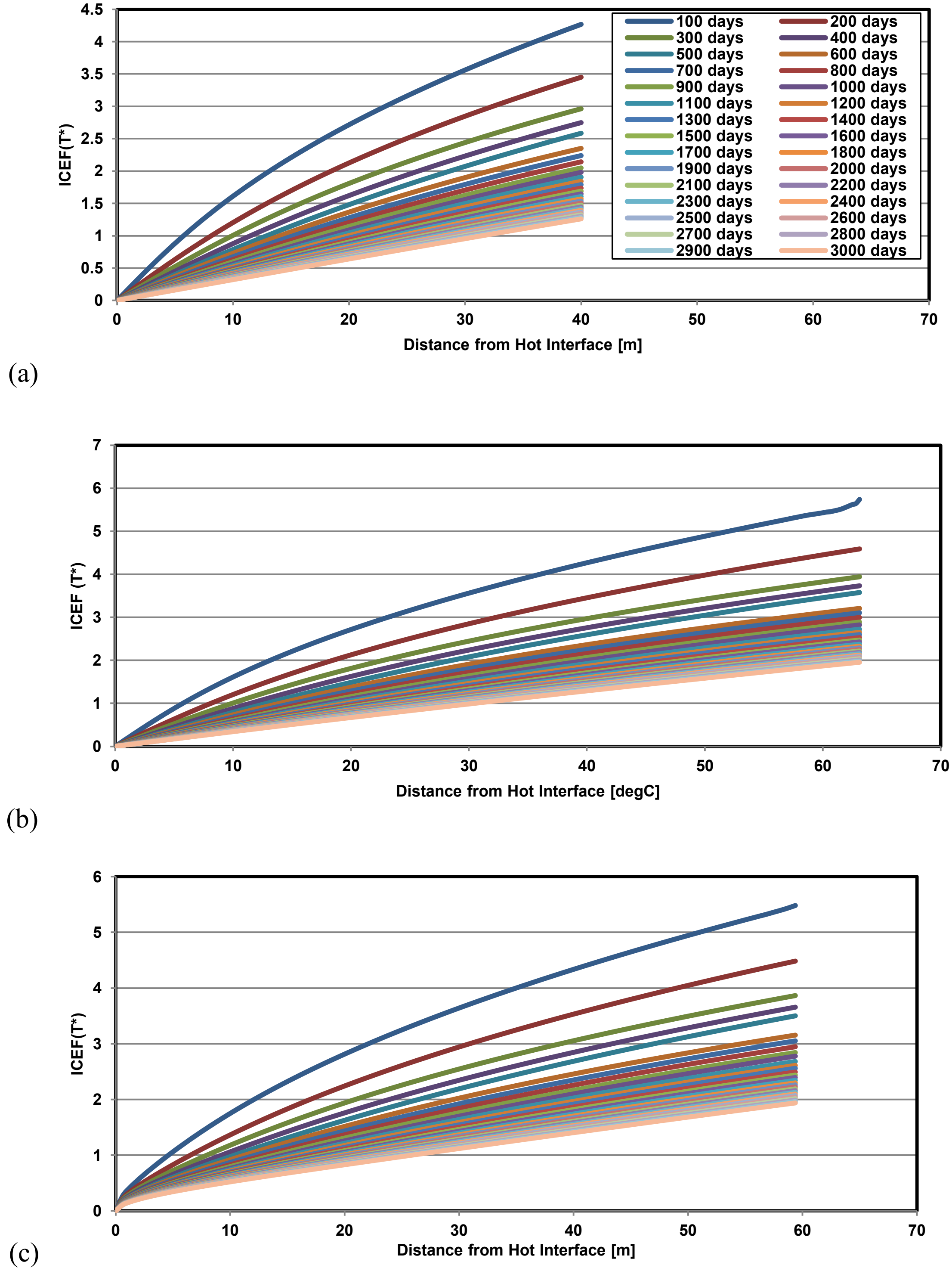

ICEF Plots. (a) center line. (b) midway between center line and edge. (c) edge of the hot interface.

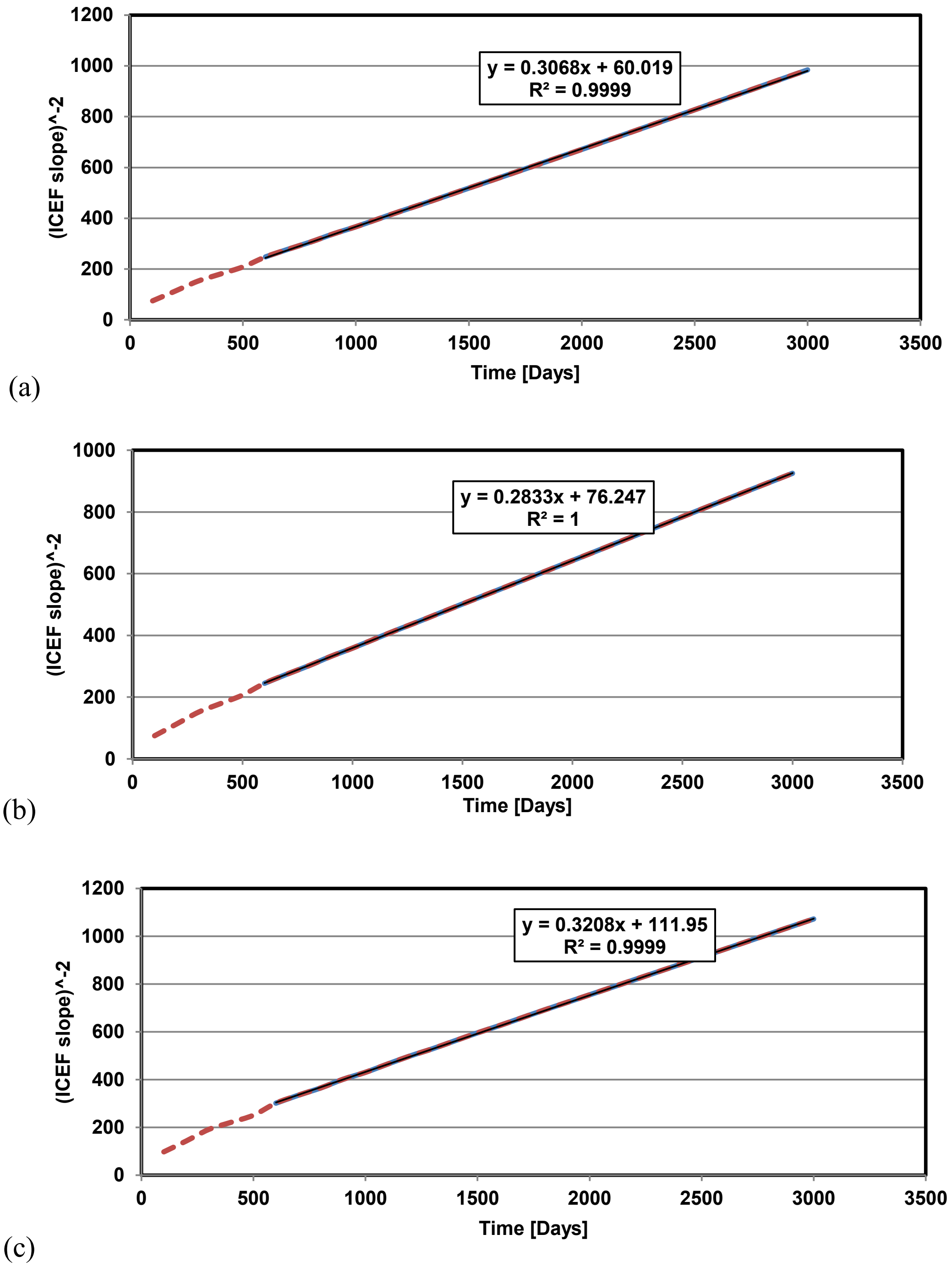

Thermal diffusivity. (a) center line. (b) midway between center line and edge. (c) edge of the hot interface.

Case 2: Spreading hot interface

In the following graphs, the slopes of ICEF plots were obtained from the linear part. Therefore, the first 5m of data on the ICEF plot were not used.

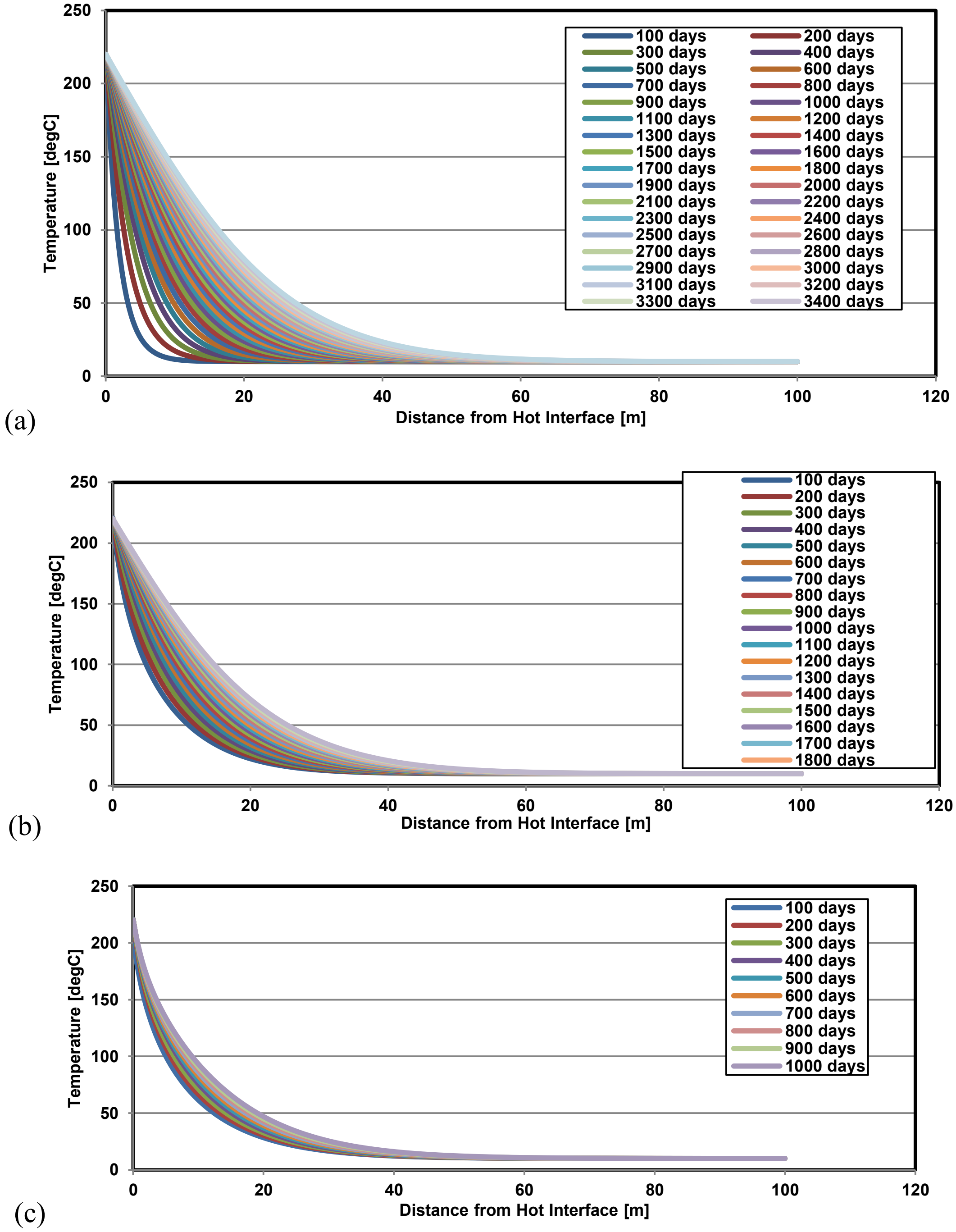

Temperature profiles. (a) center line. (b) midway between center line and edge. (c) edge of the hot interface.

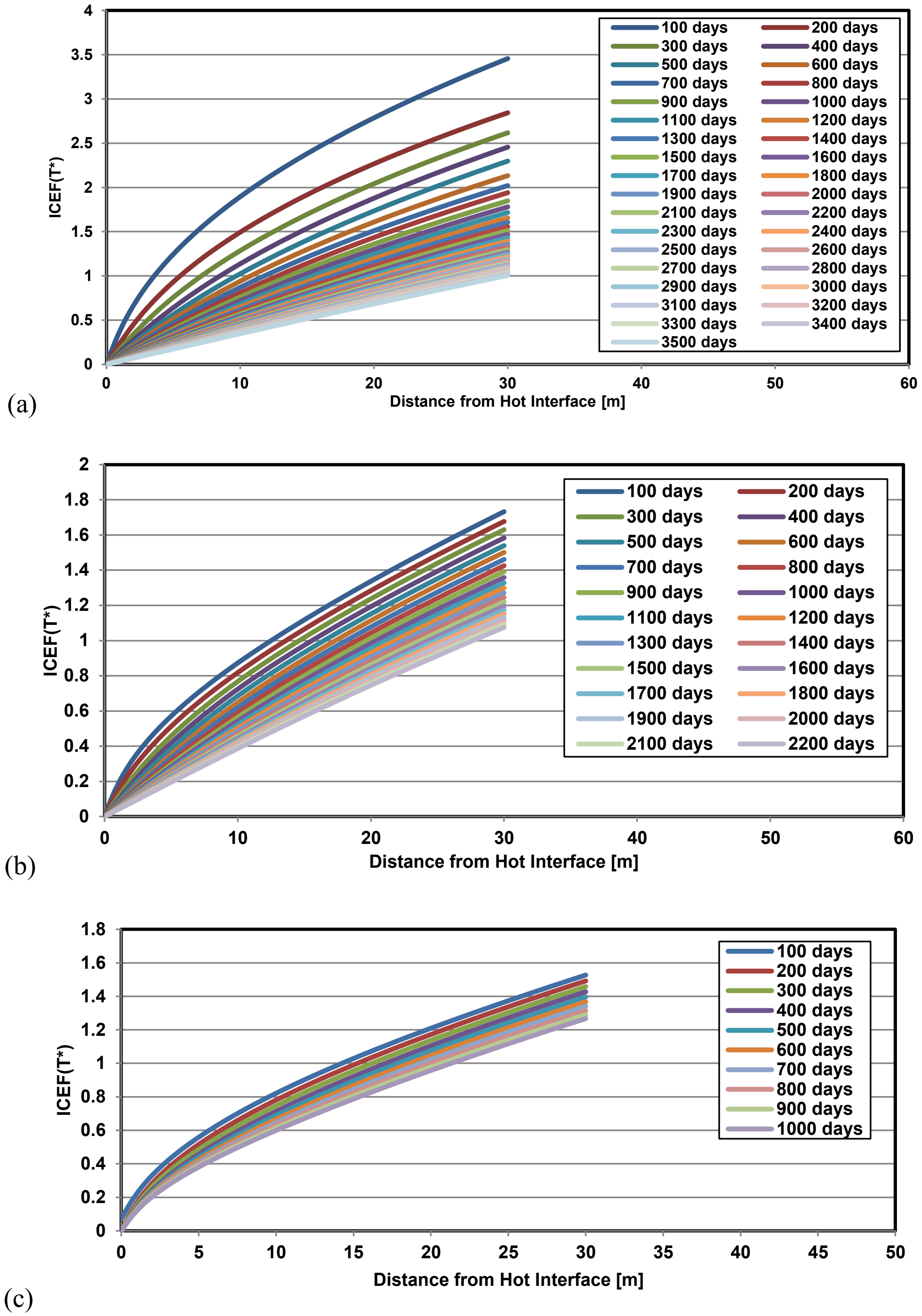

ICEF plots. (a) center line. (b) midway between center line and edge. (c) edge of the hot interface.

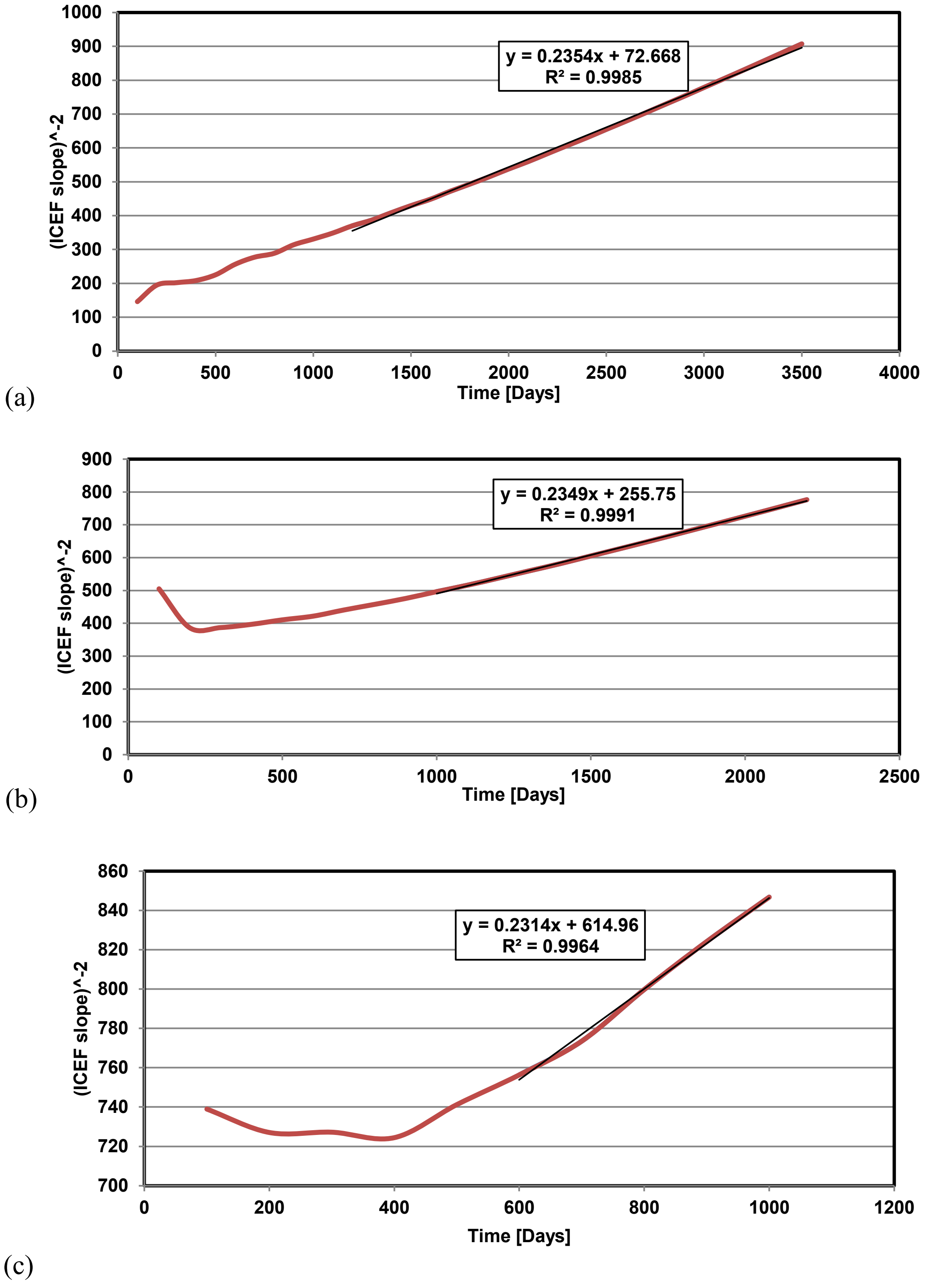

Thermal diffusivity. (a) center line. (b) midway between center line and edge. (c) edge of the hot interface.

Case 3: Spreading steam chambers with pure conduction

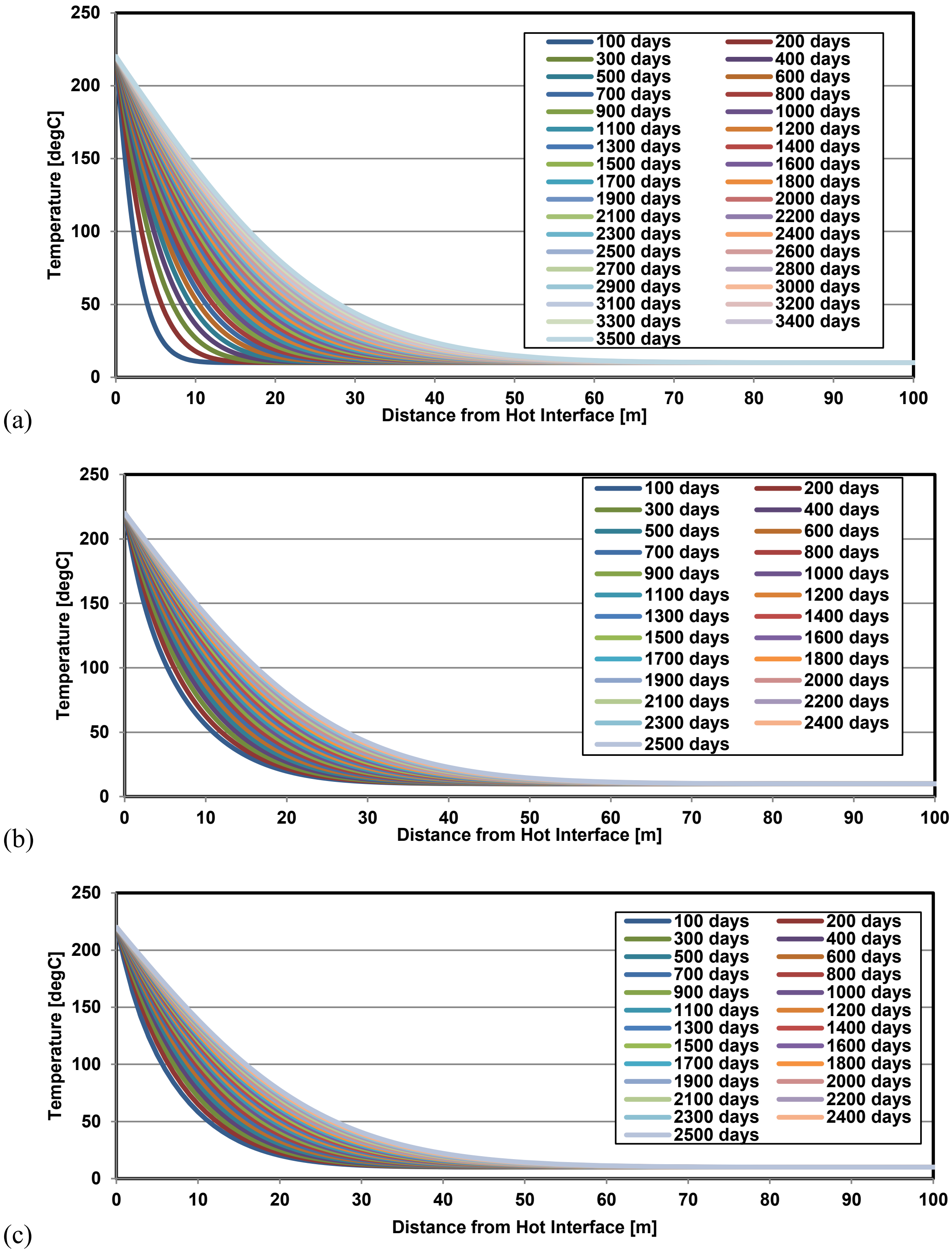

Temperature profiles. (a) L_1 . (b) L_2 . (c) L_3.

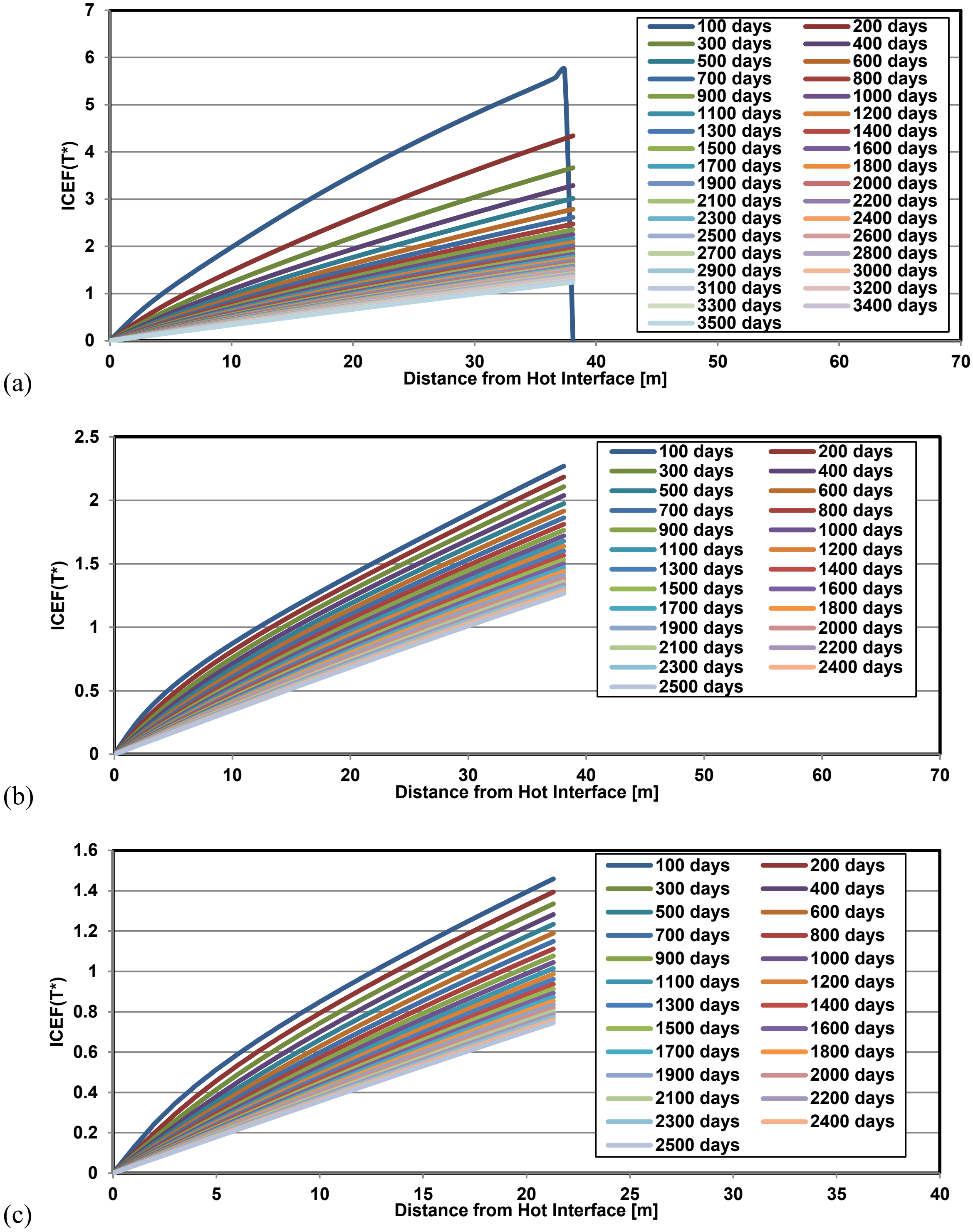

ICEF plots: (a) L_1 . (b) L_2 . (c) L_3.

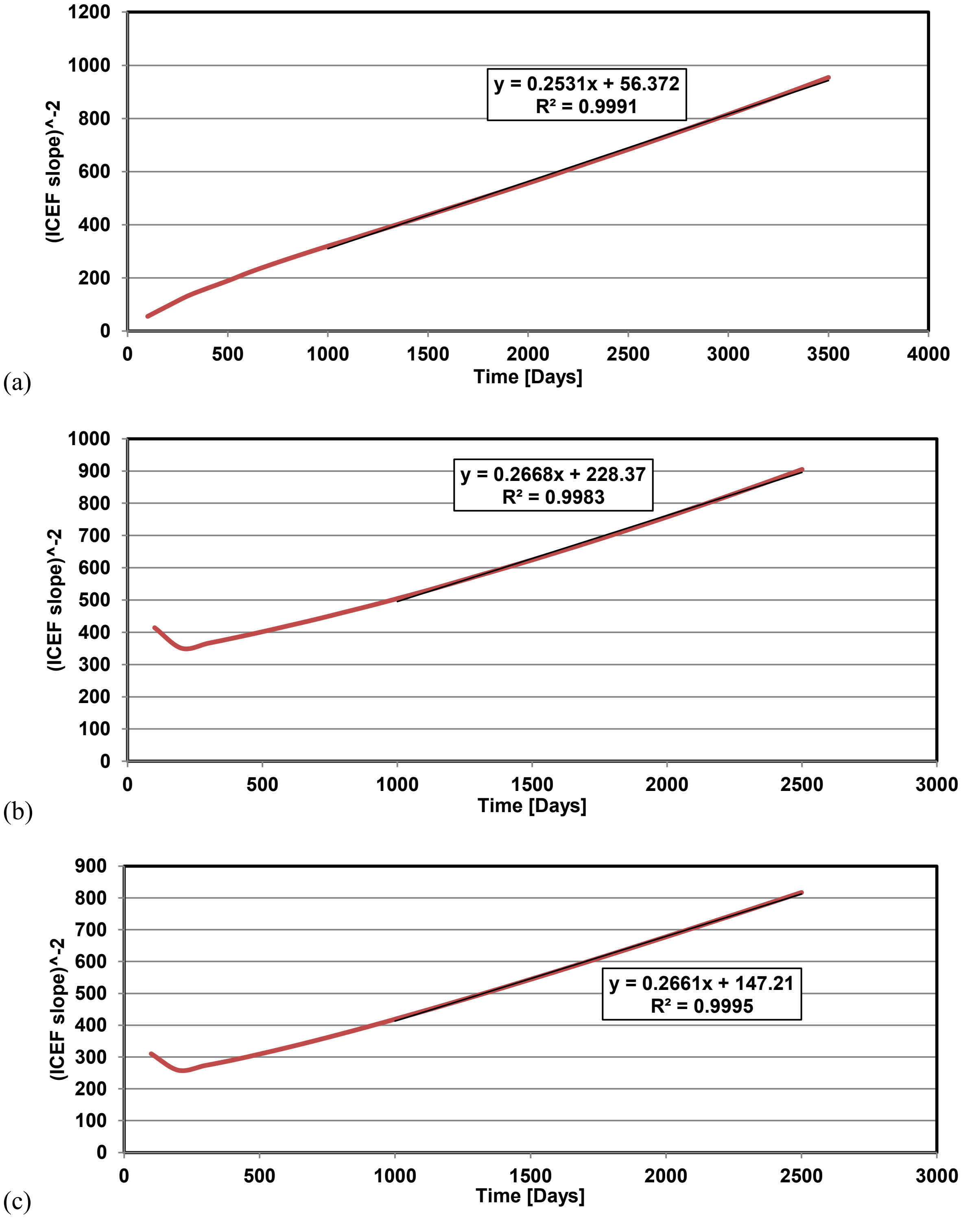

Thermal Diffusivity: (a) L_1 . (b) L_2 . (c) L_3.

Case 4: Spreading steam chambers with conduction and convection

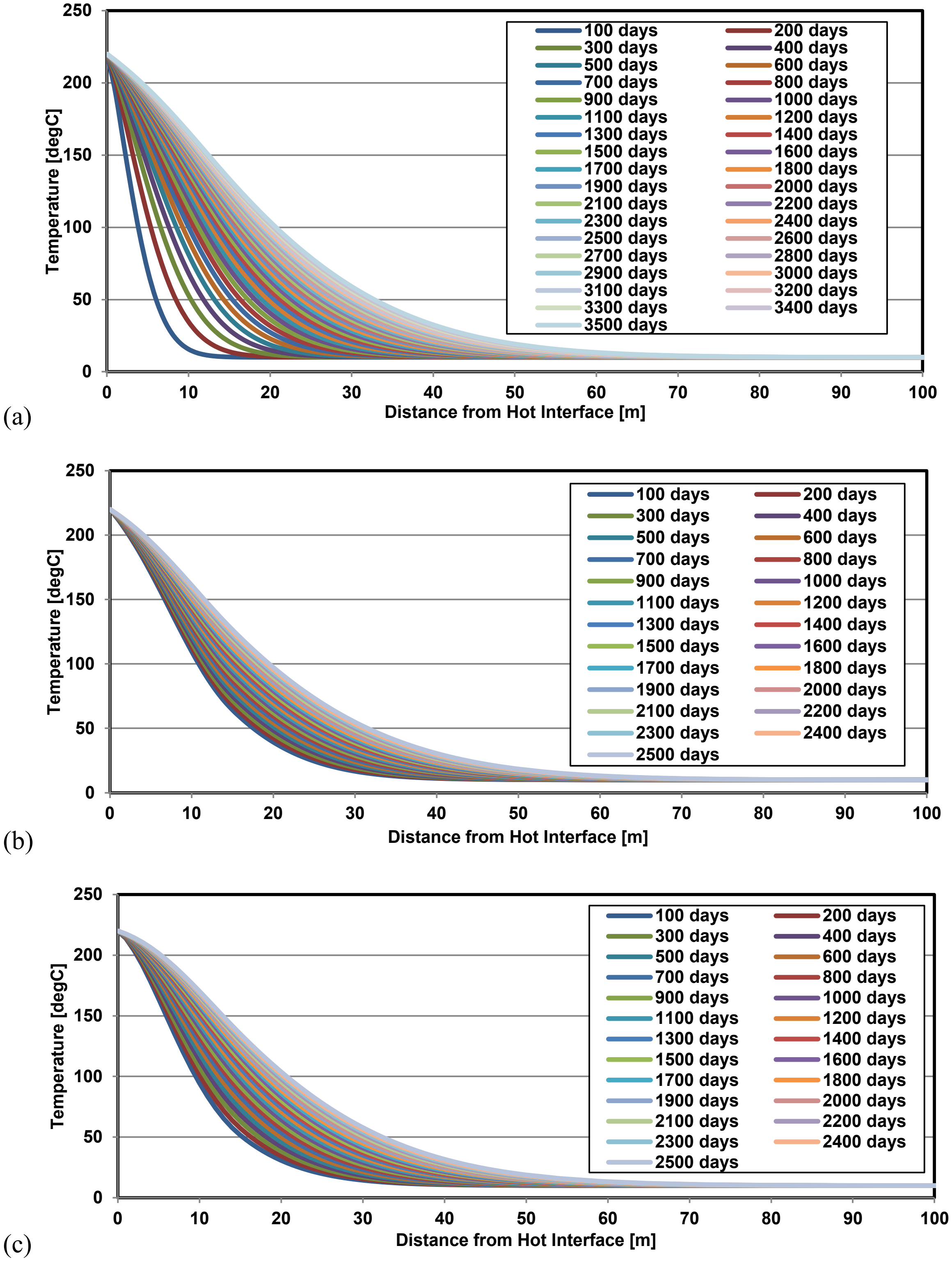

Temperature Profiles: (a) L_1 . (b) L_2 . (c) L_3.

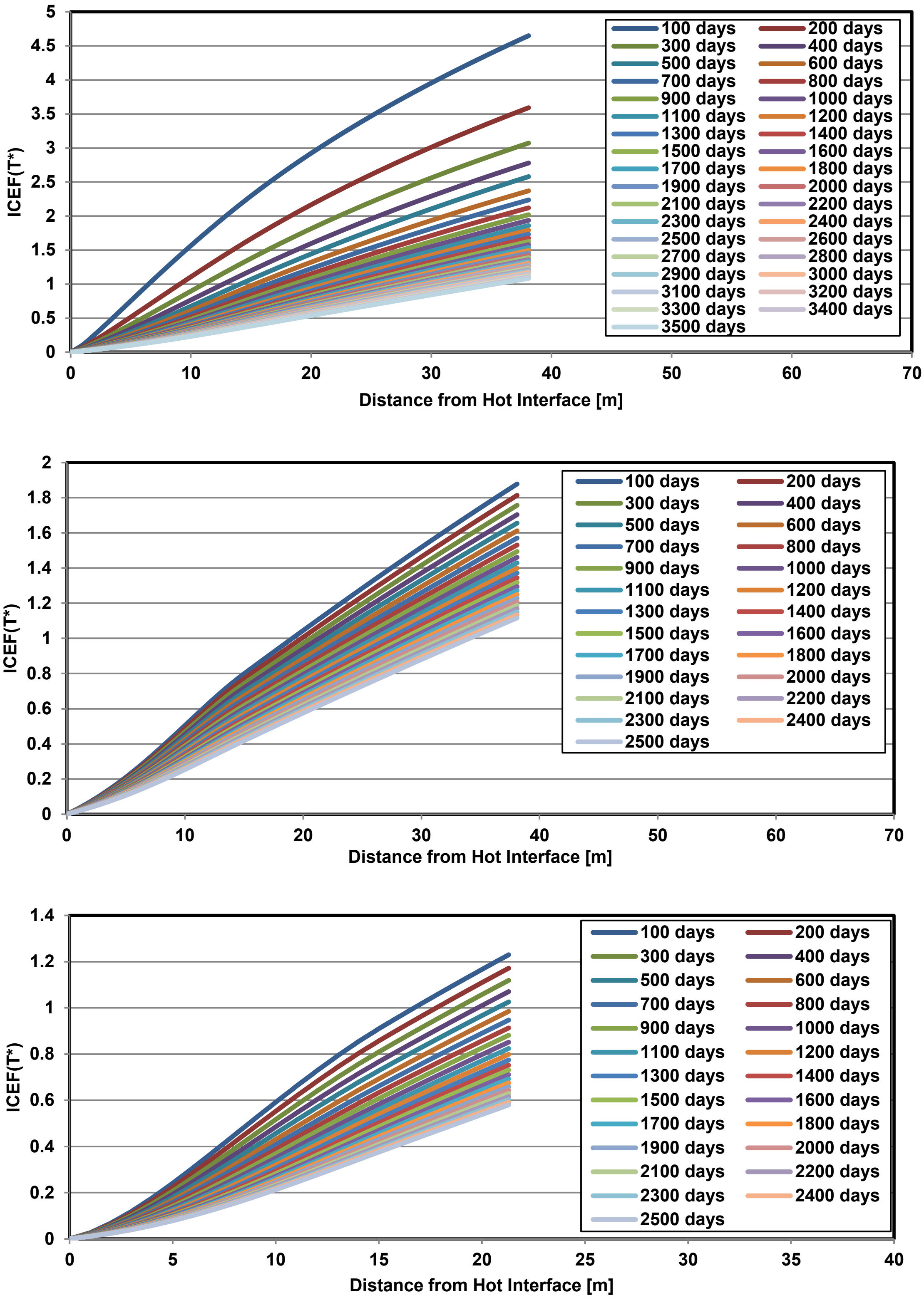

ICEF plots: (a) L_1 . (b) L_2 . (c) L_3.

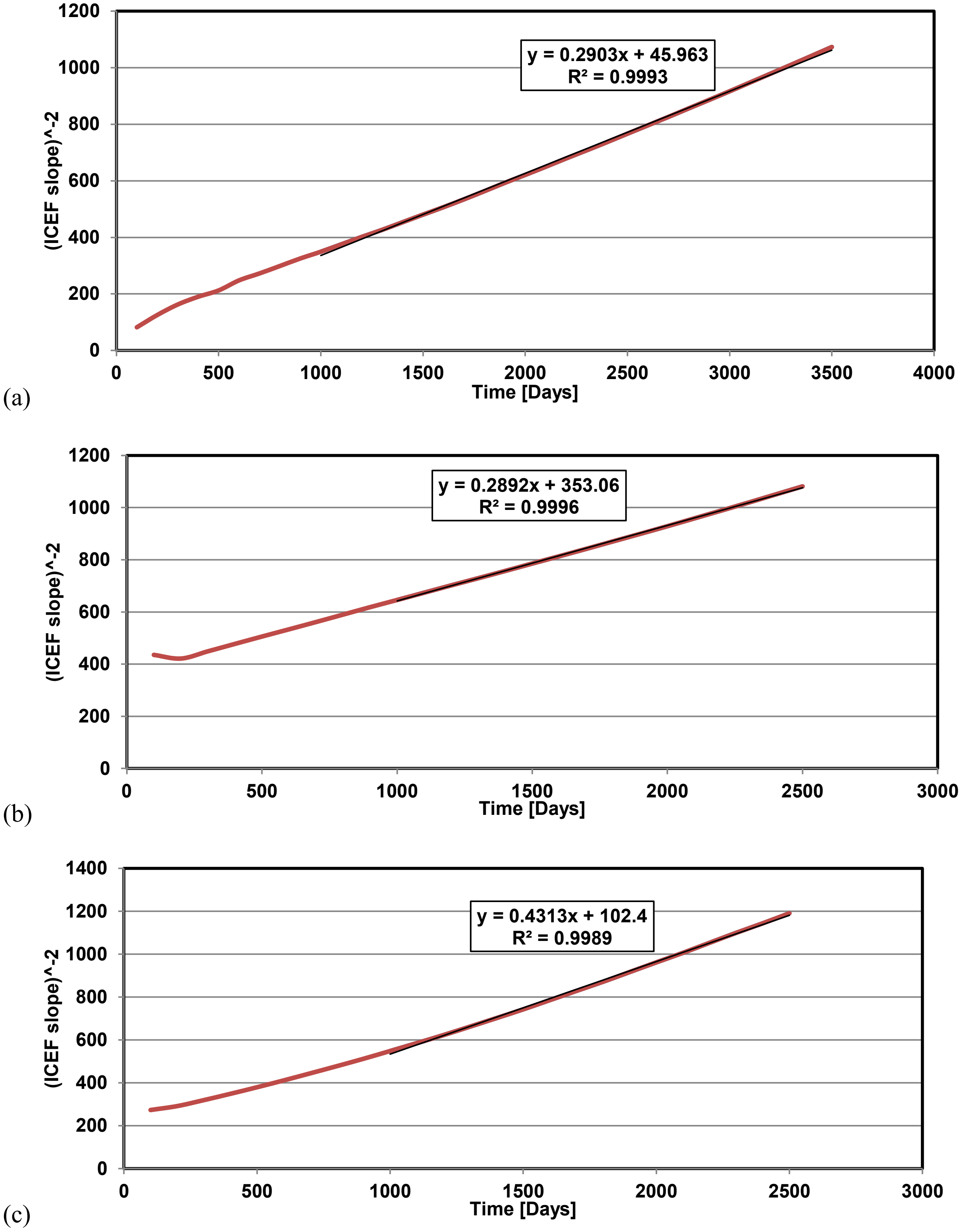

Thermal Diffusivity: (a) L_1 . (b) L_2 . (c) L_3.

Appendix III: Observation Well Data Analyses

OB 105/09-01-095-06W4/00

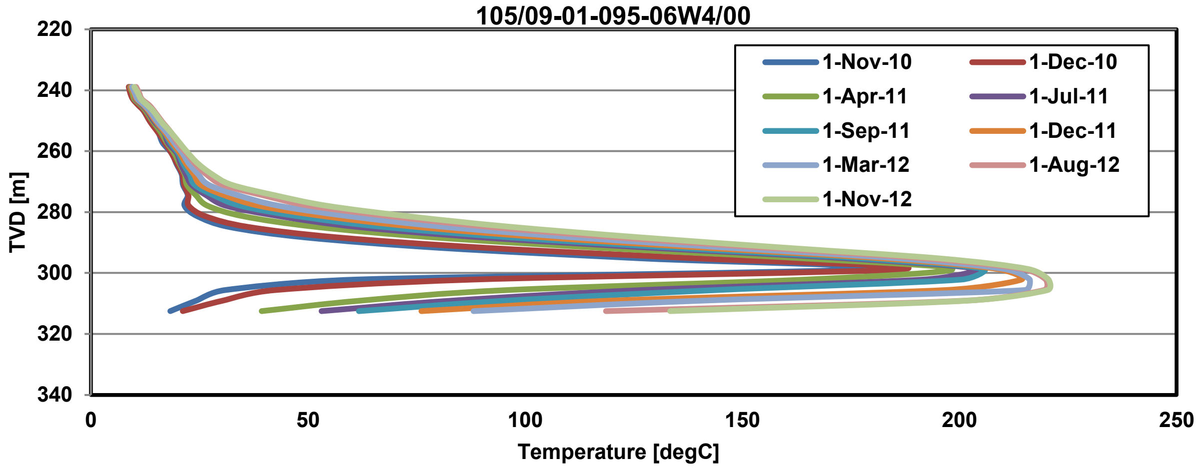

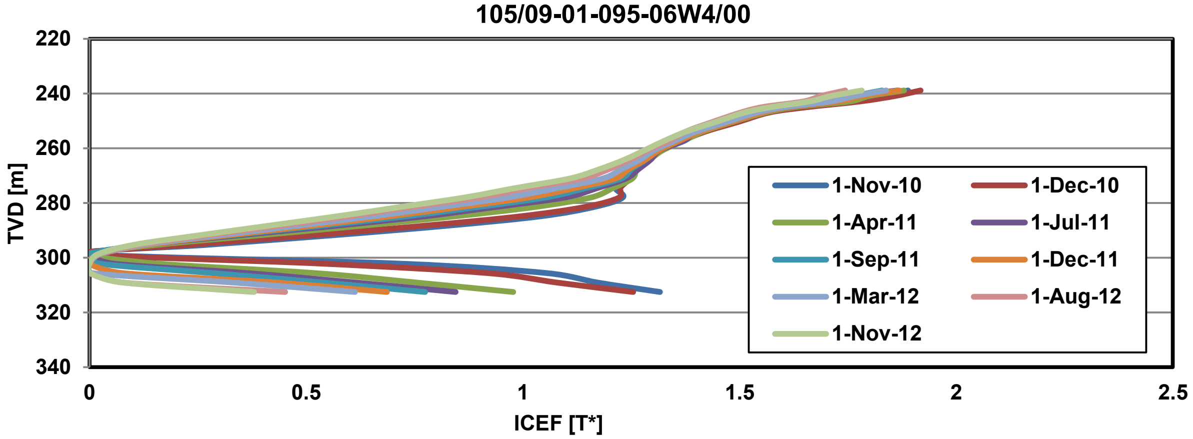

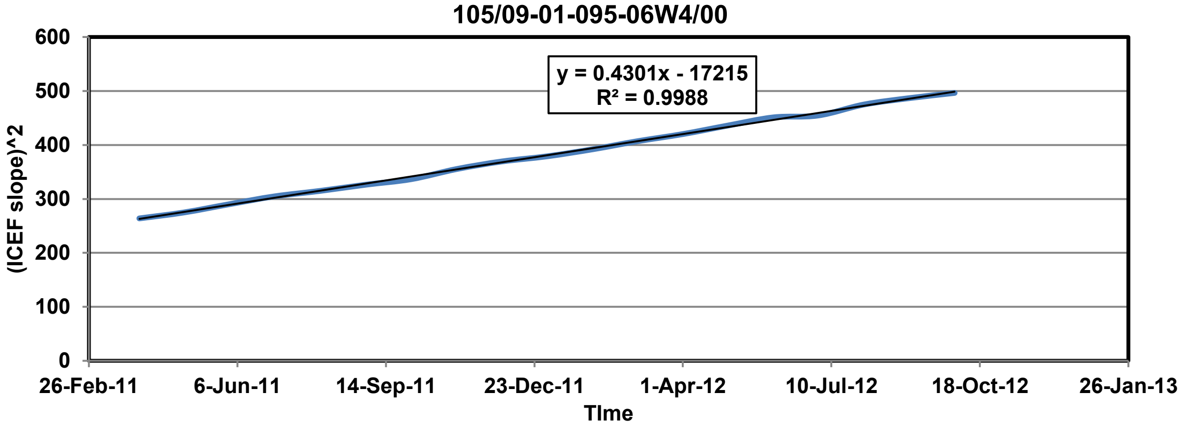

OB 102/15-12-095-06W4/00

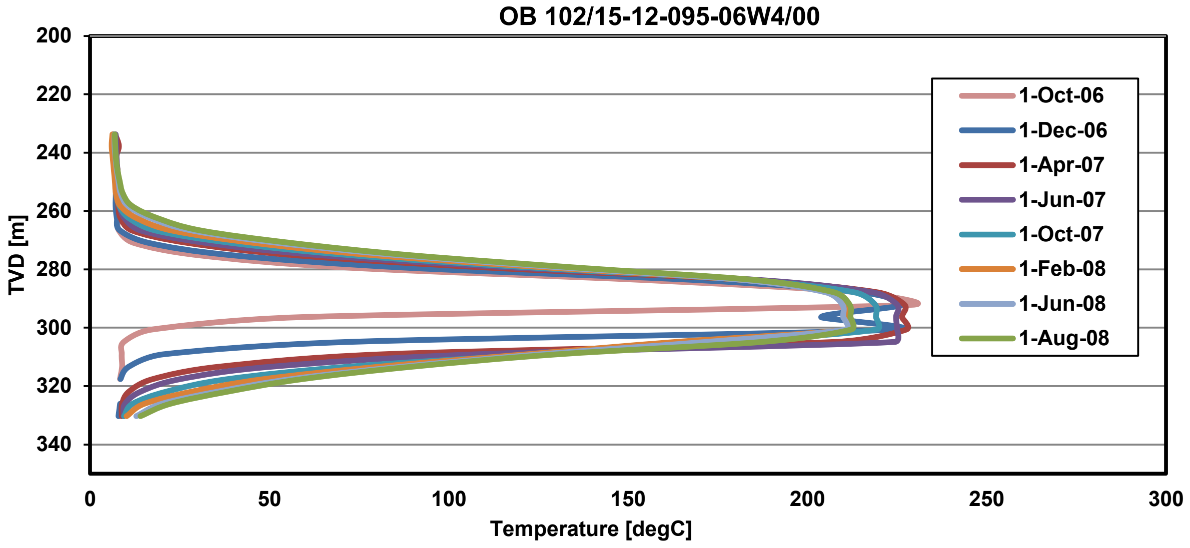

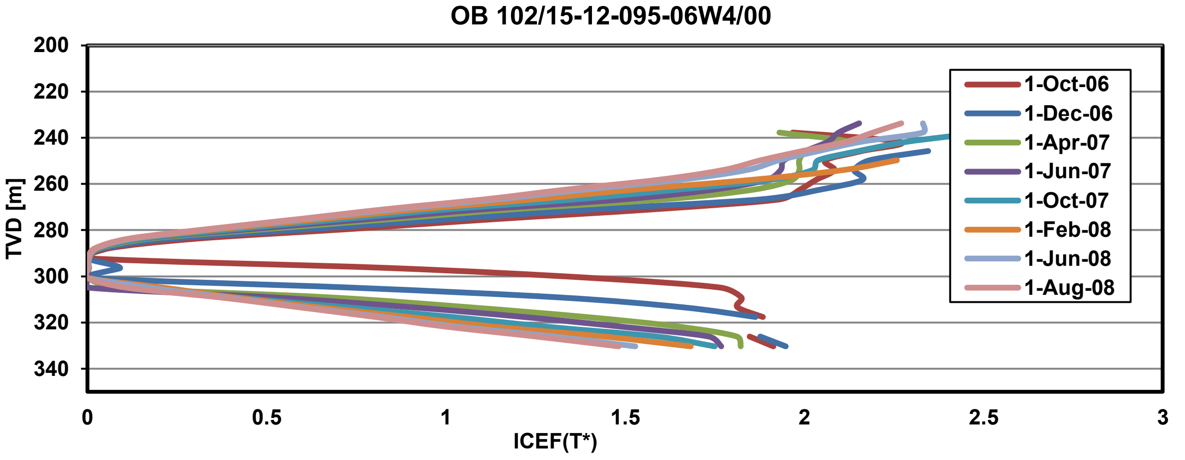

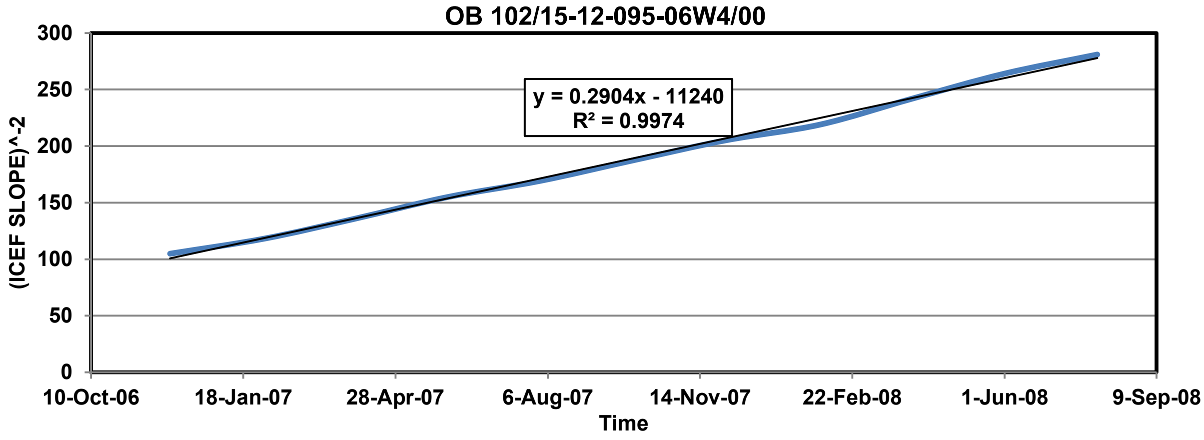

100-05-02-095-06W4/00

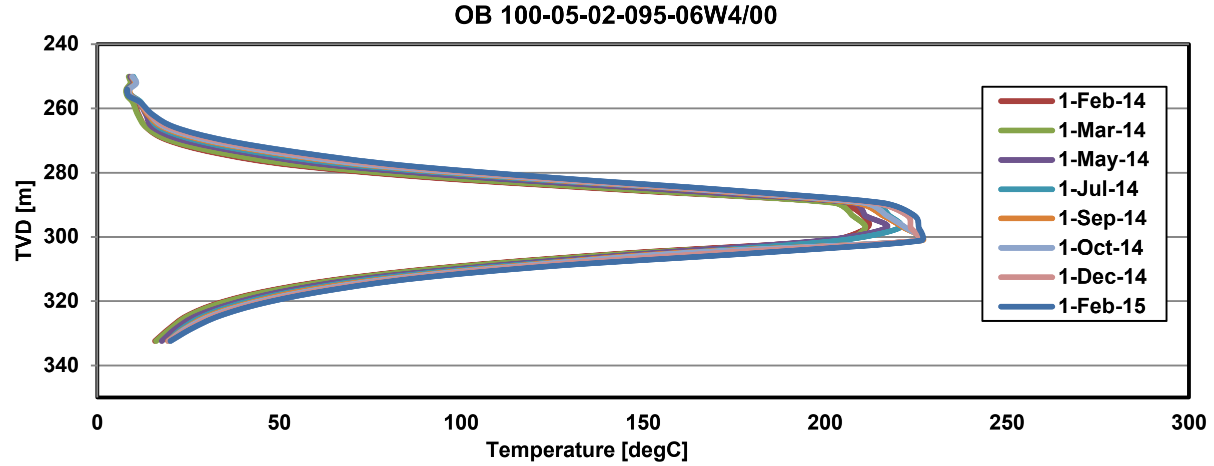

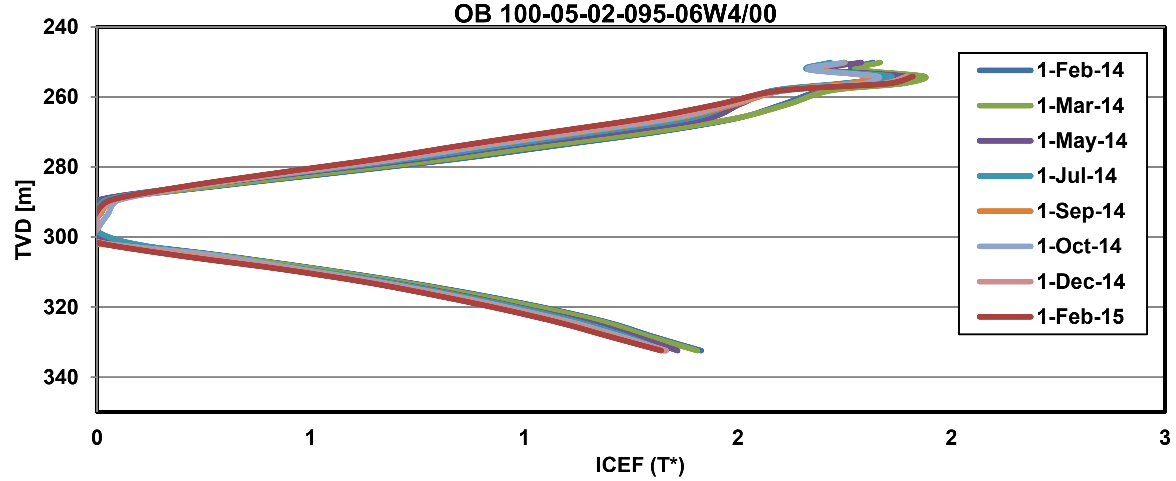

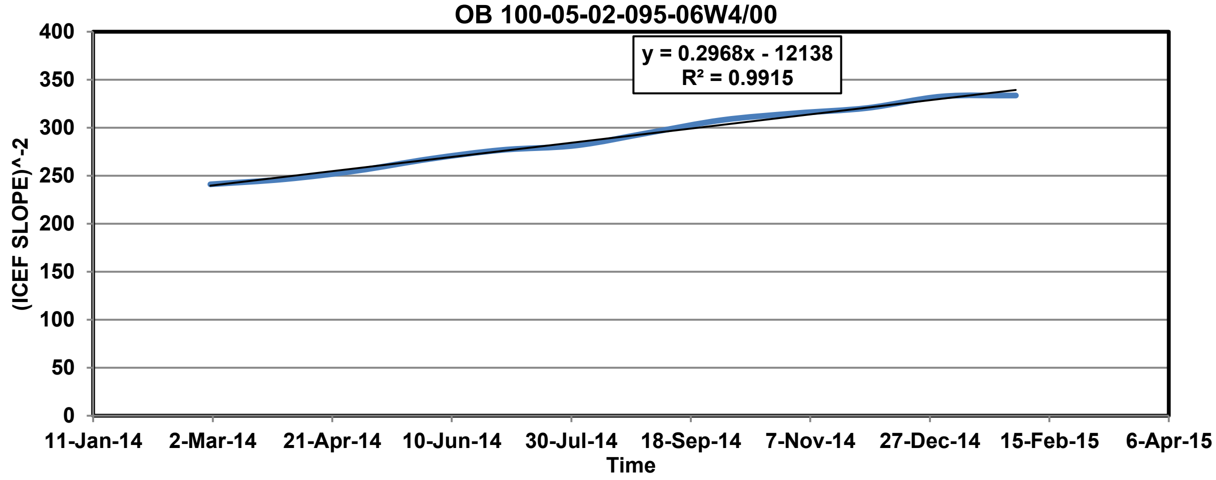

OB 100/05-11-095-06W4/00

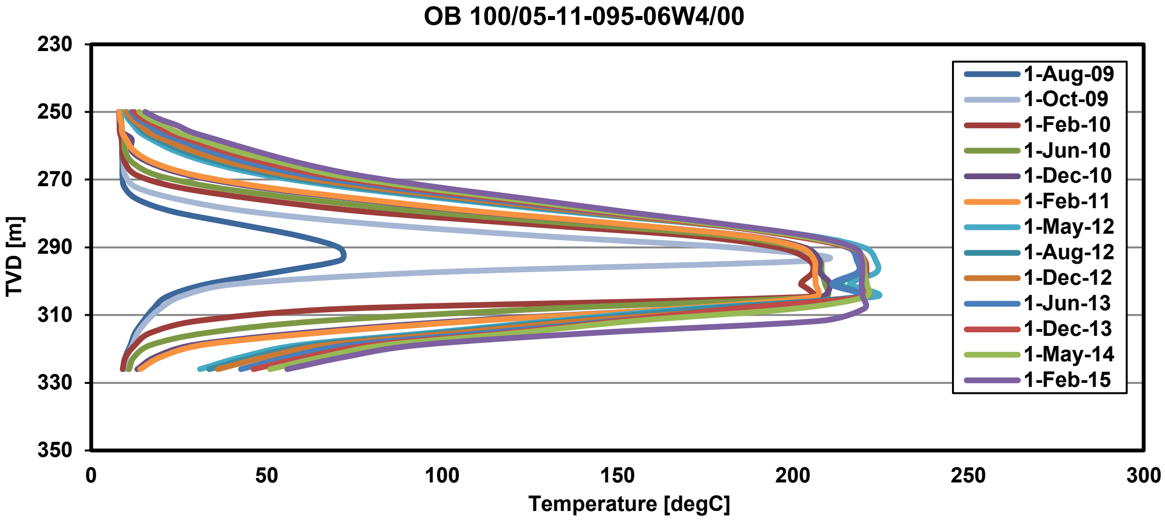

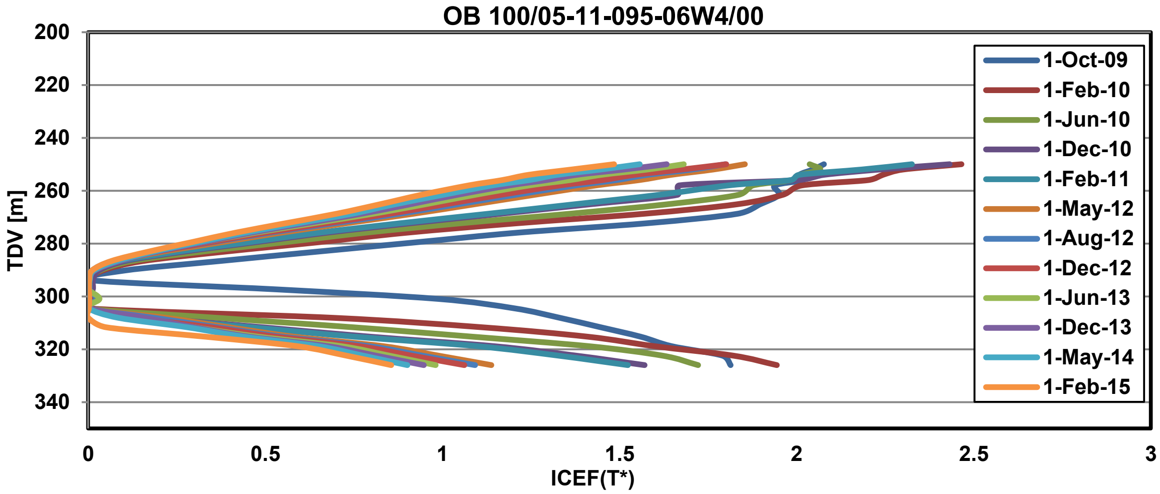

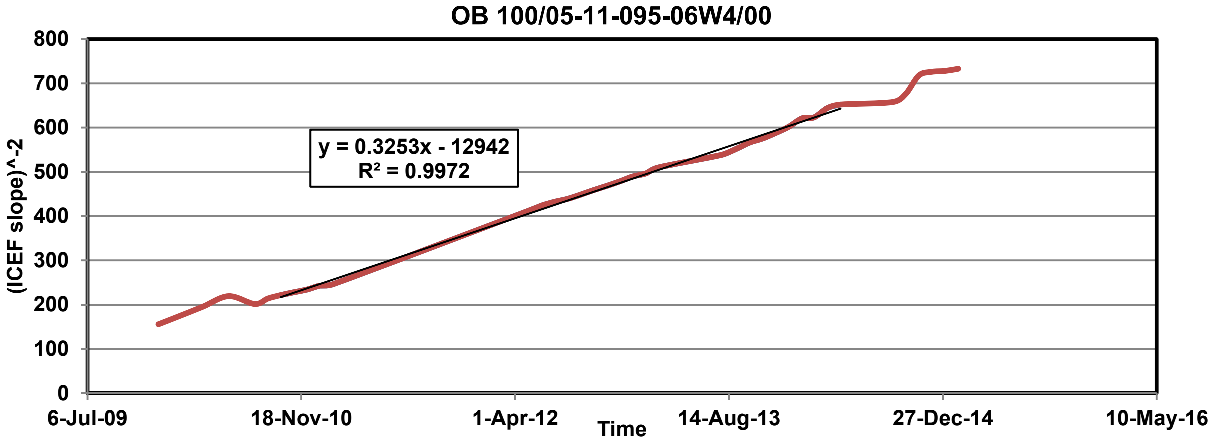

OB 104/14-02-095-06W4/00

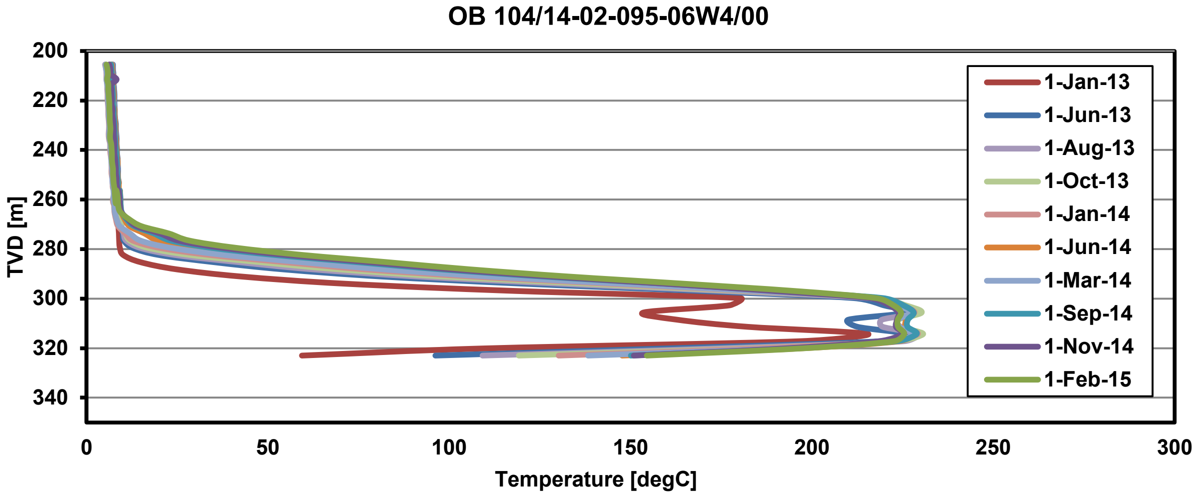

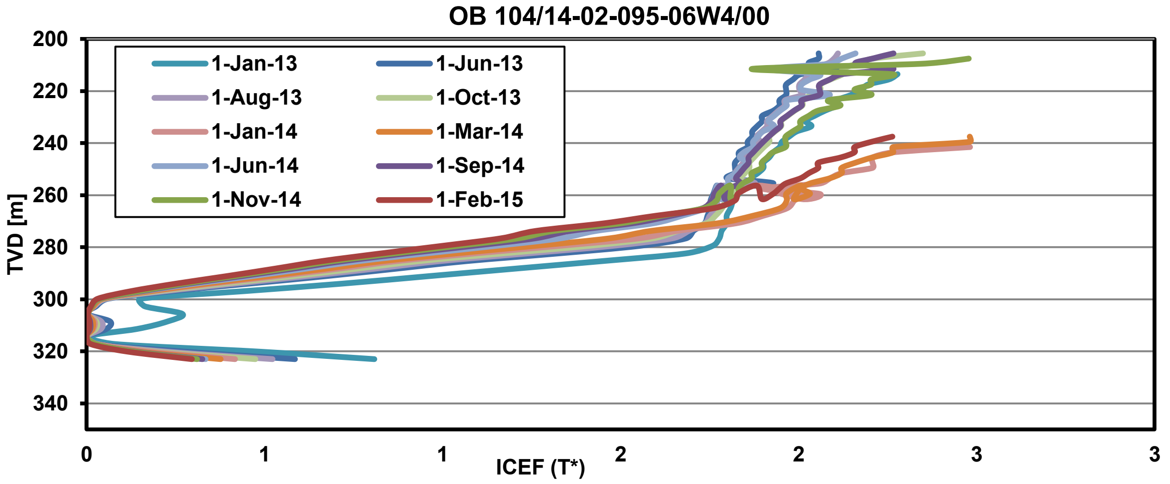

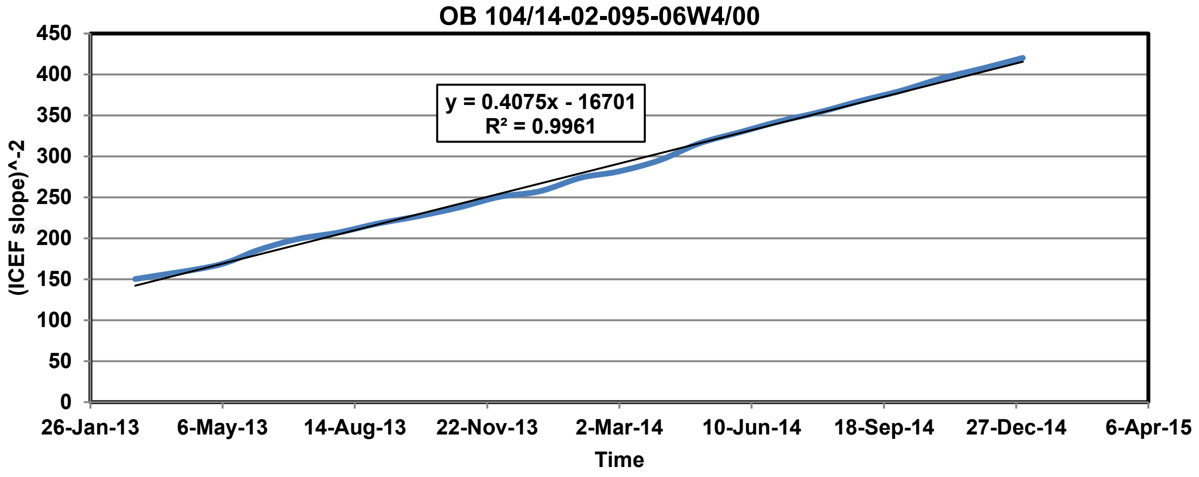

OB 100/02-02-095-06W4/00

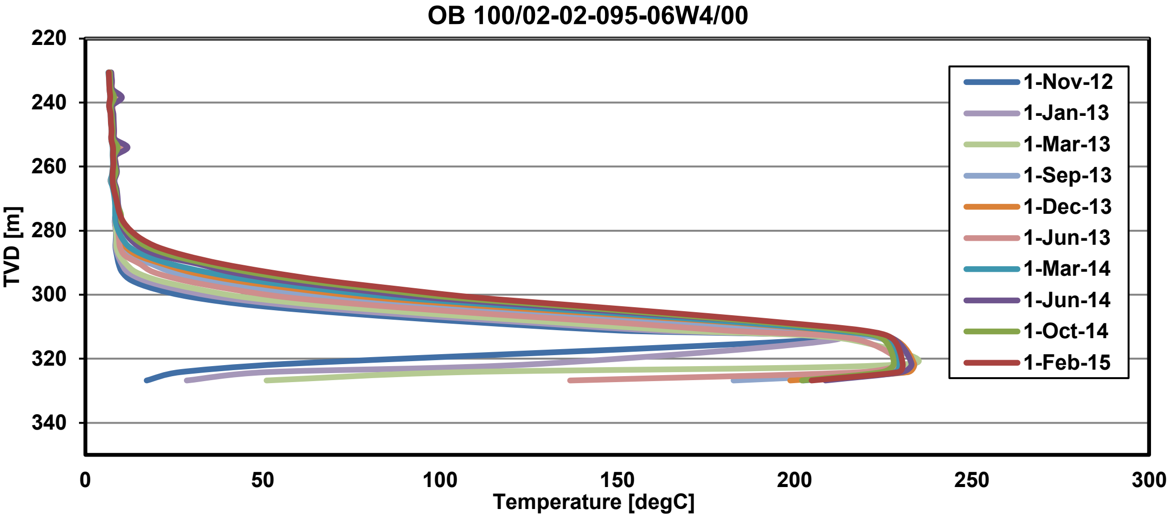

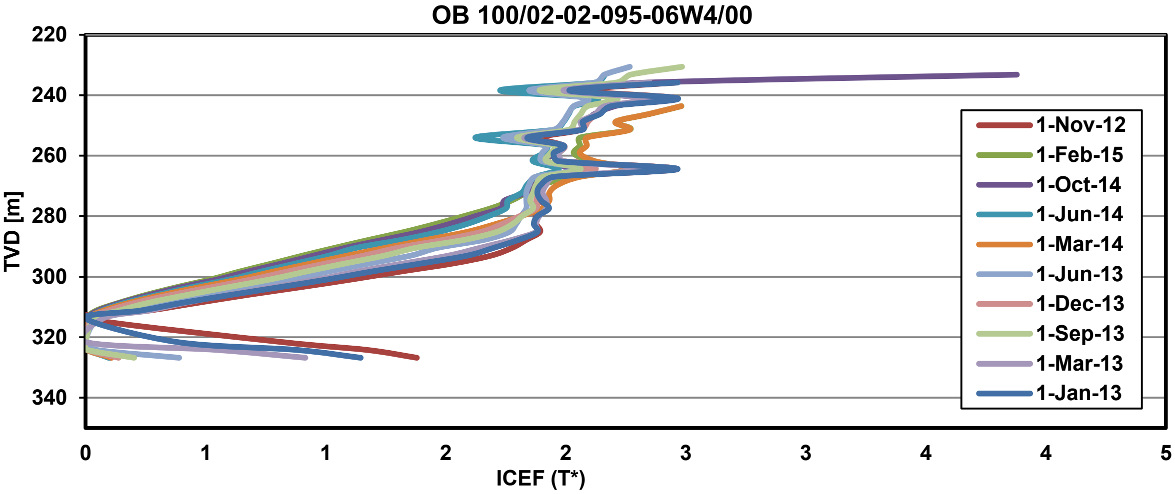

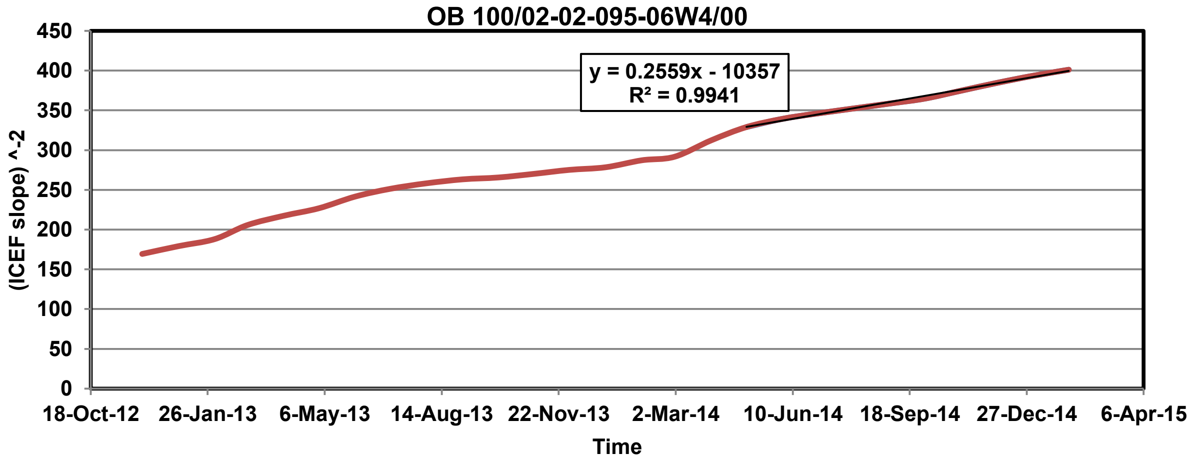

OB 103/08-01-095-06W4/00

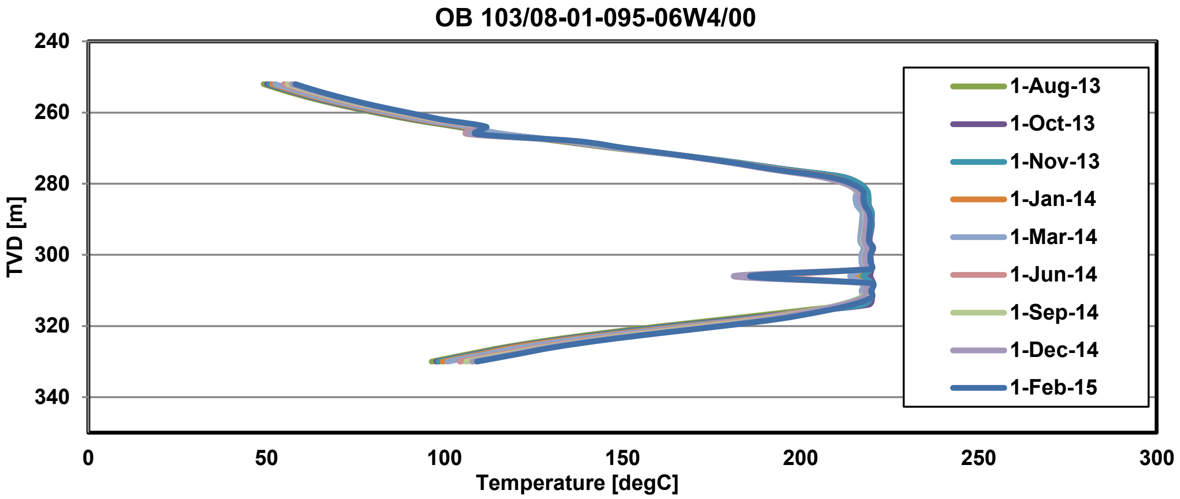

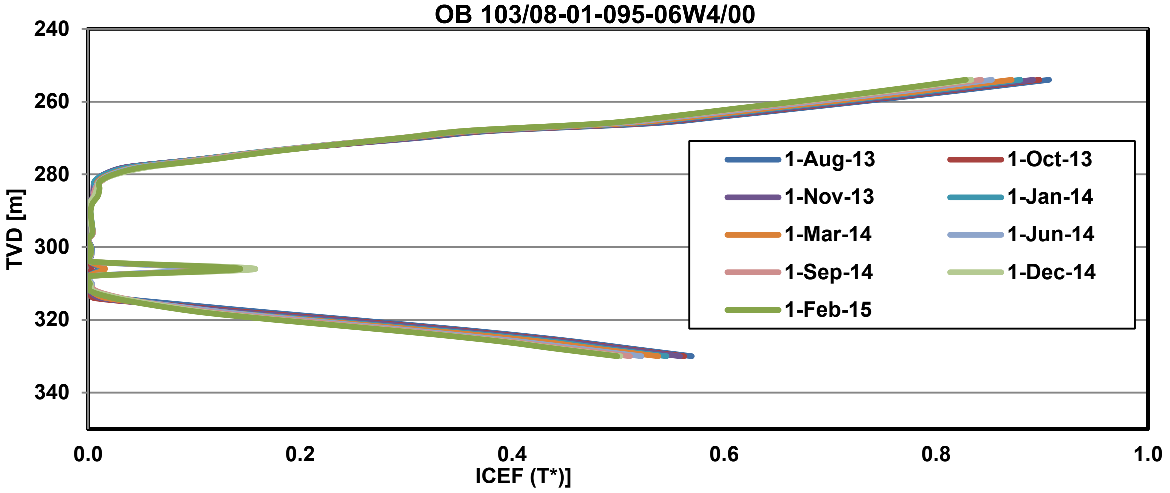

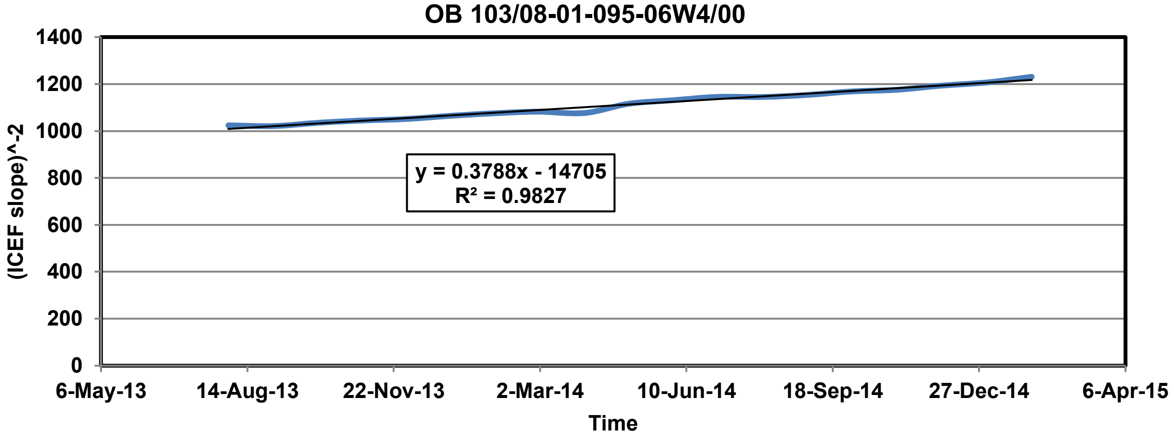

OB 109/14-36-094-06W4/00

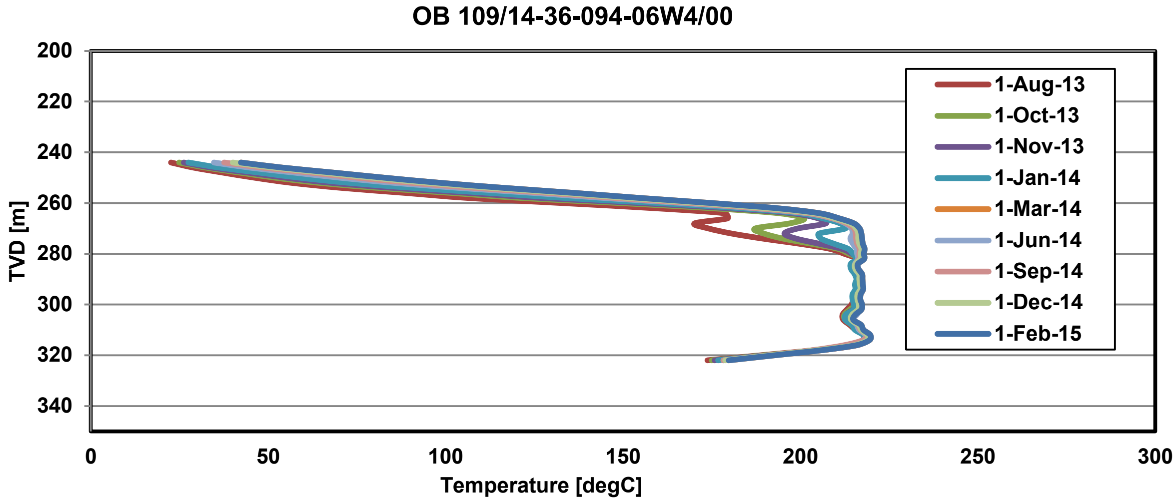

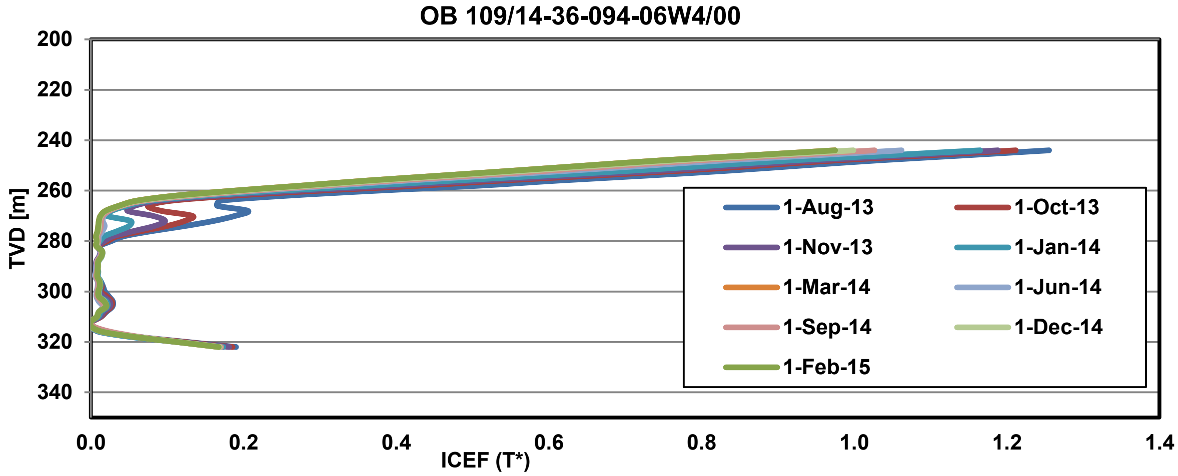

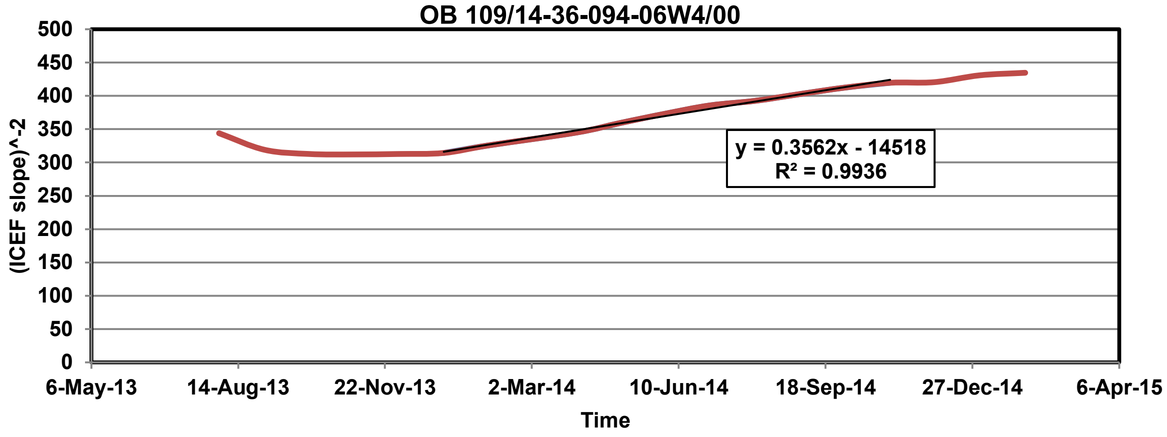

OB 100/02-14-076-06W4/00

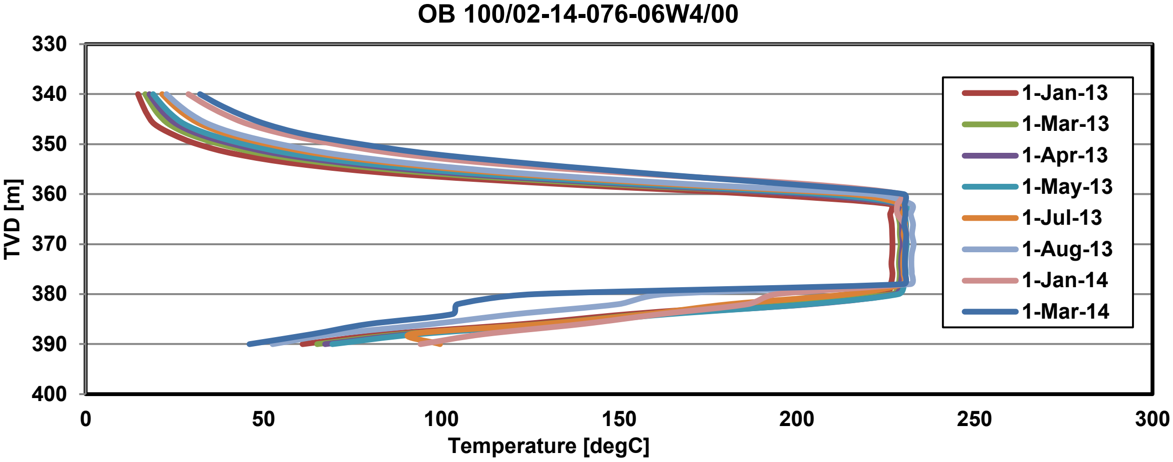

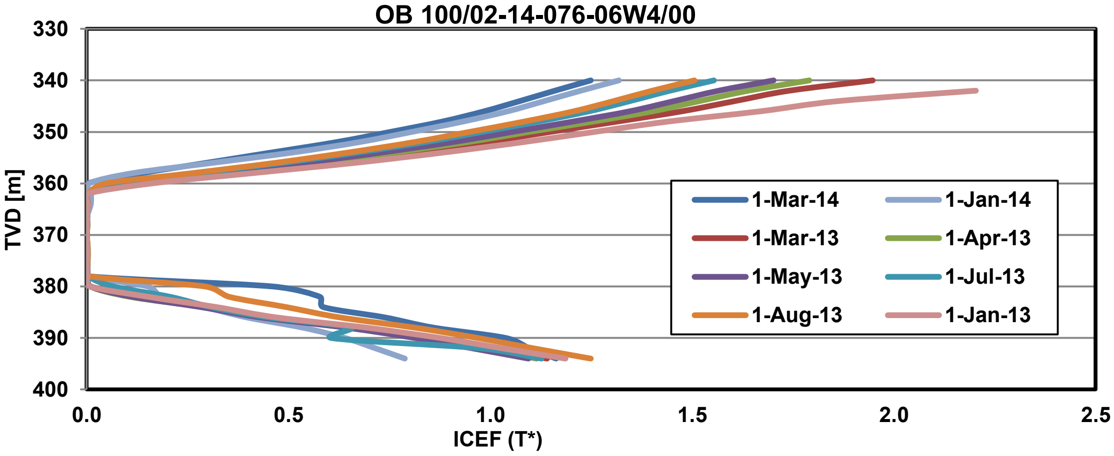

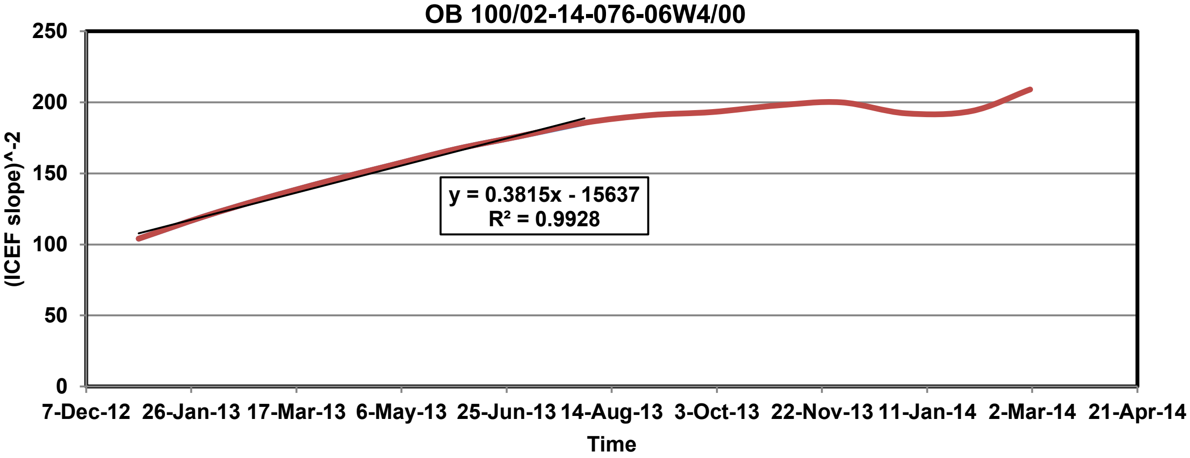

OB 100/09-11-076-06W4/00